ABSTRACT

Title of dissertation: ENGINEERED POTENTIALS IN ULTRACOLD BOSE-EINSTEIN CONDENSATES

Daniel Lawrence Campbell,
Doctor of Philosophy, 2015

Dissertation directed by: Dr. Ian Spielman
University of Maryland Department of Physics
and
National Institute of Standards and Technology

Bose-Einstein condensates (BECs) are a recent addition to the portfolio of quantum materials some of which have profound commercial and military applications e.g., superconductors, superfluids and light emitting diodes. BECs exist in the lowest motional modes of a trap and have the lowest temperatures achieved by mankind. With full control over the shape of the trap the experimentalist may explore an extremely diverse set of Hamiltonians which may be altered mid-experiment. These properties are particularly suited for realizing novel quantum systems.

This thesis explores interaction-driven domain formation and the subsequent domain coarsening for two immiscible BEC components. Because quantum coherences associated with interactions in BECs can be derived from low energy scattering theory we compare our experimental results to both a careful simulation (performed

by Brandon Anderson) and an analytical prediction. This result very carefully explores the question of how a metastable system relaxes at the extreme limit of low temperature.

We also explore spin-orbit coupling (SOC) of a BEC which links the linear and discrete momentum transferable by two counterpropagating "Raman" lasers that resonantly couple the ground electronic states of our BECs. SOC is used similarly in condensed matter systems to describe coupling between charge carrier spin and crystal momentum and is a necessary component of the quantum spin Hall effect and topological insulators.

SOC links the linear and discrete momentum transferable by two counterpropagating "Raman" lasers and a subset of the ground electronic states of our BEC. The phases of an effective 2-spin component spin-orbit coupling (SOC) in a spin-1 BEC are described in Lin et al. (2011). We measure the phase transition between two phases of a spin-1 BEC with SOC which cannot be mimicked by a spin-1/2 system. The order parameter that describes transitions between these two phases is insensitive to magnetic field fluctuations.

I also describe a realistic implementation of Rashba SOC. This type of SOC is expected to exhibit novel many-body phases [Stanescu et al. 2008, Sedrakyan et al. 2012, Hu et al. 2011].

ENGINEERED POTENTIALS IN ULTRACOLD BOSE-EINSTEIN CONDENSATES

by

Daniel L Campbell

Dissertation submitted to the Faculty of the Graduate School of the
University of Maryland, College Park in partial fulfillment
of the requirements for the degree of
Doctor of Philosophy
2015

Advisory Committee:
Dr. Ian Spielman, Advisor
Professor Steven Rolston, Chair
Professor Mohammad Hafezi
Professor Amy Mullin
Dr. Trey Porto

Contact Information: Ian Spielman

Daniel Campbell
dlcamp@umd.edu; Ph.- 585-729-1745

Table of Contents

List of Figures

List of Tables

Name	Acronym	Section	Page
Bose-Einstein condensate	BEC	1	1
Spin-orbit coupling	SOC	1	2
Harmonic oscillator	HO	2.2	6
Critical temperature	T_c	Eq. 2.11	8
Boltzmann's constant	k_B	2.2	6
Number of atoms in thermal modes	N_{th}	2.7	8
Number of atoms in the BEC	N_0	2.4.2	9
Chemical potential	μ	2.2	6
Time of flight	TOF	2.5.3	12
BEC wavefunction	ψ		
BEC density	$n = N\|\psi\|^2$		
Spinor eigenvalue	ϕ		
Many-body wavefunction	Ψ	Eq. 3.12	20
Thomas-Fermi approximation	TF	2.5.3	12
Healing length	ξ	3.3.1	28
Dipole Hamiltonian	H_{dip}	Eq. 4.5	35
Cycling transition		Eq. 4.5	35
Stern-Gerlach		4.4.3	38
Spontaneous emission rate	Γ	4.4.1	37
Adiabatic rapid passage	ARP	4.6.4.1	44
Magnetic field, dc	B_{dc}	4.1	30
Zeeman Hamiltonian	$\hat{H}_{\text{Z}}$	Eq. 4.2	33
Bohr magneton	μ_B	4.3.2	35
Rotating wave approximation	RWA	4.3.3	36
Gross-Pitaeveskii equation	GPE	3.2.3	21
spinor GPE	sGPE	5.2.2	53
Power spectral density	PSD	5.5.1	67
Levi-Cevita symbol	$\epsilon_{i,l,m}$	6.2	74
Landé g-factors	g_J, g_F	4.3.2	35
Recoil energy	E_R	6.1	72
Recoil momentum	k_R	6.1	72
Hyperfine spin operator	$\hat{\mathbf{F}}$	4.3.2	35
Reduced matrix element	u	6.2	74
Effective magnetic field	B_{eff}	6.2	75
Vector of Pauli matrices	$\boldsymbol{\sigma}$	8.1.1	119
Quasimomentum	$\mathbf{q}$	6.4	83
Magneto optical trap	MOT	C.2.5	164
Doppler temperature	T_D	C.3.2	172
Recoil temperature	T_R	C.5	174

Chapter 1: Introduction

Bose-Einstein condensation, a macroscopic occupation of bosons into their ground motional state, was first experimentally achieved in 1995 [1, 2] with ultracold neutral alkali atoms. The field of degenerate quantum (ultracold) gases expanded further to include degenerate fermions [3] and spinor gases [4].

Ultracold atoms are, in many ways, ideal platforms for quantum simulation. The potentials of these systems are nearly defect free and extremely configurable: allowing incredible agreement between theory and experiment, and the exploration of various quantum models. Perhaps the most visible example of quantum simulation after Bose-Einstein condensation itself was the realization of the Bose-Hubbard model by ultracold atoms on a 3D lattice [5]. Here, the superfluid to Mott insulator transition was driven (in part) by the play between lattice site-to-site tunneling and weak repulsive on-site interactions between bosons in the lattice. Two-body interactions can strongly modify material properties such as pressure within a Bose-Einstein condensate (BEC). Using molecular Feshbach resonances the magnitude and sign of interactions can be altered to realize the crossover between a Fermi gas and a BEC of paired fermions [6].

When atoms move in a spatially varying spin-dependent optical field they experience geometric vector and scalar potentials. These ideas allow for the engineered addition of spatially homogeneous geometric gauge potentials [7, 8, 9]. Gauge potentials in more conventional materials are characteristic of charged particles experiencing a Lorentz force in the presence of an electromagnetic field. A particle moving in the presence of a strong electric field experiences a boosted (momentum

dependent) magnetic field which couples the atom's internal degrees of freedom to its motion. In many cases, the resulting atomic Hamiltonian is equivalent to iconic models of spin-orbit coupling (SOC): Rashba, Dresselhaus and combinations thereof. As a result, interesting phenomena such as the quantum spin Hall effect [10, 11] and topological insulating-like states [12, 13] become accessible by ultracold atomic systems.

Relative to the two state electron (spin-1/2) dimensionality, the expanded ground state spin-dimensionality available to most ultracold atoms enables SOC that cannot be found elsewhere [14, 15]: for example, producing SOC with a nematic spin ordering [16]. By contrast, Rashba SOC found in electron systems cannot easily be produced for alkali atoms. SOC in ultracold gases is known to modify the interactions of ultracold bosons [7, 17] but the non-abelian nature of its gauge potential is expected to produce unconventional condensation or a composite Fermion state in bosons [18, 19] and pairing in fermions [20]. We propose a mechanism to realize this form of SOC in ^{87}Rb.

1.1 Thesis Overview

Chapter 2 introduces the non-interacting theory of Bose-Einstein condensation of dilute gases.

Chapter 3 introduces 2-body interactions in BECs. The Gross-Pitaeveskii equation and the Bogoliubov derived excitation spectrum are introduced.

Chapter 4 includes a brief description of the glass cell and surrounding coils for magnetic field control. This chapter also introduces the optical and magnetic fields necessary to manipulate our atomic cloud of ^{87}Rb. First, we describe why Rb-Li mixtures were abandoned. Then we introduce the level structure of ^{87}Rb and the Zeeman Hamiltonian. The remainder of the chapter describes the optical dipole trap and dc, ac and gradient magnetic field control.

Chapter 5 introduces our lab's first experiment. We initially prepare a uniform mixture of immiscible spin states, which is maximally out of equilibrium in spin, and the resulting instability exponentially gains the amplitude of spin noise at a characteristic spatial frequency. We observe the resulting spin (domain) structure coarsen.

Chapter 6 discusses the practical aspects of producing SOC in ^{87}Rb. Beginning the chapter we introduce the theory for 2-photon optical state control (Raman coupling) with light detuned far from the electronic excited states. We initially illustrate the relationship between the optical illumination and the SOC Hamiltonian. The details of a system where adjacent pairs of spin states are separately SO coupled (spin-1 SOC) follows at the end of the chapter.

Chapter 7 explores the full phase diagram of spin-1 SOC. We introduce an equivalence between the equilibrium magnetization and the location/existence of minima in the SOC momentum dispersion. Miscibility, a signature of many-body physics and dynamics along the 1st order phase transition are also explored.

Chapter 8 describes an experimentally realistic method for obtaining Rashba SOC fully in the spin-1 ground manifold of ^{87}Rb.

Appendix A describes the entire ultra-high vacuum portion of the apparatus.

Appendix B describes the locking of our lasers to the Doppler-free spectrum

Appendix C introduces the laser trapping and cooling setup for our experiment.

Appendix D describes the magnetic trap stage and forced evaporation.

Appendix E describes the optical dipole trap load from the magnetic trap and evaporative cooling.

Appendix F contains the approximate sequence of fields necessary to produce a BEC from a magneto-optical trap.

Chapter 2: Bose-Einstein Condensation

2.1 Introduction

Fundamental particles fall into two classes: fermions, systems of which obey Fermi-Dirac quantum statistics; and bosons, which obey Bose-Einstein statistics. These distinctions arise when we consider the exchange of coordinate and angular momentum of two identical particles. The state vector of two identical fermions is antisymmetric under exchange, a requirement that cannot be satisfied for two particles in exactly the same state. Meanwhile, the exchange of identical bosons is symmetric: many identical bosons may coexist in the same quantum state. It is a result of the spin-statistics theorem that particles with integer spin are bosons while particles with half-integer spin are fermions.

Composite spin systems, such as atoms, obey the same statistics with respect to their total angular momentum. At sufficiently low temperatures, bosons undergo a quantum phase transition where a significant fraction of the atoms (macroscopically) occupy the motional ground state of the system: this phenomenon is called Bose-Einstein condensation. In this chapter we consider the non-interacting properties of a condensed system (see also Ch. 2 of Ref. [21] and Ch. 5 of Ref. [22]).

2.2 Bose Distribution

Many aggregate thermodynamic properties such as the free energy and entropy can be expressed in terms of a partition function. A partition function for an ensemble of particles is constructed by summing over configurations of modes and

their occupations. We define a mode as a discrete motional state in phase space, i.e. a mode of the 3D quantum harmonic oscillator (HO) with energy $\epsilon_{n_1,n_2,n_3} = \hbar\omega_1(n_1+1/2)+\hbar\omega_2(n_2+1/2)+\hbar\omega_3(n_3+1/2)$ is uniquely determined by $l = (n_1, n_2, n_3)$ for $n_i \in \mathbb{N}$ where $\hbar\omega_i$ for $i \in \{1, 2, 3\}$ are characteristic energies. The l'th mode has Boltzmann weight $\exp[-\epsilon_l/k_BT]$ which is a function of mode energy ϵ_l and temperature T where k_B is Boltzmann's constant. When this mode is occupied by N particles we simply exponentiate the Boltzmann weight by N. The l'th mode of the grand canonical partition function Z can be occupied by a number of particles that range from 0 to ∞ particles: we sum over these possibilities. By contrast, the relative occupation of two different modes is independent: we multiply these possibilities. The grand canonical partition function

$$Z = \prod_l \sum_{n_l}^{\infty} (z \exp(-\beta\epsilon_l))^{n_l} = \prod_l \frac{1}{1 - ze^{-\beta\epsilon_l}} \tag{2.1}$$

includes a fugacity $z = \exp(-\mu/k_BT)$ that sets the number of particles in the system using a term with units of energy: the chemical potential μ. μ corresponds to the additional cost of adding another particle to a mode. The average occupation number per mode

$$f_l = -\frac{1}{\beta}\frac{\partial \ln Z}{\partial \epsilon_l} = \frac{1}{e^{\beta(\epsilon_l-\mu)} - 1} \tag{2.2}$$

is the Bose distribution.

2.3 Density of modes

We consider a collection of 3D harmonically trapped bosons in a single spin state. This system is described by a Hamiltonian $H = \sum_i^3 p_i^2/2m + m\omega_i^2 x^2/2$ where i indexes the Cartesian vector components of the system: p_i is the momentum operator, x_i is position operator, m is the mass, and $\omega_i/2\pi$ is the characteristic trap frequency.

The l'th mode of the quantum HO has energy

$$\epsilon_l = \sum_i^3 \hbar\omega_i(n_i + 1/2) \tag{2.3}$$

and the wavefunction expressed in terms of Hermite polynomials H_{n_i} is

$$\psi_l(\mathbf{x}) = \prod_{i=1}^{3} \left(\frac{m\omega_i}{\pi\hbar}\right)^{1/4} \frac{1}{\sqrt{2^{n_i} n_i!}} H_{n_i}\left(\sqrt{\frac{m\omega_i}{\hbar}}x\right) \exp\left(-m\omega_i^2 x^2\right)/2\hbar. \tag{2.4}$$

In the limit where $\epsilon = \sum_i^3 \hbar\omega_i n_i \gg \hbar\omega_i$, relevant for thermal modes, it is convenient to define the number of modes below ϵ in energy. We take the continuum limit and calculate the mode "volume"

$$G(\epsilon) = \frac{1}{\hbar^3\bar{\omega}^3} \int_0^{\epsilon} d\epsilon_1 \int_0^{\epsilon-\epsilon_1} d\epsilon_2 \int_0^{\epsilon-\epsilon_1-\epsilon_2} d\epsilon_3 = \frac{\epsilon^3}{6\hbar^3\bar{\omega}^3} \tag{2.5}$$

where $\epsilon_i = \hbar\omega_i n_i$ and $\bar{\omega}^3 = \omega_1\omega_2\omega_3$. The "density" of modes (also called density of states) is the number of modes at or near ϵ in energy and may be determined from $g(\epsilon) = \partial_\epsilon G(\epsilon)$

$$g(\epsilon) = \frac{\epsilon^2}{2\hbar^2\bar{\omega}^3} \tag{2.6}$$

2.4 Properties of condensation

2.4.1 Transition temperature

We distinguish between "BEC" modes, which are macroscopically occupied, and "thermal" modes which are all the other modes. Condensation may occur in any local minimum of a potential but these tend to be short lived unless they are also the ground state of the system. For the ensuing discussion we assume there is only one macroscopically occupied mode. The number of particles $N_{\rm th}$ not in the BEC is given by the sum with respect to energy ϵ over the product of the density of states

$g(\epsilon)$ and the occupation of each state f_ϵ. We had cast Eq. 2.2 into the continuum limit so that $f_l \to f(\epsilon)$ when the mode energy $\epsilon_l \to \epsilon$

$$N_{\text{th}} = \int_0^\infty d\epsilon g(\epsilon) f(\epsilon) \tag{2.7}$$

A necessary condition for condensation is that the μ be very near zero. At fixed temperature and $\mu = 0$ a particle added to the system is added (without cost) directly to the ground mode, not the thermal modes. When $\mu = 0$ we further introduce a transition temperature T_c at which the total number of atoms in the system N equals the number of atoms in the thermal distribution N_{th}.

$$N = N_{\text{th}} = \int_0^\infty d\epsilon \frac{\epsilon^2}{2\hbar^2\bar{\omega}^3} \frac{1}{e^{\epsilon/k_B T_c} - 1}. \tag{2.8}$$

We make a change of variables in Eq. 2.8: $x = \epsilon/k_B T_c$. Using the identities for the Gamma function and the Riemann zeta function we perform the integration and obtain

$$\int_0^\infty dx \frac{x^{\alpha-1}}{e^x - 1} = \Gamma(\alpha)\zeta(\alpha) \tag{2.9}$$

$$N = \frac{(k_B T_c)^3}{\hbar^3\bar{\omega}^3} \int_0^\infty \frac{x^2}{e^x - 1} = \frac{(k_B T_c)^3 \Gamma(3)\zeta(3)}{\hbar^3\bar{\omega}^3}. \tag{2.10}$$

We then solve for the critical temperature

$$T_c = \frac{\hbar\bar{\omega} N^{1/3}}{k_B(\Gamma(3)\zeta(3))^{1/3}}. \tag{2.11}$$

For the typical BEC experiment $N \approx 5 \times 10^5$ atoms, $\bar{\omega} = h \times 45$ Hz, $T_c = 127$ nK. In the case of an ideal gas, $k_B T$ has an interpretation as a thermal kinetic energy; Boltzmann statistics for N indistinguishable "classical" particles would lead us to expect substantial occupation of the ground state only when the temperature neared $\hbar\bar{\omega}/k_B \approx 2$ nK. The factor of 50 between $k_B T_c$ and $\hbar\bar{\omega}$ highlights the degree to which

Bose statistics establishes a preference for occupation of the ground state.

2.4.2 Condensate fraction

As the temperature decreases from T_c the fraction of atoms in the BEC increases very rapidly. It is convenient to parameterize the BEC fraction in terms of a dimensionless fraction T/T_c and fraction of atoms in the thermal states $N_{\rm th}(T)/N_{\rm th}(T_c)$. For an ensemble of atoms loaded into a 3D HO potential and for $T < T_c$ the thermal fraction is

$$N_{\rm th}(T) = \frac{(k_B T)^3 \Gamma(3)\zeta(3)}{\hbar^3 \bar{\omega}^3}. \tag{2.12}$$

Putting everything together we find the fraction of atoms in the BEC N_0/N where N_0 is the number of atoms in the BEC.

$$N_0(T)/N = 1 - N_{\rm th}(T)/N_{\rm th}(T_c) = \left(1 - \left(\frac{T}{T_c}\right)^3\right). \tag{2.13}$$

The N_0 rapidly approaches a significant fraction of N for temperatures modestly below T_c, i.e. one out of every 8 atoms is in the BEC when $T = T_c/2$.

2.4.3 Number of particles per mode

The number of particles per unit volume (the density in the conventional sense) outside of the BEC is

$$n_{\rm th}(\mathbf{r}) = \int \frac{d\mathbf{p}}{(2\pi\hbar)^3} \frac{1}{e^{[\epsilon(\mathbf{r},\mathbf{p})-\mu]/k_B T} - 1} \tag{2.14}$$

where $\epsilon(\mathbf{r},\mathbf{p}) = \sum_i p_i^2/2m + m\omega_i^2 x_i^2/2$ and i indexes Cartesian coordinates. The average number of particles per mode is the product of this conventional density and the mode volume defined by the thermal de Broglie wavelength: $D = \lambda_T^3 n_{\rm th}(\mathbf{r})$,

where

$$\lambda_T = \sqrt{2\pi\hbar^2/mk_BT} \tag{2.15}$$

is the thermal de Broglie wavelength. Evaluating the integral in Eq. 2.14, the number of particles per mode is

$$D(\mathbf{r}) = g_{3/2}[z(\mathbf{r})], \tag{2.16}$$

where where $z(\mathbf{r}) = (\mu - \sum_i m\omega_i^2 x_i^2/2)/k_BT$ and

$$g_\gamma[z] = \sum_{n=1}^{\infty} \frac{z^n}{n^\gamma} \tag{2.17}$$

is the polylog series. The fugacity $z(0) = \exp(\mu - V(0))/k_BT$ is related to the total number of particles in thermal modes of the system by

$$N_{\rm th} = g_3[z(0)] \left(\frac{k_BT}{\hbar\bar{\omega}}\right)^3. \tag{2.18}$$

At the cusp of condensation (and beyond!) the particle number per mode of the thermal part of the system is $\zeta_{3/2} \approx 2.6$ and $\zeta_3 \approx 1.2 = N_{\rm th}(\hbar\bar{\omega}/k_BT)$. As we might expect, large atom numbers, strong confinement and low temperatures favor condensation. The particle number per mode of the BEC D_0 is equivalent to the particle number in the BEC, $D_0 = N_0$: often, $D_0 \approx 10^5 - 10^6$.

Our computation of particle numbers per mode is modified somewhat when the more physical summation over discrete modes is performed. The validity of the continuum limit breaks down for the least energetic modes, whose spatial extents are less than/comparable to the de Broglie wavelength.

2.5 Position and Momentum profile

2.5.1 Density profile of the ground state

This section should be viewed qualitatively since the BEC density profile and momentum profiles are heavily modified by interactions. Without interactions the wavefunction of a BEC in position coordinates is the solution to the quantum HO given by the ground state of Eq. 2.4

$$\psi(\mathbf{x}) = \frac{1}{\pi^{3/4}(\prod_i a_i)^{1/2}} \exp\left(-\sum_i x_i^2/2a_i^2\right) \tag{2.19}$$

where i indexes Cartesian coordinates. $|\psi(\mathbf{x})|^2$ has a $1/e$ radius of

$$a_i = \sqrt{\frac{\hbar}{m\omega_i}}. \tag{2.20}$$

In our potential $V(\mathbf{x}) = \sum_i m\omega_i^2 x_i^2/2$, where the trap frequencies $\omega_i/2\pi$ do not equal one another, the BEC density $n_0(\mathbf{x}) = N_0|\psi(\mathbf{x})|^2$ is anisotropic. Similarly, the Fourier transform of Eq. 2.19, which transforms the wavefunction into momentum coordinates is

$$\psi(\mathbf{p})\frac{1}{\pi^{3/4}(\prod_i \tilde{a}_i)^{1/2}} \exp\left(-\sum_i p^2/2\tilde{a}_i^2\right) \tag{2.21}$$

where the $1/e$ extent in momentum is

$$\tilde{a}_i = \frac{\hbar}{a_i} = \sqrt{m\hbar\omega_i}. \tag{2.22}$$

We see that the anisotropy of the momentum density profile $n_0(\mathbf{p}) = N_0|\psi(\mathbf{p})|^2$ is the inverse of the position profile: if $a_x > a_y$ then $\tilde{a}_x < \tilde{a}_y$. In the presence of interactions this relationship between position- and momentum-dependent anisotropies remains.

2.5.2 Density profile of the thermal modes

Due to the large number and low phase space density of thermal states it is conventional to describe this part of the system with an ensemble average. In addition, the interactions play less of a role because of the low densities. We use Eq. 2.14 in the classical limit where $\exp[-(\mathbf{p}^2/2m + V(\mathbf{x}))/k_BT] \ll 1$

$$n_{\rm th}(\mathbf{x}) = \int \frac{d\mathbf{p}}{(2\pi\hbar)^3} \exp\left[-(\mathbf{p}^2/2m + V(\mathbf{x}))/k_BT\right] = \frac{N_{\rm th}}{\pi^{3/2}\prod_i R_i} \exp\left(-\sum_i x_i^2/R_i^2\right) \tag{2.23}$$

where the thermal width of the momentum distribution

$$R_i = \sqrt{\frac{2k_BT}{m\omega_i^2}} \tag{2.24}$$

which is typically much larger than the radius a_i of the BEC wavefunction. The momentum distribution, however, is isotropic in the classical limit:

$$n_{\rm th}(\mathbf{p}) = \int \frac{d\mathbf{x}}{(2\pi\hbar)^3} \exp\left[-(\mathbf{p}^2/2m + V(\mathbf{x}))/k_BT\right] = \frac{1}{(m\lambda_T\bar{\omega})^3} \exp\left(-\sum_i p_i^2/2mk_BT\right) \tag{2.25}$$

where the radius of the momentum distribution is $\tilde{R} = \sqrt{mk_BT}$.

2.5.3 Time of Flight

It is often desirable to release a cold gas of atoms from its confinement, allowing time of flight (TOF) expansion. For $t > \min(\omega_i^{-1})$, where $\min(\omega_i^{-1})$ is the smallest trap frequency in units of rad/s, the initial momentum space profile of both the BEC and thermal fractions of the gas become proportional to the profile in position coordinates of the expanding gas (we choose a frame of reference that accelerates with gravity). The expansion of the BEC in TOF is strongly modified in the presence

of interactions but we typically treat thermal clouds as if they are non-interacting.

When the potential is set to zero, the non-interacting BEC wavefunction, $\psi(\mathbf{p})$, undergoes time evolution for a free particle $\exp[-iE/\hbar]$, where $E = \mathbf{p}^2/2m$. We calculate the time evolution of the wave function in momentum coordinates, then switch back to position coordinates

$$\begin{aligned}\psi(\mathbf{x},t) =& \int \frac{d\mathbf{p}}{(2\pi\hbar)^{3/2}}\psi(\mathbf{p},t=0)\exp\left(-i\mathbf{p}^2t/2m\hbar\right)\exp\left(i\mathbf{p}\cdot\mathbf{x}/\hbar\right) \\ =& \frac{1}{\pi^{3/4}\prod_i a_i\sqrt{1+i\omega_i t}}\exp\left(-\sum_i x_i^2/(2a_i+2ia_i\omega_i t)\right)\end{aligned} \tag{2.26}$$

when the TOF time becomes larger than $\min(\omega_i^{-1})$, the position profile of the BEC becomes $\tilde{a}_i t/m = \sqrt{\hbar\omega_i/mt}$; this is proportional to the original momentum profile of the BEC. For an anisotropic potential and for sufficiently long TOF the momentum profile is always anisotropic.

When the thermal part of the gas is released into TOF the gas is no longer in thermal equilibrium and each individual particle obeys the equations of motion

$$\dot{\mathbf{r}} = \mathbf{p}/m,\ \dot{p} = 0 \tag{2.27}$$

for time evolution in the absence of an external force. Using these equations of motion, we apply a change of variables $\mathbf{p}(t) = \mathbf{p}$ and $\mathbf{x}(t) = \mathbf{x} + \mathbf{p}t/m$ to the distribution of the gas:

$$\begin{aligned}f(\mathbf{r},\mathbf{p},t) =& \exp\left(-\sum_i p_i(t)^2/2m + m\omega_i^2 x_i^2(t)\right) \\ =& \exp\left(-\left[\sum_i p_i^2/2m + m\omega_i^2(x_i+p_it/m)^2 - \mu\right]/k_BT\right)\end{aligned} \tag{2.28}$$

equivalent to Boltzmann's classical distribution function at $t = 0$. We compute the

time-evolving density

$$
\begin{aligned}
n(\mathbf{x},t) =& \int \frac{d\mathbf{p}}{(2\pi\hbar)^3} f(\mathbf{r},\mathbf{p},t) \\
=& \frac{1}{\lambda_T^3 \prod_i \sqrt{1+\omega_i^2 t^2}} \exp\left(-\sum_i m\omega_i^2 x_i^2 / 2k_B T(1+\omega_i^2 t^2)\right) \exp\left(\mu/k_B T\right)
\end{aligned}
\tag{2.29}
$$

For $t > \min(\omega_i^{-1})$ the profile of the expanding thermal gas becomes isotropic and proportional to the $t = 0$ momentum distribution: $\tilde{R}t/m = \sqrt{2k_B T/m}t$.

As a result, even for a non-interacting BEC, the anisotropic expansion of the BEC from an anisotropic trap serves as a signature of Bose-Einstein condensation. Figure 2.1a illustrates the $1/e$ radii contour at both $t = 0\,\text{sec}$ and $0.1\,\text{sec}$ TOF for the BEC and thermal gases. Figure 2.1b illustrates the 1/e radii as a function of time. These radii qualitatively describe BEC expansion but quantitatively fall far short of the actual TOF expansion in the presence of strong interactions.

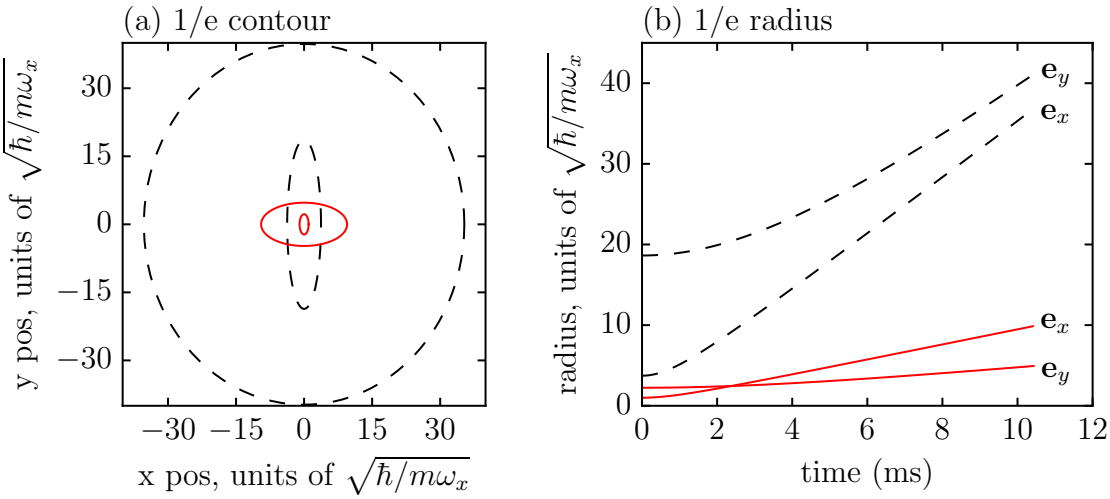

Figure 2.1: Density profile widths for non-interacting (and somewhat non-physical) BECs (a) Contour where amplitude of BEC (solid red) and thermal (dotted black) falls to 1/e of peak value. Each component of the gas (BEC or thermal) has an inner, in-situ ($t = 0$), contour and an outer, TOF ($t - 0.01\,\mathrm{sec}$), contour. (b) 1/e amplitude for different Cartesian directions, $\mathbf{e}_x$ and $\mathbf{e}_y$, over 11 ms TOF. 1/e widths in both panels are normalized to $\sqrt{\hbar/m\omega_x}$: the BEC $1/e$ radius in the orientation of its tightest confinement. This plot was produced for the following gas parameters: trap frequencies, 150 Hz along $\mathbf{e}_x$ and 30 Hz along $\mathbf{e}_y$; temperature of 50 nK; and mass given by ^{87}Rb.

Chapter 3: Interactions

So far we have neglected the impact of interactions on Bose-Einstein condensation. Two-body interactions are an essential mechanism for thermalization during the evaporative cooling stage of BEC production. As a result, the atomic isotopes that are cooled to quantum degeneracy interact, oftentimes strongly. Interactions modify the density profile of the condensed state and are necessary for the condensed state to exhibit a phonon dispersion. Additionally, vortex production under rotation and other phenomena associated with a superfluid excitation spectrum only occur in the presence of interactions.

3.1 Low energy collisions

For neutral atoms the two-particle interaction potential results from an induced dipole between colliding atoms, known as the van der Waals potential. During the collision the particles may have multiple collision channels associated with the 2-body orbital angular momentum. These collision channels are indexed with integer values of ℓ and contribute to a centrifugal barrier term in the two-particle interaction potential [1]

$$U(\mathbf{R}) = -\frac{C_6}{\mathbf{R}^6} + \frac{\hbar^2 \ell(\ell+1)}{m\mathbf{R}^2}. \tag{3.1}$$

where m is the mass of each boson, $\mathbf{R}$ is the atom-atom separation and the van der Waals coefficients C_6 generally increase with atom size and are tabulated in Ref. 3.1.

[1] (see Ch. 5 of Ref. [21]

Element	$C_6/e^2a_0^2$ [24]	$T_{\max}$ (mK)
H–H	6.5	442
^7Li–^7Li	1389	24
^{23}Na–^{23}Na	1556	4
^{39}K–^{39}K	3897	1.8
^{87}Rb–^{87}Rb	4691	0.5
^{133}Cs–^{133}Cs	6851	0.3

Table 3.1: Calculated van der Waals coefficients C_6 for the attractive potential $-C_6/r^6$ characteristic of long range interactions between neutral atoms. For identical bosons there exists a temperature $T_{\max}$ below which collisions with total orbital angular momentum $\ell \geq 2$ do not occur.

As the separation R increases, the attractive short range potential gives way to the repulsive centrifugal term. In the case of identical bosons only even integer ℓ are consistent with wavefunction symmetrization. When the relative kinetic energy of colliding particles is smaller than the maximum height of the centrifugal barrier term at $\ell = 2$ identical bosons only interact with the $\ell = 0$ potential and scatter isotropically [2].

We may solve for when the thermal kinetic energy $3k_BT/2$ equals the local maximum of the potential $U_{\max}$ in Eq. 3.1 at $\ell = 2$

$$\frac{3k_BT}{2} = U_{\max} \rightarrow T = \frac{4}{3k_B} C_6 \left(\frac{\hbar^2}{C_6 M_r} \right)^{3/2} \tag{3.2}$$

where M_r is the reduced mass. The result indicates the temperature $T_{\max}$ at which the $\ell = 2$ collision channel begins to freeze out in an equilibrium trapped thermal Bose gas [3].

3.1.1 Partial waves

When the de Broglie wavelength of colliding atoms is much larger than the range of atom-atom separations where the 2-body interaction potential rapidly changes their scattering cross section becomes insensitive to their relative kinetic energies. This

[2] $\ell = 1$ is forbidden by statistics, see Ch. 14 of ref. [23]

[3] see Ref. [23] for a vastly more general discussion of this topic

phenomenon can be understood as an approximation of the partial wave scattering formalism.

Partial wave scattering describes the wavefunction of two scattering particles as the sum of a plane wave approaching a collision along $\mathbf{e}_z$ and a plane wave outgoing along $\mathbf{e}_r$

$$\psi = e^{ikz} + f(\theta)\frac{e^{ikr}}{r} \tag{3.3}$$

The amplitude $f(\theta)$ describes probability of measuring a particle outgoing from a scattering center at angle *theta* from $\mathbf{e}_z$. The wavefunction ψ has axial symmetry and therefore may be expanded in terms of Legendre polynomials $P_\ell(cos\theta)$

$$\psi = \sum_{\ell=0}^{\infty} A_\ell P_\ell(cos\theta) R_{k\ell}(r) \tag{3.4}$$

where $\ell = \{0, 1, 2, ...\}$ correspond to the $s, p, d, ...$ partial wave terms in the summation of Eq. 3.4. The radial portion of the wavefunction $\psi = R_{k,\ell}\Theta_{k,\ell}$ satisfies the Lipmann-Schwinger equation

$$\left[\partial_r^2 + \frac{2}{r}\partial_r + k^2 - \frac{\ell(\ell+1)}{r^2} - \frac{mC_6}{\hbar^2 r^6}\right] R_{k,\ell} = 0. \tag{3.5}$$

We make the approximation that the de Broglie wavelength is large in comparison to the radial extent of the two-body interaction potential and simplify the radial wavefunction to

$$R_{k\ell} \approxeq \frac{1}{k\ell}\sin\left(kr - \ell\pi/2 + \delta_\ell\right) \tag{3.6}$$

where the phase shifts δ_ℓ depend in a complicated way upon the shape of the short range 2-body interaction potential. Atoms with larger C_6 coefficients have a larger characteristic extent for their 2-body interaction potential and may therefore have

a larger phase shifts. As the wavevector tends towards the low energy limit $k \to 0$ we solve for the $\ell = 0$ phase shift δ_0 of the asymptotic wavefunction as a function of k: $\delta_0 = -ka$, where a is called the s-wave scattering length.

For this treatment to be valid the typical spacing between particles must be large in comparison to the spatial extent of the 2-body interaction potential so that there is no cross coupling between multiple scattering events.

Using Eqs. 3.3, 3.4, and 3.6 it is possible to solve for $f(\theta)$ and obtain the s-wave scattering cross-section

$$\sigma_{\text{scatt.}} = \int |f(\theta)|^2 \mathrm{d}\mathbf{\Omega} = \frac{8\pi}{k^2} \sum_{\ell} (2\ell + 1) \sin^2 \delta_\ell \approx 8\pi a^2 \text{ for } \ell = 0 \tag{3.7}$$

which depends on the scattering length a alone. Here, $\mathrm{d}\mathbf{\Omega}$ is the differential solid angle and $\int \mathrm{d}\mathbf{\Omega} = 4\pi$.

Using the Born approximation, we link our s-wave scattering length to an effective 2-body pseudo-potential, $U(\mathbf{R})$

$$a = \frac{m}{4\pi\hbar^2} \int d\mathbf{R} U(\mathbf{R}) = \frac{mL^3}{4\pi\hbar^2} U_0 \tag{3.8}$$

where $\mathbf{R}$ is the interparticle separation and L^3 is the volume. In coordinate space, the effective potential

$$U_0 = \frac{4\pi\hbar^2 a}{m} \tag{3.9}$$

replaces the complicated interatomic potential $U(\mathbf{r}, \mathbf{r}') = U_0 \delta(\mathbf{r} - \mathbf{r}')$.

3.2 Interaction Hamiltonian

We consider N identical bosons, each is indexed with i or j with position $\mathbf{r}_i$ and momentum $\mathbf{p}_i$, trapped in a single-particle potential $V(\mathbf{r}_i)$ that interact with an effective contact interaction, $U_0 \delta(\mathbf{r}_i - \mathbf{r}_j)$. The Hamiltonian describing this interacting

Element	Triplet scattering length a[a_0]	Source
^{7}Li	-27.6(0.5)	[25]
^{23}Na	65.3(0.9)	[26]
^{41}K	65(8)	[27]
^{87}Rb	103(5)	[28]
^{133}Cs	2400(100)	[29]

Table 3.2: Triplet scattering length values for Alkali atoms.

system is

$$H = \sum_{i}^{N} \left[\frac{\mathbf{p}_i^2}{2m} + V(\mathbf{r}_i) \right] + \frac{U_0}{2} \sum_{i,j}^{N} \delta(\mathbf{r}_i - \mathbf{r}_j) \tag{3.10}$$

3.2.1 Mean field approximation

We sum the wavefunction of each boson indexed by i with location r_i to generate the many-body wavefunction

$$\Psi(\mathbf{r}) = \sum_{i} \phi(\mathbf{r_i}) \tag{3.11}$$

whose dynamics are governed by the Schrödinger equation and the Hamiltonian in Eq. 3.10. We adopt the mean field approximation and decompose this many-body wavefunction

$$\Psi(\mathbf{r}) = \psi(\mathbf{r}) + \Psi'(\mathbf{r}) \tag{3.12}$$

in terms of the expectation value of many-body wavefunction in the ground state $\psi(\mathbf{r}) = \langle \Psi(\mathbf{r}) \rangle$ and the typically small portion of the many-body wavefunction that is not in the BEC, $\Psi'(\mathbf{r})$. The complex function $\psi(\mathbf{r})$ is known as the BEC wavefunction. In the absence of external perturbations the energy of the system is minimized when the BEC wavefunction varies smoothly: this indicates that $\psi(\mathbf{r}) \approx \sqrt{N_0}\phi(\mathbf{r})$. This approach is valid in the limit where $N_0 \gg 1$.

We compose a new Hamiltonian which governs the evolution of this BEC

wavefunction

$$H = \frac{p^2}{2m} + V(\mathbf{r}) + U_0|\psi(\mathbf{r})|^2 \tag{3.13}$$

3.2.2 Energy

The expectation value of the Hamiltonian with respect to the condensed state $\psi(\mathbf{r}, t)$ is

$$E = \int d\mathbf{r}\psi^\dagger(\mathbf{r}, t)\left[\frac{\hbar^2\boldsymbol{\nabla}^2}{2m} + V(\mathbf{r}) + U_0|\psi(\mathbf{r}, t)|^2\right]\psi(\mathbf{r}, t). \tag{3.14}$$

This energy functional $E[\psi]$ evidently is modified by the sum over a density dependent and non-linear term introduced by the interactions.

3.2.3 Gross-Pitaeveskii equation

The time dependent Schrödinger equation for the interacting Hamiltonian acting on the BEC wavefunction acquires a density dependent term from the interactions

$$i\hbar\partial_t\psi(\mathbf{r}, t) = \left[\left(\frac{\mathbf{p}^2}{2m} + V(\mathbf{r})\right) + U_0|\psi(\mathbf{r}, t)|^2\right]\psi(\mathbf{r}, t) \tag{3.15}$$

which is the Gross-Piteaveskii equation (GPE). In an equilibrium system the time evolution of $\psi(\mathbf{r}, t)$ is simply $\psi(\mathbf{r}, t) = \exp(-i\mu t/\hbar)\psi(\mathbf{r})$. Schrödinger 's equation simplifies to

$$\mu\psi(\mathbf{r}) = \left[\left(\frac{\mathbf{p}^2}{2m} + V(\mathbf{r})\right) + U_0|\psi(\mathbf{r})|^2\right]\psi(\mathbf{r}) \tag{3.16}$$

3.2.4 Density profile

The sign and magnitude of interactions plays a large role in the final density profile. Attractive interactions can lead to runaway increases in density that eventually

violate the condition that average interparticle spacing should be much larger than the scattering length. Various loss mechanisms then rapidly deplete the BEC. An exception occurs when the attraction is weak enough that the kinetic energy can offset the tendency of the BEC to collapse [30]. The remainder of this section will consider repulsive interactions. These BECs are stable in the presence of both weak and strong interactions because the repulsive interactions compete with the attractive single-particle potential. In the case of strong interactions and sufficiently high density the density profile is strongly modified from the non-interacting situation.

The equilibrium density distribution of the gas is determined by the competition between both the kinetic energy and the repulsive interactions with the trapping potential. In ultracold gases the energy scale of the repulsive interactions typically dominates that of the kinetic energy. When such is the case, it is common practice to apply the Thomas-Fermi (TF) approximation, which neglects the kinetic energy, for the determination of the equilibrium density profile. We rearrange terms in Eq. 3.16 to find the density

$$n(\mathbf{r}) = \frac{\mu - V(\mathbf{r})}{U_0}, \text{ for } n(\mathbf{r}) > 0 \tag{3.17}$$

where the minimum of the occupied portion of the potential $V(\mathbf{r})$ is defined to be zero, and $\mu = U_0 n_{\text{peak}} \propto E/N$ is the chemical potential (E is the total energy from Eq. 3.14). The density profile of the bulk of the BEC therefore looks like an inverted representation of the lowest portion of $V(\mathbf{r})$, e.g. in a HO the density profile is an inverted parabola, see Fig 3.1.

There exists for any potential a cusp where the density falls to zero. We define a TF radius R_i, where i indexes Cartesian coordinates, inside which the density is finite and outside of which the density is zero. The TF radius is simply related to

the chemical potential for a HO potential

$$R_i = \frac{\sqrt{2\mu}}{\sqrt{m\omega_i}}. \tag{3.18}$$

Meanwhile, the chemical potential is a function of the characteristic trap frequency $\bar{\omega}$, atom number N_0, and scattering length a

$$\mu = \frac{1}{2}\hbar\bar{\omega}\left(15N_0 a\sqrt{\frac{m\bar{\omega}}{\hbar}}\right)^{2/5} \tag{3.19}$$

If the trap frequencies are known, it is possible to calculate the atom number by comparing Eqs. 3.18 and 3.19.

We may compare the spatial extent of the cloud with and without interactions. Then

$$\frac{R_i}{a_i} = \frac{\sqrt{2\mu}}{\sqrt{\hbar\omega_i}} \sim 7 \tag{3.20}$$

where a_i is the non-interacting extent of a BEC. Motivated by the Heisenberg uncertainty principle we claim that for an increase in the spatial extent of the BEC by a factor of 7 there should be a corresponding decrease in the momentum extent, retroactively justifying the TF approximation.

3.2.5 TOF

In the presence of interactions the removal of the trapping potential begins the process of interaction-driven expansion. The density then falls until the gas becomes non-interacting after which time the gas undergoes free expansion.

We introduce a set of dimensionless scaling factors λ_i [4] which rescale the TF

[4] See Castin and Dum Ref. [31]

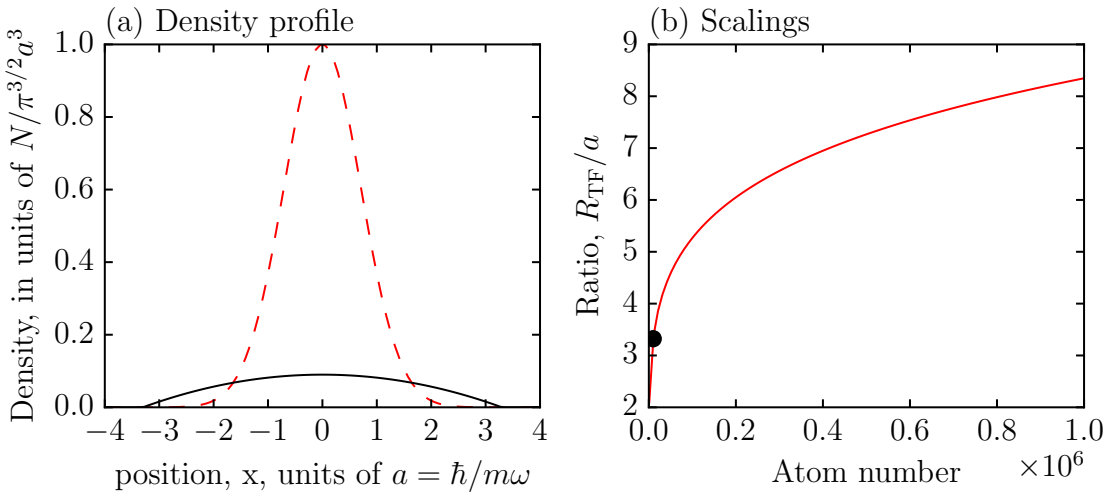

Figure 3.1: (a) Characteristic density profiles for non-interacting (solid red) and interacting (dotted black) 3D gases trapped in an isotropic HO. We normalize the BEC density to $N/\sqrt{\hbar/m\omega}$, where $\omega = 2\pi \times 30$ Hz, $N = 10^4$ and mass, m, is that of ^{87}Rb. (b) Plot of the ratio of the TF radius and the Gaussian width, $a = \sqrt{\hbar/m\omega}$ for various BEC numbers, N_0. In ^{87}Rb, a typical BEC number is $N_0 = 5 \times 10^5$.

radii during the interaction-driven and ballistic stages of TOF expansion.

$$R_i(t) = \lambda_i(t) R_i(0) \tag{3.21}$$

where $R_i(t)$ is the TF radius along $\mathbf{e}_i$ during TOF, $R(0)$ is the equilibrium TF radius, $\lambda_i(0) = 1$, and i indexes cartesian coordinates. When the system is initially in a HO potential, the scaling factors satisfy the differential equations $\dot{\lambda} = 0$ and

$$\ddot{\lambda}_i = \frac{\omega_i^2(0)}{\lambda_i \lambda_1 \lambda_2 \lambda_3} - \omega_i^2(t)\lambda_i, \tag{3.22}$$

in the case of TOF $\omega_i^2(t > 0) = 0$. The initial size $R_i(0)$ and the momentum following TOF are much larger than the non-interacting equivalents.

There are some circumstances when it is desirable to physically separate different spin states in TOF. When a magnetic gradient is applied at the beginning of TOF the density profiles of the different spin states become coupled in a non-trivial

way to the interaction driven expansion. It is safe to separate the different spin components when the time-scale over which the separation occurs is much shorter than $\bar{\lambda}/\bar{\omega}$ where $\bar{l}ambda = (\lambda_1\lambda_2\lambda_3)^{1/3}$ and when the rate of separation is much faster than the speed of sound for the BEC. With $\bar{\omega} \approx 45$ Hz and $\mu \approx h \times 2200$ Hz we found that approximately $8 - 10$ ms of interaction driven expansion followed by 10 ms for spatial separation would separate spin components without damaging the density profile.

As with the non-interacting case, interaction driven expansion is anisotropic when the initial density profile of the gas is anisotropic. This anisotropy is exaggerated with interactions: for a cylindrically symmetric cloud $\alpha(t \to \infty) \sim \alpha^{-1.8}(t = 0)$ where α is the aspect ratio between the radial and axial extents of the cloud.

3.3 Quantum excitations

Interaction-induced quantum excitations link the BEC with its next lowest lying thermal states to produce a phonon-like dispersion of excitations. We apply a formalism attributed to Bogoliubov and de Gennes (BdG) to describe a uniform BEC at zero temperature. This method assumes that the BEC is infinite in spatial extent, the density is homogeneous and the temperature is well below T_c. We should expect this method to fail for very small spatial wavevectors or near the low density periphery of the BEC.

We now switch (we are no longer working solely working with the BEC wavefunction) to the notation of second quantization in our definition of the interaction Hamiltonian so that we can explicitly work with the boson operators

$$H = \int d\mathbf{r} \left[-\Psi^\dagger(\mathbf{r}) \frac{\hbar^2}{2m} \nabla^2 \Psi(\mathbf{r}) + V(\mathbf{r}) \Psi^\dagger(\mathbf{r}) \Psi(\mathbf{r}) + \frac{U_0}{2} \Psi^\dagger(\mathbf{r}) \Psi^\dagger(\mathbf{r}) \Psi(\mathbf{r}) \Psi(\mathbf{r}) \right] \tag{3.23}$$

The idea is to establish a relationship between excitation energy and momentum.

Therefore we expand the boson annihilation operator in terms of the annihilation operators for plane wave states

$$\Psi(\mathbf{r}) = \frac{1}{\mathrm{L}^{3/2}} \sum_k e^{i\mathbf{k}\cdot\mathbf{r}} a_k \tag{3.24}$$

where L^3 is the volume and a_k are bosonic operators. Plugging into Eq. 3.23 the Hamiltonian takes the form

$$H = \sum_k \epsilon_k^0 a_k^\dagger a_k + \frac{U_0}{2\mathrm{L}^3} \sum_{k,k',q} a_{k+q}^\dagger a_{k'-q}^\dagger a_{k'} a_k \tag{3.25}$$

where $\epsilon_k^0 = \hbar^2 k^2/2m$. The annihilation of a boson from the BEC is described by $a_{k=0}$; its contribution to the total energy within the interaction term is related to the number of atoms in the BEC $a_0 |N_0\rangle = \sqrt{N_0} |N_0\rangle$. By contrast, the occupation of each plane wave mode is not a large and relatively unchanging number: the contribution of annihilation operators $a_{k\neq 0}$ to the interaction energy is $\sim 1/\sqrt{N_0}$ smaller. Because of this weighting, we neglect terms more than quadratic in $k \neq 0$. We go further and eliminate terms whose plane wave creation and annihilation operators do not conserve momentum within the term because they are energetically penalized: they do not constitute the lowest energy excitations. Our objective is to find the effective spectrum of quasiparticle excitations: these are the combinations of plane wave excitations which conserve atom number. We write this vastly simplified Hamiltonian

$$\begin{aligned} H &= \frac{N_0^2 U_0}{2\mathrm{L}^3} + \sum_{k\neq 0} (\epsilon_k^0 + n_0 U_0)(a_k^\dagger a_k + a_{-k}^\dagger a_{-k}) + n_0 U_0 \sum_{k\neq 0} (a_k^\dagger a_{-k}^\dagger + a_k a_{-k}) \\ &= \frac{N_0^2 U_0}{2\mathrm{L}^3} + \sum_{k\neq 0} \boldsymbol{\phi}_k^\dagger M_k \boldsymbol{\phi}_k \end{aligned} \tag{3.26}$$

where n_0 is the BEC density and $\boldsymbol{\phi}_k = \{a_{-k}, a_k^\dagger\}^T$ is a two component vector of

operators. M_k is a matrix of coefficients

$$M_k = \begin{pmatrix} \epsilon_k^0 - \epsilon_0^0 + U_0 n_0 & U_0 n_0 \\ -U_0 n_0 & -\epsilon_k^0 + \epsilon_0^0 - U_0 n_0 \end{pmatrix} \tag{3.27}$$

The pair of operators $\boldsymbol{\phi}_k = (a_{-k,\sigma}, a^\dagger_{k,\sigma'})$ does not transform like a vector. Instead we require that the bosonic commutation relations $[a_{k,i}, a^\dagger_{k,j}] = (-\sigma_z)_{i,j}$ be preserved during a transformation T where i and j now index the two elements of $(a_{-k,\sigma}, a^\dagger_{k,\sigma'})$. It transpires that $T^\dagger \sigma_z T$ must equal σ_z to preserve these commutation relations. We want to diagonalize the term $\boldsymbol{\phi}_k^\dagger M_k \boldsymbol{\phi}_k$ to find the excitation spectrum $\nu_{k,\sigma}$: this is equivalent to determining T where $T^\dagger M T = \nu_{k,\sigma}$. In practice, $T^{-1}\sigma_z M T = \sigma_z \nu_{k,\sigma}$ is easier to calculate because the eigenvalues of $\sigma_z M$ may be found using a simple non-Hermitian similarity transform [32].

The eigenvectors $\sigma_z \boldsymbol{\phi}$ of this system are the quasiparticle excitations and correspond to linear combinations of momentum modes with $\pm k$ momenta. The eigenvalues are the dispersion of quasiparticle excitations:

$$\nu_k = \sqrt{\epsilon_k}\sqrt{\epsilon_k + 2U_0 n_0} \tag{3.28}$$

We plot this dispersion in Fig. 3.2.

3.3.1 Coherence length/healing length

The momentum-energy dispersion for a homogeneous single spin component BEC is given in Eq. 3.28. For a homogeneous BEC with infinite extent there exists a linear (phonon) dispersion for wavevectors below a characteristic cutoff $1/\xi$. This dispersion is ungapped and hence the system supports quantum excitations of arbitrarily low energy. For wavelengths smaller than ξ dispersion mimics that of a free particle. In the presence of a phase defect or when a hole is poked into the BEC, the BEC mode can adjust to the presence of the defect over length scales less than

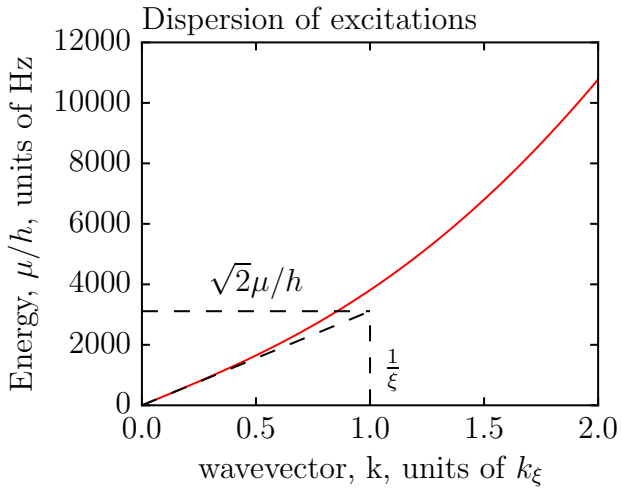

Figure 3.2: Eigenvalues of quasiparticle excitations in single component BEC. Wavevectors are in units of $k_\xi = 1/\xi$ and energy is in units of $\hbar^2 k_\xi^2/2m = \mu$, where ξ is the healing length. The vertical dotted black line denotes cutoff wavevector while the horizontal dotted black line denotes the corresponding energy scale. The diagonal dotted black line is a guide to the eye.

the cutoff, ξ. Over shorter length scales and near a defect only thermal modes exist and the density of the gas decreases to that typical of thermal modes. It is for this reason that xi is called the healing length of the BEC.

The healing length may also be determined by solving for the length scale where the kinetic energy and interaction terms equal one another

$$\frac{\hbar^2}{2m\xi^2} = nU_0 \tag{3.29}$$

$$\xi = \frac{\hbar}{\sqrt{2mU_0 n}} \tag{3.30}$$

where $U_0 n = \mu$.

3.3.2 Speed of sound

The speed of sound is given by the slope of the linear part of the dispersion

$$\frac{E}{p} = \frac{\hbar\omega}{\hbar k} = c \tag{3.31}$$

Using the cutoff kinetic energy and momentum we find the speed of sound for the BEC system

$$c = \frac{\hbar}{2m\xi} = \sqrt{\frac{\mu}{2m}} \tag{3.32}$$

which corresponds to the speed that density excitations propagate through the BEC.

Chapter 4: Engineering optical potentials

4.1 Introduction to the apparatus

The apparatus is an extended glass cell 1.1×1.1 in. wide. As shown in Fig. 4.1 50 turn coils of hollow water cooled square copper tubing are mounted above and below the glass cell. These coils are anti-aligned and form a quadrupole magnetic field with a magnetic field zero at the center of the glass cell. The intersection of two optical dipole beams was made to coincide with the magnetic field zero. These beams serve to trap the atomic cloud when the quadrupole magnetic field is absent. The efficient cooling of atoms trapped in the combined magnetic and optical fields is the subject of Ref. [33].

The quadrupole coils and their stainless steel holders have a SM1 threaded central bore that allow vertical optical access to the atomic cloud. Our primary imaging light travels through the glass cell from top to bottom and illuminates a CCD camera.

Three orthogonal pairs of coaxial coils, where each pair is connected in series, provide dc magnetic field $B_{\rm dc}$ control. Gradient control may be accomplished with three sets of coils in the presence of a > 1 G $B_{\rm dc}$. The desired configuration of coils can depend upon the orientation of the $B_{\rm dc}$.

Spin states can be coupled to one another using ac magnetic fields. We print one or two copper loops on a printed circuit board (PCB) to serve as an rf antenna. We slide this PCB in the gap between the glass cell and the nearest surface of the quadrupole coils.

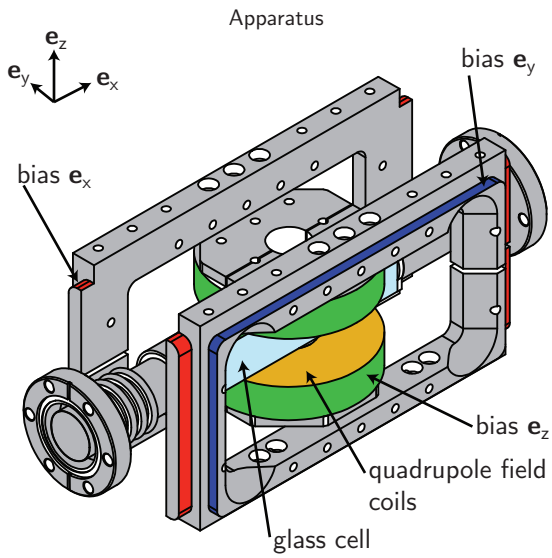

Figure 4.1: We have color coded several of the important features of this apparatus. The glass cell is suspended between two coils used to produce a quadrupole magnetic field. These are colored gold and comprise most of the volume of cylindrical disks shown in the diagram. Wrapped around the outside of these coils are B_{dc} field biasing coils oriented along $\mathbf{e}_z$. Similarly, B_{dc} biasing coils are wrapped around the region colored blue and red and produce fields along $\mathbf{e}_y$ and $\mathbf{e}_x$ respectively.

4.2 Abandoning Rb-Li mixtures

This machine was initially intended to produce a degenerate mixture of bosonic ^{87}Rb and fermionic ^{6}Li. Unfortunately for our plans, the cross-species scattering length is repulsive and small 20(6) a_B [34], which is undesirable for cross species rethermalization during evaporation. Since we began this project a group produced this mixture and sympathetically cooled the fermionic isotope ^{6}Li to quantum degeneracy using a BEC of ^{87}Rb [34]. They discovered that the nearest s-wave heteronuclear Feshbach resonance between the ground states of Rb and Li occurs at an unexpectedly high field 1066 G [35]. This resonance additionally turned out to be surprisingly lossy and had a small but attractive background scattering length, -17 a_B [36]. In light of these results we expect that the mixture would be somewhat difficult to bring to degeneracy, difficult to modify the interspecies scattering length once degeneracy had been obtained and the system too lossy to maintain long-lived many

body states near a Feshbach resonance. For now, Rb-Li mixtures are being left by the wayside. However, just like ^{87}Rb, a degenerate Fermi gas of ^{6}Li (alone) is an interesting system in its own right and could be in the works for the future.

4.3 ^{87}Rb level structure

4.3.1 Level structure

^{87}Rb is the fourth alkali in the periodic table and its fifth electronic shell $n = 5$ has one valence electron. In this sense the alkali atoms are like Hydrogen, but unlike Hydrogen's most abundant isotope many alkalis have a nuclear spin $\mathbf{I} = \hbar\sqrt{i(i+1)}$ greater than $i = 1/2$. The ground and first electronic excited states have different total orbital angular momenta $\mathbf{L} = \hbar l(l+1)$ which are labeled by quantum numbers, l: the ground states have zero total angular momentum $l = 0$ while the excited states have $l = 1$. In alkali atoms, the ground and lowest lying electronic states are resonantly coupled in the visible part of the optical spectrum, making alkalis relatively convenient and cheap to cool and trap with lasers.

The electronic excited states have a fine structure splitting that results from the coupling between the orbital angular momentum $\mathbf{L}$ and the electron spin $\mathbf{S}$: this is spin-orbit coupling in the traditional sense. The eigenstates of this coupling, the so-called fine structure (FS), have angular momentum $\mathbf{J} = \mathbf{L} + \mathbf{S}$. Transitions from the $j = 1/2$ ground electronic states to the $j = 1/2$ excited electronic states are the so-called D1 line while transitions between the ground $j = 1/2$ and excited $j = 3/2$ states are the D2 line. The fine structure states are further split by coupling with the nuclear spin angular momentum $\mathbf{I}$ to form the hyperfine structure (HFS). The eigenstates of this hyperfine interaction are determined using the rules of angular momentum addition, $\mathbf{F} = \mathbf{J} + \mathbf{I}$. See Table 4.1 for a summary.

Just as l is the quantum number associated with the $\mathbf{L}$ operator we also define the j and f quantum operators for $\mathbf{J}$ and $\mathbf{F}$. The Hamiltonian has a FS coupling

Name	Operator	Quantum number	Ground states	Excited states
energy	NA	n	5	5
orbital	$\hat{\mathbf{L}}$	l	$l = 0$	$l = 1$
electron	$\hat{\mathbf{S}}$	s	$s = 1/2$	$s = 1/2$
total	$\hat{\mathbf{J}}$	j	$j = 1/2$	$j = 1/2,\ 3/2$
nuclear	$\hat{\mathbf{I}}$	i	$i = 3/2$	$i = 3/2$
hyperfine	$\hat{\mathbf{F}}$	f	$f = 1,\ 2$	$f = 1,\ 2$ $(j = 1/2)$ $f = 0,\ 1,\ 2,\ 3$ $(j = 3/2)$

Table 4.1: Listing of angular momentum operators and their typical values for the ground and excited electronic states of ^{87}Rb

Name	Symbol	Term	Value
D1 line	$5S_{1/2} \leftrightarrow 5P_{1/2}$	$\frac{\ell(\ell+1)}{r}$	377 THz
D2 line	$5S_{1/2} \leftrightarrow 5P_{3/2}$	$\frac{\ell(\ell+1)}{r}$	384 THz
excited fine structure	A_{FS}	$\mathrm{L} \cdot \mathrm{S}$	$h \times 7$ THz
ground hyperfine structure	A_{HFS}	$\mathrm{J} \cdot \mathrm{I}$	$h \times 3.4$ GHz
excited hyperfine structure (j=1/2)	A_{HFS}	$\mathrm{J} \cdot \mathrm{I}$	$h \times 0.408$ GHz
excited hyperfine structure (j=3/2)	A_{HFS}	$\mathrm{J} \cdot \mathrm{I}$	$h \times 0.248$ GHz

Table 4.2: Listing of typical splittings between manifolds of states [37].

A_l^{FS} and HFS coupling $A_{l,j}^{\mathrm{HFS}}$ which we use to write down the Hamiltonian for the lowest electronic states of ^{87}Rb

$$H_{\mathrm{at}} = E_e \hat{P}_e + \frac{A_l^{\mathrm{FS}}}{\hbar^2} \hat{\mathbf{L}} \cdot \hat{\mathbf{S}} + \frac{A_{l,s}^{\mathrm{HFS}}}{\hbar^2} \hat{\mathbf{J}} \cdot \hat{\mathbf{I}} \tag{4.1}$$

where $\hat{P}_{g,e}$ are the projectors onto the ground or excited electronic states. The eigenvalues of the Hamiltonian E_e are approximately the values given by the D1 and D2 transitions in Table 4.2. The level structure illustrated in Fig. 4.2 are the eigenstates of Eq. 4.1. Laser cooling and trapping is discussed in the appendixes.

4.3.2 Zeeman Hamiltonian

In the presence of magnetic fields the internal states of ^{87}Rb acquire state dependent shifts given by the Zeeman Hamiltonian

$$\hat{H}_{\mathrm{Z}} = \frac{\mu_B \mathbf{B}(\mathbf{x})}{\hbar} \cdot (g_J \hat{\mathbf{J}} + g_I \hat{\mathbf{I}}) = \frac{g_F \mu_B \mathbf{B}(\mathbf{x})}{\hbar} \cdot \hat{\mathbf{F}} \tag{4.2}$$

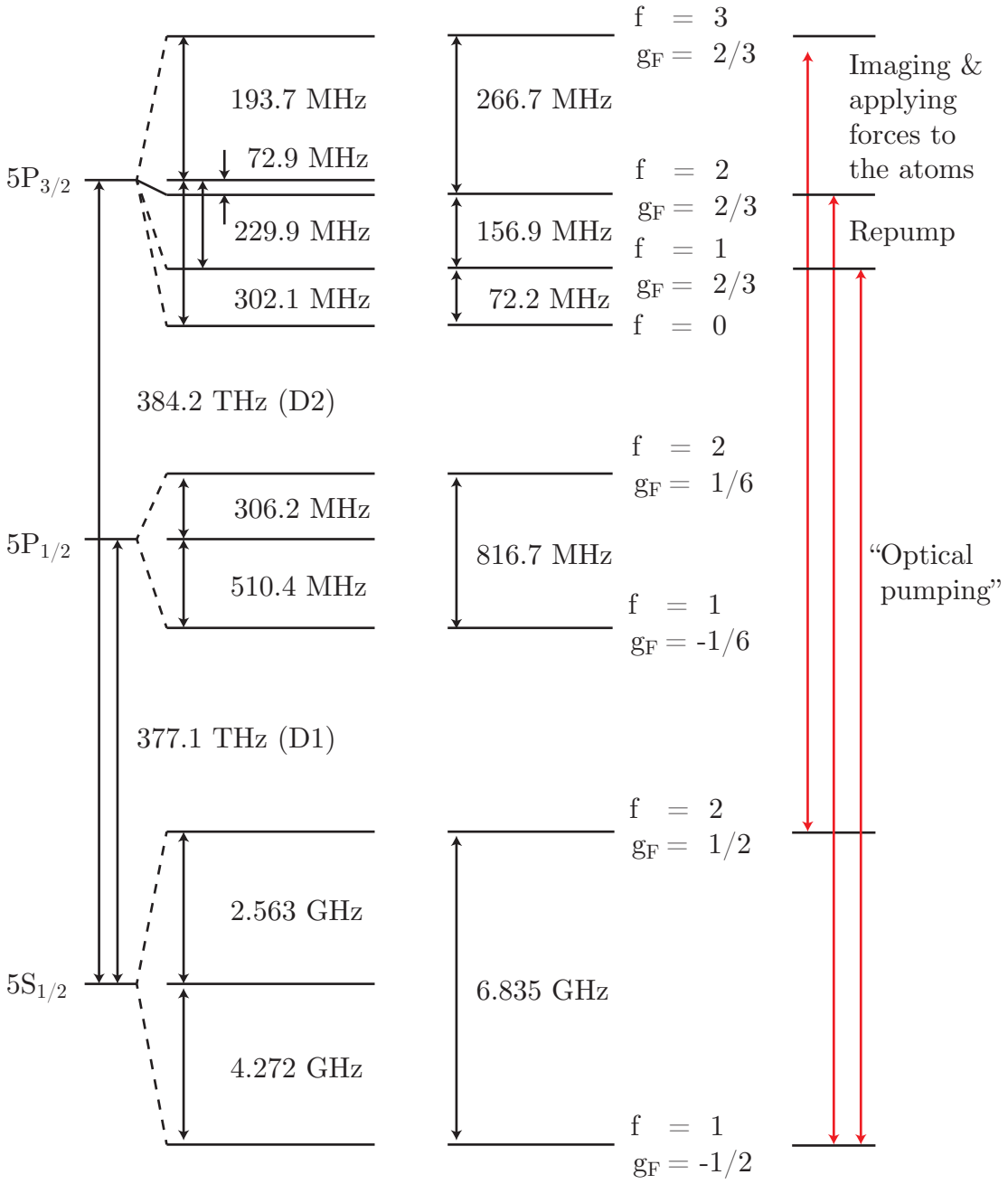

Figure 4.2: We show the ^{87}Rb hyperfine structure with frequency splittings between the hyperfine manifolds. The imaging transition (specifically the stretched spin states) maximizes the coupling matrix elements: this is advantageous for imaging and applying optical forces to the atoms. The ground $f = 1$ hyperfine manifold is not coupled by laser light to the $f = 2$ hyperfine manifold and hence a second laser is required. Coupling to excited hyperfine manifolds with reduced spin dimensionality is sometimes useful for optically transferring (optically pumping) atoms into a particular ground spin projection.

where μ_B is the Bohr magneton. In the context of a dot product the hyperfine angular momentum spin operator is a vector of spin matrices $\hat{\mathbf{F}} = \{\hat{F}_x, \hat{F}_y, \hat{F}_z\}$. The $\hat{F}_z$ spin matrix is traceless and diagonal $\langle m_F | \hat{F}_z | m_F \rangle = \hbar m_F \delta_{m_F, m'_F}$, while $F_x = (\hat{F}^+ + \hat{F}^-)/2$ and $F_y = (\hat{F}^+ - \hat{F}^-)/2$ are composed of raising and lowering operators that link $|m_F\rangle$ states. The Landé g-factors are constants of proportionality where the nuclear spin g_I is a thousand times smaller than that of the electron spin g_J. The hyperfine Landé g-factor is

$$g_F = g_J \frac{f(f+1) - i(i+1) + j(j+1)}{2f(f+1)} + g_I \frac{f(f+1) + i(i+1) - j(j+1)}{2f(f+1)} \tag{4.3}$$

where f, j, and i are the angular momentum quantum numbers for the hyperfine, nuclear and fine structure respectively.

The Breit-Rabi formula exactly diagonalizes $\hat{H}_{\mathrm{Z}}$ when the ground state has $j = 1/2$ (applicable to all alkali atoms)

$$E_{|j=1/2, m_J; I, m_I\rangle} = -\frac{\Delta E_{\mathrm{HFS}}}{2(2i+1)} + g_I \mu_B m B \pm \frac{\Delta E_{\mathrm{HFS}}}{2} \left(1 + \frac{4mx}{2i+1} + x^2\right)^{1/2}, \tag{4.4}$$

where $x = (g_J - g_I)\mu_B B / \Delta E_{\mathrm{HFS}}$ and $m = m_I \pm m_J$. More information concerning the Breit-Rabi formula can be found in Ref. [38].

4.3.3 Optical illumination

We introduce the local electric field $\mathbf{E}(t) = E_i \mathbf{e}_i \cos(\mathbf{K} \cdot \mathbf{x} - \omega t - \theta_i - \gamma)$ of a laser impinging upon an atomic system, which induces a dipole moment with the associated potential

$$H_{\mathrm{dip}} = -\mathbf{d} \cdot \mathbf{E}(t) = d_i \mathrm{E}_i \cos(\mathbf{K} \cdot \mathbf{x} - \omega t - \theta_i - \gamma). \tag{4.5}$$

Here, orthogonal Cartesian unit vectors $\mathbf{e}_i$ are indexed by $i \in \{1, 2, 3\}$ and therefore θ_i accommodates circular polarization. $\mathbf{K}$, ω, and ϕ are the laser wavevector, angular

frequency, and phase. The electric dipole operator is $\mathbf{d} = -e\sum_\alpha \hat{r}_\alpha$ where $\hat{r}_\alpha$ labels the location of each electron indexed by α.

It is convenient to transform the excited states into a rotating frame using a unitary transformation of the state vector $|\psi'\rangle = U^\dagger |\psi\rangle$ where

$$\hat{U}(t) = \hat{P}_g + \hat{P}_e \exp(-i\omega_L t). \tag{4.6}$$

The rotating frame Hamiltonian contains an extra term $\hbar\omega_L \hat{P}_e = -i\hbar\hat{U}^\dagger(t)\partial_t\hat{U}(t)$ from the time-dependent Schrödinger equation, giving

$$\hat{H}_{\text{at}} = \Delta_e \hat{P}_e + \frac{A_{l=1}^{\text{FS}}}{\hbar^2}\hat{\mathbf{L}}\cdot\hat{\mathbf{S}} \tag{4.7}$$

where $\Delta_e = E_e - \hbar\omega_L$. Because $|E_e - \hbar\omega_L| \ll E_e$ we make the rotating wave approximation (RWA) and discard the terms $\propto \exp(\pm 2\omega_L t)$, leaving a complex electric field $E_i' = E_i \exp(i[\mathbf{K}\cdot\mathbf{x} - \phi_i - \gamma])$. The dipole Hamiltonian from Eq. 4.5 takes the form

$$\hat{H}'_{\text{dip}} \approx \frac{1}{2}\left[E_i'^{*}\hat{P}_g\hat{d}_i\hat{P}_e + E_i'\hat{P}_e\hat{d}_i\hat{P}_g\right]. \tag{4.8}$$

4.4 Imaging

4.4.1 Atomic energy levels coupled

We image our atoms using collimated and circularly polarized imaging light that is resonant with the stretched states ${}^5S_{1/2}\,|f = 2, m_F = 2\rangle$ and ${}^5P_{1/2}\,|f' = 3, m_{F'} = 3\rangle$. The excited state $|f' = 3, m_{F'} = 3\rangle$ can only decay through spontaneous emission to the ground state $|f = 2, m_F = 2\rangle$. Resonantly coupling states with this property is called coupling to a cycling transition. Cycling transitions are advantageous because relatively few atoms fall out of resonance with the laser, the dipole matrix elements are maximized, and both the dipole matrix element and spontaneous emission rate

Γ experienced by the majority of the atoms are well known.

Typically, the BEC components are the $f = 1$ electronic ground states. For imaging, the atoms must be first excited to the $f = 2$ ground hyperfine level with light that couples between the $^5S_{1/2}$ $f = 1$ ground electronic states and the $^5P_{3/2}$ $f = 2$ excited electronic states as shown in Fig. 4.2. Spontaneous emission then populates the $f = 2$ ground electronic states.

4.4.2 Geometry

We image our atomic clouds after TOF. The imaging beam at ~ 0.5 mm in diameter is designed to be not too much larger than the TOF extent of the atomic cloud. With an imaging intensity of $I(x, y, z)$ the light absorbed is given by Beer's law:

$$\frac{dI(x, y, z)}{dz} = n(x, y, z)\frac{3\pi c^2 I(x, y, z)}{2\omega_0^2}\frac{\Gamma^2}{(\omega - \omega_0)^2 + \Gamma^2/4}. \tag{4.9}$$

where the density of the atomic cloud is $n(x, y, z)$. The image of the scattering center, a combination of the scattered light and the remaining probe light, is projected onto a CCD camera: this is absorption imaging. We illustrate our imaging setup in Fig. 4.3.

4.4.3 Spin-sensitive imaging

Interaction-driven expansion converts the state-independent momentum distribution of a BEC into an expanding spatial distribution within $1/\bar{\omega} \approx 2$ ms. In ^{87}Rb the state-dependent interactions are proportional to $c_1 \approx -0.005c_0$. Since the spin healing length is approximately 14 times larger than the spin-independent healing length, the fidelity of the spatial structure of the state-dependence to begins to fail around ≈ 28 ms of TOF. During interaction driven expansion, the presence of moderate magnetic field gradients add state dependent dislocations to the overall density profile. Hence, we allow 8 ms of interaction driven expansion in a small

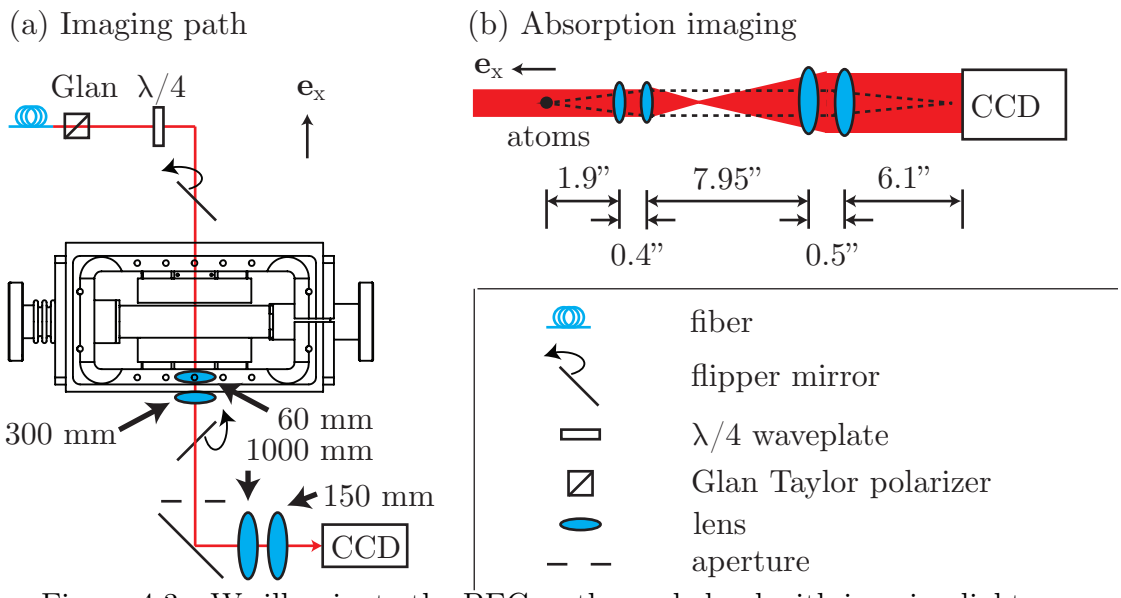

Figure 4.3: We illuminate the BEC or thermal cloud with imaging light 0.5 mm in diameter. (a) We show the path of imaging beam through the glass cell and a (b) schematic diagram of absorption imaging. We image the shadow cast by the BEC along with some of the scattered light onto the CCD, some rays of which are represented by the dotted lines. The lenses shown create a beam expander for the imaging light: producing a magnification of 3.19. The resolution of our setup is 2 μm.

uniform magnetic field–the cloud becomes essentially non-interacting–and we then apply a strong gradient to separate the states spatially during TOF. We call this state dependent force applied during imaging a Stern-Gerlach pulse.

4.5 Optical dipole trapping potential

Optical dipole trapping decouples the internal magnetic moment of the atom from the position dependence of the trap. This allows exploration of spinor physics, which usually involves magnetically untrappable states, and Feshbach resonances which require large uniform magnetic fields [39].

This trap is produced using an angular frequency ω of light detuned $\delta = (\omega - \omega_0)$ far to the red of the ground to excited electronic transitions $\hbar\omega_0$ of an atom. This light induces a dipole moment in the illuminated atom. The atom then experiences a force proportional to the gradient of the amplitude of the light's

electric field. The laser light has a Gaussian intensity distribution

$$I(\mathbf{r}, z) = \frac{2P}{\pi(w_x^2 + w_y^2)(1 + (z/z_R)^2)} e^{-2\mathbf{r}^2/(w_x^2+w_y^2)(1+(z/z_R)^2)} \tag{4.10}$$

with a $1/e$ waist w_x and w_y along the unit vectors $\mathbf{e}_x$ and $\mathbf{e}_y$ respectively. The power is given by P while the Raleigh length is given by z_R.

In the limit where $\delta \approx \omega$, the RWA breaks down and counter rotating frequencies $-\omega$ must be included. Nonetheless, the depth of the trapping potential remains proportional to the intensity and inversely proportional to the detuning

$$U_{\text{dipole}} = \frac{\hbar\Gamma}{4} \frac{\Gamma\omega_0}{\omega^2 - \omega_0^2} \frac{I(\mathbf{r}, z)}{I_{\text{sat}}} = \frac{\hbar\Omega^2(\mathbf{r}, z)}{4\delta} + \frac{\hbar\Omega^2(\mathbf{r}, z}{4(\delta - 2\omega)}. \tag{4.11}$$

and may be cast in terms of co-rotating and counter-rotating ac Stark shifts. The optical dipole beam produces a potential that has a Gaussian profile for radial displacements from the center of the beam. Axially, along the beam, the potential is greatly elongated $z_R \gg r_x$, r_y. For slight tilts with respect to Earth's surface the gravitational potential can win out and cause atoms to leave the trap.

4.5.1 Trapping frequencies

For small radial deviations from the center of the trap a Gaussian potential looks parabolic. By analogy, we define harmonic trap angular frequencies ω_x and ω_y for an atom trapped at the waist of this beam

$$U_{\text{dipole}}(\mathbf{r}) = \frac{\hbar\Gamma}{4} \frac{I(0,0)\Gamma\omega_0}{I_{\text{sat}}(\omega^2 - \omega_0^2)} \left(\frac{r_x^2}{2w_x^2} + \frac{r_y^2}{2w_y^2} \right) = \frac{m}{2}(\omega_x^2 r_x^2 + \omega_y^2 r_y^2) \tag{4.12}$$

where m is the mass of ^{87}Rb.

4.5.1.1 Measuring the trapping frequencies

Atomic clouds with a non-zero m_F spin projection can be displaced by the adiabatic turn on of a magnetic field gradient. Suddenly turning off this gradient is equivalent to loading a spin component of the atomic cloud with non-zero potential energy, zero kinetic energy and displacement aligned or anti-aligned with the magnetic field gradient. Subsequently, the atomic cloud center of mass experiences underdamped oscillation in the HO trap with HO frequency. In TOF imaging the momentum of the cloud is transformed into a displacement on the camera and the position of the cloud can usually be ignored. Hence, peak displacement on the camera will occur a quarter trap period after the release of the magnetic field gradient.

4.5.2 Crossed optical dipole trap

It is possible to make the trap nearly isotropic by adding a second optical dipole beam that intersects the first. If the second beam propagates along $\mathbf{e}_x$ the trap potential and corresponding trap frequencies are modified

$$\begin{aligned} U_{\text{dipole}}(\mathbf{r}) &= \frac{\hbar\Gamma}{4}\frac{\Gamma\omega_0}{I_{\text{sat}}(\omega^2-\omega_0^2)}\left(\frac{I(0,0)r_x^2}{2w_x^2}+\frac{(I(0,0)+I_c(0,0))r_y^2}{2w_y^2}+\frac{I_c(0,0)r_z^2}{2w_z^2}\right) \\ &= \frac{m}{2}(\omega_x^2 r_x^2+\omega_y^2 r_y^2+\omega_z^2 r_z^2). \end{aligned} \tag{4.13}$$

4.5.3 Trap lifetime

High intensity can lead to spontaneous emission although this type of heating can be suppressed at a given trap depth by increasing the detuning and compensating with increased intensity. The spontaneous emission scattering rate is

$$\Gamma_{\text{spon.}} = \frac{\Gamma}{8}\frac{\Gamma^2}{\delta^2}\frac{I}{I_{\text{sat}}}. \tag{4.14}$$

The spontaneous emission scattering rate scales as I/δ^2 while the depth of the dipole potential scales as I/δ. Hence, for a particular trap depth it is always possible to reduce the scattering rate by detuning farther from the electronic excited states.

At sufficiently large detunings (we use 98 THz) other sources of heating dominate: Ref. [39] attributes much of this heating to beam jitter. For example, our ≈ 10 s trap lifetimes would then be attributed to dipole beam jitter. There is also a vacuum limited lifetime associated with fast moving atoms intersecting the atomic cloud after impacting the walls of the vacuum system. For our ultrahigh vacuum system this lifetime exceeds 50 s.

4.6 Magnetic field control

4.6.1 Magnetic rf fields

In the presence of an rf magnetic field $\mathbf{B}_{\rm rf}(\mathbf{x})\cos(\omega_{\rm rf}t+\gamma_{\rm rf})$ the added contribution to the Hamiltonian is

$$\hat{H}_B = g_F\mu_B\hat{\mathbf{F}}\cdot\mathbf{B}_{\rm rf}(\mathbf{x})\cos(\omega_{\rm rf}t+\gamma_{\rm rf}) \tag{4.15}$$

where $\hat{F}_z$ is a diagonal spin matrix and a $B_{\rm dc}$ much larger than $\mathbf{B}_{\rm rf}(\mathbf{x})$ and oriented along $\mathbf{e}_z$ is present. When the angular frequency is resonant with the linear Zeeman shift $\omega_{\rm rf} = |g_F\mu_B B(\mathbf{x})|/\hbar$ we apply the RWA to the rf coupling Hamiltonian

$$\hat{H}_B = \hbar\Omega_{\rm rf}(\mathbf{x})\left[\hat{F}_x\cos(\omega_{\rm rf}t+\gamma_{\rm rf}) + \hat{F}_y\sin(\omega_{\rm rf}t+\gamma_{\rm rf})\right]. \tag{4.16}$$

The rf Rabi frequency is $\Omega_{\rm rf}(\mathbf{x}) = g_F\mu_0|B(\mathbf{x})|/2$ and the spatial variation of $\Omega_{\rm rf}(\mathbf{x})$ is typically small over the extent of the atomic cloud. It is convenient to transform the both the rf coupling Hamiltonian and the Zeeman Hamiltonian into the rotating

frame using the unitary transformation

$$\hat{U}(t) = \begin{pmatrix} e^{-i(\omega_{\rm rf}t+\gamma_{\rm rf})} & 0 & 0 \\ 0 & 1 & 0 \\ 0 & 0 & e^{i(\omega_{\rm rf}t+\gamma_{\rm rf})} \end{pmatrix} \tag{4.17}$$

which acquire an extra term from the time dependent Schrödinger equation $i\hbar\hat{U}^\dagger(t)\partial_t\hat{U}(t) = -\hbar\omega_{\rm rf}\hat{F}_z$. We make the changes of variables $\delta = \omega_{\rm rf} - (E{-}1 - E_{+1})/2\hbar$ and $\epsilon = -(2E_0 - E_{-1} - E_{+1})/\hbar$ where E_m are the eigenvalues of the Breit-Rabi equation. The transformed Hamiltonian is

$$\hat{H} = \begin{pmatrix} \hbar\delta & \hbar\Omega_{\rm rf}/\sqrt{2} & 0 \\ \hbar\Omega_{\rm rf}/\sqrt{2} & -\hbar\epsilon & \hbar\Omega_{\rm rf}/\sqrt{2} \\ 0 & \hbar\Omega_{\rm rf}/\sqrt{2} & -\hbar\delta \end{pmatrix} \tag{4.18}$$

which is equivalent up to an overall shift in energy to

$$\hat{H} = \delta\hat{F}_z + \epsilon\hat{F}_z^2/\hbar + \Omega_{\rm rf}\hat{F}_x. \tag{4.19}$$

4.6.2 Adiabatic preparation of states

The quadratic shift $\hbar\epsilon$ breaks the symmetry of total spin while preserving that of total magnetization within the ground hyperfine manifolds. This shift is absent when the $B_{\rm dc}$ is zero and increases quadratically as the field increases. It is possible to make the quadratic shift much larger than typical rf Rabi frequencies ~ 10 kHz and the break-even point is 8.4 G. The particular rf and $B_{\rm dc}$ fields used as an example in Fig. 4.4 can be used to adiabatically load any spin state.

In most experimental setups the $m_F = -1$ spin state will be initially loaded because it can be magnetically trapped. In the presence of some $B_{\rm dc}$ we ramp on an rf magnetic field with a coupling strength of $\Omega_{\rm rf} = 10$ kHz and a frequency of

$\omega_{\rm rf}/2\pi = 8.5$ MHz. If $B_{\rm dc} = 8.4$ G then slow changes of the $B_{\rm dc}$ (equivalent to ramping δ) will follow the bottom eigenstate in Fig. 4.4(b). Likewise, if $B_{\rm dc} = 8.6$ G then slow changes will follow the top eigenstate. In either case, ramping through resonance and then ramping $\Omega_{\rm rf} \to 0$ will adiabatically load $m_F = +1$. Ramping to resonance along the bottom eigenstate and then ramping $\Omega_{\rm rf} \to 0$ will load the $m_F = 0$ state.

Equal superpositions of any pair of spin states may also be produced by ramping to the appropriate $B_{\rm dc}$ along the appropriate eigenstate and snapping off $\Omega_{\rm rf}$. The spin composition using this method matches that of the rf eigenstate prior to the snap off. $\Omega_{\rm rf}$ must be small enough prior to snap off that very little of the third spin state is represented in the rf eigenstate. If the rf magnetic field amplitude is stable in time, producing a $50:50$ mixture of $m_F = -1, 0$ can be a fairly sensitive measure of $B_{\rm dc}$ stability. Stable populations of $m_F = \pm 1$ are relatively more difficult to produce using this method because the curvature of the uppermost rf eigenstate as a function of $B_{\rm dc}$ at its avoided crossing is much greater than the others.

If $B_{\rm dc}$ stability is an issue then $50:50$ mixtures may also be produced using a diabatic ramp through an avoided crossing region. This is often an improvement over the adiabatic method (especially for $m_F = \pm 1$ production) because a system that does not have precision $B_{\rm dc}$ control may still be able to control the ramp rate with a high degree of reproducibility. The probability of diabatic transition from the m'th eigenstate is given by the Landau-Zener formula [40]:

$$P_D = e^{-\frac{2\pi|\Omega_{\rm rf}|^2}{\hbar\partial_t E_m}} \tag{4.20}$$

4.6.3 Pulsing rf

Pulsing with rf magnetic fields is an effective way to produce arbitrary mixtures of spin states, quickly. Magnetic dc field drift contributes approximately equally

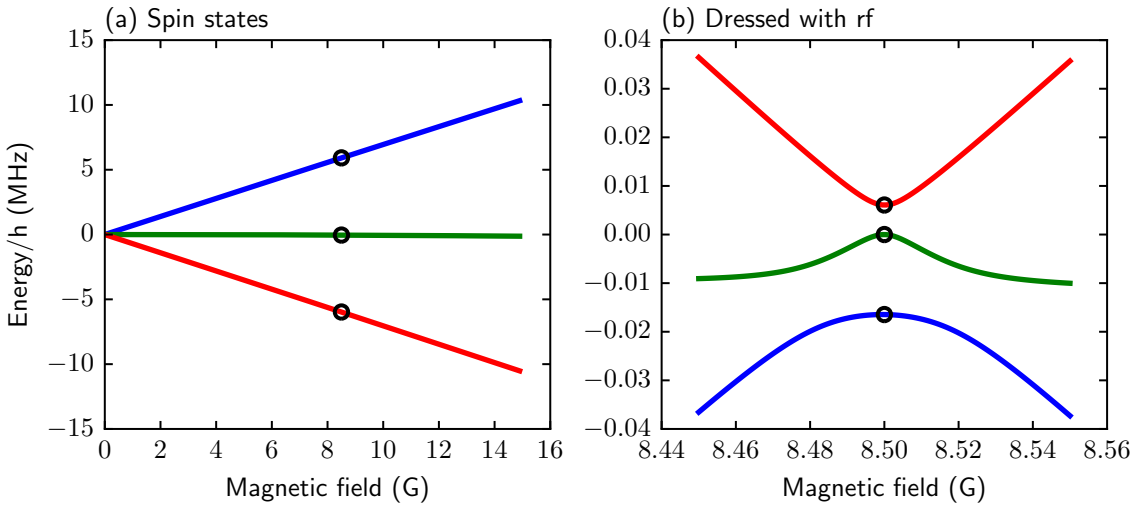

Figure 4.4: (a) Spin state energy as a function of magnetic field for the $f = 1$ ground hyperfine manifold of ^{87}Rb. (b) Spin states dressed by an rf magnetic field with frequency $\omega_{\rm rf}/2\pi = 8.5$ MHz and $\Omega_{\rm rf} = 10$ kHz. Black circles are a guide to the eye indicating coincident points in both plots.

to fluctuations in spin population in both methods. However, if the spin states are immiscible or if there are sizeable magnetic gradients present the faster pulse preparation method may be advantageous. We define a three component state vector

$$|\psi\rangle = \begin{pmatrix} |m_F = -1\rangle \\ |m_F = 0\rangle \\ |m_F = +1\rangle \end{pmatrix} \tag{4.21}$$

and solve the RWA Hamiltonian from Eq. 4.19 exactly

$$|\psi(t)\rangle = e^{-i\frac{\hat{H}t}{\hbar}} |\psi\rangle \,. \tag{4.22}$$

4.6.4 Measuring the $B_{\rm dc}$

4.6.4.1 Zeroing out the ambient magnetic fields

A practical method for measuring the $B_{\rm dc}$ present in an experiment is to measure spin population using adiabatic rapid passage (ARP) with rf magnetic fields. The

experimentalist adds a $B_{\rm dc}$ on top of the already present fields. After ramping up the amplitude of the rf the $B_{\rm dc}$ is swept across resonance. The spin population of the eigenstate is compared to that predicted by the eigenstates of Eq. 4.19 after the ARP. For a given orientation of the applied $B_{\rm dc}$ we fit to the ARP at several different applied field strengths. Plotting the rf magnetic field as a function of magnetic field at resonance the resulting trace will be proportional to $|B - B_0|$ for large B. We apply an offset $-B_0$ in the magnetic field and repeat the scans with a different orientation of the magnetic field. Eventually, the magnetic field will be zeroed along every Cartesian direction.

4.6.4.2 Single pulse measurement of the magnetic fields

We adiabatically load into the $m_F = 0$ state at ~ 8.5 G before reducing our fields to < 1 G. We assume $\Omega_{\rm rf} \ll \omega_{\rm rf}$. The objective is to pulse nearly all the atoms from $m_F = 0$ into a superposition of $m_F = \pm 1$. The time evolution of this superposition is

$$|\psi(t)\rangle = \frac{e^{-iE_{-1}t/\hbar}\,|m_F = -1\rangle + e^{-iE_{+1}t/\hbar}\,|m_F = +1\rangle}{\sqrt{2}} \tag{4.23}$$

which starts from $t = 0$. A subsequent pulse may be performed many milliseconds later and the following happens

$$\frac{|m_F = -1\rangle + |m_F = +1\rangle}{\sqrt{2}} \rightarrow |m_F = 0\rangle \tag{4.24}$$

$$\frac{|m_F = -1\rangle - |m_F = +1\rangle}{\sqrt{2}} \rightarrow \text{no change.} \tag{4.25}$$

which is an interferometric measurement of the integrated $B_{\rm dc}$ whose coherence is not damaged by a noisy $B_{\rm dc}$.

We consider the case of a two-level system where the states are pulsed into a $50:50$ superposition. Then, a changing magnetic field decouples the evolving phase

difference of the spins from the phase of the laser. In our system two-state Rabi pulses decohere after ~ 1 ms for this reason.

4.6.5 Gradients

The gradient $\nabla = \partial_x \mathbf{e}_x + \partial_y \mathbf{e}_y + \partial_z \mathbf{e}_z$ of a Zeeman potential $U_B(\mathbf{x})$ is a force

$$\mathbf{F}_{\text{grad}} = \nabla U_B(\mathbf{x}) = \nabla(g_F \mu_B \hat{\mathbf{F}} \cdot \mathbf{B}(\mathbf{x})) \tag{4.26}$$

$$= g_F \mu_B \hat{\mathbf{F}} \cdot (\nabla \mathbf{B}(\mathbf{x})), \tag{4.27}$$

while the gradient of a magnetic vector field $\nabla \mathbf{B}(\mathbf{x})$ is a dyadic product of vectors. In the absence of a charge current the dyadic is symmetric $\nabla \times \mathbf{B}(\mathbf{x}) = 0$: $\partial_m B_n(\mathbf{x}) = \partial_n B_m(\mathbf{x})$. As always, the magnetic field gradient is traceless $\nabla \cdot \mathbf{B}(\mathbf{x}) = 0$. The remaining terms are the Cartesian elements of the rank-2 spherical tensor.

$$\nabla \mathbf{B}(\mathbf{x}) = \sum_{m,n} \left[\frac{\partial_m B_n(\mathbf{x}) + \partial_n B_m(\mathbf{x})}{2} - \frac{\boldsymbol{\nabla} \cdot \mathbf{B}(\mathbf{x})}{3} \right] \mathbf{e}_m \mathbf{e}_n. \tag{4.28}$$

Often, we know the overall orientation of $\mathbf{B}(\mathbf{x})$ over the entirety of the atomic cloud, e.g. a strong B_{dc} with a perturbative gradient. If the component along $\mathbf{e}_z$ dominates the B_{dc} then we may infer that the spin components of $\hat{F}_z$ are diagonalized for spin projections along $\mathbf{e}_z$ as well. Only those components of the magnetic gradient dyadic that project onto $\mathbf{e}_z$ then contribute to the force experienced by the atoms

$$\mathbf{F}_{\text{grad}} = g_F \mu_B m_F \left[\left(\partial_x B_z - \frac{1}{3} \partial_z B_z \right) \mathbf{e}_x + \left(\partial_y B_z - \frac{1}{3} \partial_z B_z \right) \mathbf{e}_y + \frac{2}{3} \partial_z B_z \mathbf{e}_z \right] \tag{4.29}$$

where we found the product $(\hat{F}_z \mathbf{e}_z) \cdot \boldsymbol{\nabla} \mathbf{B}(\mathbf{x})$ and applied the identity $\partial_m B_n(\mathbf{x}) = \partial_n B_m(\mathbf{x})$. These are the gradient terms that we attempt to compensate.

4.6.6 Gradient measurement

4.6.6.1 TOF method

When an atomic cloud is trapped in a spin-independent trap, e.g. an optical dipole trap, the gradients may be roughly determined by preparing the cloud with different magnetic moments and releasing each at separate times in TOF. The accuracy of this method increases with the difference of the magnetic moments and time in TOF before imaging. Assuming that the gradient is uniform over the TOF region the displacement is a simple function of $\mathbf{F}_{\text{grad}}$

$$\mathbf{d} = \frac{\mathbf{F}_{\text{grad}} t^2}{2m} \tag{4.30}$$

For a TOF time of 30 ms a gradient of 1 mG/cm produces a displacement of 29 μm between $m_F = \pm 1$.

4.6.6.2 Interference method

We adiabatically prepare our atoms in the $m_F = 0$ state. Then pulse to an equal superposition of $m_F = \pm 1$ at low field. In an extended atomic cloud each portion of the cloud experiences a local magnetic field

$$|\psi(t)\rangle = \frac{e^{-iE_{-1}(\mathbf{x})t/\hbar}\,|m_F = -1\rangle + e^{-iE_{+1}(\mathbf{x})t/\hbar}\,|m_F = +1\rangle}{\sqrt{2}} \tag{4.31}$$

where the eigenvalues of the Breit-Rabi equation are $E_m(\mathbf{x}) = g_F \mu_B m |B(\mathbf{x})|$. When the atomic cloud is pulsed again, some regions return to $m_F = 0$ while others remain in $m_F = \pm 1$ as shown in Fig. 4.5. The resultant fringe pattern reveals the projection of the gradient along the extended spatial axis $\mathbf{e}_x$ of the cloud and whose components have magnetic field orientation aligned with the $B_{\text{dc}}\mathbf{e}_z$. This gradient

may be determined from the fringe pattern

$$\partial_x B_z(\mathbf{x}) = \frac{2\pi\hbar}{2g_F\mu_B\lambda_{\text{grad}}t} \tag{4.32}$$

where λ_{grad} is the spatial wavelength of the stripe pattern. When the gradient is nearly balanced the gradient can change throughout the atomic cloud. In that case the fringe pattern can reveal the exact profile of the gradient.

We can test that this interpretation of the fringe pattern by allowing the system to evolve under a gradient for time τ, pulsing to swap spin states $m_F = \pm 1 \rightarrow m_F = \mp 1$, and evolving for another time τ. Under this spin echo the fringe pattern should reverse itself as shown in Fig. 4.6.

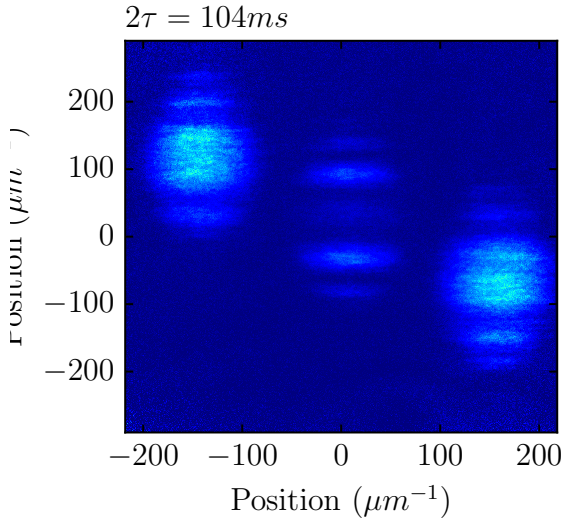

Figure 4.5: This is a density plot of the three $f = 1$ ground hyperfine spin components separated horizontally using Stern-Gerlach in TOF. The $m_F = -1$ spin component appears on the far left while $m_F = +1$ is on the far left. We show the fringe pattern of a our gradient balanced system after 104 ms of time evolution. We then used an rf pulse to partially transfer atoms from the $|m_F = \pm 1\rangle$ spin components into $|m_F = 0\rangle$. The optical dipole trap has a 22:1 aspect ratio with the long dimension aligned with the vertical axis of this plot.

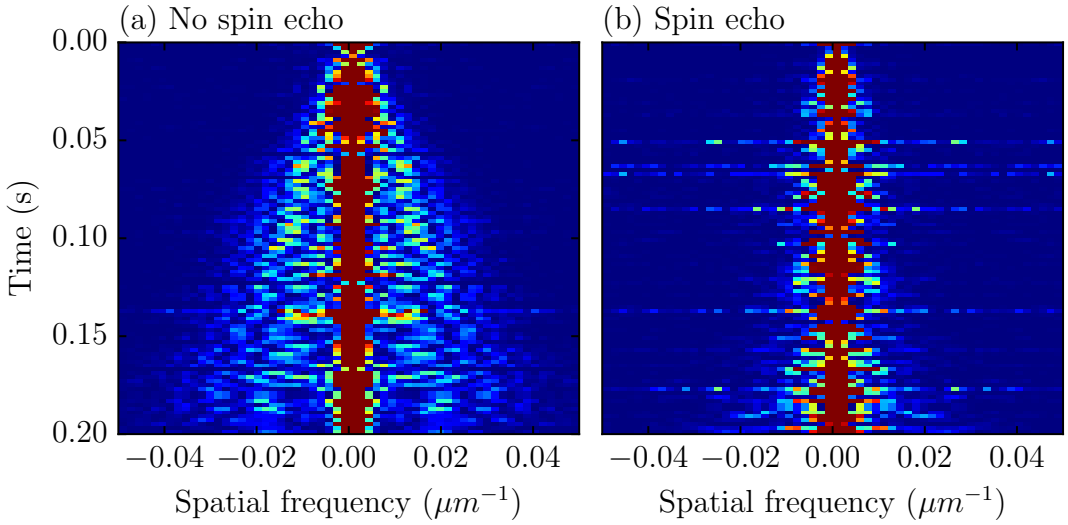

Figure 4.6: (a) Power spectral density (PSD) as a function of spatial frequency along a vertical slice of the $|m_F = 0\rangle$ spin component. These slices are arranged in descending order with increasing time. As time increases the fringe pattern has a higher spatial frequency. (b) PSD as a function of spatial frequency with spin echo halfway through the time evolution. The PSD returns to its configuration at $t = 0$.

4.6.7 Gradient compensation

Since the force produced by the gradient (Eq. 4.29) is dominated by the subset of terms aligned with B_{dc} we can use a set of coils with three independently controlled currents to cancel the force on the atoms. We found that a set of clover leaf coils as shown in Fig. 4.7 is always sufficient for this purpose.

(a) Coil configuration (top)

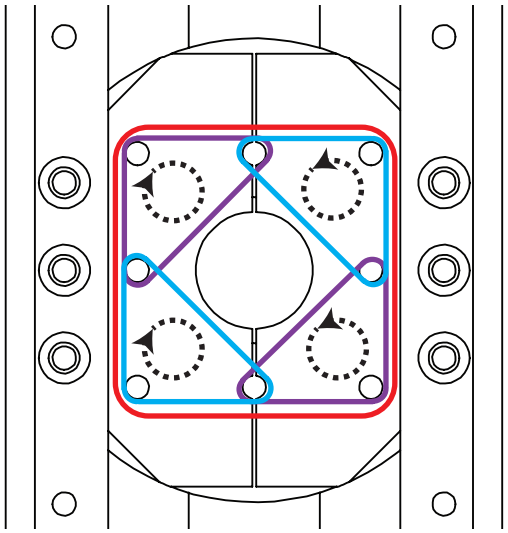

(b) Coil locations

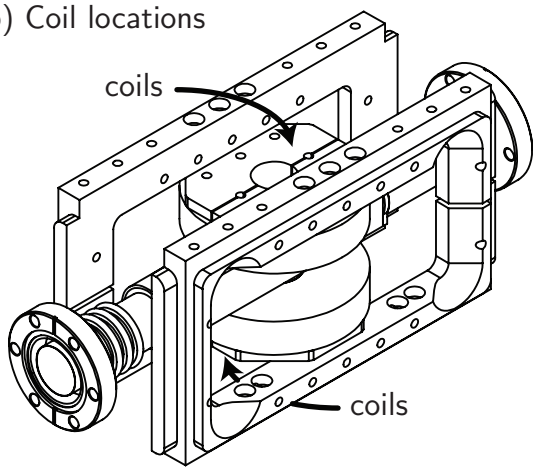

(c) Clover leaf coil magnetic field

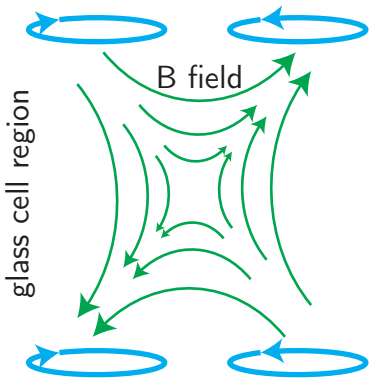

(d) Quadrupole coil magnetic field

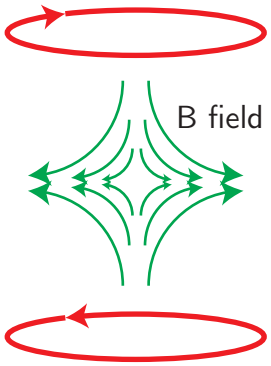

Figure 4.7: (a) These are the three sets of coils necessary for gradient compensation when B_{dc} is aligned with $\mathbf{e}_z$. Coils with the same color are connected in series. The dashed arrows indicate the direction of current flow. (b) The same set of coils are mounted above and below the glass cell. (c) We depict four coils in a clover leaf configuration that are connected in series. The magnetic field is shown in green. (d) We also depict the two coils in a quadrupole configuration that are connected in series.

Chapter 5: Domain Coarsening

5.1 Introduction

Out of equilibrium domains often form when a system is quenched through a phase transition: the system diabatically changes from having one kind of symmetry to having another. The range of applicable phenomena are incredibly diverse: including grain formation in minerals [41], domain nucleation in magnetic systems [42], Kibble-Zurek phenomena such as structure growth in the early universe [43], and spontaneous vortex formation in quenched BEC's [44]. In our experiment the 100 μs interaction equilibration timescale is well separated from the 20 ms spin interaction equilibration timescale. Using the approximately 20 μs population transfer timescale associated with a state changing rf magnetic field we diabatically prepared a uniformly mixed and transversely magnetized two-component spinor BEC of ^{87}Rb from a single component condensate, leaving the spin-independent interactions largely unchanged. We prepared this immiscible binary condensate in a cigar shaped trap, encouraging spin domains to form along the weakly confined axis. Our binary condensates then observed the full range of timescales from the initial domain growth to the long timescale increase in domain lengthscale (coarsening). Once a spin domain reaches full contrast in a region there is an energy cost for an atom with opposite spin to "hop" over the domain.

Other studies of miscible [45, 46] and immiscible [47, 48] binary condensates did not explore condensate dynamics over timescales necessary to see coarsening. One three component and surfboard shaped (2D in spin) system [49] did observe

coarsening but this and other three component systems [50, 51, 52, 53, 49, 54, 55] do not have the relative simplicity of our binary and essentially 1D system.

5.2 2-state Hamiltonian

5.2.1 Interactions

We explore the evolution of the $|f = 1, m_F = \pm 1\rangle$ ground electronic spin projections of ^{87}Rb. When the system is far away from any molecular (Feshbach) resonances– the nearest is predicted to appear at more than 200 G [56]– the scattering lengths of these two states must be identical by spin symmetry. Absent stray trapping fields, this symmetry eliminates the tendency of immiscible and repulsively interacting spin states forming a shell, one around the other, because they have disparate densities [45, 46, 47, 48]: in the Thomas-Fermi approximation the density for a single $m_F = \pm 1$ component is $\propto 1/a_2$. The singlet a_0 and triplet a_2 scattering lengths are subscripted according to the total angular momentum collision channels of a pair of colliding $f = 1$ atoms where bosonic statistics eliminate the total angular momentum of 1 collision channel. Interactions between atoms with the same spin have a scattering length of a_2 while interactions between atoms with opposite spin are $(2a_0 + a_2)/3$. We separate the interaction coefficient for interactions between identical spins $c_0 + c_1$ and interactions between different spins $c_0 - c_2$, which have units of energy over density, into a spin-independent

$$c_0 = \frac{\pi\hbar^2}{m}(a_0 + 2a_2)/3 \tag{5.1}$$

and spin dependent

$$c_2 = \frac{4\pi\hbar^2}{m}(a_2 - a_0)/3 \tag{5.2}$$

coefficients [57, 58]. In ^{87}Rb's $f = 1$ manifold, $c_0 = (100.86) \times 4\pi\hbar^2 a_{\rm B}/m$ vastly exceeds $c_2 \approx -4.7 \times 10^{-3} c_0$, where $a_{\rm B}$ is the Bohr radius [59].

5.2.2 The Hamiltonian

Our BEC's are described in terms of a spinor wave-function

$$\psi(\mathbf{r}) = (\psi_\uparrow(\mathbf{r}), \psi_\downarrow(\mathbf{r})) \tag{5.3}$$

where $N|\psi(\mathbf{r})|^2$ describes the overall density profile and the $|\uparrow,\downarrow\rangle$ pseudo-spins label the $|f=1, m_F=\pm 1\rangle$ atomic spin states. It's dynamics are governed by a spinor GPE (sGPE) with 2-state dimensionality

$$\begin{aligned} i\hbar\partial_t \psi_{\uparrow,\downarrow}(\mathbf{r}) = \Big[& -\frac{\hbar^2\nabla^2}{2m} + V(\mathbf{r}) + \mu_{\uparrow,\downarrow} B(\mathbf{x}) + (c_0 - c2) N \left|\psi(\mathbf{r})\right|^2 \\ & + 2c_2 N \left|\psi_{\uparrow,\downarrow}\right|^2 \Big] \psi_{\uparrow,\downarrow}(\mathbf{r}) \end{aligned} \tag{5.4}$$

where $N|\psi(\mathbf{r})|^2$ is the total density, m is the atomic mass and $V(\mathbf{r})$ is a spin-independent external potential. $\mu_{\uparrow,\downarrow} = \pm g_F \mu_B$. The dynamics of each spin state in this Hamiltonian are symmetric under exchange of $\uparrow,\downarrow$ indices so long as the magnetic field $\mathbf{B}_{\rm dc}$ is uniform. We often neglect uniform $\mathbf{B}_{\rm dc}$ from our equations.

5.2.3 Attractive condensate analogy

Because the spin-independent interaction coefficient is much larger than the spin-dependent coefficient the overall density $N|\psi(\mathbf{r})|^2$ is relatively insensitive to the position-dependent spin population. Hence, it is appropriate to use either the $\uparrow$ or $\downarrow$ spin component to track the dynamics of Eq. (5.4) with the knowledge that $\int d\mathbf{r}|\psi(\mathbf{r})|^2 = 1$: essentially, if we know the distribution of one spin population we can infer the distribution of the other.

Since c_2 is negative, the dynamics described by a single component of this

sGPE are manifestly similar to that of a single component attractive BEC as it collapses [60, 61, 62, 63]. 1D condensates quenched from repulsive to attractive interactions have a modulational instability with gain at $k = 1/\xi$ that produces a "chain of pearls" pattern. However, the density of this conventional attractive BEC can quickly reach a regime where 3-body losses are large [62]. For our spinor system the analogy to a condensate with attractive interactions breaks down when a spin state becomes fully polarized $|\psi_{\uparrow,\downarrow}(\mathbf{r})|^2 = 1$ (for some values of $\mathbf{r}$) because the fraction of spin population in an individual spinor wavefunction cannot exceed unity.

5.3 Determining the reduced dimensionality of our Hamiltonian

5.3.1 Separating spin and density degrees of freedom

Motivated by the factor of 200 difference between the magnitude of the spin-independent and spin-dependent interactions we make the substitution $\psi_{\uparrow,\downarrow}(\mathbf{r}) = \phi(\mathbf{r})\chi_{\uparrow,\downarrow}(\mathbf{r})$ into Eq. 5.4

$$\begin{aligned} i\hbar[\chi_{\uparrow,\downarrow}(\mathbf{r})\partial_t\phi(\mathbf{r}) + \phi(\mathbf{r})\partial_t\chi_{\uparrow,\downarrow}(\mathbf{r})] =& \chi_{\uparrow,\downarrow}(\mathbf{r})\Bigg[-\frac{\hbar^2\nabla^2}{2m} + V(\mathbf{r}) + c_0 N\left|\phi(\mathbf{r})\right|^2\Bigg]\phi(\mathbf{r}) \\ &+\phi(\mathbf{r})\Bigg[-\frac{\hbar^2\nabla^2}{2m} + c_1 N\left|\phi(\mathbf{r})\right|^2\left(-1+2\left|\chi_{\uparrow,\downarrow}(\mathbf{r})\right)\right|^2\Bigg]\chi_{\uparrow,\downarrow}(\mathbf{r}) \\ &+\frac{-2\hbar^2\nabla\phi(\mathbf{r})\nabla\chi_{\uparrow,\downarrow}(\mathbf{r})}{2m}. \end{aligned} \tag{5.5}$$

The right hand side (RHS) and Line 1 of Eq. (eq:DomainSep) disappear along with the $\nabla\phi(\mathbf{r})$ term when the TF approximation $|\phi|^2 = (\mu - V(\mathbf{r}))/c_0$ is valid. In the TF approximation $\nabla\phi(\mathbf{r})\nabla\chi_{\uparrow,\downarrow}(\mathbf{r})$ must be small in the bulk of the condensate where the density profile $|\phi(\mathbf{r})|$ changes slowly but can become large in the low density region at the periphery of the BEC. Our analysis neglects this term nevertheless.

The remaining LHS term and Line 2 of the RHS describe the dynamics of $\chi(\mathbf{r})$

$$i\hbar\phi(\mathbf{r})\partial_t\chi_{\uparrow,\downarrow}(x) \approxeq \phi(\mathbf{r})\Bigg[-\frac{\hbar^2\nabla^2}{2m} + c_2 N\left|\phi(\mathbf{r})\right|^2\left(-1+2\left|\chi_{\uparrow,\downarrow}(x)\right)\right|^2\Bigg]\chi_{\uparrow,\downarrow}(x). \quad (5.6)$$

In our system the anisotropy of our trap eliminated the spin dynamics along all but the axial direction, $\mathbf{e}_z$. Since the BEC is very much a 3D system we cannot reduce the dimensionality of the sGPE but we can integrate over the spatial directions that have a energetic penalty to domain formation. Integrating along $\mathbf{e}_x$ and $\mathbf{e}_y$ in Eq. 5.6, and assuming an initial density profile $\phi(r) = (\mu - V(\mathbf{r}))/c_0$ for $\phi(\mathbf{r}) > 0$, we obtain an effective sGPE along $\mathbf{e}_z$. Note that it is important to retain the $\phi(\mathbf{r})$'s on both sides of the equation during the integration. Following the integration we remove overall factors $\propto \phi(x)$ so that the effective sGPE is dimensionless

$$i\hbar\partial_t\chi_{\uparrow,\downarrow}(x) \approxeq \Bigg[-\frac{\hbar^2\nabla^2}{2m} - \frac{3c_2}{5c_0}(\mu - V(x)) + 2\frac{3c_1}{5c_0}(\mu - V(x))\left|\chi_{\uparrow,\downarrow}(x)\right|^2\Bigg]\chi_{\uparrow,\downarrow}(x) \quad (5.7)$$

where $V(x) = m\omega_x^2 x^2/2$, ω_x is the trap frequency along $\mathbf{e}_x$ and m is the mass of ^{87}Rb.

5.3.2 Energy density

The 1D energy density for a BEC at coordinate x, where $c_0 n_{1\mathrm{D}}(x) = \mu - V(x)$ and $n_{1\mathrm{D}}(x) = N|\phi(x)|^2$ is approximately

$$E(x) = n_{1\mathrm{D}}(x)\sum_{\sigma=\downarrow}^{\uparrow}\chi_\sigma^\dagger(x)\left[\epsilon_k + \frac{2c_1}{3}n_{1\mathrm{D}}(x)(-1+2\left|\chi_\sigma(x)\right|^2)\right]\chi_\sigma(x) \quad (5.8)$$

Our preparation of a uniform mixture of immiscible spin components $|\chi_\sigma(x)|^2 = 0.5$ is maximally out of equilibrium in the spin degree of freedom, this is most apparent when we consider the contribution of the interactions to the energy $\sum_{\sigma=\downarrow}^{\uparrow}\left(\left|\chi_\sigma(x)\right|^2 - 2\left|\chi_\sigma(x)\right|^4\right)$

which is zero when $|\chi_\sigma(x)|^2 = 0.5$ and negative otherwise.

5.3.3 Determination of the 1D spin healing length

Following the treatment of section 3.3 we consider a local region of the condensate and treat the density profile as if it were essentially flat. This is the local density approximation (LDA) in which it is appropriate to expand our combined spinor wavefunction for the condensed and uncondensed regions $\chi'_{\sigma=\uparrow,\downarrow}$ in terms of plane waves with boson modes:

$$\chi'_\sigma(x) = \frac{1}{\mathrm{L}^{1/2}} \sum_k c_{k,\sigma} e^{ikx} \hat{a}_{k,\sigma}. \tag{5.9}$$

$\hat{a}^\dagger$ and $\hat{a}$ are the raising and lowering operators, and $k=0$ corresponds to the (spatially uniform) condensate state. The macroscopically occupied condensate mode have weight $c_0 = \chi_\sigma(x)$ (note the absence of a prime) while the excited modes have weight $c_k = 1/\sqrt{N}$.

We substitute the full spinor wavefunction $\chi'_\sigma(x)$ into the energy density Eq. 5.8 and the resulting sum over interaction terms is indexed by four different wavevectors, k. Following the Bogoliubov approximation we neglect terms with a combined weight that is more than quadratic in $1/\sqrt{N}$. This requires that we replace $\hat{a}_0$ or $\hat{a}_0^\dagger$ with $\chi'_\sigma(x)$ at least twice in each interaction term. We focus on the restrictive case where both momentum and spin are conserved within each product of the expansion over wavevectors in $\chi'_\sigma(x)$. The objective is to find momentum and number conserving quasiparticles [32]; the spectrum of these quasiparticles is the excitation spectrum for the equilibrium or quasi-equilibrium condensate. Using Einstein summation convention the energy density $E(k)$ for excitations takes the

form

$$
\begin{aligned}
E(k) = & \sum_{\sigma,\sigma',\sigma'',\sigma'''} \chi^{\dagger}_{k,\sigma}\epsilon_k\chi_{k,\sigma'}\delta_{\sigma,\sigma'} \\
& + \Bigg[\frac{2c_2}{3} n_{1\mathrm{D}}(x)\hat{a}^{\dagger}_{k,\sigma}\chi^{\dagger}_{0,\sigma'}\chi_{0,\sigma''}\hat{a}_{k,\sigma'''} \\
& + \frac{2c_2}{3} n_{1\mathrm{D}}(x)\chi^{\dagger}_{0,\sigma}\hat{a}^{\dagger}_{-k,\sigma'}\hat{a}_{-k,\sigma''}\chi_{0,\sigma'''} \\
& + \frac{2c_2}{3} n_{1\mathrm{D}}(x)\hat{a}^{\dagger}_{k,\sigma}\hat{a}^{\dagger}_{-k,\sigma'}\chi_{0,\sigma''}\chi_{0,\sigma'''} \\
& + \frac{2c_2}{3} n_{1\mathrm{D}}(x)\chi^{\dagger}_{0,\sigma}\chi^{\dagger}_{0,\sigma'}\hat{a}_{k,\sigma''}\hat{a}_{-k,\sigma'''} \Bigg] \delta_{\sigma-\sigma',\sigma''+\sigma'''}
\end{aligned}
\tag{5.10}
$$

We may reorganize terms in Eq. 5.10 into the form of a matrix. Adopting the uniform and equal spin population that is the initial condition for our experiment the spin population is $\chi_{0,\sigma} = 1/\sqrt{2}$ (for both $\sigma = \uparrow, \downarrow$). Simplifying, the Hamiltonian is

$$
\hat{H} = (\text{other terms}) + \sum_{k\neq 0,\sigma,\sigma',\sigma'',\sigma'''} (\hat{a}^{\dagger}_{-k,\sigma}, \hat{a}_{k,\sigma'})\hat{M}(\hat{a}_{-k,\sigma''}, \hat{a}^{\dagger}_{k,\sigma'''})^T \tag{5.11}
$$

where $\hat{M}$ is a matrix with four 2×2 blocks of spin. $(\hat{a}_{-k,\sigma}, \hat{a}^{\dagger}_{k,\sigma'})$ does not transform like a vector. In fact the bosonic commutation relations $[\hat{a}_{k,i}, \hat{a}^{\dagger}_{k,j}] = (-\sigma_z)_{i,j}$ must be preserved during a transformation T where i and j indexes the two elements of $(\hat{a}_{-k,\sigma}, \hat{a}^{\dagger}_{k,\sigma'})$, not the spin. $T^{\dagger}\sigma_z T$ must equal σ_z to preserve these commutation relations. We need to find a transformation $T^{\dagger}\hat{M}T = \nu_{k,\sigma}$ that diagonalizes the Hamiltonian. In practice, $T^{-1}\sigma_z\hat{M}T = \sigma_z\nu_{k,\sigma}$ is easier to calculate because the eigenvalues of $\sigma_z\hat{M}$ may be found with a simple non-Hermitian similarity transform [32].

$$
\hat{M} = \tag{5.12}
$$

$$
\begin{pmatrix}
(\epsilon_{-k}-\epsilon_0)\hat{1} + \frac{c_1}{3}n_{1\mathrm{D}}(x)(\hat{1}+\hat{\sigma}_x) & \frac{c_1}{3}n_{1\mathrm{D}}(x)(\hat{1}+\hat{\sigma}_x) \\
\frac{c_1}{3}n_{1\mathrm{D}}(x)(\hat{1}+\hat{\sigma}_x) & (\epsilon_k-\epsilon_0)\hat{1} + \frac{c_1}{3}n_{1\mathrm{D}}(x)(\hat{1}+\hat{\sigma}_x)
\end{pmatrix}
$$

where $\hat{\sigma}_x$ and the identity $\hat{1}$ act on the 2×2 spin basis and$\epsilon_{\pm k} = \hbar^2 k^2/2m + E_\sigma$.

The eigenvalues $\nu_{k,\sigma}$ are typically identical under exchange of $\pm k, \pm\sigma$. There are some cases where this exchange symmetry breaks down i.e. in the presence of spin-orbit coupling. We neglected several terms that typically contribute to the excitation Hamiltonian Eq. 5.11 including the quantum depletion and the BEC energy. See page 285 of Ref. [64] for a more general treatment of BEC excitations.

The energy dispersion for excitations, shown in Fig. 5.1, has the form $\nu_{k,\sigma} = \sqrt{\epsilon_k(\epsilon_k - 4c_2 n_{1\mathrm{D}}(x)/3}$ [55]. We nicely showcase the relationship between the healing length $\xi_{1\mathrm{D}}$ and the wavevector of excitations k by rewriting the energy dispersion

$$\frac{\hbar\omega}{\mu_{1\mathrm{D}}} = (k\xi_{1\mathrm{D}})^2[(k\xi_{1\mathrm{D}}) - 2] \tag{5.13}$$

where the 1D spin healing length is $\xi_{1\mathrm{D}} = \hbar/\sqrt{2m(2c_2 n_{1\mathrm{D}}(x)/3)}$ and the chemical potential $\mu_{1\mathrm{D}} = \hbar^2/2m\xi_{1\mathrm{D}}$ is the typical 1D spin interaction energy. The 1D spin healing length is substantially larger than the fully 3D spin healing length $\xi_{1\mathrm{D}} = \sqrt{3/2}\xi_s$ and the chemical potential is correspondingly smaller: $\mu_{1\mathrm{D}} = 2\mu_s/3$.

When the $\nu_{k,\sigma} = \sqrt{\epsilon_k(\epsilon_k - 4c_2 n_{1\mathrm{D}}(x)/3}$ is imaginary, this occurs over the range $k\xi_{1\mathrm{D}} \in (0, \sqrt{2})$, It is energetically favorable for quasiparticles to form with non-zero wavevector k. The associated modes grow exponentially with peak gain at $k = 1/\xi_{1\mathrm{D}}$, amplifying any existing spin fluctuations, classical or quantum.

5.4 sBEC preparation

5.4.1 Trap geometry

As we depict in Fig. 5.2, our ^{87}Rb BEC's are prepared in an extremely anisotropic crossed dipole trap that nevertheless produces a cigar-shaped BEC whose wavefunction is governed by the 3D sGPE. Because the typical $c_0 n(\mathbf{r})$ spin-independent energy vastly exceeds the $c_2 n(\mathbf{r})$ spin-dependent energy scale, we make the conven-

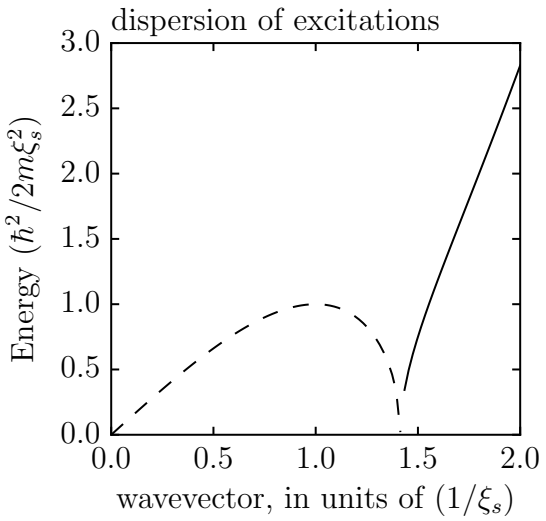

Figure 5.1: Dispersion of spin excitations for Eq. 5.13. The dotted line is the magnitude of the imaginary component of the spectrum and while the solid line is the magnitude of the real component. For wavevectors where the dispersion is imaginary the system experiences exponential gain: peak gain is ξ_s.

Description	Symbol	Value
Atom number	N	$7.0(5)\times10^5$
Magnetic field	$\mathbf{B}$	107.0(2) μT$\mathbf{e}_z$
Axial TF* radius	R_z	170(7) μm
Radial TF radius	R_r	3.9(1) μm
Initial spin population	χ	$\{1/\sqrt{2}, 0, 1/\sqrt{2}\exp(-i\phi)\}$
Magnetization along $\mathbf{e}_z$	M_z	$\lvert\psi_\uparrow(\mathbf{r})\rvert^2 - \lvert\psi_\downarrow(\mathbf{r})\rvert^2$
Magnetization along $\mathbf{e}_x$	M_x	$\{2\mathrm{Re}[\psi_\uparrow^*(\mathbf{r})\psi_\downarrow]$
Density	$n(\mathbf{r})$	$[\mu - V(\mathbf{r})]/(c_0 + c_2 M_z(\mathbf{r})$
Condensate wavefunction	$\psi(\mathbf{r})$	$n(\mathbf{r})\chi(\mathbf{r})/\sqrt{N}$
Healing length**	ξ	$\hbar/\sqrt{2m\mu} \approx 0.2$ μm
Spin healing length	ξ_s	$\hbar/\sqrt{2mc_2\mu/c_0} = 3.20(4)$ μm
1D Spin healing	$\xi_{1\mathrm{D}}$	$\sqrt{3/2}\xi_s$
Axial trap freq	$\omega_z/2\pi$	3.1(2) Hz
Radial trap freq	$\omega_r/2\pi$	135(3) Hz
Axial Dipole waist	$1/e^2$ radius	$\approx$300 μm
Radial Dipole waist	$1/e^2$ radius	$\approx$67 μm
Temperature	T	90(8) nK

Table 5.1: Coarsening experimental parameters. *TF refers to the Thomas-Fermi approximation wherein the contribution of the kinetic energy to the density profile is neglected. **Healing lengths, ξ, are shortest at peak density, $\mu \approx c_0 n_{\mathrm{peak}}$, and longer at the BEC periphery. All uncertainties herein reflect the uncorrelated combination of single-sigma statistical and systematic uncertainties.

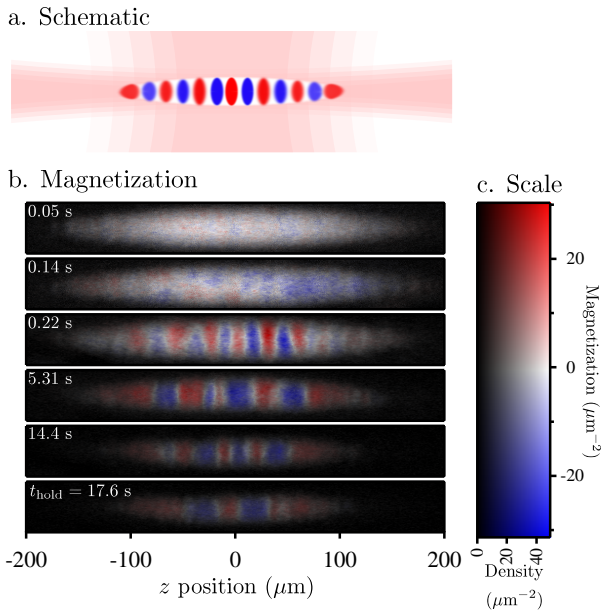

Figure 5.2: Magnetization $M_z(\mathbf{r})$. (a) Schematic, illustrating a spinor BEC with domains in an anisotropic crossed-dipole trap. (b) Images showing the progression from a uniformly magnetized condensate (short times) in which domains appear (intermediate times), and then grow spatially (long times); during this process the condensate slowly decays away. (c) Color scale indicating the degree of magnetization (colors from blue to red), and the density (intensity from black to colored).

tional Thomas-Fermi approximation for the overall density distribution $n(\mathbf{r})$. This apparatus is characterized by a chemical potential μ, and a minimum healing length $\xi = \hbar/\sqrt{2m\mu}$. This gives $n(\mathbf{r}) = [\mu - V(\mathbf{r})] / [c_0 + c_2 M_z^2(\mathbf{r})]$, which depends very weakly on the z component of local magnetization vector,

$$\begin{aligned}\mathbf{M}(\mathbf{r}) &= \{M_x(\mathbf{r}), M_y(\mathbf{r}), M_z(\mathbf{r})\} \\ &= \left\{2\mathrm{Re}[\psi_\uparrow^*(\mathbf{r})\psi_\downarrow(\mathbf{r})], 2\mathrm{Im}[\psi_\uparrow^*(\mathbf{r})\psi_\downarrow(\mathbf{r})], |\psi_\uparrow(\mathbf{r})|^2 - |\psi_\downarrow(\mathbf{r})|^2\right\}.\end{aligned} \tag{5.14}$$

The BECs' 170 μm axial radius is not small compared to dipole laser's 300 μm Gaussian beam waist along the axial direction and as a result we expect small deviations from the conventional inverted parabola density profile.

5.4.2 Initializing the experiment with rf

We prepare a uniform 50:50 mixture of $m_F = \pm 1$ with high fidelity by first loading into the $m_F = 0$ component of ^{87}Rb's $f = 1$ ground hyperfine manifold, reducing $B_{\mathrm{dc}} = 0.7$ G, and then applying a fixed duration 34 μs square pulse of rf magnetic field oriented perpendicular to $B_{\mathrm{dc}}\mathbf{e}_z$. At this B_{dc} the power broadened width of the rf pulse is much larger than the quadratic Zeeman shift. Population transfer using this rf magnetic pulse occurred on a timescale much shorter than typical spin equilibration timescale $\tau(z) = 2m\xi_{1\mathrm{D}}^2(z)/\hbar \approx 42$ ms: quenching the system into a uniform but immiscible two-component spin configuration.

5.4.3 Confining spin dynamics to 1D

The quenched binary mixture was held for a variable duration t_{hold}, up to 17.6 s, during which spin structure formed and subsequently evolved. Spin mixing collisions are suppressed because the relatively large 82 Hz quadratic Zeeman shift greatly exceeds the $c_2 n(\mathbf{r}) \approx 6$ Hz spin dependent energy [50]. As a result, we observe no population in $m_F = 0$ for the entire duration of our experiment. Because our extremely

anisotropic condensate's ≈ 3.9 μm radial extent is comparable to the minimum spin healing length $\xi_s = 3.20(4)$ μm there is a cost associated with modulation of spin density along the radius of the trap [54]. Evaporation and thermalization eventually align spin density modulations to the long axis of the trap and with precise control of gradients we were able to eliminate radial spin modulations. We summarize the physical properties of these BECs in Table 5.1.

5.4.4 Imaging

After $t_{\rm hold}$, we removed the confining potential and allowed the atomic ensemble to expand (largely transverse to the alignment of our domains) for 19.3 ms, during which time we Stern-Gerlach [65] separated the spin components. We detected the resulting density distribution by absorption imaging, and reconstructed both $M_x(x,z)$ and $M_z(x,z)$, which were projected onto the $\mathbf{e}_z - \mathbf{e}_x$ imaging plane. A brief rf pulse just before TOF could partially re-populate $|m_F = 0\rangle$; following TOF expansion and Stern-Gerlach separation, the distribution of all three spin states contained sufficient information to obtain M_x and M_z simultaneously. We depict representative reconstructions of $M_z(x,y)$ at six hold times in Fig. 5.2.

The transverse magnetization, $M_x(z)$ may be measured using a $t = 1/4\Omega_{\rm rf}$ rf pulse that transfers some (but not all) the population $|\psi_{\uparrow,\downarrow}|^2$ back into the ψ_0 state. We may then process the image of all three spin states $m_F = 0, \uparrow, \downarrow$ to extract $M_z(z)$ and $M_x(z)$

$$M_x(z) = \frac{|\psi_0'(\mathbf{r},t)|^2}{\sin^2(t\Omega_{\rm rf})} \tag{5.15}$$

$$M_z(z) = \frac{\psi^{\dagger\prime}(\mathbf{r},t)\hat{F}_z\psi'(\mathbf{r},t)}{\cos(t\Omega_{\rm rf})} \tag{5.16}$$

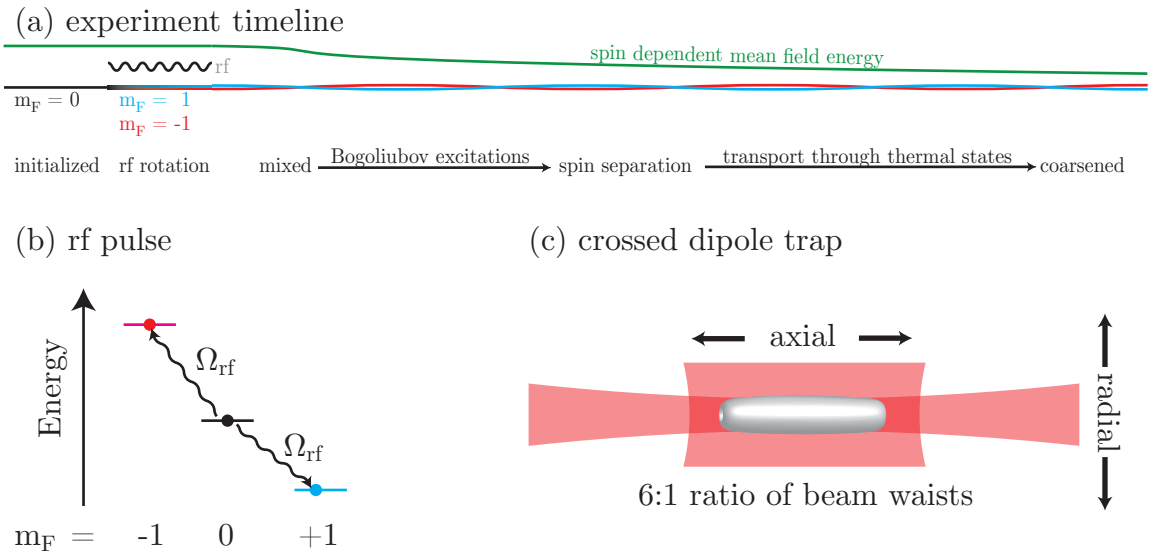

Figure 5.3: (a) We pulse from $|m_F = 0\rangle$ into an evenly mixed superposition of $|\uparrow, \downarrow\rangle$ with equal population. Bogoliubov spin excitations quickly produce domains in our system. These relax to a longer length scale when they reach full contrast. With the green trace we show the evolution of the spin dependent mean field energy. (b) Following this initial coarsening which ends $\sim$ 500 ms domain spatial extent increases very gradually. (b) Our initial $|m_F = 0\rangle$ spin population is transferred to $|\uparrow, \downarrow\rangle$ with a single rf pulse. (c) Our system is prepared in a crossed-dipole trap whose waists differ by a factor of 6. The greater anisotropy of our trap frequencies is produced with relative beam intensities.

5.4.5 Gradient compensation

When the magnetic field is position dependent, i.e. gradients are present, the $M_x(z)$ is not only time but position dependent. For all times before $M_z(z)$ rises above the background noise the measurement of the spatial periodicity in $M_x(z)$ is sufficient to determine the axial gradient $\nabla_z B = \gamma z^2$, where $\gamma = 0.092(4)$ G/cm^2. Although small, we saw some preference for $|m_F{=}{+}1\rangle$, $|{\uparrow}\rangle$, to migrate axially to the edges of the cloud. We were able to mitigate this using a spin echo π-pulse: flipping $|{\downarrow}\rangle$ and $|{\uparrow}\rangle$ midway between the quench and the beginning of TOF. The spin echo removed the large-scale spin structure from the inhomogeneous magnetic fields, but left the spin dynamics – which were associated with much shorter length scales – otherwise unaffected. Furthermore, well above our ambient gradients, a counterflow instability [46] seeds spin-structure growth.

5.4.6 Symmetry

Our spinor experiment is initialized by a rf-pulse that puts each atom into a equal-amplitude superposition of the $|{\uparrow},{\downarrow}\rangle = |m_F = \pm 1\rangle$ spin states; the system then evolves according to Eq. (5.4) when the rf is off. While a single component BEC breaks just a single U(1) symmetry associated with a wave function's overall phase (generated by the identity)

$$|\psi\rangle = e^{-i\phi_{\rm total}}\,|m_F{=}0\rangle\,, \tag{5.17}$$

our spinor Hamiltonian adds a U(1) symmetry associated with the relative phase of the spin (generated by the Pauli matrix $\check{\sigma}_z$), as well as a discrete Z_2 symmetry associated with equal population of the spin components

$$|\psi\rangle = e^{-i[\phi_{\rm total}+\phi_{\rm rel}]}\,|{\downarrow}\rangle + e^{-i[\phi_{\rm total}-\phi_{\rm rel}]}\,|{\uparrow}\rangle\,. \tag{5.18}$$

Post quench, the formation of spin domains corresponds to breaking the Z_2 symmetry, while within a specific domain, a new U(1) symmetry is broken. This phase is generated by a combination of the overall and relative phases: each spin domain has a broken generator $(\check{1} - \check{\sigma}_z)/2$, leaving behind a "sneaky" unbroken U(1) symmetry generated by $(\check{1} + \check{\sigma}_z)/2$: essentially,

$$\phi_{\text{broken}} = \phi_{\text{total}} + \phi_{\text{rel}}|\chi_\downarrow|^2 - \phi_{\text{rel}}|\chi_\uparrow|^2 \tag{5.19}$$

$$\phi_{\text{unbroken}} = \phi_{\text{total}} + \phi_{\text{rel}}|\chi_\downarrow|^2 + \phi_{\text{rel}}|\chi_\uparrow|^2. \tag{5.20}$$

5.5 Domain growth

5.5.1 Initial times

The quench prepared a uniform and transversely magnetized $\boldsymbol{\chi}(z) = (|\uparrow\rangle + |\downarrow\rangle)/\sqrt{2}$ spin superposition. Exponential gain increases the magnetization $M_z(z)$, the difference in spin populations, for wavevectors in the range $k\xi_{1\text{D}} = (0, \sqrt{2})$ with peak gain at $k = 1/\xi_{1\text{D}}$. Figure 5.4a depicts the time evolving magnetization $M_z(z)$ of the condensate. After the quench, spin structure amplitude (red and blue) above and below $M_z(z) = 0$ (white) grew with a minimum exponential time constant $\tau(z) = 2m\xi_{1\text{D}}^2(z)/\hbar \approx 42$ ms but only became visible after $t_{\text{hold}} \approx 200$ ms.

In Fig. 5.4b, we compare our experimental result with those of a stochastic-projective GPE (SP-GPE) simulation [66] which has parameters nearly matched to our experiment. The SP-GPE's stochastic noise term was chosen to match the experimentally observed temperature, and was not tuned to match the onset-time for domain formation.

Although our simulations predict that spin structure began to grow immediately, the structure remained undetected until its amplitude exceeded the technical noise (primarily due to shot noise in density fluctuations across the BEC) in the system. When counting the number of spin domains in our system, we found the

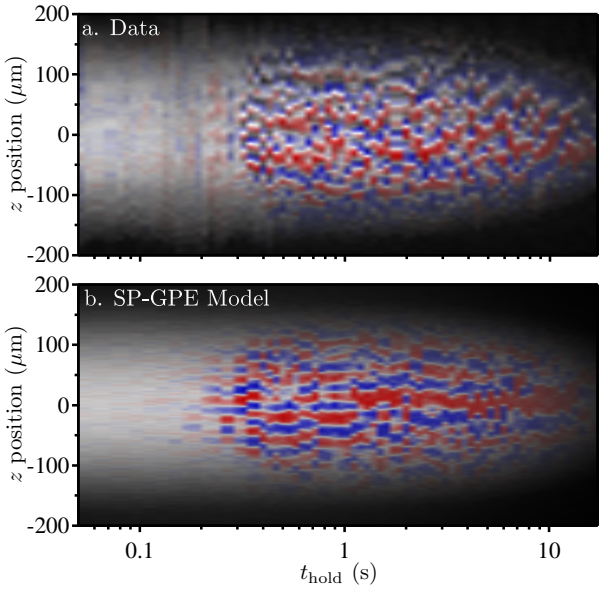

Figure 5.4: Time evolution of magnetization $M_z(z)$ found by taking slices along the axial dimension of BEC spin components that had been separated in TOF. (a) Experimental data and (b) finite temperature simulation using the SP-GPE method. In both simulation and experiment, the spatial structure of $M_z(z)$ coarsens after an initial growth period as domains coalesce. The overall spatial extent and brightness of the clouds decrease as atoms leave our trap.

number of modulations in $M_z(z)$ that were larger in amplitude than the measured noise in $M_z(z)$. The threshold amplitude above which we counted a domain was flat in $|\psi_{\uparrow,\downarrow}|^2$. We chose not to compensate for the density of the condensate because more tailored thresholds produced a number of false positives. We show the rapid increase in domain number following a short delay after the quench in Fig. 5.5. In Fig. 5.5 we compare the domain count of our experiment and the SP-GPE simulation to the domain count predicted by summing over the $\pi\xi_{1\mathrm{D}}(x)$ periodicity expected from our analytics

$$N_{\mathrm{D}} = \int_{-R_z}^{R_z} dx \frac{1}{\pi\xi_{1\mathrm{D}}(x)} = \frac{R_z}{2\xi_{1\mathrm{D}}} \tag{5.21}$$

where $\xi_{1\mathrm{D}}(x) = n_{1\mathrm{D}}(x)\xi_{1\mathrm{D}}/n_{1\mathrm{D}}(0)$. The abrupt increase in domain count at short timescales is primarily a consequence of the growing domain contrast surpassing the threshold for detection. This increase occurs over a finite time because the domains grow in amplitude faster at the high density regions of the condensate than the low density periphery. The bulge in domain amplitude at the center of the atomic cloud can be seen for a brief window in time in Figure 5.4. Potentially as a consequence of poor domain counting near the periphery of the condensate neither experiment nor simulation reach the domain count predicted by the analytics.

It is difficult to obtain a quantitative measure of domain size from domain counting because a number of ancillary factors come into play: threshold amplitudes for domains, atom loss. Moreover, while measurements at neighboring times have similar domain sizes as seen in Fig. 5.4 the exact domain pattern is subject to subtle differences in the initial conditions and has a significant element of randomness – primarily in the form of phase shifts. We address these concerns by applying the power spectral density (PSD)

$$\mathrm{PSD}_{x,z}(k) = \left| \int M_{x,z}(z) \exp(ikz) \mathrm{d}z \right|^2 \tag{5.22}$$

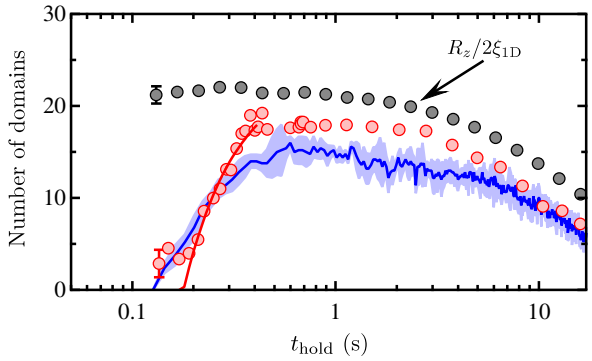

Figure 5.5: Number of domains as a function of t_{hold}. The red symbols depict the experimentally observed number of domains (typical uncertainty plotted on the leftmost point) and the blue curve plots the results of our SP-GPE simulation (uncertainties denoted by the blue band). In both cases, the uncertainties reflect the standard deviation over many realizations. In addition, the red curve fits the data to a model assuming exponential growth along with a non-zero observation threshold, in the LDA. The grey symbols correspond to the ratio $R_z/2\xi_{1\mathrm{D}}$: an estimate of domain number, assuming a condensate with radius $2R_z$ is partitioned into domains of local size $\pi\xi_{1\mathrm{D}}(z)$ (the size at which domains initially form); the weighted average of this over our system is about $4\xi_{1\mathrm{D}}$.

to the measured magnetization which entirely removes phase information. The PSD largely decouples domain amplitude and overall atom number from their spatial wavevector. Hence, the PSD is a direct measure of domain size that is valid for short times when domain amplitude is small and long times when the condensate number and spatial extent shrinks.

Figure 5.6a shows $\mathrm{PSD}_z(k)$ derived from $M_z(z)$ shown in Fig. 5.4. For short times ($t_{\mathrm{hold}} \lesssim 300$ ms), a narrow peak associated with the growing spin modulations develops. Figure 5.6b compares this peak location for both experiment and theory against $1/\xi_{1\mathrm{D}}$. These domains have a wavevector set by the dynamic growth process (Bogoliubov excitations) and not by the system's equilibrium thermodynamics. Hence, we analytically predict and saw in our SP-GPE simulation that the wavevector at the center of the cloud, and at peak amplitude in the PSD(k), should be $1/\xi_{1\mathrm{D}}$. By contrast, the peak in $\mathrm{PSD}_z(k)$ for the experiment is at slightly smaller k. Fig. 5.6 plots experimental data with red symbols and SP-GPE simulation with

the blue curve.

5.5.2 Intermediate times

Once the spin domains reach unity polarization, the magnetization's magnitude saturates and the boundaries between domains – domain walls – sharpen, broadening $\mathrm{PSD}_z(k)$ in Fig. 5.6ab starting at $t_{\mathrm{hold}} \approx 250$ ms. Starting around 350 ms the broadened peak moves to smaller k over 150 ms corresponding to an observable increase in domain size. In the simulation, the exact start time and slope of this reequilibration depended strongly on temperature; most (but not all) experimental data runs showed this feature. More subtly, peak $\mathrm{PSD}_z(k)$ for domains between 500 ms and 2 seconds appears to be constant: the ratio between peak $\mathrm{PSD}_z(k)$ and $1/\xi_{1\mathrm{D}}(z)$–a measure of the kinetic energy penalty for domain structure–reached a minimum in this range.

5.5.3 Long times

Our BEC has a $\tau = 10(1)$ s lifetime which causes the spatial extent of the BEC to shrink even as the healing length $\xi_{1\mathrm{D}}$ increases: both effects reduce the maximum expected domain count N_{D}. Once a domain becomes smaller than the ever increasing $\approx 2\xi_{1\mathrm{D}}(z)$, it is no longer reaches full spin-polarization at its center, and it ceases to be a barrier for the hydrodynamic flow of the other spin state. As a result, small domains can move freely and coalesce with another domain of the same spin. Hence, experiment and simulation domain count should shrink no slower than N_{D} which is largely borne out in Fig. 5.5.

Unlike $\mathrm{PSD}_z(k)$, $\mathrm{PSD}_x(k)$ is peaked about zero; this is because $M_x(z)$ is only appreciable in the domain walls where the gas is not fully polarized: it consists of a series of narrow peaks. By showing that the width of the peak in $\mathrm{PSD}_x(k)$ tracks the inverse spin-healing length, i.e. domain walls are broadening, Fig. 5.6c demonstrates that the domain walls are sized in proportion to $\xi_{1\mathrm{D}}$ (grey symbols).

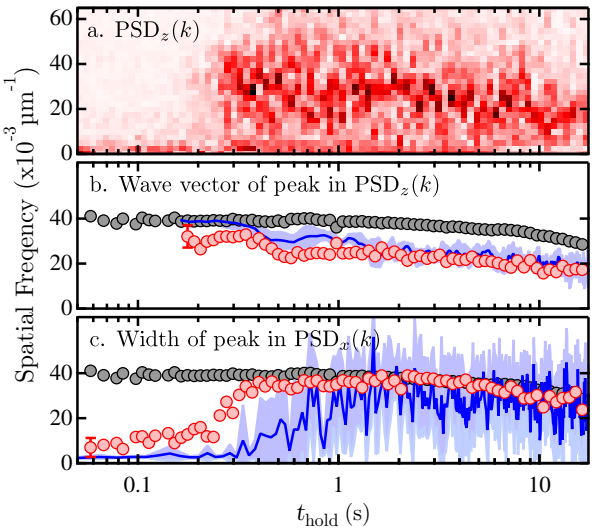

Figure 5.6: Power spectral density. (a) PSD$_z(k)$ as a function of t_{hold} showing the formation of a peak at finite wave-vector k, followed by the gradual movement of that peak to smaller k as the spin domains expand. Each vertical slice represents a single experimental realization, i.e., no averaging. The color scale depicts increasing spectral power with darker color. (b) Wave-vector of PSD$_z(k)$'s peak. (c) Width of PSD$_x(k)$, which always peaked around zero. In (b) and (c), the red symbols depict the experimentally observed peak location (typical uncertainty plotted on the leftmost point) and the blue curve plots the results of our SP-GPE simulation (uncertainties denoted by the blue band). In these three cases, the uncertainties reflect the standard deviation over eleven realizations, i.e., (b) and (c) are averaged data. The grey symbols mark $1/\xi_{1\mathrm{D}}$, the homogenous-system wave-vector of maximum gain (the uncertainties are comparable to the symbol size).

It is plausible that the dominant mechanism for domain growth results from this increasing cutoff in the minimum domain size $\approx 2\xi_{1D}(z)$. For this case we might anticipate that the dynamic energy cost $\hbar^2k^2/2m$ of having structure at the peak wavevector k in $\mathrm{PSD}_z(k)$ would be a constant fraction of the peak spin interaction energy $-\hbar^2/2m\xi_{1D}^2$. We see in Figure 5.6b for times $t_{\mathrm{hold}} > 2\,\mathrm{sec}$ that k tracks $1/\xi_{1D}$ as this model would predict. To highlight this possible relationship, we display the ratio between $\mathrm{PSD}_z(k)$ and $1/\xi_{1D}(z)$ – essentially constant – on a linear time scale in Figure 5.7 (the uncertainties reflect the standard deviation of the mean at each t_{hold}).

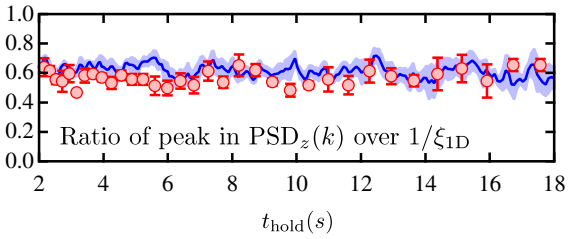

Figure 5.7: Ratio of peak in $\mathrm{PSD}_z(k)$ over $1/\xi_{1D}$ plotted on a linear time scale. We use only the seven data runs that include $t_{\mathrm{hold}} > 6\,\mathrm{sec}$. Unlike the rest of the paper the uncertainties given here represent standard deviation of the mean. The red symbols depict the experimentally observed peak location and the blue curve plots the results of our SP-GPE simulation (uncertainties denoted by the blue band).

5.6 Concluding remarks

We observe the dynamic formation of spin-domains from an initially uniform, but immiscible, 2-component spinor system. A modulational instability gains spin noise with wavevector $k = 1/\xi_{1D}(z)$, setting the initial domain wavevector. These domains subsequently relax to smaller wavevectors and larger domains, i.e. coarsening. For times $> 2\,\mathrm{sec}$ the peak wavevector remains a constant fraction of the spin healing length $\xi_{1D}(0)$ as the system coarsens.

Chapter 6: Spin-orbit coupling ultracold atoms, the basics

6.1 Introduction

Because ultracold gases are neutral, the class of effects experienced by charged particles moving in an electric and/or magnetic field would appear to be inaccessible to quantum simulation in ultracold systems. However, a two photon Raman process can mimic the coupling between spin and momentum in conventional materials. In materials, the link between momentum and spin is given by a boosted magnetic field produced by the motion of a charged particle in a strong electric field. Using a two photon Raman process the atom absorbs a photon from one Raman beam and emits into the other by stimulated emission. Then, the momentum difference between the photons must be transferred to the atom. In most materials this photon recoil $k_R = 2\pi/\lambda$ (where $\lambda = 790.024$ nm is the laser wavelength) is negligibly small but in ultracold gases the recoil energy $E_R = \hbar^2 {k_R}^2/2m = h \times 3678$ Hz exceeds the characteristic energy scale of the interactions $\mu = c_0 n(0) \sim h \times 2200$ Hz and the recoil momentum k_R greatly exceeds the in-situ momentum extent $\sim k_R/300$ of the BEC (see section 3.2.4).

6.2 The atomic physics

In this section we use the atomic Hamiltonian from Eq. 4.1, which describes the ground ($\ell = 0$) and first ($\ell = 1$) electronic excited states of an atom, and then apply an optical illumination described by the dipole Hamiltonian Eq. 4.5. We specify to the case where the hyperfine structure (HFS) splitting $A_{\mathrm{HFS}} \sim 200$ MHz$-$

6.8 GHz for both the ground and excited electronic states is unresolved by the optical coupling. At the same time we keep our light detuned less than the fine structure (FS) splitting $A_{\mathrm{FS}} \sim 7.2$ THz.

The electron spin and orbit angular momentum are coupled with $A_{\mathrm{FS}}\hat{\mathbf{L}}\cdot\hat{\mathbf{S}}$ and for the eigenstates of this coupling $\mathbf{J}\,|j, m_J\rangle = \hbar\sqrt{j(j+1)}\,|j, m_J\rangle$ where $\mathbf{J} = \mathbf{L} + \mathbf{S}$. We redefine our projection operators which were initially defined in section 4.3.1 to act upon this basis. The eigenenergies for this system are then $\hat{H}_{\mathrm{at}}\,|j, m_J\rangle = E_e\,|j, m_J\rangle$ where we defined $E_g = 0$. The Clebsh-Gordan coefficients and level diagram for the coupling in this basis are given in Fig. 6.1.

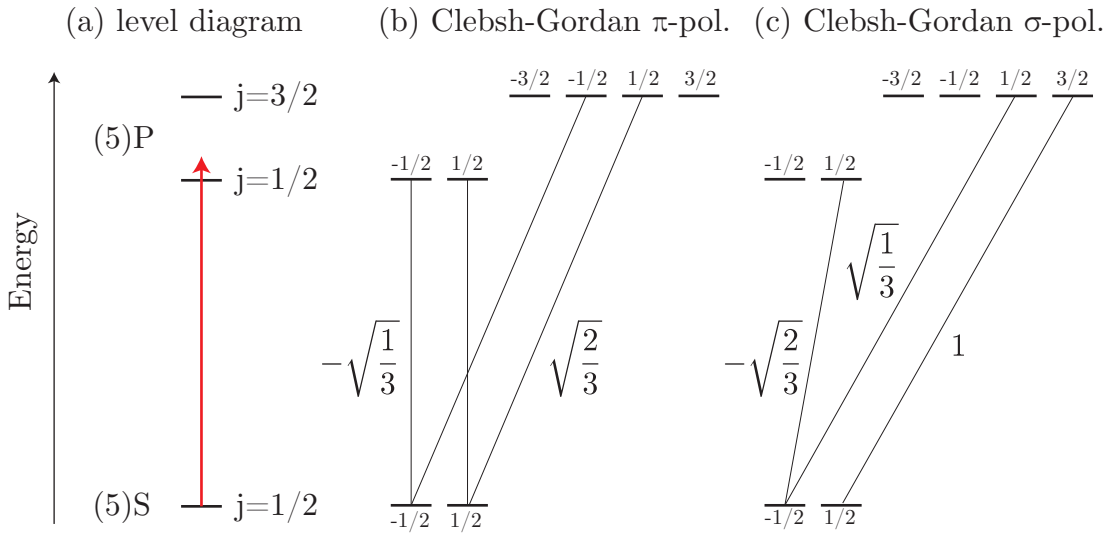

Figure 6.1: Coupling far off-resonant with the hyperfine splittings resolves states with reduced dimensionality $|j, m_F\rangle$. (a) Level diagram for coupling between ground $j = 1/2$ and excited $j = 1/2$, 3/2 states. The sign and magnitude of the coupling may be determined using the reduced matrix element between the ground and excited electronic states $\left\langle \ell = 0 \left|\left| \hat{\mathbf{d}} \right|\right| \ell = 1 \right\rangle$ and Clebsh-Gordan coefficients for (b) π and (c) σ polarized light.

Using the dipole Hamiltonian in Eq. 4.8 we compose an effective Hamiltonian that encapsulates two-photon coupling within the $j = 1/2$ electronic ground states

$$\hat{H}_{\mathrm{eff}} = -\hat{P}_g \hat{H}'_{\mathrm{dip}} \hat{P}_e \hat{H}_{\mathrm{at}}^{-1} \hat{P}_e \hat{H}'_{\mathrm{dip}} \hat{P}_g. \tag{6.1}$$

Expanding Eq. (

refeq:Heff1 in terms of Eq. 4.8

$$\hat{H}_{\text{eff}} = -\frac{1}{4} E_i^{*'} \hat{P}_g \hat{d}_i \hat{P}_e \hat{H}_{\text{at}}^{-1} \hat{P}_e \hat{d}_l \hat{P}_g E_l' = E_i^{*'} \hat{\alpha}_{i,l} E_l'. \tag{6.2}$$

The eigenenergies $\Delta_{1/2} = \Delta_e - A_{\ell,j}^{\text{FS}}$ and $\Delta_{3/2} = \Delta_e + A_{\ell,j}^{\text{FS}}/2$, which are defined in relation to $\hat{H}_{\text{at}} |j, m_J\rangle = \Delta_j |j, m_J\rangle$, are the two-photon detunings from the $j = 1/2$ and $j = 3/2$ excited electronic FS, respectively. The polarizability tensor operator $\hat{\alpha}_{i,j}$ acts within the ground electronic states. All alkali atoms have ground electronic $j = 1/2$: in this special case, the polarizability tensor can be decomposed into scalar $\delta_{i,j}$ and vector $\epsilon_{i,l,m}\sigma_m$ terms. The coefficients in Eq. 6.3 may be calculated using the Clebsh-Gordan coefficients

$$\hat{H}_{\text{eff}} = -\frac{E_i^{*'} E_l' \left|\langle ||\mathbf{d}|| \rangle\right|^2}{4} \left[\frac{(2\delta_{i,l} + i\epsilon_{i,l,m}\sigma_m)}{3\Delta_{3/2}} + \frac{(\delta_{i,l} - i\epsilon_{i,l,m}\sigma_m)}{3\Delta_{1/2}} \right] \tag{6.3}$$

where $\epsilon_{i,l,m}$ is the Levi-Cevita symbol; and $\langle ||\mathbf{d}|| \rangle \equiv \langle l = 0 \, ||\mathbf{d}|| \, l = 1 \rangle$ is the far-off resonant Wigner-Eckert reduced matrix element. In our experiment, we choose Δ_e such that $\Delta_{1/2} = -2\Delta_{3/2}$, thereby removing the scalar (but not vector) terms from Eq. 6.3. This simplifies the Hamiltonian

$$\hat{H}_{\text{eff}} = \frac{iu(\mathbf{E}^{*'} \times \mathbf{E}')}{\hbar} \cdot \hat{\mathbf{J}} \hat{P}_g \tag{6.4}$$

where $u = \left|\langle ||\mathbf{d}|| \rangle\right|^2 / 8\Delta_{1/2}$. Using Landé's projection theorem we stretch Eq. 6.4 to act on the hyperfine ground states:

$$\hat{H}_{\text{eff}} = \frac{f(f+1) - i(i+1) + j(j+1)}{2f(f+1)} \frac{iu(\mathbf{E}^{*'} \times \mathbf{E}')}{\hbar} \cdot \hat{\mathbf{F}} \approx \frac{g_F}{g_J} \frac{iu(\mathbf{E}^{*'} \times \mathbf{E}')}{\hbar} \cdot \hat{\mathbf{F}}. \tag{6.5}$$

The approximate equality in Eq. 6.5 neglects the contribution to g_F from g_I, which modifies g_F at the 0.1% level.

The physical interpetation of $\hat{H}_{\text{eff}}$ is similar to that of the formally identical Zeeman Hamiltonian

$$\hat{H}_Z = \frac{g_F \mu_B}{\hbar} \mathbf{B} \cdot \hat{\mathbf{F}} \tag{6.6}$$

where μ_B is the Bohr magneton and $\mathbf{B}$ is the magnetic field. By analogy, we use $\mathbf{B}_{\text{eff}} = \hat{H}_{\text{eff}}/\mu_B g_J$ to define an effective time and position dependent magnetic field

$$\mathbf{B}_{\text{eff}} \approxeq \frac{-iu \left[\mathbf{E}^{*\prime}(\mathbf{x},t) \times \mathbf{E}^{\prime}(\mathbf{x},t)\right]}{\mu_B g_J} \tag{6.7}$$

which is exact for $f = 1$ and $j = 1/2$ when g_J is replaced with $-4g_F$. Combined, the Zeeman and Raman coupling terms of the Hamiltonian are

$$\hat{H}_Z + \hat{H}_{\text{eff}} = \frac{g_F \mu_B}{\hbar} (\mathbf{B} + \mathbf{B}_{\text{eff}}) \cdot \hat{\mathbf{F}}. \tag{6.8}$$

Because B_{dc} or B_{eff} interacts with the spin basis in the form of the angular momentum spin matrices $|f, m_F\rangle$ states separated by more than ± 1 units of angular momentum cannot be coupled. Using spin-1 as an example, $|f = 1, m_F = \pm 1\rangle$ cannot be directly coupled with Raman.

The full electric field measured at an atom illuminated by multiple linearly polarized lasers, which we index with β, is

$$\mathbf{E}(t) = \sum_{\beta} E_\beta \mathbf{e}_\beta \cos\left[\mathbf{K}_\beta \cdot \mathbf{x} - \omega_\beta t - \gamma_\beta\right] \tag{6.9}$$

where $\mathbf{K}_\beta$, $\omega_\beta/2\pi$, and γ_β are each laser's wavevector, frequency, and phase, respectively. Because the lasers are linearly polarized, we neglect the Cartesian coordinate-dependent phase θ_i from Eq. 4.5 and treat the electric field $E_\beta \mathbf{e}_\beta$ from each laser as a real vector. Using Eq. 4.6, we enter the frame rotating with angular frequency ω_L

and neglect terms of order $\exp(\pm 2\omega_L t)$

$$\mathbf{E}'(\mathbf{x},t) = \sum_{\beta} E'\mathbf{e}_\beta \exp\left(i[\mathbf{K}_\beta \cdot \mathbf{x} - (\omega_\beta - \omega_L)t - \gamma_\beta]\right)/2. \tag{6.10}$$

Because $|\omega_\beta - \omega_L| \ll E_e$, all of the approximations up through Eq. 6.7 remain valid. The pairwise product of terms in Eq. 6.10 produced by the operation in Eq. 6.7 contain the terms $\exp(\pm i\Phi_{\beta,\beta'})$, which do not cancel in the RWA. We define $\Phi_{\beta,\beta'}$ to be

$$\Phi_{\beta,\beta'} = \mathbf{K}_{\beta,\beta'} \cdot \mathbf{x} - \omega_{\beta,\beta'} t - \gamma_{\beta,\beta'} \tag{6.11}$$

where $\mathbf{k}_{\beta,\beta'} = \mathbf{K}_\beta - \mathbf{K}_{\beta'}$ is the difference between laser wavevectors; $-\omega_{\beta,\beta'} = \omega_\beta - \omega_{\beta'}$ is the difference between laser angular frequencies; and $\gamma_{\beta,\beta'} = \gamma_\beta - \gamma_{\beta'}$ is the difference between laser phases. Both $\Phi_{\beta,\beta'}$ and $\epsilon_\beta \times \epsilon_{\beta'}$ switch sign under the exchange of indices, allowing the rearranging of terms

$$\hat{H}_{\text{eff}} = \sum_{\beta \neq \beta'} \frac{-g_F u E_\beta E_{\beta'}}{2\hbar g_J} \sin\left[\Phi_{\beta,\beta'}\right](\mathbf{e}_\beta \times \mathbf{e}_{\beta'}) \cdot \hat{\mathbf{F}}, \tag{6.12}$$

which are valid only when laser polarizations are linear. When the Raman frequency differences are detuned near to resonance with the linear Zeeman splitting of the ground hyperfine manifold, essentially $|\omega_{\beta,\beta'} - \delta_Z| \ll \delta_Z$ where $\delta_Z = g_F \mu_B B_{\text{dc}}$, we apply a RWA to eliminate terms proportional to $\exp(i2|\omega_{\beta,\beta'}|t)$. For example, under the RWA

$$-\hat{F}_{x,y} \sin\left[\Phi_{\beta,\beta'}\right] \rightarrow \left[\hat{F}_{x,y} \cos\left[\Phi_{\beta,\beta'}\right] \mp \hat{F}_{y,x} \sin\left[\Phi_{\beta,\beta'}\right]\right]\theta(\omega_{\beta,\beta'}) \tag{6.13}$$

$$\hat{F}_z \sin\left[\Phi_{\beta,\beta'}\right] \rightarrow \hat{F}_z \sin\left[\Phi_{\beta,\beta'}\right] \tag{6.14}$$

where θ is the Heaviside function and the upper sign choice corresponds initial $\mathbf{F}_x$ on the LHS. Notice that the term containing $\mathbf{F}_z$ remained unchanged under the RWA.

For an atom illuminated by a single pair of Raman lasers (and no other fields) the sign choice in Eq. 6.13 is not of physical importance.

When there are multiple Raman couplings the relative orientation of different $\mathbf{e}_\beta \times \mathbf{e}_{\beta'}$ (even in the absence of other fields) can have physical consequences. When we take the RWA $(\mathbf{e}_\beta \times \mathbf{e}_{\beta'}) \cdot \mathbf{F}$ the polarization geometry of the lasers can be expressed using a phase $\xi_{\beta,\beta'}$ and sign $\eta_{\beta,\beta'}$

$$-(\mathbf{e}_\beta \times \mathbf{e}_{\beta'}) \cdot \hat{F} \sin\left[\Phi_{\beta,\beta'}\right] \rightarrow \hat{F}_x \cos\left[\Phi_{\beta,\beta'} + \xi_{\beta,\beta'}\right] - \hat{F}_y \sin\left[\Phi_{\beta,\beta'} + \xi_{\beta,\beta'}\right]\big)\theta(\omega_{\beta,\beta'}) \tag{6.15}$$

$$-\eta_{\beta,\beta'} \hat{F}_z \sin\left[\Phi_{\beta,\beta'}\right].$$

The phase is the orientation of the $\mathbf{B}_{\text{eff}}$ in the plane orthogonal to $B_{\text{dc}}\mathbf{e}_z$

$$\xi_{\beta,\beta'} = \text{atan}[(\mathbf{e}_\beta \times \mathbf{e}_{\beta'})_y / (\mathbf{e}_\beta \times \mathbf{e}_{\beta'})_x], \tag{6.16}$$

and the sign measures the case where the $\mathbf{B}_{\text{eff}}$ is either aligned or antialigned with $\mathbf{e}_z$

$$\eta_{\beta,\beta'} = \text{sign}[(\mathbf{e}_\beta \times \mathbf{e}_{\beta'}) \cdot \mathbf{e}_z]. \tag{6.17}$$

What will prove to be of physical consequence is the sum of the differences between $\xi_{\beta,\beta'}$ for different Raman pairings and the value of $\eta_{\beta,\beta'} = \pm 1$. For simple tripod schemes (three lasers coupling three states with no additional couplings) there are three different in-plane projections of $\mathbf{B}_{\text{eff}}$ that couple states from the three different Raman pairings. In this case, the sum of the differences between $\xi_{\beta,\beta'}$ always sum perfectly to 2π. Meanwhile, the appearance of $\eta_{\beta,\beta'}$ in the Hamiltonian will be tied to axial coupling ($\mathbf{B}_{\text{eff}}$ along $\mathbf{e}_z$) and does not contribute to the tripod Hamiltonian.

In the RWA, the amplitudes of the couplings are split between an in-plane

$\Omega^{\perp}_{\beta,\beta'}$ projection of the $\mathbf{B}_{\text{eff}}$ and an axial $\Omega^{||}_{\beta,\beta'}$ projection of the $\mathbf{B}_{\text{eff}}$ along $\mathbf{e}_z$. Then,

$$A^{\perp}_{\beta,\beta'} = |(\mathbf{e}_\beta \times \mathbf{e}_{\beta'})| \tag{6.18}$$

$$A^{||}_{\beta,\beta'} = |(\mathbf{e}_\beta \times \mathbf{e}_{\beta'}) \cdot \mathbf{e}_z| \tag{6.19}$$

$$\Omega^{\perp}_{\beta,\beta'} = g_F u E_\beta E_{\beta'} A^{\perp}_{\beta,\beta'} \sqrt{1 - A^{||2}_{\beta,\beta'}}/4\hbar g_J \tag{6.20}$$

$$\Omega^{||}_{\beta,\beta'} = g_F u E_\beta E_{\beta'} A^{||}_{\beta,\beta'}/2\hbar g_J. \tag{6.21}$$

The Hamiltonian in the RWA is

$$\hat{H}_{\text{eff}} = \sum_{\beta \neq \beta'} \Big[\Omega^{\perp}_{\beta,\beta'} \big(\hat{F}_x \cos\left[\Phi_{\beta,\beta'} + \xi_{\beta,\beta'}\right] - \hat{F}_y \sin\left[\Phi_{\beta,\beta'} + \xi_{\beta,\beta'}\right] \big) \theta(\omega_{\beta,\beta'}) - \eta_{\beta,\beta'} \Omega^{||}_{\beta,\beta'} \hat{F}_z \sin\left[\Phi_{\beta,\beta'}\right] \Big]. \tag{6.22}$$

It is often safe to neglect the coupling diagonal with $\mathbf{B}_{\text{dc}}$ since it does not couple $|m_F\rangle$ states. The phase of the couplings in Eq. 6.22 can also be neglected in most circumstances without issue. The simplified Hamiltonian

$$\hat{H}_{\text{eff}} = \sum_{\beta \neq \beta'} \Big[\Omega^{\perp}_{\beta,\beta'} \big(\hat{F}_x \cos\left[\mathbf{K}_{\beta,\beta'} \cdot \mathbf{x} - \omega_{\beta,\beta'} t\right] - \hat{F}_y \sin\left[\mathbf{K}_{\beta,\beta'} \cdot \mathbf{x} - \omega_{\beta,\beta'} t\right] \big) \theta(\omega_{\beta,\beta'}) \tag{6.23}$$

usually suffices to describe Raman coupling.

6.2.1 The light shift terminology

Equation 6.22 describes couplings within the $j = 1/2$ ground electronic states. In this two state subspace terms proportional to $E^{*'}_i E'_j \delta_{i,j}$ (i and j index Cartesian coordinates) describe a state-independent AC Stark shift: these are scalar light shifts. The strength of the electric field for the β'th laser follows the intensity $E^{*'}_i E'_i = I(x,y,z)/c\epsilon'_0$ which typically has a Gaussian cross section. When $2/3\Delta_{3/2} + 1/3\Delta_{1/2}$ is negative the scalar light shift of the β'th laser produces a

trapping potential and when it is positive it anti-traps.

For a circularly polarized lasers E' is complex and $E_i^{*'}E'_j\epsilon_{i,j,k}$ has a non-zero component along the propagation direction of the laser $\mathbf{e}_L$ which dots with the vector of Pauli matrices $\hat{\boldsymbol{\sigma}}$. Using Landé's projection theorem we stretch the spin-1/2 vector of operators $\hbar\hat{\boldsymbol{\sigma}}$ to the spin-1 vector of angular momentum operators $\hat{\mathbf{F}}$

$$\hat{H}_{\text{eff}} \approxeq \frac{g_F}{g_J}\frac{iuE^{*'}(\mathbf{x},t)E'(\mathbf{x},t)}{\mu_B g_J}\mathbf{e}_L \cdot \hat{\mathbf{F}} \tag{6.24}$$

The resulting state-dependent potential is reminiscent of a B_{dc} along $\mathbf{e}_L$: this is the vector light shift. B_{dc} that scale with laser intensity are generally undesirable, positioning a real and large B_{dc} field orthogonal to $\mathbf{e}_L$ can minimize the impact of the vector light shift and adopting perfect linear polarization for the laser entirely eliminates it.

By contrast, our 2-photon coupling is equivalent to that of a position dependent ac magnetic field. A representation of the level diagrams that produce scalar, vector and 2-photon vector light shifts is given in Fig. 6.2.

6.3 Geometry of Raman coupling

Here we consider two Raman geometries as an example implementation of the theory introduced in the previous section of this chapter.

We first consider a geometry of two counterpropagating lasers as shown in Fig. 6.3a. Here, the momentum recoil associated within the Raman coupling is coaligned with the axis of laser propagation. The linear laser polarizations are perpendicular to the laser propagation, of course, but the amplitude of $\mathbf{B}_{\text{eff}}$ is maximized when the laser polarizations are mutually perpendicular. For all polarizations $\mathbf{B}_{\text{eff}}$ is coaligned with the axis of laser propagation and the desired $\mathbf{B}_{\text{dc}}$ is any orientation perpendicular to the axis of laser propagation.

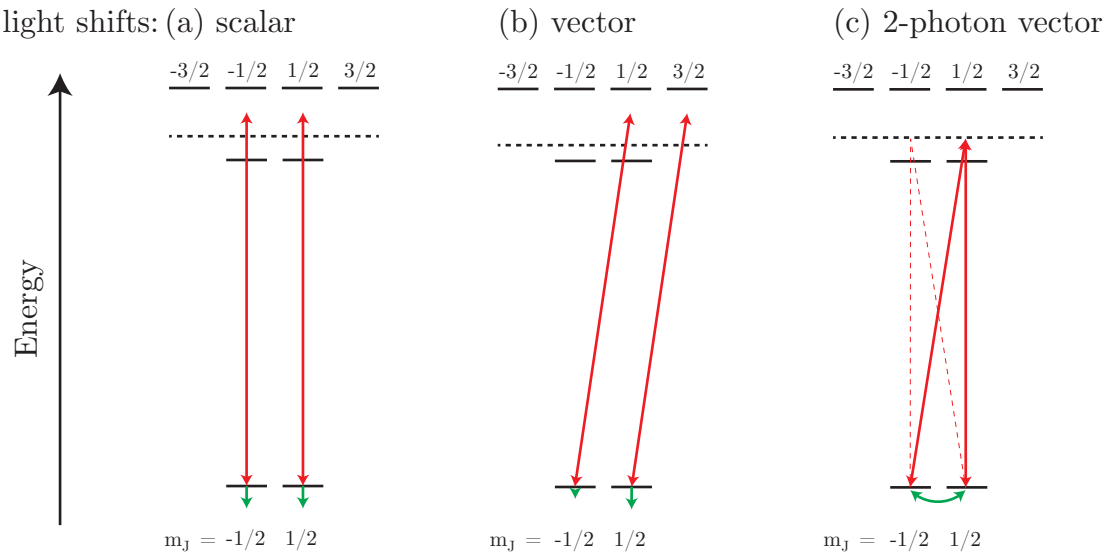

Figure 6.2: Level diagram for various light shifts. (a) Scalar light shifts vanish for coupling on the dotted line: where $\Delta_{3/2} = -2\Delta_{1/2}$. Depicted, is coupling to $2\Delta_{3/2} = -\Delta_{1/2}$. (b) Circularly polarized light produces a state dependent ac Stark shift. The vector light shift is merely an scalar shift at the dotted line. (c) $\pi - \sigma$ coupling between states. When both beams are linear, the dotted red coupling may also exist. For resonant coupling of states split by a $B_{\rm dc}$ the RWA eliminates some of the couplings e.g. the dotted red coupling.

Next we consider a geometry of two lasers whose propagation directions are mutually orthogonal. In this case, the amplitude of $\mathbf{B}_{\rm eff}$ is maximized when the polarization of laser one is aligned with the propagation direction of the laser two, laser two must have a polarization perpendicular to the propagation of laser one. $\mathbf{B}_{\rm eff}$ is aligned with laser one in this case and the desired $\mathbf{B}_{\rm dc}$ is any orientation perpendicular to laser one.

6.4 Gauge and rotating frame transformations

In this section, we derive the Raman coupled atomic Hamiltonian in the RWA in several steps. When $\mathbf{B}_{\rm dc}$ is applied along $\mathbf{e}_z$ the atomic Hamiltonian describing the

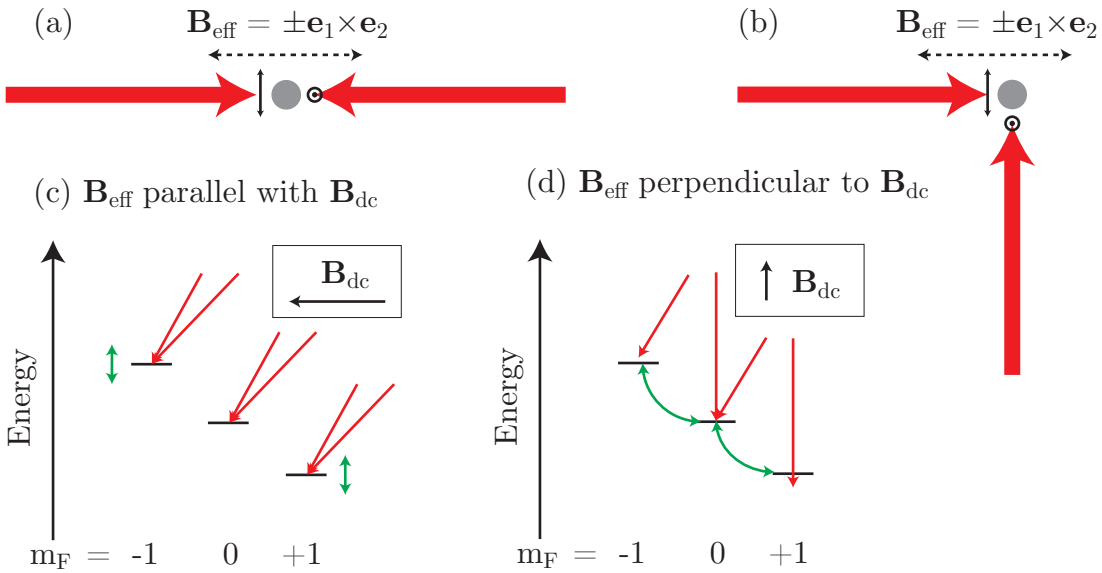

Figure 6.3: The Raman lasers (in red) illuminate cold atoms (grey circle) with linearly polarized light. The polarization in the plane of the diagram is shown with a double sided arrow while polarization in and out of the diagram is given by the circle-dot. (a) Counterpropagating Raman beams produce a $\mathbf{B}_{\text{eff}}$ that is parallel to both beams. (b) Perpendicular Raman beams can produce a variety of $\mathbf{B}_{\text{eff}}$ orientations but we show an in-plane configuration. (c) When the states are split by a field $\mathbf{B}_{\text{dc}}$ which is parallel to $\mathbf{B}_{\text{eff}}$ the Raman coupling ($\propto \hat{F}_z$) cannot drive transitions. (d) When $\mathbf{B}_{\text{eff}}$ is perpendicular to $\mathbf{B}_{\text{dc}}$ Raman coupling links spins exactly like a position dependent rf magnetic field.

ground hyperfine states

$$\hat{H}_0 = \begin{pmatrix} \frac{\hbar^2\mathbf{k}^2}{2m} + E_{-1} & 0 & 0 \\ 0 & \frac{\hbar^2\mathbf{k}^2}{2m} + E_0 & 0 \\ 0 & 0 & \frac{\hbar^2\mathbf{k}^2}{2m} + E_{+1} \end{pmatrix} \tag{6.25}$$

may be coupled (this is one of a number of ways) with a counterpropagating laser configuration that produces $\mathbf{B}_{\text{eff}}$ along $\mathbf{e}_x$. Then the Raman coupling amplitude is $\Omega = g_F \mu_B B_{\text{eff}}/g_J$. This laser configuration maps a $2k_R$ wavevector ($\lambda/2$ periodicity) into the coupling Hamiltonian $\hat{H}_R = \Omega(\hat{F}_x \cos[2k_R x - \omega t] - \hat{F}_y \sin[2k_R x - \omega t])$ which we cast into matrix form

$$\hat{H}_R = \frac{\Omega}{\sqrt{2}} \begin{pmatrix} 0 & e^{i[2k_R x - \omega t]} & 0 \\ e^{-i[2k_R x - \omega t]} & 0 & e^{i[2k_R x - \omega t]} \\ 0 & e^{-i[2k_R x - \omega t]} & 0 \end{pmatrix}. \tag{6.26}$$

where the wavevector is $k_R = 2\pi/\lambda$. The time and position dependence of this off-diagonal Raman coupling can be removed with a unitary transformation that is a combination of rotating frame transformation (the time part) and gauge transformation (the position part)

$$\hat{U} = \begin{pmatrix} e^{-i[2k_R x - \omega t]} & 0 & 0 \\ 0 & 1 & 0 \\ 0 & 0 & e^{i[2k_R x - \omega t]} \end{pmatrix}. \tag{6.27}$$

Because the position dependent part of the transformation does not commute with the momentum operator in the kinetic energy of $\hat{H}_0$, $\hat{U}$ acts like a momentum-displacement operator

$$\exp(\mp i[2k_R x - \omega t])\mathbf{k}^2 \exp(\pm i[2k_R x - \omega t]) = (\mathbf{q} \pm 2k_R \mathbf{e}_x)^2$$

where we have made a convenient change of variables to quasimomentum $\hbar\mathbf{q}$. We apply this transformation to the Hamiltonian $\hat{H}_0' = \hat{U}\hat{H}_0\hat{U}^\dagger$ and obtain a form of the Hamiltonian that has a state-dependent Gauge potential.

$\hat{H}_0$ also acquires a state dependent offset from the time dependent Schrödinger equation $i\hbar\hat{U}^\dagger\partial_t\hat{U}$ in the rotating frame of the transformed state vector $|\psi'\rangle = \hat{U}|\psi\rangle$. The transformed Hamiltonian, which is free of off-diagonal position and time dependence, is particularly easy to conceptualize in this form

$$\hat{H}' = \hat{H}_0' + \hat{H}_R' = \begin{pmatrix} \frac{\hbar^2(\mathbf{q}-2k_R\mathbf{e}_x)^2}{2m} + \delta & \Omega/\sqrt{2} & 0 \\ \Omega/\sqrt{2} & \frac{\hbar^2\mathbf{q}^2}{2m} + \epsilon & \Omega/\sqrt{2} \\ 0 & \Omega/\sqrt{2} & \frac{\hbar^2(\mathbf{q}+2k_R\mathbf{e}_x)^2}{2m} - \delta \end{pmatrix} \tag{6.28}$$

where $\hat{H}_R' = \hat{U}\hat{H}_R\hat{U}^\dagger = \Omega\hat{F}_x$. The detuning is $\delta = (E_{-1} - E_{+1})/\hbar - 2\omega_R$ and the quadratic Zeeman shift is $\epsilon = (2E_0 - E_{-1} - E_{+1})/\hbar$ (ϵ is always negative). The Hamiltonian $\hat{H}'$ is the spin-1 equivalent to an equal combination of Rashba and Dresselhaus SOC (1D SOC) in a spin-1/2 . There are a number of theoretical and experimental works that use SOC of this form [67, 7, 17, 68, 8, 9, 69].

6.5 Quasimomentum, spin population and center of mass momentum

SOC establishes a discrete momentum difference ($2k_R$ for counterpropagating laser configurations) between the free energy dispersions of $|m_F\rangle$ BEC spin components as shown in Fig. 6.4. The characteristic energy scale $E_R = 4\hbar^2{k_R}^2/2m$ is the gap in energy from the minima of the ground eigenband to the next least energetic eigenband. During evaporative cooling, condensates form at the eigenminima of the quasimomentum dispersion shown in Fig. 6.4.

The ground eigenstate at the minima of the dispersion has a mixture of spin states with a fixed momentum difference between them. In the limit of the Raman coupling tending to zero the eigenminima map continuously to a pure spin state.

The condensate wavefunction is strongly peaked in momentum, so much so that we often substitute a population weighted dirac delta function instead

$$\psi(\mathbf{q}) = \phi(\mathbf{q}) \left[\sqrt{N_{q_1}}\delta(\mathbf{q}-\mathbf{q}_1) + \sqrt{N_{q_2}}\delta(\mathbf{q}-\mathbf{q}_2) + \sqrt{N_{q_3}}\delta(\mathbf{q}-\mathbf{q}_3) \right] \tag{6.29}$$

where $\phi(\mathbf{q})$ is the three-component ground eigenstate given by the single particle dispersion. Three is the maximum number of eigenminima in the ground eigenstate, however it is possible to have fewer.

We may reconcile the quasimomentum basis with a zero center of mass momentum for the atomic cloud $\mathbf{K}_{\mathrm{CM}}$ (usually $\mathbf{K}_{\mathrm{CM}} = 0$ is set by the dipole trap) using the equation:

$$\psi^{\dagger}(\mathbf{q})(\mathbf{q}\hat{1} - \mathbf{k}\hat{F}_z)\psi(\mathbf{q})/\hbar = \mathbf{K}_{\mathrm{CM}}|\psi(\mathbf{q})|^2 \tag{6.30}$$

where the momentum dependence between spin states is $|\mathbf{k}| = 2k_R$ for a counter-propagating Raman configuration. We may solve for the relationship between spin fractional population and quasimomentum when $\mathbf{K}_{\mathrm{CM}} = 0$

$$\mathbf{q} = \frac{-\mathbf{k}|\psi_{-1}|^2 + \mathbf{k}|\psi_{+1}|^2}{|\psi(\mathbf{x})|^2} = |\mathbf{k}|M_z \tag{6.31}$$

where $M_z = \langle \hat{F}_z \rangle$ is the magnetization.

6.5.1 Loading into the spin-orbit coupling ground state

The turn on time of the Raman coupling is limited by the propensity for the equilibrium $\mathbf{q}$ to change as Ω redistributes the spin populations, see Fig. reffig:Ramandispersion. Empirically, we found that $\mathbf{q}$ should arrive at its new value on a timescale long in comparison to $\tau = 1/\omega_{\mathrm{trap}}$ which is inversely proportional to the dipole trap frequency ω_{trap} projected along the Raman momentum difference $\mathbf{k}$.

For an initial load into $|m_F = -1\rangle$ at $\Omega = 0$ the quasimomentum of the en-

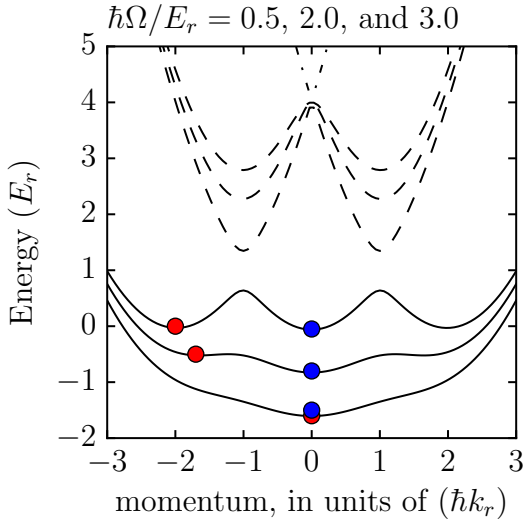

Figure 6.4: Dispersion of Raman eigenstates for $\delta = 0$, $\epsilon = -0.01$ and various coupling strengths Ω. The solid and dashed dispersions are closest to one another for the smallest Ω. The red circles starting on the left of the diagram correspond to initially loading from $|m_F = -1\rangle$ while the blue circles starting at the center correspond to initially loading from $|m_F = 0\rangle$.

semble starts at $\mathbf{q} = -\mathbf{k}$ but follows a shift in the local minimum in the dispersion towards $\mathbf{q} = 0$ as Ω is increased. In most circumstances (no cleverly applied detunings, extra frequencies or rf coupling) there exists an Ω where the local minimum of the dispersion vanishes at finite $\mathbf{q}$, leaving the atoms to evolve diabatically and recollect in the global minimum of the dispersion at $\mathbf{q} = 0$. Hence, it can be challenging to load the spin-orbit coupled state in the large coupling limit from $|m_F = \pm 1\rangle$. By contrast, $|m_F = 0\rangle$ remains at $\mathbf{q} = 0$ for all Ω when the detuning $\delta = 0$. Therefore, Ω can be ramped quickly compared to τ (we use 1 ms turn on times).

In our apparatus, evaporative cooling in the magnetic trap requires that all of the atoms be in the low magnetic field seeking $|m_F = -1\rangle$ state. Therefore transferring the atomic population to the $m_F = 0$ state can be a concern. This may be accomplished using ARP at several G $B_{\rm dc}$ or with smaller magnetic fields using the technique outlined below. We applied a rf magnetic field with $\hbar\Omega_{\rm rf} = h \times 1$ kHz Rabi frequency that is resonant with the Raman using the following procedure:

1. Start with the rf detuned, $\delta < 0$. In this case the rf eigenstate is very similar to $|m_F = -1\rangle$.

2. Ramp on the rf coupling $\Omega_{\rm rf} \to 1$, with the rf frequency identical to the Raman frequency $\omega_{\rm rf} = \omega$.

3. Ramp the detuning to zero $\delta \to 0$, preparing an rf eigenstate that is a balanced mixture of all three spin states.

4. Ramp on the Raman $\Omega \to 1$.

5. Ramp off the rf $\Omega_{\rm rf} \to 0$.

Thus we adiabatically load the ground eigenminimum of the Raman dispersion. The overlap of the eigenstate of the coupling $|\psi\rangle$ (rf and Raman) with the ground eigenminimum of the spin-orbit coupling |Raman⟩ is plotted in Fig. 6.5.

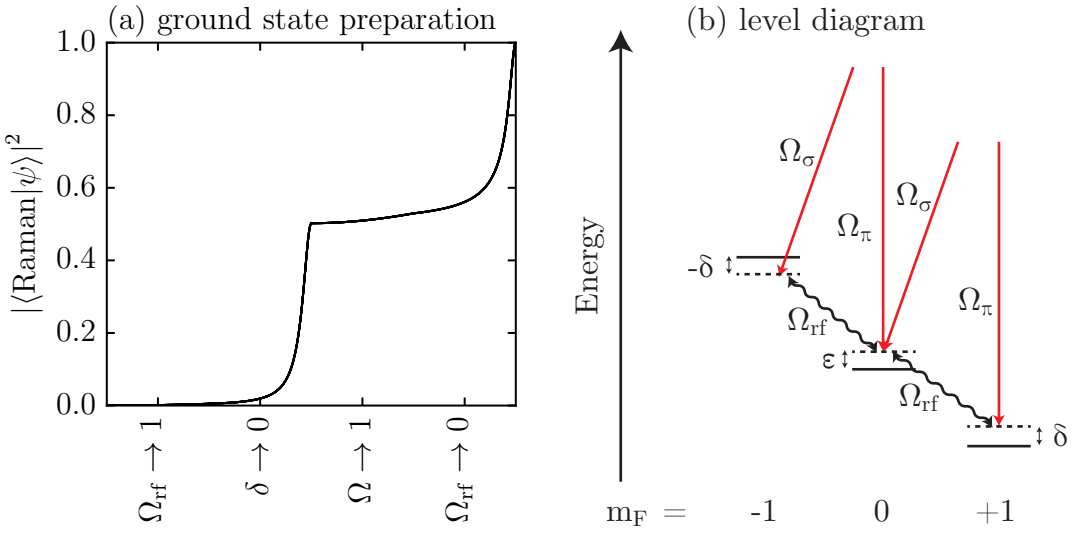

Figure 6.5: (a) Starting in $|m_F = -1\rangle$ we ramp on $\Omega_{\rm rf} = E_R/\hbar$ with a detuning of $\delta = 10E_R/\hbar$, we ramp the detuning to zero, then we ramp the Raman coupling $\Omega = E_R/\hbar \propto \Omega_\pi\Omega_\sigma$ and finally ramp off the rf. (b) The rf frequency is exactly equivalent to the Raman frequency difference. Ω and $\Omega_{\rm rf}$ are both non-zero only when $\delta = 0$.

6.6 Spin-1 spin-orbit coupling

In this chapter we discuss the laser arrangement, production of the coherent Raman light, and the generation of the spin-1 spin-orbit coupled Hamiltonian. The laser geometry used in this experiment is generally useful and is something of a "default" setup for 1D spin orbit coupling.

6.6.1 Raman laser board

The two Raman beams need to be temporally coherent. As illustrated in Fig. 6.6 we produce both Raman beams from the same laser diode, the "master" and gain the intensity using a pass through first a $500mW$ tapered amplifier (TA) and subsequently a $2W$ TA. For such this setup, the requirement of temporal coherence is satisfied when the coherence length of the light is much longer than the actual path length from the output of the master laser to the atoms. Our DL pro toptica $40mW$ 790 nm master laser has a Lorentzian width $\Delta\nu$ in frequency of 200 kHz which translates to a coherence length of $c/\pi\Delta\nu \approxeq 0.5$ km.

We use a 500 mW `Eagleyard` tapered amplifier diode on board 1 and a 2 W diode from m2k on board 2. These are mounted and temperature controlled with components machined and assembled in the lab. These diodes add a broad shoulder of amplified spontaneous emission (ASE) to the laser light and, as a result, we needed to add in-line 808 nm `Semrock` laser-line filters to remove the ASE. These filters made the difference between 200 μs lifetimes and 1 s lifetimes in the presence of Raman coupling.

The amplified light on board 1 is frequency shifted 107.5 MHz (and amplitude controlled) using an AOM and then sent over fiber to serve as the Raman 1 beam on the experiment table. A fraction of this light is diverted to a second fiber which is sent to board 2 for further amplification. Because the maximum allowable power into the input of this second TA is 30 mW the downside of this daisy-chain configuration

is that it is easily possible to accidentally send vastly more than the maximum power to the input of the second TA. This necessitates a PD-based interlock at the output of the fiber using a pickoff oriented so that the reflection is minimized for the expected polarization of the light.

On board 2 the amplified light is split into two beams, one is frequency shifted by 82.5 MHz while the other is frequency shifted by 82.680 MHz by different AOMs. The frequency difference between the AOMs on board 2 corresponds to twice the quadratic Zeeman shift when the linear Zeeman splitting is $h \times 25$ MHz. The AOM frequencies for this experiment are summarized here:

$$f^{-} = 107.5 \text{ MHz} \tag{6.32}$$

$$f^{+}_{-1} = 82.5 \text{ MHz} + \Omega_2 \tag{6.33}$$

$$f^{+}_{-1} = 82.680 \text{ MHz} - \Omega_2. \tag{6.34}$$

$$\tag{6.35}$$

6.6.2 Raman beam geometry

Light is injected into polarization maintaining fibers at the Raman board 1 and 2 and sent to the experiment. There, we collimate the light in free space. Because most beam samplers are polarization sensitive (and you should never trust a fiber to perfectly preserve the polarization) we place Glan-Taylor polarizors (PBS with 10000:1 extinction of the other polarization) immediately before a beam sampler and also as close to the output of the fiber as possible. Light from the beam sampler is sent to a pickoff to measure for relative Raman beam intensity. We then use $\lambda/2$ and $\lambda/4$ waveplates to produce the desired polarization. When working with dielectric mirrors it is helpful to maintain strict vertical or horizontal polarization, keeping the beam paths as level as possible, because the mirrors tend to act as birefringent optical elements.

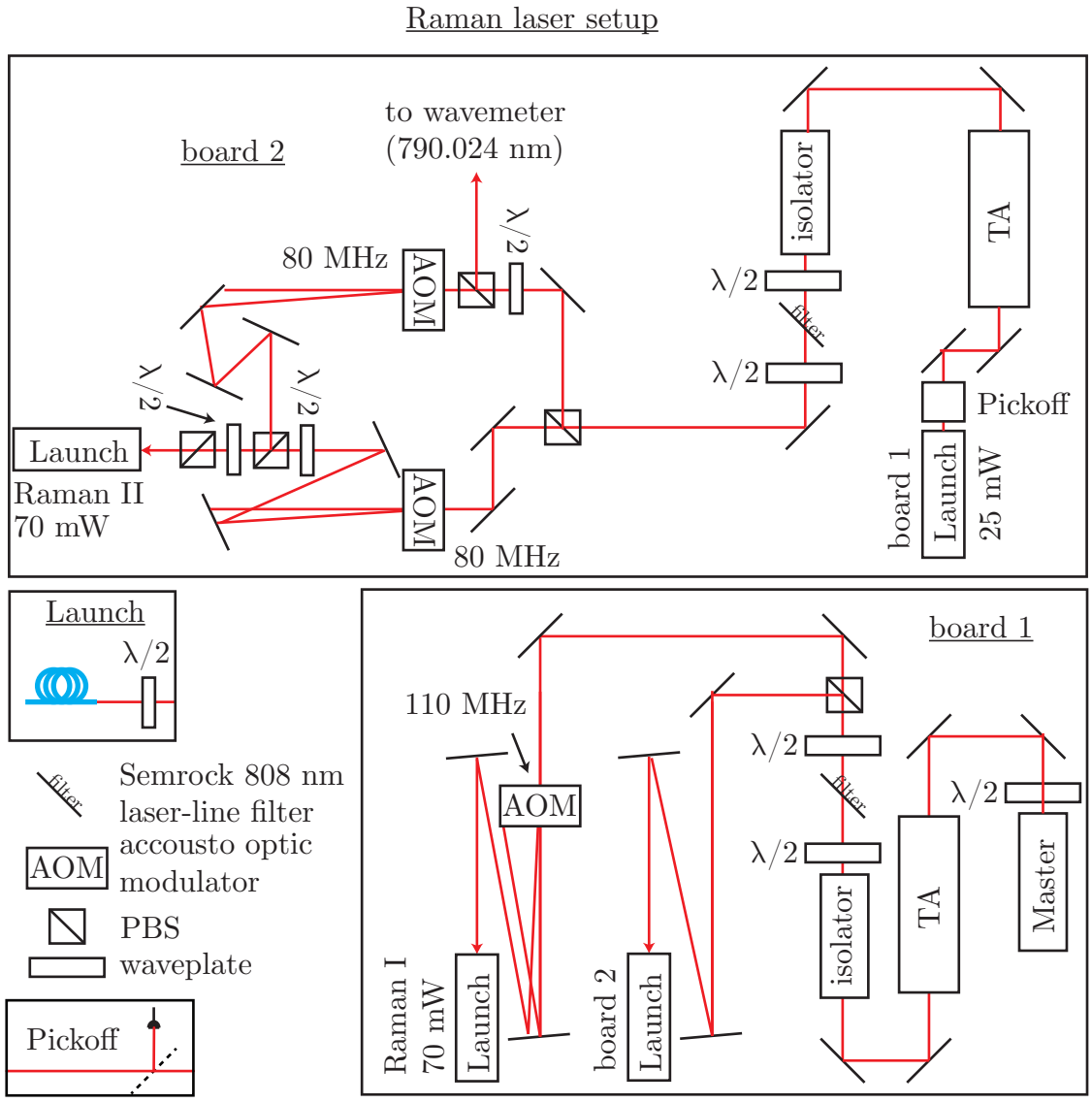

Figure 6.6: Our Raman laser setup is prepared on two spatially separated optics breadboards that are connected by fiber. A 40 mW DL pro toptica laser sourced power to a daisy chained series of tapered amplifier diodes. Board 1 sources light to the Raman 1 beam on the experiment table while board 2 sources light to the Raman 2 beam. In this experiment Raman II has two different frequencies. We found it most convenient to apply the frequency shifts in different AOMs and combine them on a PBS. The polarization is then rotated 45 degrees for the combined beam and a second PBS eliminates half the light: producing a beam where both frequency components have the same polarization.

We prepare the Raman 1 beam with horizontal linear polarization and the Raman II beam with vertical linear polarization. For our counterpropagating geometry shown in Fig. 6.7 the Raman beams couple to the atoms like a position dependent ac magnetic field $\propto \Omega_1(x,t)$ oriented along $\mathbf{e}_x$.

We included PBS cubes so that we can pass the Raman light that on route to the atoms and reflect Raman light that have already interacted with the atoms. These cubes proved to be an effective method for removing cross-talk between our PDs which measure the power in the Raman beams.

Our Raman beams nearly copropagate with one of our optical dipole trapping beams. The addition of a second optical dipole trapping beam allows confinement of the atomic cloud in a flat disk. The disk is symmetric under rotation in the $\mathbf{e}_x$ and $\mathbf{e}_y$ plane while in the $\mathbf{e}_z$ direction the dipole trap is 4 times more tightly confined. In the event of domain formation or other component dynamics it is energetically favorable for these to spatially occur in the $\mathbf{e}_x$ and $\mathbf{e}_y$ plane. This is desirable because it is perpendicular to our imaging axis along $\mathbf{e}_z$.

6.6.2.1 Calculating coupling strengths

The laser field corresponding to Ω^+ produces a time dependent sine wave when it impinges upon its PD detector. This sine wave is only full contrast when both Raman 2 frequencies components, produced by two different AOMs, have the same amplitude; the relative amplitude needed to be set using a waveplate on Raman board 2 at the beginning of each day. Each time the Raman beams illuminated the BEC we captured the beat of these two frequencies on an oscilloscope and saved to file. The average voltage measured by the PD illuminated by Raman 1 is V_{PD1} while the voltage measured by the PD illuminated by Raman 2 is a peak to peak sinusoidal oscillation that is four times V_{PD2}.

At the end of an experimental data run we would prepare our BEC entirely in $|m_F = 0\rangle$ and pulse on our Raman beams with $\Omega_2 = -4E_R$. This corre-

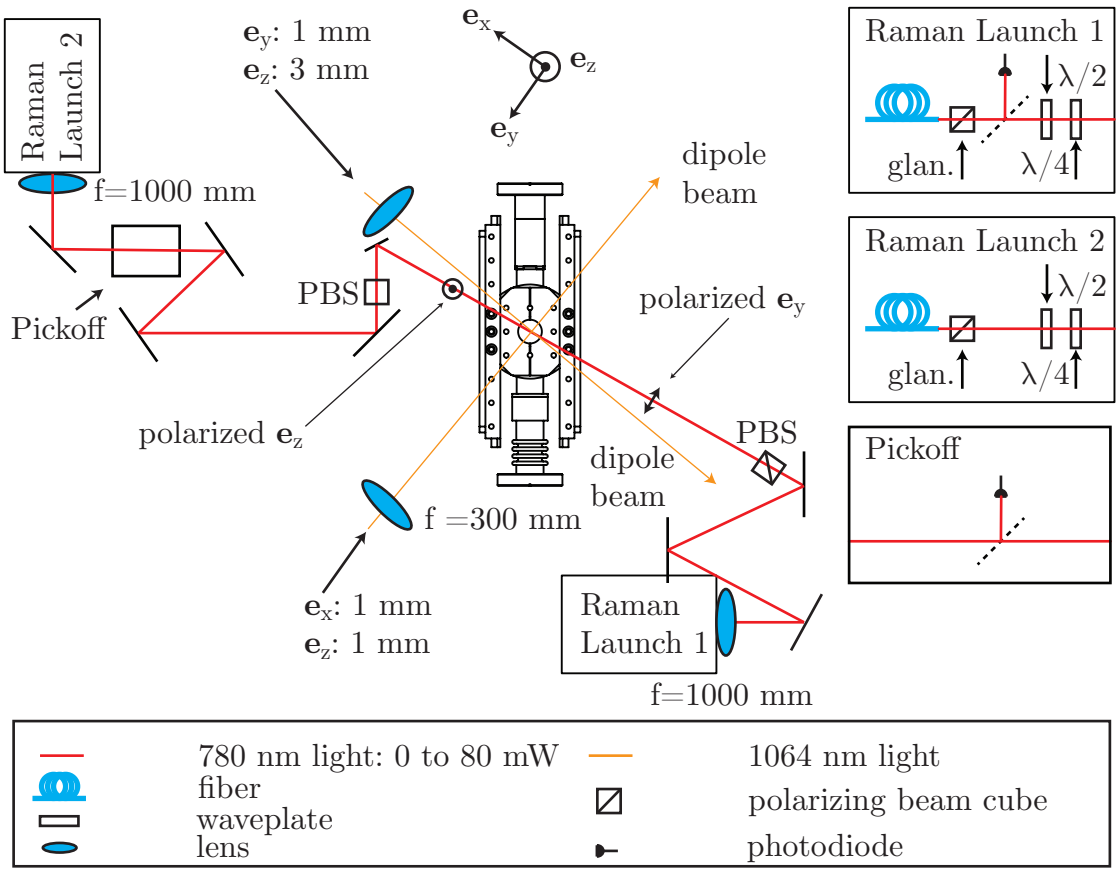

Figure 6.7: Here we have a typical counterpropagating Raman laser geometry with crossed linear polarizations. The Raman beams have a nearly 1 m travel from fiber to the atoms and hence are focused with a $f = 1000$ mm lens: this produces 150 μm waist at the atoms. The PBS cubes reject light after it passes through the glass cell, useful to prevent crosstalk between our PDs.

sponds to a special case where $|m_F = 0\rangle$ is made degenerate with $(|m_F = -1, 2k_R\rangle + |m_F = +1, -2k_R\rangle)/\sqrt{2}$ by our Raman illumination, causing resonant (full contrast) Rabi oscillations. For sufficiently low powers or sufficiently large ϵ (the quadratic Zeeman shift) the coupling strength may be determined by fitting the Rabi oscillations to the time evolution of the 3×3 interaction Hamiltonian

$$\hat{H} = \begin{pmatrix} (0 - 2k_R)^2 - 4E_R & \Omega_1/\sqrt{2} & 0 \\ \Omega_1/\sqrt{2} & 0 & \Omega_1/\sqrt{2} \\ 0 & \Omega_1/\sqrt{2} & (0 + 2k_R)^2 - 4E_R \end{pmatrix} \tag{6.36}$$

$$\psi(t) = e^{-i\hat{H}t/\hbar}\psi(0). \tag{6.37}$$

We then found a constant of proportionality $\Omega_1/\sqrt{V_{\mathrm{PD1}}V_{\mathrm{PD2}}}$ that would apply for all of the previous data run.

There was a small, but persistent drift in the coupling throughout the day. Initially, this was not appreciated and we would see changes in $\Omega_1/\sqrt{V_{\mathrm{PD1}}V_{\mathrm{PD2}}}$ on the order of 15%. Once we switched to finding $\Omega_1/\sqrt{V_{\mathrm{PD1}}V_{\mathrm{PD2}}}$ immediately after a data run the consistency between theory and experiment dramatically improved to less than 2.5% variation.

6.6.3 Aligning the Raman beams

It is much easier to overlap one Raman beam with our cloud of atoms than have the intersection of two Raman beams overlap with the cloud of atoms. The first step of our favored procedure is to tune the frequency midway between 790.024 nm and 780 nm. A non-zero single beam ac stark shift forms a trapping potential between these frequencies (this is strongest close to 780 nm). Our laser waists ~ 150 μm are much larger than the extent of the BEC and hence when the Raman beams are misaligned (but not too far misaligned) the atoms experience a force towards the center of the Raman beam. This is equivalent to suddenly displacing the trap

potential for the atomic cloud. If we know the trap frequencies of our optical dipole trap, we can quickly ramp on ~ 1 ms our Raman beams, wait for a quarter optical dipole trap period (the time necessary for the atoms to roll down the new potential), and image the clouds after TOF. We then calibrate the position of each Raman beam by attempting to eliminate the deflection of the condensate on the camera by steering the laser.

6.6.4 Level diagram and Hamiltonian

Following the treatment of Raman coupling from the beginning of this section we find that adding a second frequency component to the Raman II beam produces two terms in B_{eff}

$$\mathbf{\Omega}_1(x,t) = \Omega_1 \mathbf{e}_x[\cos(2k_R x - (\omega^- - \omega^+_{-1})t) + \cos(2k_R x - (\omega^- - \omega^+_{+1})t)] \tag{6.38}$$

$$\hat{H}_{\text{eff}} = \Omega_1(x,t) \cdot \hat{\mathbf{F}}. \tag{6.39}$$

The couplings shown in the resonant level diagram of Fig. 6.8 are actually only a subset of couplings that are near resonant with respect to the linear Zeeman splitting of $\sim h \times 25$ MHz. We eliminate the fast frequency $\omega_{\text{fast}} = \omega^- - (\omega^+_{+1} + \omega^+_{-1})/2 \approx 2\pi 24.91$ MHz in the RWA. We apply the rotating frame and gauge transformations

$$\hat{U}(x) = \begin{pmatrix} e^{i[2k_R x - \omega_{\text{fast}} t]} & 0 & 0 \\ 0 & 1 & 0 \\ 0 & 0 & e^{-i[2k_R x - \omega_{\text{fast}} t]} \end{pmatrix} \tag{6.40}$$

the latter of which does not commute with the momentum operator of the kinetic energy term in the Hamiltonian. Altogether the Hamiltonian

$$\hat{H} = \frac{(k\hat{1} + 2k_R \hat{F}_z)^2}{2m} + \frac{\hbar\Delta\omega}{2}\hat{F}_z + V(\mathbf{r})\hat{1}/\hbar + \Omega_1 \hat{F}_x \cos(\Delta\omega t/2) \tag{6.41}$$

where $\hat{1}\hbar$ is the identity and $\Delta\omega = \omega_{-1}^{+} - \omega_{+1}^{+} = 2\epsilon + 2\Omega_2$ is a frequency difference tuned to the sum of our real and effective quadratic Zeeman shifts.

6.6.4.1 Spin-1 Floquet

Because our Hamiltonian is time periodic $H(t) = H(t + 4\pi/\Delta\omega)$ the Schrödinger equation has the form of a Floquet differential equation

$$i\hbar\partial_t\psi(t) = \hat{H}(t)\psi(t) \tag{6.42}$$

for which the well known solution is to expand ψ in terms of Floquet bands

$$\psi(t) = \sum_n e^{in\Delta\omega t/2}\phi(t) \tag{6.43}$$

where n is the set of integers and $\phi(t)$ is defined on any interval $[t, t + 4\pi/\Delta\omega]$. Because our Hamiltonian can be exactly decomposed into complex exponentials ϕ is time independent and is equivalent to an eigenvector in the Floquet Hamiltonian. We write out the Floquet Hamiltonian

$$\hat{H} = \sum_{n,n'} \left(\left[\hat{H}_0 + \frac{\hbar\Delta\omega n}{2\hbar}\hat{1} \right] \delta_{n,n'} + \Omega\hat{F}_x\delta_{n-1,n'} + \text{h.c.} \right) |n\rangle \langle n'| \tag{6.44}$$

where a 3×3 block of spin states is defined for each repeating unit in the Floquet Hamiltonian (Floquet band) $|n\rangle \langle n'|$. The diagonal blocks are quasienergy states that repeat with the characteristic periodicity of the Hamiltonian $\hbar\Delta\omega$

$$\hat{H}_0 = \frac{(k\hat{1} + 2k_R\hat{F}_z)^2}{2m} + \frac{\hbar\Delta\omega}{2}\hat{F}_z + V(\mathbf{r})\hat{1}/\hbar. \tag{6.45}$$

At zero coupling the Floquet Hamiltonian looks like the effective 3×3 Hamiltonian

$$\hat{H}_{3\times3} = \frac{(k\hat{1} + 2k_R\hat{F}_z)^2}{2m} + V(\mathbf{r})\hat{1}/\hbar + \Omega_1\hat{F}_x \tag{6.46}$$

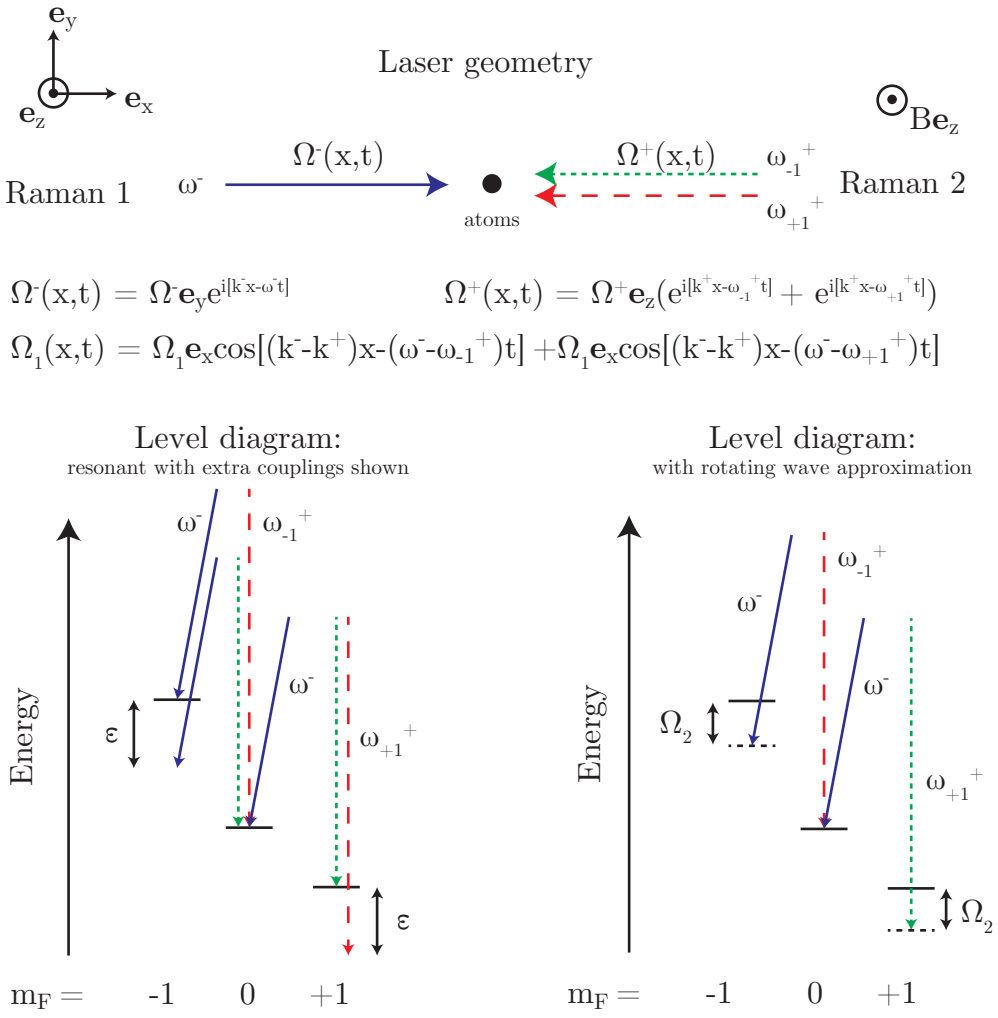

Figure 6.8: The laser geometry consists of two counterpropagating Raman beams with crossed linear polarizations. The effective coupling is therefore along $\mathbf{e}_x$. Two frequency components exist in Raman 2 but both components are temporally coherent and have the same polarization. The extra frequency component allows all three spin states to be resonantly coupled and an effective quadratic Zeeman shift may be tuned with laser frequencies. Even at resonance additional couplings exist that are detuned by the quadratic Zeeman shift, the RWA may not apply for these.

that is tiled in energy with spacing $\hbar\Delta\omega/2 + \Omega_2$ as shown in Fig. 6.9.

For sufficiently large ϵ the spacing between Floquet bands, collections of eigenstates that when tiled produce the Floquet spectrum, becomes large enough that the coupling between bands is small. In our system $\epsilon = h \times 90$ kHz and for parameters (Ω_1, Ω_2) that mark changes in the phase diagram the Floquet bands predict slightly higher Ω_1 than does $\hat{H}_{3\times3}$ (holding Ω_2 constant).

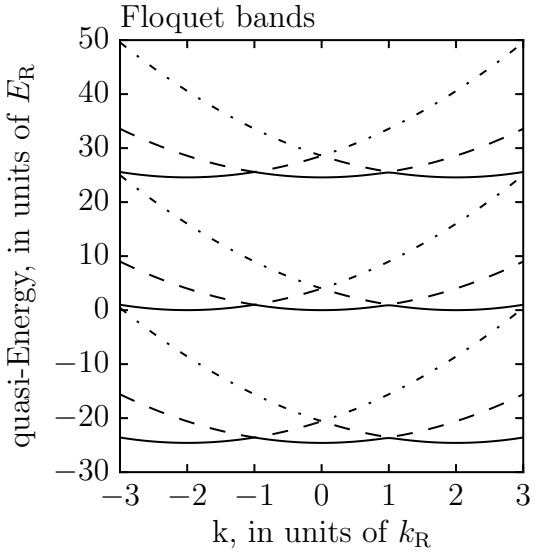

Figure 6.9: Three of infinite tiled Floquet bands. Plotted are Floquet quasi-energy dispersions. Solid traces correspond to 3x3 ground eigenvalues, dashed traces are the 1st excited eigenvalues and dashed dotted traces are the most excited eigenvalues.

Chapter 7: Spin-1 spin orbit coupling

7.1 Introduction

The spin-1 SOC Hamiltonian, which we introduce at the end of the previous chapter, allows effective modulation of the quadratic Zeeman shift. At low Raman coupling this degree of freedom allows the central eigenminima of the SOC to move up and down through a three-way degeneracy: this is reminiscent of the spinor physics that turns on and off spin-changing collisions in a spin-1 atomic cloud. "Standard" SOC within the spin-1 hyperfine manifold of alkali atoms allow at most pairs of eigenminima to become degenerate [7, 8, 9], although the addition of microwave or rf couplings might be able to mimic our spin-1 version. The addition of a second Raman frequency produces non trivial time periodicities in the Hamiltonian which require a Floquet technique. In light of the complications introduced by adding just one additional frequency we may consider this spin-1 SOC technique an important stepping stone to more complicated SOC proposals which generalize SOC in ultracold gases to higher dimensions [70, 71, 72, 14, 15].

As SOC is increased, all three eigenminima experience an effective 2-photon ac stark shift but the central eigenminimum is shifted $\sim \sqrt{2}$ more than the other two: exaggerating the quadratic Zeeman shift already present. By adding an additional Raman coupling frequency we are able to bring all three eigenminima into degeneracy. Triple degeneracy of the eigenminima allows spin changing 2-body collisions,

e.g.

$$2\phi_{q_2} \leftrightarrow \phi_{q_1} + \phi_{q_3}, \tag{7.1}$$

which can be likened to the spin-mixing interaction active in spin-1 condensates at small magnetic fields [52].

We manually set the parameters for our system so that energy is conserved under exchange of $\phi(q_1) \leftrightarrow \phi(q_3)$: this is a degree of freedom that Ref. [7] explores in an effective 2-state system but we do not. Instead, we modify the spin-orbit coupling strength Ω_1 and (with frequencies) modify the single particle energy $\epsilon(q_2)$ of the eigenminimum located at q_2 relative to $(\epsilon(q_1)+\epsilon(q_3))/2$. $\epsilon(q_2)$ is ramped from to above to below triple degeneracy $2\epsilon(q_2) = \epsilon(q_1) + \epsilon(q_3)$ a nematic [74] symmetry in the energies is tunably restored and then broken again. The fractional population condensed in the central eigenminima is

$$M_{zz} = \int \mathrm{d}\mathbf{r} \frac{\psi^\dagger(\mathbf{r})\hat{S}_z^2\psi(\mathbf{r})}{\hbar|\psi(\mathbf{r})|^2}, \tag{7.2}$$

where $\hat{S}_z$ is the diagonal and traceless spin-1 spin operator, is a nematic order parameter for a three state system, for which there is no corollary in a two-state system.

7.2 Magnetic connection

There is a 1-1 mapping between spin composition of an eigenstate and quasimomentum q as discussed in section 6.5. Therefore, our spin-orbit coupled BECs constitute a magnetically ordered system where a combination of the atoms' kinetic energy, the spin-orbit coupling and collisions drive a transition between two different ordered phases; this is analogous to the ferromagnetic and polar phases in spin-1 spinor BECs [75]. Most magnetic systems are composed of localized magnetic

particles such as electrons [76], atomic nuclei [77], and ultracold atoms in optical lattices [78, 79, 80, 81], each with moment $\boldsymbol{\mu}$. By contrast, the magnetic atoms produced by our SOC are free to move about and hence are part of a magnetic system that is itinerant. Our system produces magnetism through a very different mechanism than Stoner itinerant ferromagnetism [82]. For both fermionic [83] and bosonic [84, 85] ultracold systems our spin-orbit coupling provides a new mechanism for stabilizing ferromagnetism in itinerant systems.

We introduce a free energy $G(M_z)$ which includes both the total internal energy and thermodynamic contributions to describe the phase transitions of our system. It depends upon the magnetization

$$M_z = \int \mathrm{d}\mathbf{r} \frac{\psi(\mathbf{r})^\dagger \hat{S}_z \psi(\mathbf{r})}{\hbar |\psi(\mathbf{r})|^2} \tag{7.3}$$

which tracks the imbalance in spin composition. This construction for the magnetization manifestly resembles the definition for a spin-1/2 system: in that case, $\hat{S}_z$ simply operates on states with a reduced spin dimensionality. However, there is no equivalent for M_{zz} (defined in section 7.1) in a spin-1/2 system.

For our near $T = 0$ system and near equilibrium system all of the atoms in the ensemble are close to a ground or metastable minimum in the free energy $G(M_z)$. Both M_z and M_{zz} (defined in section 7.1) are sufficient to determine the free energy when the single particle spectrum is known. At long times all the atoms fall into the ground eigenminimum, which is accelerated by Bose stimulation. For all other timescales we initially prepare the system with $M_z = 0$ and measure the population for times short enough that the ensemble average $0.2 > M_z > -0.2$. The ensemble average of M_{zz} changes over nearly its full range when we cross a phase transition.

7.3 The Hamiltonian

7.3.1 Equivalence with spatially periodic effective magnetic field

Atomic gases with equal contributions of Rashba and Dresselhaus SOC are described by the Hamiltonian

$$\hat{H} = \frac{\hbar^2(\mathbf{q} - \mathbf{k}\hat{F}_z)^2}{2m} + \delta\hat{F}_z + \frac{\epsilon}{\hbar}\hat{F}_z^2 + \Omega\hat{F}_x \tag{7.4}$$

which can equivalently be described with by a spatially periodic effective magnetic field-like coupling term [86, 87] $\mathbf{\Omega}_1(x)/\Omega_1 = \cos(2k_R x)\mathbf{e}_x - \sin(2k_R x)\mathbf{e}_y$

$$\hat{H} = \frac{\mathbf{p}^2}{2m} + \delta\hat{F}_z + \frac{\Omega_2}{\hbar}\hat{F}_z^2 + \mathbf{\Omega}_1(x)\cdot\hat{\mathbf{F}}, \tag{7.5}$$

where $\hbar k_R$ is the photon recoil momentum. The "strength" of the SOC is equivalent to the magnitude of the two photon recoil velocity $\hbar|\mathbf{k}|/m$ while the gaps opened at avoided crossing in the dispersion are $\Omega_1\hat{F}_x$.

Diagonalizing Eq. 7.5, we find the eigenvalues $\epsilon(x)$ and eigenvectors $\psi(x)$. We may obtain the entire free energy spectrum as a function of $M_z(x)$ over the domain $x = [0, \lambda/2]$ where λ is the wavelength of our counterpropagating lasers. Selections of the free energy dispersion are depicted in Fig. (7.1)c. Alternatively, we may map the quasimomentum dispersion, see section 6.5, to M_z and the free energy using a conservation of momentum argument (or by calculating $\langle M_z(q)\rangle$ over the domain $q = [-\infty, \infty]$).

In Eq. (7.5) the three components of the hyperfine momentum operator $\hat{\mathbf{F}}$ transform vectorially under rotations, like $\hat{\mathbf{S}}$. Fully representing the possible couplings in a spin-1 system requires an additional five-component rank-2 tensor operator, the quadrupole tensor, which is not simply associated with any spatial direction [50, 88, 55]. Our Hamiltonian includes one such tensor coupling $F_{zz}^{(2)} = \hat{F}_z^2 - 2/3$

which has strength Ω_2 and is controlled by our Raman frequencies.

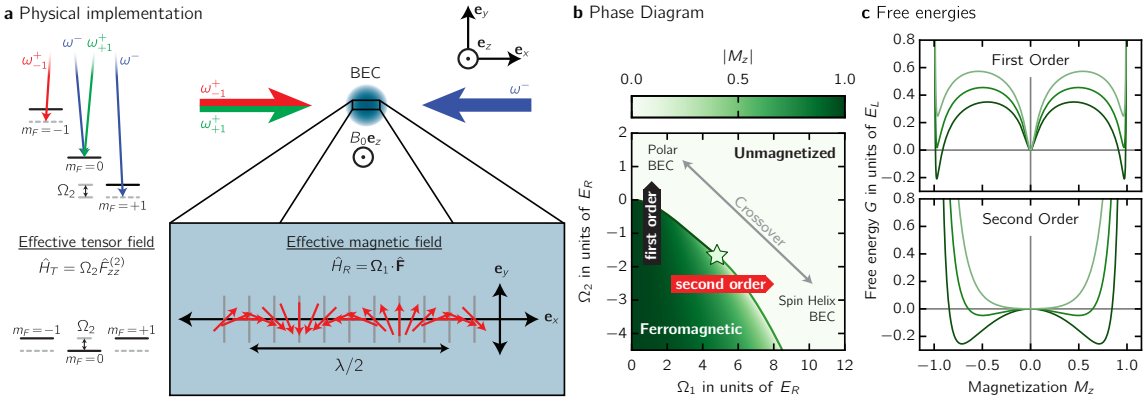

Figure 7.1: **Experimental system a** Schematic and level diagram. The $|-1\rangle \leftrightarrow |0\rangle$ and $|0\rangle \leftrightarrow |+1\rangle$ transitions of the $f = 1$ ground state manifold of ^{87}Rb were independently Raman coupled, giving experimental control of Ω_1 and Ω_2. **b** Phase diagram. The ferromagnetic order parameter $|M_z|$ is plotted against Ω_2 and Ω_1. The solid (dashed) red curve denotes the first-order (second-order) transition from the magnetized phase. **c** Free energies. Top: near the first-order phase transition at $\Omega_1/E_R = 1$ for $\Omega_2/E_R = -0.35, -0.1$ and 0.15 for the black, blue and red traces respectively, as marked by the red flags in **b**. Bottom: near the second-order phase transition at $\Omega_2/E_R = -2.5$ for $\Omega_1/E_R = 4.5, 5.5$, and 6.5 for the black, blue and red traces respectively.

7.4 Phase transitions

In this section we describe the single particle phase diagram which is qualitatively identical but quantitatively very slightly modified in the presence of 2-body interactions. We set $\epsilon(q_1) = \epsilon(q_3)$ equal to one another and modified the energy of the $\epsilon(q_2)$ relative to $\epsilon(q_{1,3})$ using $\hbar\Omega_2$. We also change the magnitude Ω_1 of the helically precessing transverse magnetic field. The set of points in parameter space (Ω_1, Ω_2) is divided into two regions by the line of critical points $\{(\Omega_1^C, \Omega_2^C)\}$ which mark an abrupt change in the value of the order parameter M_{zz} as illustrated in Fig. (7.1). For a single particle, the upper region corresponds to $M_{zz} = 0$, is unmagnetized, while the lower-left region corresponds to $M_{zz} > 0$, and is ferromagnetic.

The line of critical points $\{(\Omega_1^C, \Omega_2^C)\}$ are a line of phase transitions that mark a change in our thermodynamic order parameter M_{zz}. For Ω_1 small relative to $4E_R$

our spin-orbit coupled BECs are analogous to spinor condensates and crossing from the $M_{zz} = 0$ region to $M_{zz} > 0$ is very similar to a transition from a polar spinor BEC to a ferromagnetic spinor BEC [52]. As shown in the top panel of Fig. (7.1)c there is very much a single-particle barrier present between minima in the free energy throughout the transition, light green to dark green traces, from the unmagnetized phase to the magnetized phase: this is a 1st order phase transition. Population is transferred from one set of minima to another by collisional processes. By contrast, for Ω_1 large relative to $4E_R$ the minima in the free energy merge smoothly: this is a 2nd order phase transition. The line of 1st and 2nd order phase transitions connect at a triple point (Ω_1^*, Ω_2^*) which is starred in Fig. (7.1)b.

7.4.1 Vertical scans

To perform vertical scans of the phase transition we first initialized the system in the unmagnetized phase. This is most easily accomplished in our system by transferring atoms to $|m_F = 0\rangle$ using an adiabatic transfer from $|m_F = -1\rangle$ using rf in the absence of Raman coupling. We then applied a short $\approx$ 10 ms linear ramp of Ω_1 to the desired value and subsequently ramped Ω_2 to its final value, which may or may not be on the magnetized side of the phase diagram. The BEC was then held between 10 ms and 2 seconds; always the longest time short of the time necessary for population imbalances described by M_z to enter the system. The Raman illumination and trapping potential were then released simultaneously, the BEC expanded in TOF for 8 ms, we applied a magnetic field gradient for an additional 10 ms and allowed another 10 ms of expansion before absorption imaging. In this way we can extract the spin populations, the eigenminima populations (not the same thing) and their spatial distribution. The BEC was then reinstantiated to take another data point.

The rate of population transfer at 1st order phase transitions is maximal when all the eigenminima are degenerate (triple degenerate) and declines as Ω_2 is instan-

tiated further and further away from degeneracy. The rate of transfer and the measured width of the 1st order phase transitions scales as $(\Omega_1^C)^2$: we were able to consistently measure the width to an accuracy of $\hbar\Omega_2/50$ ($\Omega_2^C \propto (\Omega_1^C)^2$) which was limited by the timescale for substantial asymmetries in M_z to build up in our system. We measured the width of a transition at $\Omega_1 = 0.41(1)E_R$ as shown in Fig. (7.2) to be $0.0011(3)E_R = h \times 4(1)$ Hz. The narrowness of this transition is the result of an energetic penalty associated with condensation into multiple modes for repulsively interacting bosons.

(Ω_1^C, Ω_2^C) measured by experiment using the method described in this section agreed well to those points predicted by the Floquet theory described in section (6.6.4.1); our Floquet theory has no adjustable parameters. Our determination of the coupling strength, described in section (6.6.2.1), was our greatest source of error. By contrast, we compared our frequency sources to a Rubidium clock and as a result we claim that we know $\hbar\Omega_2$ on the $h \times 1$ Hz level.

7.4.2 2nd order phase transition

Horizontal scans were most useful crossing through the second-order phase transition. Since the angle of incidence to the line of phase transitions is very shallow for the low Ω_1 this measure is naturally less accurate for the 1st order phase transition measurements. The same does not apply for the vertical scans of the second order phase transition because the critical line becomes fairly linear at large Ω_1 and has a slope near -1. We used the horizontal scans to provide a qualitative understanding of how the eigenminima split as Ω_1 is ramped to smaller values across the phase transition line. In addition, we are able to change Ω_1 more smoothly than Ω_2, 10 μs verses 200 μs step rates, which results in less heating during relatively fast ramps.

We transferred atoms from $|m_F = -1\rangle$ to $|m_F = 0\rangle$ using rf to perform the adiabatic transfer. Ω_1 was then ramped for 10 ms to $8E_R$ and was followed by an additional 10 ms ramp of Ω_2 from its initial value of $1E_R$ to its final value ($\Omega_2 < \Omega_2^*$).

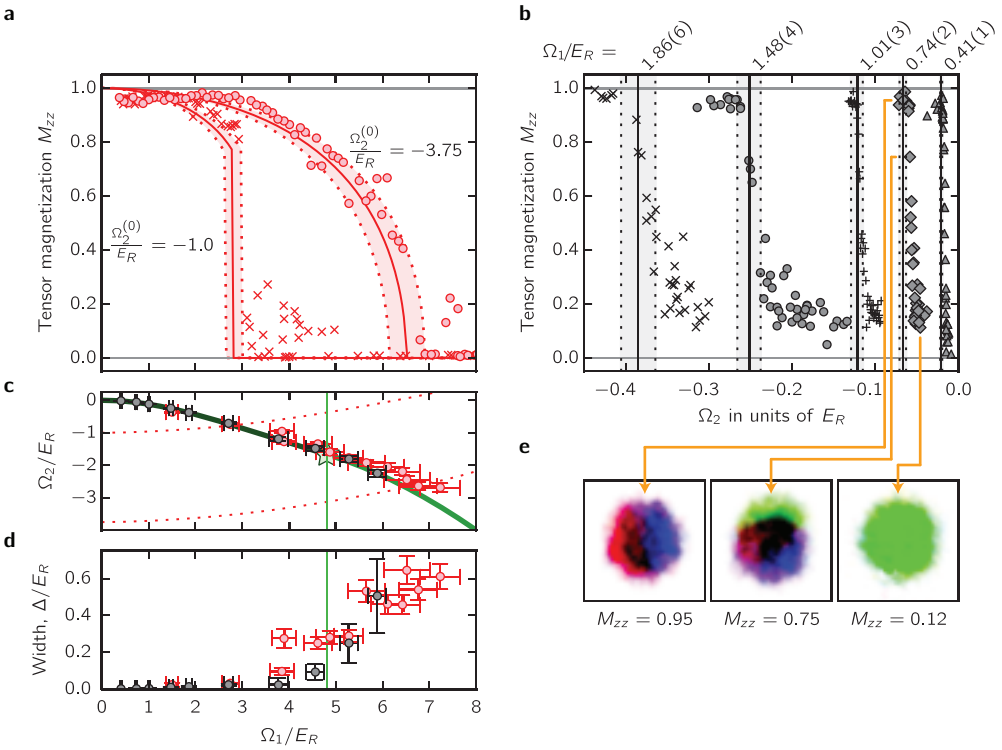

Figure 7.2: The measured phase transition. **a** Tensor magnetization M_{zz} measured as a function of Ω_1, showing both second-order $[\Omega_2(\Omega_1 = 0) = -3.7500(3)E_R]$ and first-order $[\Omega_2(\Omega_1 = 0) = -1.0E_R]$ phase transitions in comparison with theory. These curves followed the nominally horizontal trajectories (see Methods Summary) marked by red dashed curves in **c**. **b** Tensor magnetization measured as a function of Ω_2 at $\Omega_1/E_R = 1.86(6)$, 1.48(4), 1.01(3), 0.74(2), and 0.41(1), plotted along with the predicted critical Ω_2. In **a** and **b** the light-colored region reflects the uncertainty in theory resulting from our $\approx 5\%$ systematic uncertainty in Ω_1. **c, d** Phase transition. Black (red) symbols depict data obtained using vertical (nominally horizontal) cuts through the phase diagram. **c**, measured phase transitions plotted along with theory: solid (phase transition), and green vertical line (tricritical point, Ω_1^*). **d**, 20% to 50% transition width showing the clear shift from first to second-order with increasing Ω_1. **e** Domain formation for $\Omega_1 = 0.41(1)$ showing interaction-driven spin structure near the first-order phase transition. In all images, red corresponds to spatial regions with local $M_z \approx -1$, the green regions correspond to $M_z \approx 0$ and the blue regions correspond to $M_z \approx +1$. In the polar regime at $M_{zz} = 0.12$ only the $m_F = 0$ cloud is visible; near the first-order phase transition at $M_{zz} = 0.75$ all three $m_F = 0$ clouds are visible and have partially phase separated; and in the ferromagnetic regime at $M_{zz} = 0.95$ only $m_F \pm 1$ clouds are visible and they have completely phase separated.

We finally ramped Ω_1 linearly to its final value, keeping the ramp *rate* fixed so that a ramp from $8E_R$ to $0E_R$ takes 1 second. The BEC was held for an additional 50 ms before performing the TOF steps outlined in section 7.4.1.

As shown in Fig. 7.2a M_{zz} increases suddenly but continuously from 0 for the second order phase transition, only reaching 1 at $\Omega_1 = 0$. As we expect, the same scan across the 1st order phase transition shows a relatively discontinuous change in M_{zz}. Our horizontal scans were plotted in red in Fig. 7.2c. The widths in Fig. 7.2d correspond to the range in Ω_1 necessary for M_{zz} to fall from 0.5 to 0.2 of its full value. This metric avoids measuring the shallow slope of M_{zz} vs Ω_1 shown in panel a but also avoids much of the noise near $M_{zz} = 0$, also shown in panel a for the 1st order phase transition. These widths quantitatively show the expected behavior that as we cross over from 1st order phase transitions (with discontinuous jumps in M_{zz}) to 2nd order phase transitions (where M_{zz} changes gradually away from $M_{zz} = 0$) the apparent width in Ω_1 dramatically increases.

7.4.3 Metastable

Systems ramped through a 1st order phase transition can remain in long-lived metastable states. We showed that with differing ramp rates, 0.5 to $0.2E_R/s$, from the unmagnetized to the magnetized portion of the phase diagram the transition width continuously decreases with decreasing ramp rate as shown in Fig. (7.3). This is consistent with slow relaxation from a metastable initial state.

We explored the full regime of metastability by counting the number of eigenminima that exist at each (Ω_1, Ω_2) in the phase diagram. For points near the first-order phase transition three eigenminima exist (Fig. 7.4); near the second-order transition this count decreases, giving two local minima which merge to a single minimum beyond the second-order transition. We identified the case of one eigenminima when $|M_z| = 0$ and its variance was small. For two states, $|M_z| > 0$ and its variance was also small. For three states, which might include populations at

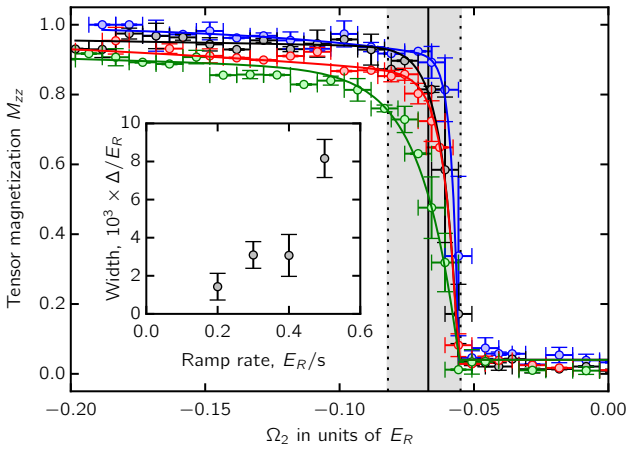

Figure 7.3: Quenching dynamics. The system was prepared in the unmagnetized phase with $\Omega_1 = 0.74(8)E_R$ and Ω_2 was ramped through the phase transition at ramp-rates $d\Omega_2/dt = -0.2, -0.3, -0.4$, and $-0.5E_R$/s (blue, black, red, and green symbols, respectively). The curves are guides to the eye. The inset shows the decreasing width, defined as the required interval for the curve to fall from 50% to 20% of its full range, of the first-order transition as the ramp-rate decreases.

$M_z = 0$ and $M_z > 0$ simultaneously, we would measure $|M_z| > 0$ with large variance. In this way we fully mapped the system's metastable states in agreement with theory, as shown in Fig. (7.4).

In many cases, population transfer from these metastable states was quite fast and neared the optical dipole trap period aligned with the SOC $\sim 2\pi/\omega_{\text{trap}}$. This required us to prepare the metastable state quickly relative to this relaxation time and yet ramp Ω_1 slowly enough that the metastable state remained near its local equilibrium. We found that the rate $\lesssim 200E_R/s$ was a good compromise between these two requirements for evolution through most of parameter space. However, unlike the 1st order phase transition–which we can diabatically ramp through–we cannot rapidly ramp through the 2nd order phase transition because the quasimomenta associated with each eigenminimum rapidly changes. Although a local metastable minimum might exist there would be sloshing and heating as if it did not. For this reason, we ramp very slowly through the 2nd order phase transition and rapidly elsewhere.

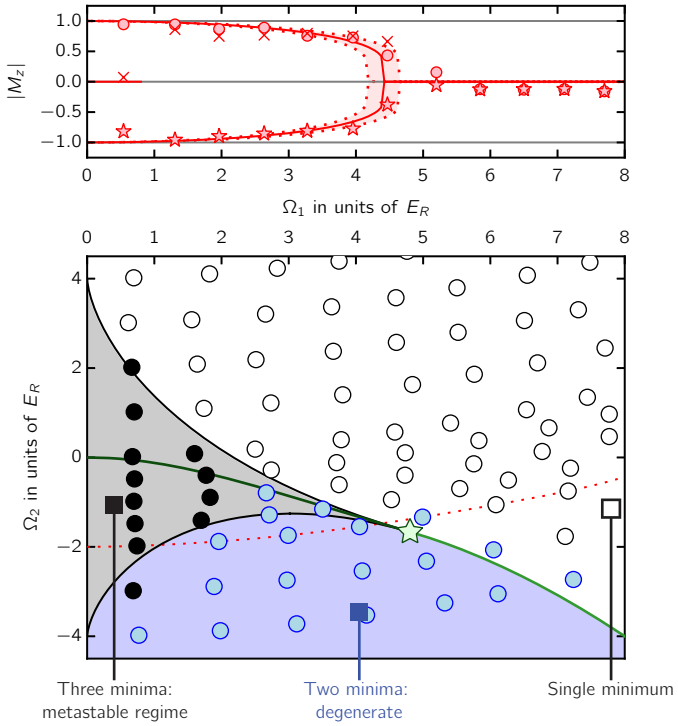

Figure 7.4: Metastable states. Top, Measured magnetization plotted along with theory. The system was prepared at the desired $\Omega_2 = -2E_R$; $\Omega_1(t)$ was then increased to its displayed final value; during this ramp Ω_2 also changed, and the system followed the curved trajectory in the bottom panel. Each displayed data point is an average of up to 10 measurements, and the colored region reflects the uncertainty in theory resulting from our $\approx 5\%$ systematic uncertainty in Ω_1. Circles/crosses/stars represent data starting in $m_F = +1$, 0, and -1 respectively. Bottom, state diagram: theory and experiment. Blue: two states; black: three states; white: one state. Colored areas denote calculated regions where the color-coded number of stable/metastable states are expected. Symbols are the outcome of experiment. Each displayed data point is an average of up to 20 measurements.

7.5 Many-body physics

Collisional processes (2-body interactions) are necessary for the evaporative and damping processes that allow Bose-Einstein condensation in the eigenminima of our coupling. In addition, these processes enable population transfer from metastable eigenminima to the ground eigenminimum. Hence, interactions are critical for understanding the magnetic-like phase transitions in our system.

7.5.1 Spin-orbit coupled Gross-Pitaeveskii Equation

Our quadratic Zeeman shift is much larger than the spin interaction energy $\approx h \times 90$ kHz $\gg h \times 6$ Hz and as such the spin interaction terms which exchange $|m_F = 0\rangle \leftrightarrow |m_F = \pm 1\rangle$ are energetically forbidden. We organize the remaining interaction coefficients into a three component matrix

$$g = \begin{pmatrix} c_0 + c_2 & c_0 + c_2 & c_0 - c_2 \\ c_0 + c_2 & c_0 & c_0 + c_2 \\ c_0 - c_2 & c_0 + c_2 & c_0 + c_2 \end{pmatrix} \tag{7.6}$$

where $c_0 = (100.86) \times 4\pi\hbar^2 a_{\mathrm{B}}/m$ and $c_2 \approx -4.7 \times 10^{-3} c_0$. The spin-orbit coupled GPE is then described by a system of three coupled equations

$$\begin{aligned} i\hbar\partial_t \psi_\sigma(\mathbf{x}) = &\sum_{\sigma'} \left[\frac{\hbar^2 \boldsymbol{\nabla}^2}{2m} \delta_{\sigma,\sigma'} + V(\mathbf{x})\delta_{\sigma,\sigma'} + (\boldsymbol{\Omega}_1(x)\cdot\hat{\mathbf{F}})_{\sigma,\sigma'} + (\Omega_2 \hat{F}^{(2)}_{zz})_{\sigma,\sigma'} \right] \psi_{\sigma'}(\mathbf{x}) \\ &+ \sum_{\sigma'} N g_{\sigma,\sigma'} |\psi_{\sigma'}(\mathbf{x})|^2 \psi_\sigma(\mathbf{x}) \end{aligned} \tag{7.7}$$

which computes the time evolution of the spinor wavefunction $\psi_\sigma(\mathbf{x})$, normalized to $\int \mathrm{d}\mathbf{x} \sum_\sigma |\psi_\sigma(\mathbf{x})|^2 = 1$. It is more correct to add normal ordering to the bosonic operators in the interaction term but the correction is very small for our typically

$N = 500000$ condensate occupation of the ground-state mode.

In simulation, the wavefuction is time evolved on a 3D or 3D projected onto 2D (via integration of a spatial axis) set of sites. Since these computations can be time consuming, it is desirable to transform out as much of the time dependence as possible. Hence, we perform the rotating frame and gauge transformations $\hat{U}(\mathbf{x}, t)$ in section 6.4 and diagonalize the single particle Hamiltonian

$$\psi_\sigma(\mathbf{x}) = \hat{U}_{\sigma,\sigma'}(\mathbf{x}, t)\mathcal{F}^{-1}[\hat{U}_{\sigma',n}(\mathbf{q})\psi_n(\mathbf{q})]; \tag{7.8}$$

where $\hat{U}_{\sigma,n}(\mathbf{q})^\dagger \hat{U}^\dagger_{\sigma',\sigma}(\mathbf{q}, t) H \hat{U}_{\sigma',\sigma''}(\mathbf{x}, t)\hat{U}_{\sigma'',n'}(\mathbf{q})$ diagonalizes the Hamiltonian. One approach to evolving a GPE with time is to use a split time propagation method [89] where we Fourier transform the wavefunction and Hamiltonian to compute the coupling kinetic energy parts of the Hamiltonian. In the case of spin-orbit coupling it is necessary to fourier transform from the spin states with gauge and rotating frame transformations applied, then transform to single particle eigenstates of the spin-orbit coupling. In this case, the potential and interaction terms are calculated in the transformed spin basis while the kinetic energy and optical coupling terms are computed in the Fourier and eigenstate basis. The same wavefunction is time evolved by two GPEs, one after the other

$$i\hbar\partial_t\psi'_\sigma(\mathbf{x}) = V(\mathbf{x})\psi'_\sigma(\mathbf{x}) + \sum_{\sigma'} N g_{\sigma,\sigma'}|\psi_{\sigma'}(\mathbf{x})|^2\psi'_\sigma(\mathbf{x}) \tag{7.9}$$

$$i\hbar\partial_t\psi_n(\mathbf{q}) = \epsilon_n(\mathbf{q})\psi_n(\mathbf{q}) \tag{7.10}$$

where $\psi'_\sigma(\mathbf{x}) = U_{\sigma',\sigma}(\mathbf{x}, t)\psi_\sigma(\mathbf{x})$ is the gauge transformed wavefunction in the rotating frame, $\psi_n(\mathbf{q}) = U^\dagger_{\sigma,n}(\mathbf{q})\mathcal{F}[\psi'_\sigma(\mathbf{x})]$. The transformation in Eq. (7.8) can be extremely computationally expensive but we still win because now our stepsize must be small in comparison to $c_2 n/h$ and $1/\omega_{\text{trap}}$ rather than $1/\Omega_1$.

7.5.2 Free energy with interactions

The contribution to the free energy from interactions is given by

$$G_{\text{int}} = \int \mathrm{d}\mathbf{x} N g_{\sigma,\sigma'} |\psi'_{\sigma}(\mathbf{x})|^2 |\psi'_{\sigma'}(\mathbf{x})|^2. \tag{7.11}$$

We want to know how the free energy is modified as a function of M_z and $M_z z$. Since the condensate wavefunctions are strongly peaked in $\mathbf{k}$ it is convenient to write an approximate and local overall condensate wavefunction for the ground eigenstate $n = 0$ in momentum coordinates

$$\psi'(q) = \left[\eta_1 e^{-i\gamma_1}\delta(q - q_1) + \eta_2 e^{-i\omega t}\delta(q - q_2) + \eta_3\delta(q - q_3)\right]\phi(\mathbf{q}) \tag{7.12}$$

where η_1^2, η_2^2, and η_3^2 are the fraction of the total population collected in each eigenminima, $q_{1,2,3}$ are the quasimomenta at each local minimum in the free energy, $\hbar\omega$ is the energy difference between the central and outer eigenminima, and $\phi(q)$ is the eigenstate of the spin-orbit coupling at quasimomentum q. If we were to define phases (other than 0) for the components at q_2 and q_3 the free energy would be a function of $2\gamma_2 - \gamma_1 - \gamma_3$.

Plugging $\psi(\mathbf{q})$ back into Eq. (7.11), we find the free energy in position space

$$\psi(\mathbf{x}, t) = e^{i[q_1 x - \gamma_1]}\phi_{q_1}(\mathbf{x}) + e^{i[q_2 x - \omega t]}\phi_{q_2}(\mathbf{x}) + e^{iq_3 x}\phi_{q_3}(\mathbf{x}). \tag{7.13}$$

We were are able to treat the overall density profile as a delta function in quasimomentum because its ≈ 10 μm extent dramatically exceeds the periodicity of the plane waves $\lambda/2$. $|\psi(\mathbf{x})|^2$ corresponds to a spin vector with small sinusoidal modulations in each spin component. The amplitude of these modulations is $\Omega_1/3$. Since these modulations are squared in Eq. (7.11) the interaction energy increases with the square of the modulation amplitude ($\propto \Omega_1^2$). The phase γ_1–only relevant when

condensates occupy three eigenminima and spatially overlap–allows some terms in the free energy to destructively interfere: reducing the increase in the free energy from what might be expected of a two state spin-orbit coupled system system [7].

7.5.3 Miscibility

The spin-orbit coupling modification of the interactions depends upon the exact distribution of η_1^2, η_2^2, and η_3^2 as well as $\hbar\omega$. We find an effective interaction strength by integrating over one period of the spin-orbit coupling modulation

$$g_{\text{eff}} = \int_0^{4\pi/(q_1-q_3)} \mathrm{d}x g_{\sigma,\sigma'} |\phi_\sigma(x,t)|^2 |\phi_{\sigma'}(x,t)|^2 \tag{7.14}$$

where $\psi(\mathbf{x},t) = N\phi(\mathbf{x},t)$; and

$$\phi(\mathbf{x},t) = \eta_1 e^{i[\mathbf{q}_1\cdot\mathbf{x}-\gamma_1]}\phi(\mathbf{q}_1) + \eta_2 e^{i[\mathbf{q}_2\cdot\mathbf{x}-\omega t]}\phi(\mathbf{q}_2) + \eta_3 e^{i\mathbf{q}_3\cdot\mathbf{x}}\phi(\mathbf{q}_3). \tag{7.15}$$

It is the spatial modulation of the density that occurs when more than one eigenminimum in the spin-orbit coupling dispersion is occupied that modifies the effective interaction strength. We want to compare the effective interaction strength for a mixed system to g_{sep} of a BEC where the eigenminima components are spatially separated

$$g_{\text{sep}} = g_1^{\eta_1^2} g_2^{\eta_2^2} g_3^{\eta_3^2} \tag{7.16}$$

Unlike g_{eff}, g_{sep} is simply a reflection of the spin-composition of the eigenstate at the eigenminima and therefore varies on the order of c_2. By analogy with the miscibility condition $g_{\text{eff}} \leq g_1^{1/2} g_2^{1/2}$ where $\eta_{1,2}^2 = 1/2$ we might expect to be able to define an equivalent miscibility condition for the three state system using g_{sep}. The utility of such an expression for the two component case can be seen in Fig. 7.5 where as the effective 2-state interactions (red squares) cross $g_1^{1/2} g_2^{1/2}$ (red dotted line) with

increasing Ω_1 the immiscibility shown in panel b sharply increases.

Using the same intuition, 3-state interactions (blue circles) should undergo an increase in immiscibility as η_2^2 sweeps from above 0.5 to below when $\eta_1^2 = \eta_3^2$ and $\Omega_1 > 1.7E_R$: this was not observed (nor was it plotted in Fig. 7.5) in experiment. Instead, we plotted the immiscibility of our condensates when the $\eta_2^2 \approx 0.5$, $\eta_{1,3} \approx 0.25$. The relatively smaller immiscibility of the three state vs two state SOC BEC components suggests that γ_1 is closer to π (filled blue circles) than 0 (open blue circles).

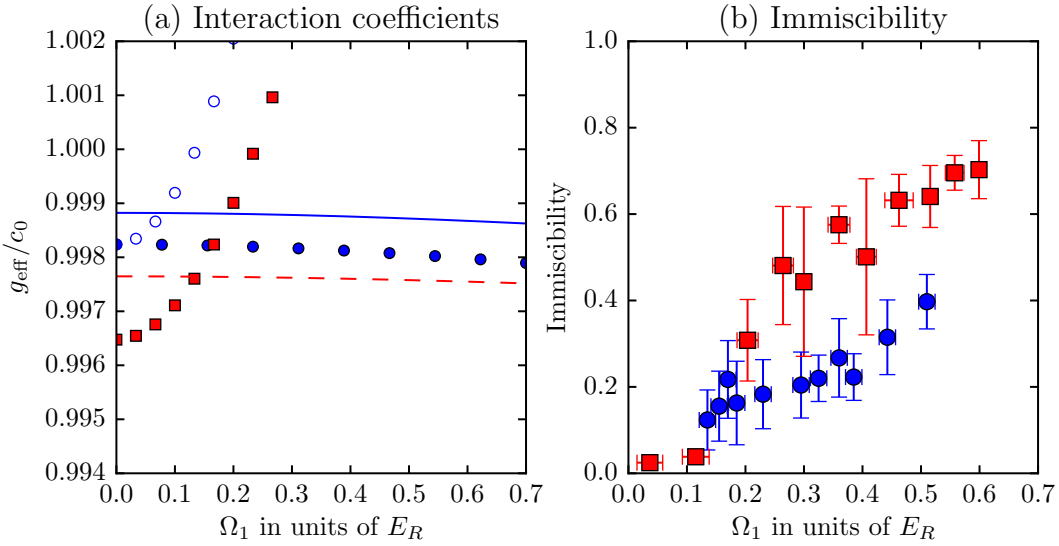

Figure 7.5: (a) Effective interaction coefficient as a function of Ω_1. Three state miscibility depends strongly on relative spin population, here: $\eta_2^2 = 0.75$ and $\eta_{1,3}^2 = 0.075$; and a phase $\gamma_1 = 0$ (empty circles) and $\gamma_1 = \pi$ (filled circles). The solid trace is $g_1^{\eta_1^2} g_2^{\eta_2^2} g_3^{\eta_3^2}$ which is proportional to the free energy when the BEC components are spatially separated. Red squares show the interaction coefficient when a mixture $\eta_{1,2}^2 = 0.5$ is present. The red dotted line shows $g_1^{1/2} g_2^{1/2}$ (b) Using the measured condensate component densities the immiscibility was calculated using the metric $1 - \overline{n_{1,3}(\mathbf{x}) n_2(\mathbf{x})} / \sqrt{\overline{n_{1,3}(\mathbf{x})^2} + \overline{n_2(\mathbf{x})^2}}$. We plotted the immiscibility of $n_2 = |\phi_{q_2}(\mathbf{x})|^2$ with $n_{1,3} = |\phi_{q_3}(\mathbf{x})|^2 + |\phi_{q_1}(\mathbf{x})|^2$. 2-state spin-orbit coupled immiscibility (red circles) determined using $1 - \overline{n_1(\mathbf{x}) * n_2(\mathbf{x})} / \sqrt{\overline{n_1(\mathbf{x})^2} + \overline{n_2(\mathbf{x})^2}}$ has a much clearer turn on with respect to Ω_1 and quickly reaches higher immiscibility than the fully three state version.

We might hypothesize that the measured miscibility should vary substantially

as we detune in Ω_2 from triple degeneracy because the increasing time evolution in γ_1 would spoil the destructive interference in g_{eff}. The experimental results were inconclusive since the rate of population transfer from an initial preparation in ϕ_{q_2} slowed down, making this a less desirable mechanism for tripartite mixture preparation (usually the population of only one of the three states would dominate). We attempted to initialize the system with a tripartite mixture and domains already present, but this resulted in substantial thermalization for quick initializations $\approx 10 - 20$ ms and substantial population transfer with some thermalization for long initializations $\approx 30 - 50$ ms (the boundary between short and long turn-on times was defined by our ≈ 30 Hz trap frequencies along the Raman coupling).

7.5.4 Free energy with interactions

Unlike the two-state spin-orbit coupling a portion of the three state coupling may be turned on and off by tuning Ω_2 relative to the single particle triple degeneracy Ω_2^*: Ω_2^* depends upon the exact value of Ω_1. This is physically similar to the introduction of a time modulation of γ_1 whose frequency increases with detuning. In addition, because our Raman coupling breaks spin symmetry, the system may relax to a lower energy configuration of eigenminima through two mechanisms of which we are aware:

1. a purely collisional process which is sensitive to the single particle spectrum at the $h\times$ Hz level and changes M_{zz}. The maximum rate of population transfer should be $2(\Omega/3E_R)^2 c_0 n_0/h$.

2. a slower process that allows M_z population imbalances and whose relaxation rate is strongly tied to our optical dipole trap frequencies (it is possible that the only dipole frequency that matters is the one aligned with the Raman coupling).

The per particle free energy of our system may be determined variationally with respect to η_1, η_2, η_3, and γ_1

$$G(M_z) = \epsilon_1|\phi_{q_1}|^2 + \epsilon_2|\phi_{q_2}|^2 + \epsilon_3|\phi_{q_3}|^2 + n(0)g_{\text{eff}}(\eta_1, \eta_2, \eta_3, \gamma_1) \tag{7.17}$$

and computed for all Ω_1 and Ω_2; where $N|\phi_{q_1}|^2 = n_1(\mathbf{x})$, the density for the eigenminimum located at q_1.

In practice, the free energy is always minimized for $\gamma_1 = \pi$ and the fractional populations are not independent, leaving just two variational parameters. The free energy plotted in Fig. 7.6 is generally minimized when the BEC is almost entirely in ϕ_{q_2} or ϕ_{q_1} or ϕ_{q_3}; domains are metastable, hence when domains are present the free energy is not minimized. Near the triple degenerate line which exists along the first order phase transition it is energetically favorable for small amounts of other eigenminima components to be uniformly mixed in with the dominant spin-state: this is emphasized in the color scales of Fig. 7.6bc which focus on a very small range near $|M_z| = 1$ and 0, respectively.

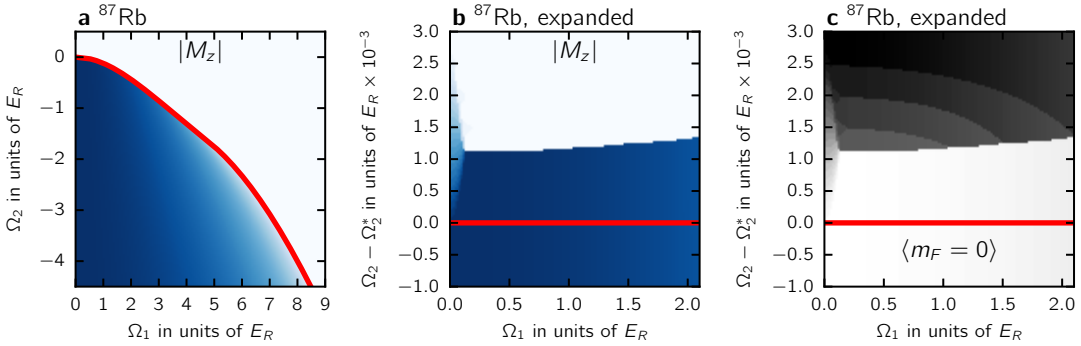

Figure 7.6: These plots use a variational method, essentially adjusting spin populations to minimize the free energy with the single-particle energies and interactions at peak density $n(0)$: there are density dependent shifts not visible in these plots. (a) Plot of $|M_z|$ that minimizes free energy for every point (Ω_1, Ω_2): colored is $|M_z| > 0$. For $\Omega_1 < \Omega^*$, $|M_z|$ changes discontinuously while for $\Omega_1 > \Omega^*$ the transition is abrupt but continuous. (b) We subtract the line of critical points (Ω_1^C, Ω_2^C)–the red line–from the free energy. Interactions shift the location of triple degeneracy very slightly from the single particle spectrum. (c) The same plot for $1 - |M_z|$.

There is a small shift due to the spin and density dependent interactions, this is of order $c_2 n(0) = h \times 6$ Hz. In the case where the condensate is prepared at Ω_2 between the single-particle triple degenerate line (the red line) and the interaction shifted triple-degeneracy at peak density $n(0)$ (the border between the blue and the white in Fig. 7.6) different density regions of the condensate are minimized with vastly different eigenminima composition. Figure 7.7a shows the eigenminima dependent shift $\approx c_2 n(\mathbf{r})$ in the free energy as a function of position. When the cloud is offset from the single particle triple degeneracy, the white dot in panel b, the eigenminima dependent shift can cause the high density regions of the condensate to cross triple degeneracy: the condensate has a position dependent eigenminima composition as shown in panels c and d. Alternatively, we may consider the equivalent scenario in Fig. 7.6b where the interaction dependent shift (highlighted with the white double sided arrow) shrinks and expands proportional to density. For a system initially prepared in ϕ_{q_2}, the highest density regions of the condensate populate $\phi_{q_3} + \phi_{q_1}$ which then experience a modulational instability that drives them to spatially separate, Fig. 7.7cd.

We might claim that the $\approx c_2 n(\mathbf{r})$ shift is very small and hence we should be able to test our interpretation for cloud structures like those in Fig. (7.6)cd by observing the donut shape within a several Hz band in Ω_2 and not elsewhere. Experimentally, this donut pattern occurs over a much wider band in Ω_2, essentially the width of our 1st order phase transitions $\approx \Omega_2^C/50$, which might not be unexpected considering the non-zero immiscibility shown in Fig. (7.5). This would imply that some other physics is at play here than simple ground state minimization.

7.5.5 Hysteresis

Preparing our system in ϕ_{q_2} then ramping across the 1st order phase transition causes population transfer to $\phi_{q_3} + \phi_{q_1}$ which subsequently phase separate. Ramping back across the phase transition uses the same collisional process in reverse, $\phi_{q_3} + \phi_{q_1}$

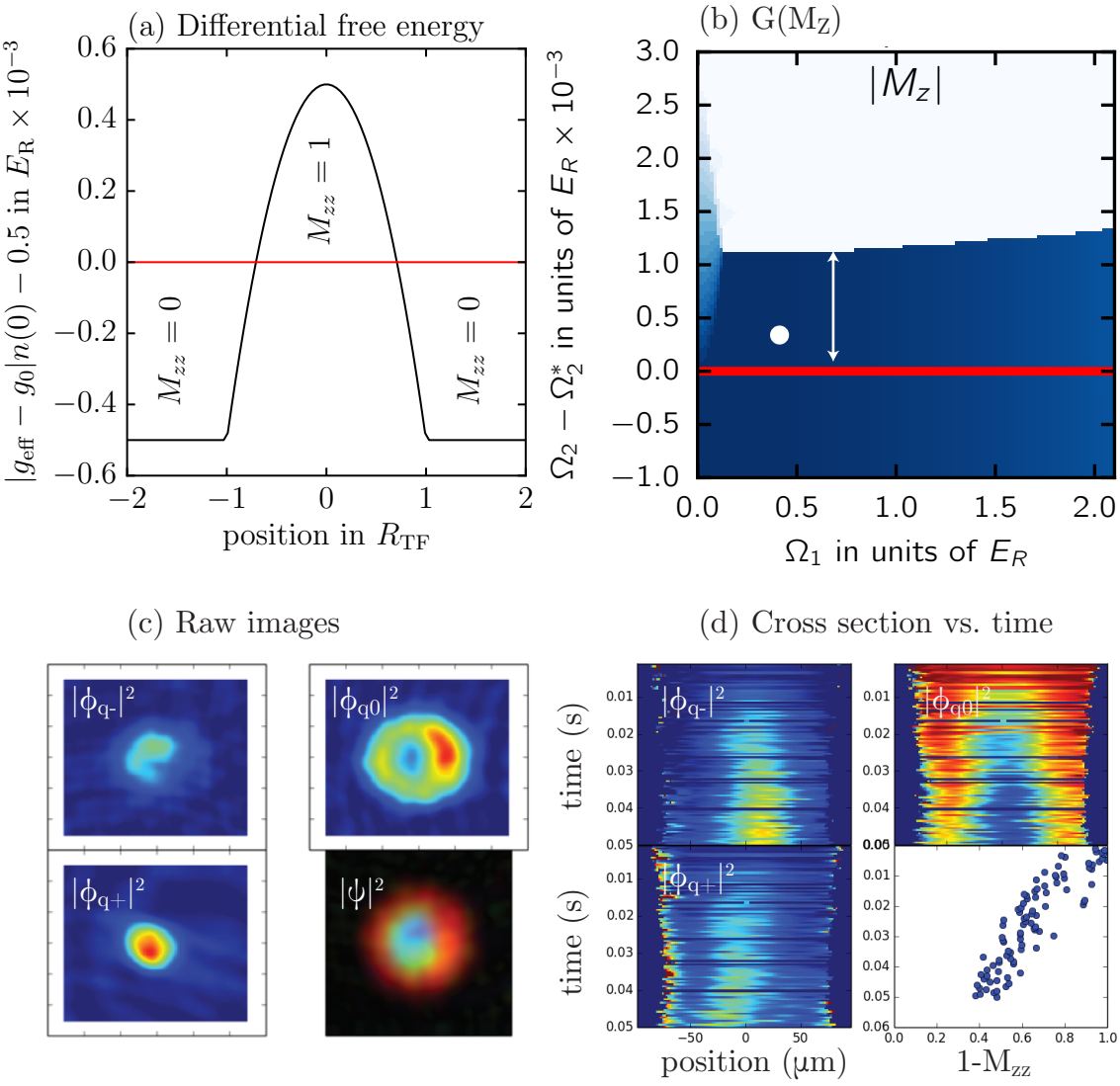

Figure 7.7: The differential shift between spin-state interactions are responsible for the displacement of the 1st order phase transition from single-particle triple degeneracy. (a) We show a condensate in the q_2 eigenminima near single particle triple degeneracy. The eigenminimum dependent shift causes the high density region of a condensate to cross the overall triple degeneracy (red line). (b) Equivalently, the interaction shift is denoted by the double-sided white arrow. This region shrinks and expands as a function of density past the white dot, which represents the location of our condensate. (c) Pictures of eigenminima spatial distribution at a snapshot in time. Note the donut shape in ϕ_{q_2}. (d) Cross-sections through the center of the condensate density distribution (see panel (c)) which descend as time increases. Note that population forms in $\phi_{q_3} + \phi_{q_1}$ and then spatial separation of the components occurs.

becomes ϕ_{q_2}. Because ϕ_{q_3} and ϕ_{q_1} have phase separated, population transfer to ϕ_{q_2} only occurs along the $\phi_{q_3} + \phi_{q_1}$ boundary and hence the reverse ramp is much slower than the forward ramp. Data for the reverse ramp is also extremely variable, hence we took data almost exclusively using the forward ramp.

Chapter 8: Rashba

We theoretically explore a Rashba spin-orbit coupling scheme which operates entirely in the absolute ground state manifold ($^5S_{1/2}$ electronic, $f = 1$ hyperfine) of ^{87}Rb, thereby minimizing all inelastic processes. Our technique uses far-detuned "Raman" laser coupling to create the Rashba Hamiltonian. For a given coupling, intense illumination and large detuning suppress spontaneous emission. At the same time, coupling that changes m_F magnetic sublevel quantum number by two is also suppressed: this coupling is necessary to produce the Rashba Hamiltonian within a single total angular momentum f manifold. However, the same optical couplings can link the three XYZ states familiar to quantum chemistry. We show that the XYZ states are essentially the eigenstates of ^{87}Rb in the presence of a quadratic Zeeman shift coupled by a strong radio-frequency magnetic field. We perform a full Floquet analysis on the required laser coupling scheme.

8.1 introduction

Geometric gauge potentials are encountered in many areas of physics [90, 91, 92, 93, 94, 95, 96, 97, 98]. In atomic gases, the geometric vector and scalar potentials were first considered in the late 90's to fully describe atoms "dressed" by laser beams [99, 100, 101]. Atoms that move in a spatially varying internal state dependent dressed optical field experience geometric vector and scalar potentials in addition to the energies associated with the local eigenenergies. These ideas have since been refined, and now allow for the engineered addition of spatially homogeneous geometric gauge potentials [7, 8, 9]. In many cases, the resulting atomic Hamiltonian is equivalent to

iconic models of spin-orbit coupling: Rashba, Dresselhaus and combinations thereof.

As made evident by the observation of the superfluid to Mott insulator transition [102, 103], with quantative agreement with theory [104, 105], quantum gas systems bring atomic physics's hallmark precision to many-body systems. Often, systems with spin-orbit coupling will have multiply degenerate single particle eigenstates with topological character: this combination suggests that strongly correlated phases will exist in the presence of interactions for both Bose and Fermi systems. Topological insulating states and the spin-Hall effect are often present in spin-orbit coupled systems [11, 12]. Rashba spin-orbit coupling (present for 2D free electrons in the presence of a uniform perpendicular electric field, such as in asymmetric semiconductor heterostructures) [106, 107], is perhaps the simplest of these 2D spin-orbit couplings. Indeed, interesting many-body phases [108, 68, 109] predicted for atomic systems with Rashba SOC include unconventional and fragmented Bose-Einstein condensation [18], composite fermion phases of bosons [19] and anisotropic or topological superfluids in fermionic systems [110].

8.1.1 Rashba SOC

The simplest model of Rashba spin-orbit coupling describes a 2D free electron system in terms of electron momentum $\hbar\mathbf{k}$ and gyromagnetic ratio g in the presence of an out-of-plane electric field $\mathbf{E}(t) = E\mathbf{e}_z$. We consider the electrons relativistically: in the electron's moving frame an in-plane magnetic field $\mathbf{B}_{\mathrm{SOC}} = \hbar\mathbf{k}/m \times \mathbf{E}/c^2$ appears in proportion to momentum, as shown in Fig. (8.1). The additional contribution to the spin-1/2 electron's Hamiltonian from $\mathbf{B}_{\mathrm{SOC}}$ is

$$\hat{H}_{\mathrm{SOC}} = \frac{2\alpha}{m}(\mathbf{k} \times \mathbf{e}_z) \cdot \hat{\mathbf{F}} \tag{8.1}$$

where $\alpha = g\mu_B|\mathbf{E}|/2c^2$; $\hat{\mathbf{F}} = \hbar\hat{\boldsymbol{\sigma}}/2$ is the spin operator for spin-1/2; and $\hat{\boldsymbol{\sigma}} = (\hat{\sigma}_x, \hat{\sigma}_y, \hat{\sigma}_z)$ is the vector of Pauli matrices. As shown in Fig. (8.1)ab, this Hamilto-

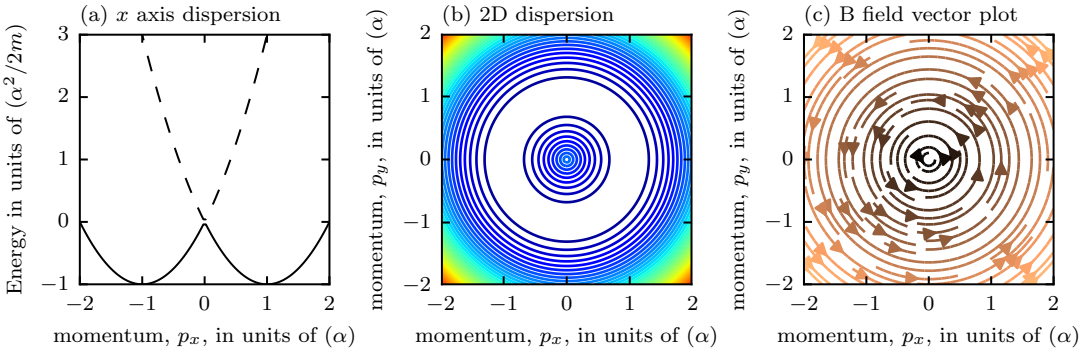

Figure 8.1: Rashba dispersion. (a) Dispersion cross-section through the origin. Electron energies are minimized for $|\mathbf{p}| \neq 0$. (b) Contour plot of dispersion demonstrating cylindrical symmetry. (c) Vector plot of $\mathbf{B}_{\text{SOC}} = \hbar\mathbf{k}/m \times \mathbf{E}/c^2$: the ground state electron spin is antialigned with $\mathbf{B}$. A spin following an adiabatic path about the dispersion origin traces out a loop about the equator of the Bloch sphere, producing a π phase winding.

nian has a highly degenerate ground state manifold comprising a ring of momentum states with magnitude $k_x^2 + k_y^2 = \alpha^2$. Centered in this ring, where $\mathbf{k} = 0$, there exists a Dirac point which connects the eigenstates of the Rashba Hamiltonian.

Ignoring overall energy shifts, the Hamiltonian including $\hat{H}_{\text{SOC}}$ and the kinetic energy can be reexpressed as $\hat{H} = (\hbar\mathbf{k} - \hat{\mathcal{A}})^2/2m$, in terms of an effective vector potential $\hat{\mathcal{A}} = \alpha(\hat{\sigma}_y\mathbf{e}_x - \hat{\sigma}_x\mathbf{e}_y)$. The Cartesian components of the vector potential manifestly fail to commute: the vector potential is non-abelian.

In this context, Berry's connection describes the phase accumulated by a particle moving adiabatically within one of two eigenstates $|\mathcal{Q}, \pm\rangle$ along a closed trajectory $\mathcal{Q}$ in the plane defined by the momentum vector $\hbar\mathbf{k} = \hbar(k_x, k_y)$. The acquired Berry's phase

$$\gamma_\pm = \oint_{\mathcal{Q}} d\mathcal{Q}\, \langle \mathcal{Q}, \pm | \boldsymbol{\nabla}_{\mathcal{Q}} | \mathcal{Q}, \pm \rangle \tag{8.2}$$

is $\pm\pi$ for paths $\mathcal{Q}$ that encircle $\mathbf{k} = 0$ and zero otherwise. This Berry's phase can introduce non-trivial interference effects for wavefunctions or trajectories that encircle $\mathbf{k} = 0$.

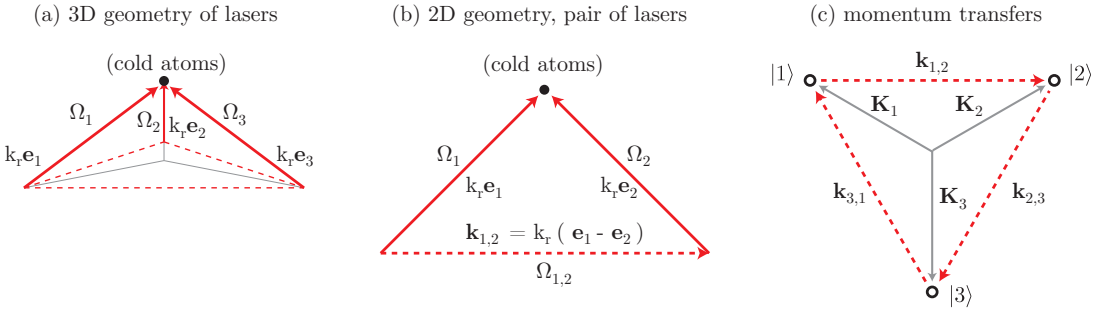

Figure 8.2: Schematic view of laser geometry giving spin-orbit coupling of three spin states. (a) 3D sketch of three lasers illuminating cold atoms. Dotted red lines correspond to the wavevector differences between beams $|\mathbf{k}_{\beta,\beta'}|$ where $\beta = \{1, 2, 3\}$ indexes lasers. Small grey lines show relationship of $|\mathbf{K}_\beta|$ magnitude with 3D geometry. (b) 2D view of a pair of Raman lasers. For a geometry that has 90 degrees between all Raman lasers the magnitude of $|\mathbf{k}_{\beta,\beta'}| = \sqrt{2}k_r$. (c) There are a range of acceptable example for $\mathbf{K}_\beta$, e.g. $\mathbf{K}_\beta = k_r\mathbf{e}_\beta$, the parameterization in this panel has the benefit of not displacing the dispersion along a momentum axis that is not Raman coupled and giving the minimum possible magnitude for $|\mathbf{K}_\beta|$. The minimum magnitude is $|\mathbf{K}_\beta| = \sqrt{2/3}k_r$ given $|\mathbf{k}_{\beta,\beta'}| = \sqrt{2}k_r$.

8.2 Rashba SOC in cold atoms

8.2.1 Overview

In ultracold neutral atoms, SOC is produced using laser fields, for example with two-photon Raman transitions that couple internal spin states such as the hyperfine $|f, m_F\rangle$ states in alkali atoms. We consider several lasers, each labeled by an index β, illuminating an atom with ground electronic states $|j\rangle$. The wavevectors of all the lasers share the same magnitude k_R, but propagate along different unit vectors $\mathbf{e}_\beta$. The Raman coupling, with strength $\Omega_{j,j',\beta,\beta'}$, from any pair of those lasers imparts a two-photon recoil momentum, $\hbar\mathbf{k}_{\beta,\beta'} = \hbar k_R(\mathbf{e}_\beta - \mathbf{e}_{\beta'})$. Figure (8.2) illustrates the relationship between laser recoil $\hbar k_r\mathbf{e}_\beta$, and Raman recoil $\hbar\mathbf{k}_{\beta,\beta'}$. The Hamiltonian

describing Raman coupling in this general form is

$$\hat{H}(\mathbf{k}) = \sum_{j,j'} \left\{ \left[\frac{\hbar^2 \mathbf{k}^2}{2m} + E_j \right] \delta_{j,j'} + \sum_{\beta \neq \beta'} \hbar \Omega_{j,j',\beta,\beta'} \exp\left(i[\mathbf{k}_{\beta,\beta'} \cdot \mathbf{x} - \omega_{\beta,\beta'} t - \gamma_{\beta,\beta'}](1 - \delta_{j,j'})\right) \right\} |j\rangle \langle j'| \tag{8.3}$$

where E_j is the energy of state $|j\rangle$ prior to laser-coupling, $-\omega_{\beta,\beta'} = \omega_\beta - \omega_{\beta'}$ is the difference between the positive and real angular frequency of each laser $\omega_\beta/2\pi$, and $\gamma_{\beta,\beta'} = \gamma_\beta - \gamma_{\beta'}$ is the difference between each laser's phase γ_β.

We consider the case where the Raman coupling resonantly links states in a ring: each pair of states resonantly coupled with a unique Raman pair of lasers and each state is Raman resonantly coupled to exactly two other states. We adopt a cyclic labelling so that $|j \pm N\rangle = |j\rangle$ and require that coupled states are adjacent in j.

Often, transitions are forbidden, which dramatically reduces the number of atomic states coupled to one another. Ignoring the consideration that some of these transitions might be forbidden, when there are N atomic states N lasers can resonantly couple each atomic state to $N-1$ other atomic states. For $N > 3$ states, more than N lasers is required to reduce the number of resonant couplings. In the case where the number of lasers exceeds the number of resonantly coupled atomic states it is convenient to define the resonance conditions

$$-\hbar\omega_{j,j'} = E_j - E_{j'} \tag{8.4}$$

$$\tag{8.5}$$

where ω_j and $\omega_{j,j'}$ are now indexed with respect to the atomic states. When the number of lasers exceeds the number of resonantly coupled states there is more than

one ω_j for at least one j. We compensate by defining multiple offset frequencies, ω_L

$$\hbar(\omega_L - \omega_j) = -E_j \tag{8.6}$$

If we follow the chain (loop) of resonant couplings we require that

$$\mathbf{k}_{j,j'} = \mathbf{K}_j - \mathbf{K}_{j'} \tag{8.7}$$

$$\sum_{j=0}^{N-1} \mathbf{k}_{j,j-1} = 0. \tag{8.8}$$

While there is some leeway in the definition of $\mathbf{K}_j$, it is always possible to define it as the wavevector of the laser that has a frequency of ω_j.

We apply a unitary transformation

$$\hat{U}(\mathbf{x}, t) = \sum_j \exp\left(i[\mathbf{K}_j \cdot \mathbf{x} - (\omega_L - \omega_j)t]\right) |j\rangle \langle j| , \tag{8.9}$$

which is both a rotating frame and a gauge transformation, that transfers the time and position dependence from the Hamiltonian to the states. In the rotating frame, the Hamiltonian gains an extra term

$$\sum_j \hbar(\omega_L - \omega_j) |j\rangle \langle j| = -i\hbar \hat{U}^\dagger(t) \partial_t \hat{U}(t) \tag{8.10}$$

from the time-dependent Schrödinger equation. The position dependence of the unitary transformation does not commute with the kinetic energy term of the Hamiltonian $\hat{H}(\mathbf{q}) = \hat{U}(\mathbf{x}, \mathbf{t}) \hat{H}(\mathbf{k})(\mathbf{k}) \hat{U}^\dagger(\mathbf{x}, \mathbf{t})$, and instead U acts as a spin-dependent momentum-displacement operator:

$$e^{-i\mathbf{K}_j \cdot \mathbf{x}} \mathbf{k}^2 e^{i\mathbf{K}_j \cdot \mathbf{x}} = (\mathbf{q} - \mathbf{K}_j)^2 \tag{8.11}$$

where $\mathbf{q}$ is the momentum operator in the momentum-displaced basis.

Altogether, the modified Hamiltonian has the form

$$\hat{H}(\mathbf{q}) = \sum_{j,j'} \Bigg\{ \left[\frac{-\hbar^2(\mathbf{q}-\mathbf{K}_j)^2}{2m} + (E_j - \hbar(\omega_L - \omega_j)) \right] \delta_{j,j'} + \hbar\Omega_{j,j'} \exp\left(-i\gamma_{j,j'}\right)\delta_{j-1,j'} + \text{h.c.} \Bigg\} |j\rangle \langle j'| \tag{8.12}$$

where $\Omega_{j,j'}$ is an ac Stark shift-like term which is a positive or negative real number whose value depends upon details of both the lasers and the states they couple. The value of ω_L is made evident here because it allows us to set the scalar energy for each uncoupled atomic state to zero after the rotating frame transformation.

The resonance conditions in Eqs. (8.4, 8.6) require that $\sum_{i=1}^{N} \omega_{i,i-1} = 0$ in a system of N coupled states. The same is not the case for the phase, instead $\sum_{i=1}^{N} \gamma_{i,i\mp1} = \pm N\bar{\gamma}$. $\bar{\gamma}$ strongly modifies the eigenstates of the Hamiltonian in Eq. (8.12) and tuning it can bring two eigenstates into degeneracy. It is in the subspace of two degenerate eigenstates that the Rashba Hamiltonian may be realized in a cold atom system.

8.2.2 Rashba subspace

We obtain the Rashba subspace from Eq. (8.12) by applying a discrete Fourier transform to the N cyclically defined states $|j\rangle$ where j indexes spin states from 1 to N and n indexes Fourier eigenstates from 0 to $N-1$

$$|n\rangle = \frac{1}{\sqrt{N}} \sum_{j=1}^{N} \exp\left(-i2\pi jn/N\right) |j\rangle \tag{8.13}$$

This transformation maps the off-diagonal terms onto the diagonal of the Hamiltonian and the differences between diagonal terms to the off diagonal. When $\mathbf{K}_j = k_{\text{eff}}[\cos(2\pi j/N)\mathbf{e}_x + \sin(2\pi j/N)\mathbf{e}_y]$ are the vertices of an equilateral triangle and when all the resonant coupling amplitudes are both negative (red detuned)

and equal $\Omega_{j,j'} = -\Omega(\delta_{j,j'+1} + \delta_{j,j'-1})$ the Hamiltonian in the Fourier basis becomes

$$\hat{H} = \sum_{n=0}^{N-1} \left[\frac{\hbar^2 \mathbf{q}^2}{2m} - \Omega \cos\left(2\pi n/N + \bar{\gamma}\right) \right] |n\rangle \langle n| + \frac{\hbar^2 k_{\text{eff}}}{m} \left[(iq_x + q_y) |n\rangle \langle n-1| + \text{h.c.} \right]. \tag{8.14}$$

Each laser wavevector can have an identical component along $\mathbf{e}_z$ in momentum space, $k_r \sin(\theta)\mathbf{e}_z$: then $k_{\text{eff}} = k_r \cos\theta$.

The energies of Fourier basis states, $\hat{H}|n\rangle = E_n |n\rangle$, at $\mathbf{q} = 0$ are $E_n = -\Omega \cos\left(2\pi n/N + \bar{\gamma}\right)$. When the laser phase accumulated over a loop of coupling $N\bar{\gamma}$ is π two Fourier basis states are degenerate and the ground state of the system. This degeneracy requirement implicitly includes the sign of $\Omega_{j,j'}$ where $-1 \to \exp i\pi$ which sums to $N\pi$ over a loop of coupling. Hence, for odd N and positive $\Omega_{j,j'}$ the accumulated laser phase degeneracy requirement changes to $\bar{\gamma} = 0$. The sign of $\Omega_{j,j'}$ is tied to the Raman detuning from the excited electronic states: we call detunings that produce negative $\Omega_{j,j'}$ red detuned; the positive case is blue detuned.

With two nearly degenerate Fourier basis states as the ground states we neglect the most energetic state and recover the two-state Rashba Hamiltonian in the large coupling limit $\Omega \gg |\mathbf{k}_{j,j'}|^2/2m \equiv E_R$

$$\hat{H}_{\text{sub}} = \frac{\hbar^2 \boldsymbol{q}^2}{2m} \hat{1} + \frac{2\hbar k_r}{m} (\hat{\sigma}_x q_y - \hat{\sigma}_y q_x) \tag{8.15}$$

where $\hat{1}$ is the identity for a two state system.

8.2.3 Physical implementation and limitations

It is not always easy to see how $\bar{\gamma}$ may be engineered into the electronic ground states of an alkali atom with Raman coupling. The laser phase accumulated over a loop of coupling $N\bar{\gamma} = 0$ when three lasers resonantly couple three states. In this case, a unitary transformation of the form given by Eq. (8.9) can always transfer

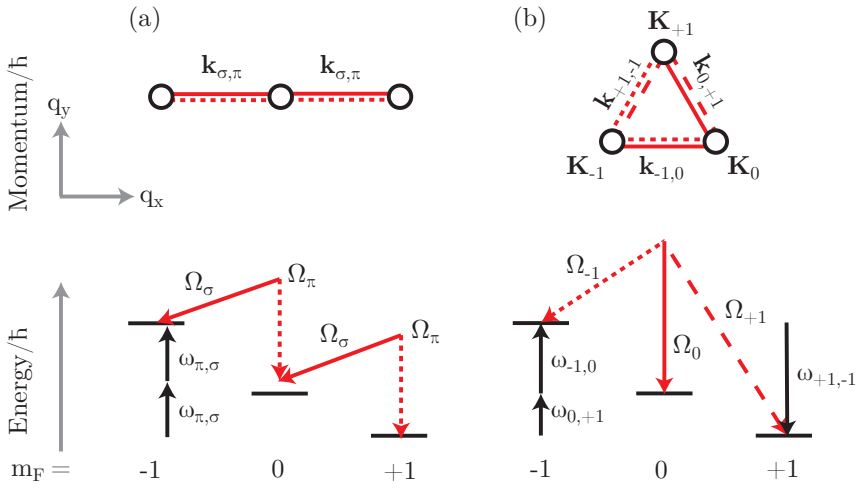

Figure 8.3: Schematic view of spin-orbit coupling in the spin-1 ground state of ^{87}Rb. (a) In current experiments, the same Raman lasers simultaneously couple pairs of adjacent spin states. Momentum transfers in the quasimomentum basis are arranged in a line. (b) For Rashba spin-orbit coupling, all pairs of spin states are independently coupled and momentum transfers in the quasimomentum basis are the vertices of an equilateral triangle.

the laser phase differences from the Hamiltonian into the definition of the states. This consideration is very compelling from an experimental perspective since small variations in the pathlength of each laser cannot produce dramatic changes in the potential. The Rashba subspace are the ground states of the system when $\bar{\gamma} = 0$ so long as the Raman coupling is blue detuned (positive and real). Three-state laser schemes that produce the Rashba Hamiltonian with the geometry shown in Fig. (8.3)b, without laser phase sensitivity, are blue-detuned 'tripod' schemes [71] and a special case of ring coupling [111].

Direct Raman coupling of the hyperfine ground states of alkali atoms with off-resonant coupling of the electronic excited states cannot couple differences beyond ± 1 units of angular momentum: $\Omega_{m_F=-1,m_F=+1} = 0$: coupling as shown in Fig. (8.3)a is possible, while coupling as shown in Fig. (8.3)b is not. Detuning near the excited electronic hyperfine states lifts the angular momentum restriction sufficiently to realize the a coupling scheme similar to Fig. (8.3)b but spontaneous emis-

sion events also sharply increase as a fraction of coupling: atomic ensemble lifetimes become much shorter than typical equilibration times. Consequently, we consider Raman lasers many thousands of linewidths detuned from the hyperfine resonances: reducing spontaneous emission to levels that allow ≈ 1 s of equilibration. Recent proposals circumvent the $0, \pm 1$ angular momentum transfers by including states from both f manifolds (ground and metastable) within the ground electronic states of alkali atoms [14] and a blue-detuned tripod scheme was experimentally realized in this context []. Although feasible, hyperfine (f) changing collisions are expected to lead to rapid atom-loss and heating, potentially decohering fragile many-body phases. Here, we detail a scheme that produces the Rashba Hamiltonian entirely in the $f = 1$ ground state manifold of ^{87}Rb and hence minimizes known forms of heating.

8.3 Physical Implementation

8.3.1 Construction of a fully coupled set of basis states

In the previous section we found that Raman coupling is proportional to $\hat{\mathbf{F}}$, which limits coupling to the first off-diagonal within or between the ground hyperfine manifolds. In this section, we show that rf coupling applied in the presence of a quadratic Zeeman term produces a set of initial eigenstates where every pair of states may be Raman coupled. The energies E_{m_F} for bare spin states $|f, m_F\rangle$ may be calculated with precision better than $h \times 1$ Hz using the Breit-Rabi (BR) equation. For the remainder of this manuscript we narrow our discussion to the $f = 1$ ground hyperfine manifold of ^{87}Rb and adopt the simplified notation $|m_F\rangle$ with $m_F \in \{-1, 0, +1\}$ to label spin states. The quadratic Zeeman splitting is $\epsilon = (2E_0 - E_{-1} - E_{+1})$ while the linear Zeeman splitting is $\hbar\Delta_Z = (E_{-1} - E_{+1})/2$.

We introduce the $|X, Y, Z\rangle = |X\rangle, |Y\rangle$ and $|Z\rangle$ eigenstates, familiar from quantum chemistry, which consist of linear combinations of $|m_F\rangle$ states in the $f = 1$

hyperfine manifold

$$|X\rangle = \frac{-|-1\rangle + |+1\rangle}{\sqrt{2}},\ |Y\rangle = i\frac{|-1\rangle + |+1\rangle}{\sqrt{2}},, \text{ and } |Z\rangle = |0\rangle \tag{8.16}$$

These $|X, Y, Z\rangle$ states have the property that

$$\epsilon_{jlm}\hat{F}_j |l\rangle = i |m\rangle \tag{8.17}$$

for indices j, l, m in $\{x, y, z\}$.

XYZ-like states can be eigenstates of an alkali atom in a dc magnetic field subject to a suitable oscillating magnetic field $B_{\rm rf}\mathbf{e}_{\rm rf}\cos(\omega_{\rm rf} + \gamma_{\rm rf})$ that resonantly links the $m_F = \pm 1$ projections of the spin-1 basis states in the presence of quantizing magnetic field, $B_{dc}\mathbf{e}_z$. The rf coupling is described by

$$\hat{H}_{\rm rf} = g_F\mu_0(\hat{\mathbf{F}}\cdot\mathbf{e}_{\rm rf})B_{\rm rf}\cos[\omega_{\rm rf}t + \gamma_{\rm rf}]/\hbar \tag{8.18}$$

where $\mathbf{e}_{\rm rf}$ is orthogonal to $B_{dc}\mathbf{e}_z$ and the frequency is set equal to the two rf photon resonance $\hbar\omega_{\rm rf} = \hbar\Delta_Z = (E_{-1} - E_{+1})/2$. We transform the spin states into the rotating frame of the rf using the transformation

$$\hat{U}_{\rm rf}(t) = \exp(-i\omega_{\rm rf}m_F t)\,|m_F\rangle\langle m_F| \tag{8.19}$$

The rotating frame Hamiltonian gains a term $\hbar\omega_{\rm rf} = -i\hbar\hat{U}^\dagger_{\rm rf}(t)\partial_t\hat{U}_{\rm rf}(t)$ from the time dependent Schrödinger equation. In the rotating frame and after making the RWA, the Hamiltonian that describes the dc and rf magnetic fields is

$$\begin{aligned}\hat{H}_B =&(\Delta_Z - \omega_{\rm rf})\hat{F}_z + \epsilon(\hat{1} - \hat{F}_z^2) \\ &+\Omega_{\rm rf}\left[\hat{F}_x\cos(\gamma_{\rm rf} + \xi_{\rm rf}) + \hat{F}_y\sin(\gamma_{\rm rf} + \xi_{\rm rf})\right]\end{aligned} \tag{8.20}$$

where $\hbar\Omega_{\rm rf} = g_F\mu_B B/2$. The phase $\xi_{\rm rf} = \text{atan}(\mathbf{e}_{\rm rf}\cdot\mathbf{e}_y/\mathbf{e}_{\rm rf}\cdot\mathbf{e}_x)$ is defined in exactly

the same spirit as in the previous section, however we will ultimately choose a set up where there are canceling contributions from $\xi_{\rm rf}$. The rf eigenenergies E_j of the Hamiltonian in the presence of the rf magnetic field are plotted verses dc magnetic field in Fig. (8.4)b. We represent our rf eigenstates $|x,y,z\rangle$ in terms of the $|X,Y,Z\rangle$ states: these are adiabatically connected as $\epsilon/\Omega \to -\infty$

$$\begin{aligned}
|x\rangle =& |X\rangle \xrightarrow{\epsilon/\Omega\to-\infty} |X\rangle \\
|y\rangle =& \frac{-i2\Omega_{\rm rf}|Y\rangle + \epsilon + \Omega_*|Z\rangle}{\sqrt{2}\Omega_*\sqrt{1+\frac{|\epsilon|}{\Omega_*}}} \xrightarrow{\epsilon/\Omega\to-\infty} |Y\rangle \\
|z\rangle =& \frac{-i2\Omega_{\rm rf}|Y\rangle + \epsilon - \Omega_*|Z\rangle}{\sqrt{2}\Omega_*\sqrt{1-\frac{|\epsilon|}{\Omega_*}}} \xrightarrow{\epsilon/\Omega\to-\infty} |Z\rangle .
\end{aligned}$$

Here we defined $\Omega_* = \sqrt{\epsilon^2 + 4\Omega_{\rm rf}^2}$.

We couple these eigenstates with weak and resonant additional couplings, rf or Raman, i.e. couplings much smaller than $\Omega_{\rm rf}$. We define a rf eigenstate coupling operator

$$\hat{D}^l_{j,j'} = |j\rangle\langle j|\hat{F}_l|j'\rangle\langle j'|, \; \hat{D}^l = \sum_{j,j'} D^l_{j,j'} \tag{8.21}$$

which gives the representation of $\hat{\mathbf{F}}$ in the rf eigenbasis. The $\hat{D}^x$ and $\hat{D}^y$ terms may be transformed into one another by changing the rf phase in Eq. (8.20): we choose the phases $\gamma_{\rm rf} + \xi_{\rm rf} = 0$ while defining the matrix elements, and we incorporate the rf phases into the definition of the total coupling in the next section.

We tabulate some of the complex-valued matrix elements $\langle j|\hat{D}^l|j'\rangle$ of the

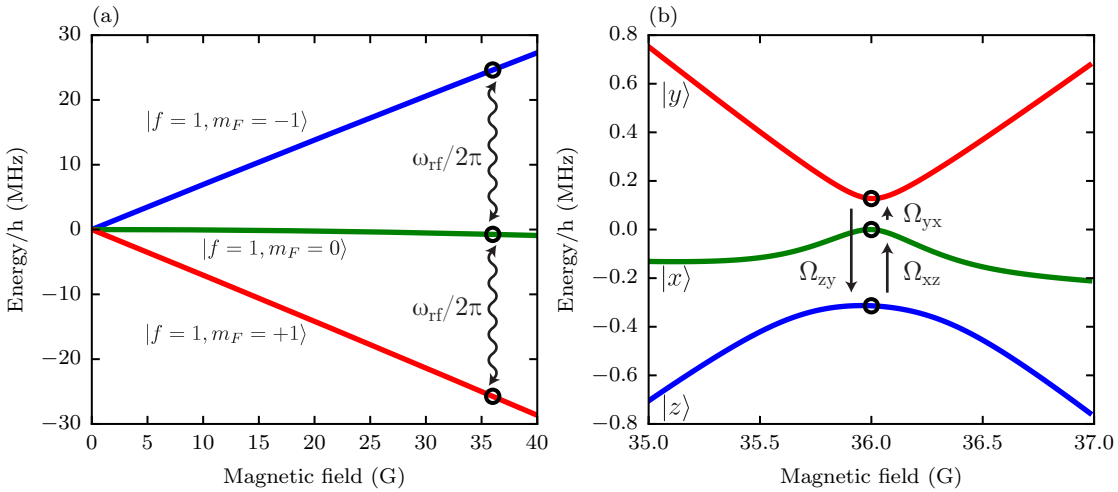

Figure 8.4: (a) Breit-Rabi calculation of the energy dependence of the magnetically sensitive spin-1 states. A rf magnetic field with amplitude 1 Gauss (G) applied within the $\mathbf{e}_x - \mathbf{e}_y$ plane links $|m_F\rangle$ states split by a dc field $B_{\rm dc} = 36$ G. (b) In the frame rotating with the oscillating magnetic field the coupling opens gaps between the rf eigenstates, $|x\rangle$, $|y\rangle$, and $|z\rangle$. These eigenstates are linked with resonant $\Omega_{y,x}$, $\Omega_{z,y}$, and $\Omega_{x,z}$+h.c. Raman coupling.

operator $\hat{D}^l$ which link pairs of rf eigenstates

$$\langle x|\,\hat{D}^y\,|z\rangle = i\hbar\sqrt{1-(\epsilon/\Omega_*)} \tag{8.22}$$

$$\langle y|\,\hat{D}^z\,|x\rangle = \frac{2\hbar(\Omega_{\rm rf}/\Omega_*)}{\sqrt{1+(\epsilon/\Omega_*)}} \tag{8.23}$$

$$\langle z|\,\hat{D}^x\,|y\rangle = \sqrt{2}\hbar(\epsilon/\Omega_*) \tag{8.24}$$

where we see that Ω_* sets a scale of energy. The matrix elements in Eq's (8.24) and (8.22) replace instances of $\mathbf{F}_x$ and $\mathbf{F}_y$ while Eq (8.23) replaces instances of $\mathbf{F}_z$.

8.3.2 Raman coupling rf eigenstates

In the previous section, we defined a relationship between the rf eigenstates $|x, y, z\rangle$, the $|X, Y, Z\rangle$ states of quantum chemistry and the spin states. This section finds the Hamiltonian for rf eigenstates that are linked by weak Raman coupling. With the rf rotating frame transformation, $\hat{U}_{\rm rf}$, from Eq. (8.19), the Raman optical coupling

from Eq. (6.3), and the Raman eigenstate coupling operator from Eq. (8.21) the effective coupling in the rf eigenbasis is

$$\begin{aligned}\hat{H}_{\text{eff}} = \sum_{\beta\neq\beta'} \Omega^{\perp}_{\beta,\beta'} \Big(& \hat{D}^x \cos\left[\Phi_{\beta,\beta'} + \omega_{\text{rf}} t + \gamma_{\text{rf}} + \xi_{\text{rf}} - \xi_{\beta,\beta'}\right] \\ & -\hat{D}^y \sin\left[\Phi_{\beta,\beta'} + \omega_{\text{rf}} t + \gamma_{\text{rf}} + \xi_{\text{rf}} - \xi_{\beta,\beta'}\right] \Big) \theta(\omega_{\beta,\beta'}) \\ & -\eta_{\beta,\beta'} \Omega^{||}_{\beta,\beta'} \hat{D}^z \sin\left[\Phi_{\beta,\beta'}\right]\end{aligned} \tag{8.25}$$

We apply the RWA to discard the terms that do not satisfy

$$-\hbar(\omega_{j,j'} \pm \hbar\omega_{\text{rf}}(\delta_{j,z} - \delta_{j',z})) = E_j - E_{j'} \tag{8.26}$$

$$\hbar(\omega_L - \omega_j) = E_j \pm \hbar\omega_{\text{rf}}\delta_{j,z} \tag{8.27}$$

where E_j are the rf eigenenergies. The upper (lower) sign choice corresponds to red (blue) detuning of the Raman relative to the rf. The term $\delta_{j,y}$ can be substituted for $\delta_{j,z}$ in Eq. (8.26): this yields smaller matrix elements. Substituting $\delta_{j,x}$ meanwhile, yields a matrix element of zero between $|y\rangle$ and $|z\rangle$, which is undesirable. This RWA is justified in the limit that $\Omega_{j,j'} \ll \omega_{j,j'}$. In practice this is set by Ω_{rf}.

Using the laser polarizations recommended in the previous section, essentially choosing axial $\mathbf{B}_{\text{eff}}$ for coupling between $|y\rangle$ and $|x\rangle$ and azimuthal for all other couplings, we may maximize the matrix elements. The resonant terms that correspond to these choices (polarization and red/blue detuning) yield an effective Hamiltonian

$$\begin{aligned}\hat{H}_{\text{eff}} = & \frac{\Omega^{\perp}_{z,y}}{2} \hat{D}^x_{z,y} e^{\mp i[\Phi_{z,y} + \omega_{\text{rf}} t + \gamma_{\text{rf}} + \xi_{\text{rf}} - \xi_{z,y}]} + \text{h.c.} \\ & -i\eta_{y,x} \frac{\Omega^{||}_{y,x}}{2} \hat{D}^z_{y,x} e^{i\Phi_{y,x}} + \text{h.c.} \\ & \mp i \frac{\Omega^{\perp}_{x,z}}{2} \hat{D}^y_{x,z} e^{\pm i[\Phi_{x,z} + \omega_{\text{rf}} t + \gamma_{\text{rf}} + \xi_{\text{rf}} - \xi_{x,z}]} + \text{h.c.}.\end{aligned} \tag{8.28}$$

The laser phases are physically unimportant $\bar{\gamma} = 0$ in this scheme but many

other quantities can contribute to bringing two eigenstates of the Hamiltonian in Eq. (8.28) to degeneracy. The overall phase (not limited to laser phase) must sum to zero for a three state system. These contributions include:

Excited state detuning The sign of u and by extension $\Omega_{\beta,\beta'}$ given in the exact form of the coupling section depends upon the detuning of the Raman lasers from the excited electronic states. For our chosen detuning u has a negative value whereas u can easily be positive for other detuning choices. In the case of negative u, the negative sign of the coupling amplitude can equivalently be represented as a π shift in the phase of each Raman coupling. Our three resonant Raman couplings give an overall 3π contribution to the total phase accumulated over a loop of coupling.

Orientation and phase of the rf coupling In Eqs. (8.26, 8.27) we required all of our Raman coupling frequency differences to be greater than (blue detuned from) or smaller than (red detuned from) $\omega_{\rm rf}$. When some Raman coupling frequency differences are red detuned and others blue detuned the rf phase $\gamma_{\rm rf}$ and the orientation of the rf magnetic field relative to the Raman $\mathbf{B}_{\rm eff}$ are physically relevant. Otherwise, $\gamma_{\rm rf}$ and $\xi_{\rm rf}$ cancel.

Detuning of the Raman relative to the rf For red detuned Raman $\pi/2$ is contributed to the phase; for blue detuned, $-\pi/2$.

Orientation of the Raman $\boldsymbol{B}_{\rm eff}$ $\mathbf{B}_{\rm eff}$ aligned axial or perpendicular to $B_{\rm dc}\mathbf{e}_z$ contribute phases differently. We proposed a situation where we have two perpendicular and one axially aligned $\mathbf{B}_{\rm eff}$. Because $\xi_{j,j'}$ and $\eta_{j,j'}$ are derived in Eqs. (6.16) from pseudovectors there is an equivalence when we change the sign of the polarization of each laser $\mathbf{e}_j \leftrightarrow -\mathbf{e}_j$. This change in sign alters the phase of the j'th laser which we have already established has no physical consequences. The contribution to the phase sum is $-\xi_{x,z}+\xi_{z,y}-\pi/2+\eta_{y,x}\pi/2 = -|-\xi_{x,z}+\xi_{z,y}|-\pi$. In our geometry this contribution is $-3\pi/2$ but it can

be continuously increased or decreased by changing the polarizations of the lasers.

The RWA Two of the Raman couplings may be expressed in terms of $\sin(\Phi_{j,j'})$ while between $|y\rangle$ and $|z\rangle$ the coupling is expressed in terms of $\cos(\Phi_{j,j'})$. The RWA decomposes each function and keeps only one of its complex exponentials. For our implementation the phase contributed is π.

Matrix elements of rf eigenstates As with the sign of u the complex matrix elements of Raman coupled rf eigenstates contribute to the total phase. In our specific scheme the normalized product of the matrix elements is $\langle z| D^{\perp}_{z,y} |y\rangle \langle y| D^{||}_{y,x} |x\rangle \langle x| D^{\perp}_{x,z} |z\rangle \rightarrow i$ and the phase contributed is $\pi/2$.

Altogether, the phase winding for a loop of coupling must be

$$\pm\frac{\pi}{2} + -\xi_{z,y} + \xi_{x,z} - \frac{\pi}{2} + \frac{\pi}{2}\eta_{y,x} = 0. \tag{8.29}$$

where the upper (lower) sign choice corresponds to red (blue) Raman detuning relative to ω_{rf}. Equation. (8.29) assumes that Raman detuning from the excited electronic states is red: otherwise there is an extra π. The phase winding can always be set to zero using one laser parallel with $B_{\mathrm{dc}}\mathbf{e}_z$ and two perpendicular lasers. The latter set of lasers should be perpendicular to one another as well. The desired Raman detuning relative to ω_{rf} is blue detuned whenever the Raman detuning from the excited electronic states is red, and blue detuned otherwise.

We may also determine the ratio $R_{j,j'}$ of additional power required to produce coupling in Eq. (8.28) between $|j\rangle$ and $|j'\rangle$ equivalent to

$$\Omega_{j,j'} = g_F u E_j E_{j'}/2\hbar g_J. \tag{8.30}$$

These ratios are

$$R_{z,y} = \frac{4\hbar}{A^{\perp}_{z,y}\sqrt{1 - A^{||2}_{z,y}}\left|\left\langle z\right|\hat{D}^{\perp}\left|y\right\rangle\right|} \tag{8.31}$$

$$R_{y,x} = \frac{2\hbar}{A^{||}_{y,x}\left|\left\langle y\right|\hat{D}^{||}\left|x\right\rangle\right|} \tag{8.32}$$

$$R_{x,z} = \frac{4\hbar}{A^{\perp}_{x,z}\sqrt{1 - A^{||2}_{x,z}}\left|\left\langle x\right|\hat{D}^{\perp}\left|z\right\rangle\right|}. \tag{8.33}$$

Adjusting the relative intensities of our beams we define a coupling strength Ω which equally couples each pair of rf eigenstates.

We obtain a simplified form for the Hamiltonian, equivalent to Eq. (8.3):

$$\hat{H} = \sum_{j,j'}\left\{\left[\frac{-\hbar^2\mathbf{k}^2}{2m} + E_j\right]\delta_{j,j'} + \hbar\Omega\exp\left(i[\Phi^{\mathrm{rf}}_{j,j'} - \bar{\gamma}/3]\right)\delta_{j-1,j'} + \mathrm{h.c.}\right\}\left|j\right\rangle\left\langle j'\right| \tag{8.34}$$

where $\Phi^{\mathrm{rf}}_{j,j'} = \mathbf{k}_{j,j'}\cdot\mathbf{x} - (\omega_{j,j'} \mp \omega_{\mathrm{rf}}(\delta_{j,z} - \delta_{j',z}))t$.

8.4 Floquet

It is a result of Floquet theory that differential equations with the form of the Schrödinger equation $i\hbar\partial_t\left|\psi(t)\right\rangle = \hat{H}_{\mathrm{eff}}(t)\left|\psi\right\rangle$ have solutions of the form

$$\left|\psi(t)\right\rangle = \sum_{\alpha} c_\alpha\left|\psi(t)\right\rangle_\alpha = \sum_{\alpha} c_\alpha\exp\left(-i\epsilon_\alpha t/\hbar\right)\left|\phi(t)\right\rangle_\alpha \tag{8.35}$$

when the Hamiltonian is periodic with time $H_{\mathrm{eff}}(t) = H_{\mathrm{eff}}(t+T)$. For constant wave (CW) optical illumination the Floquet states are $\left|\psi(t)\right\rangle_\alpha = \exp\left(-in_\alpha\omega t\right)\left|\phi\right\rangle_\alpha$ where n is the set of integers and each $\left|\phi\right\rangle_\alpha(t) = \left|\phi\right\rangle_\alpha(t+T)$ map to the vector of rf eigenstates. Because our Hamiltonian can be exactly decomposed into terms proportional to complex exponentials $\left|\phi\right\rangle_\alpha$ is time independent. We decompose our Hamiltonian into an infinite sum of Floquet states and apply a rotating frame transformation to each Floquet state: this makes the Floquet Hamiltonian stationary in

time while also contributing an extra term $n_\alpha \hbar\omega_\alpha \left|\psi\right\rangle_\alpha \left\langle\psi\right|_\alpha$.

Our Hamiltonian in Eq. (8.25) has two time periodicities, there are three Raman frequencies but using Eqs. (8.26, 8.27) we may always determine the third frequency difference given the two others. In the rotating frame the Floquet Hamiltonian becomes

$$\hat{H}_{\text{Fl.}} = \sum_{l,m} \Bigg\{ \left[\hat{H}_0 + (n_l \hbar\omega_{x,z} + n_m \hbar\omega_{y,x}\hat{1}\right] \delta_{l,l'}\delta_{m,m'} \tag{8.36}$$

$$+\frac{\Omega^{\perp}_{x,z}}{2}\hat{D}^{\perp}\delta_{l-1,l'}\delta_{m,m'}e^{i[-\gamma_{x,z}+\gamma_{\text{rf}}-\xi_{x,z}+\xi_{\text{rf}}]} \tag{8.37}$$

$$+\frac{\Omega^{||}_{y,x}}{2}\hat{D}^{||}\delta_{l,l'}\delta_{m-1,m'}e^{i[-\gamma_{y,x}-\frac{\pi}{2}+\frac{\pi}{2}\eta_{y,x}]} \tag{8.38}$$

$$+\frac{\Omega^{\perp}_{y,z}}{2}\hat{D}^{\perp}\delta_{l-1,l'}\delta_{m-1,m'}e^{i[-\gamma_{y,z}+\gamma_{\text{rf}}-\xi_{y,z}+\xi_{\text{rf}}]} + \text{h.c.}\Bigg\} \left|\psi\right\rangle_{l,m} \left\langle\psi\right|_{l',m'} \tag{8.39}$$

where $\hat{1}$ is the identity in the rf eigenbasis and the operators $\hat{H}_0$, $\hat{D}^{\perp}$ and $\hat{D}^{||}$ are 3×3 matrices of spin that operate on $\left|\phi\right\rangle_{l,m}$. These are

$$\hat{H}_0 = \begin{pmatrix} \left(\frac{\hbar^2(\boldsymbol{q}-\boldsymbol{K}_y)^2}{2m}+E_y\right) & 0 & 0 \\ 0 & \left(\frac{\hbar^2(\boldsymbol{q}-\boldsymbol{K}_x)^2}{2m}+E_x\right) & 0 \\ 0 & 0 & \left(\frac{\hbar^2(\boldsymbol{q}-\boldsymbol{K}_z)^2}{2m}+E_z\right) \end{pmatrix} \tag{8.40}$$

$$\hat{D}^{\perp} = \begin{pmatrix} 4(\Omega_{\text{rf}}/\Omega_*) & i\sqrt{1+(\epsilon/\Omega_*)} & \sqrt{2}(\epsilon/\Omega_*) \\ -i\sqrt{1+(\epsilon/\Omega_*)} & 0 & i\sqrt{1-(\epsilon/\Omega_*)} \\ \sqrt{2}(\epsilon/\Omega_*) & -i\sqrt{1-(\epsilon/\Omega_*)} & -4(\Omega_{\text{rf}}/\Omega_*) \end{pmatrix} \tag{8.41}$$

$$\hat{D}^{||} = \begin{pmatrix} 0 & \frac{2(\Omega_{\text{rf}}/\Omega_*)}{\sqrt{1+(\epsilon/\Omega_*)}} & 0 \\ \frac{2(\Omega_{\text{rf}}/\Omega_*)}{\sqrt{1+(\epsilon/\Omega_*)}} & 0 & \frac{1}{\sqrt{2}}\sqrt{1-(\epsilon/\Omega_*)} \\ 0 & \frac{1}{\sqrt{2}}\sqrt{1-(\epsilon/\Omega_*)} & 0 \end{pmatrix}. \tag{8.42}$$

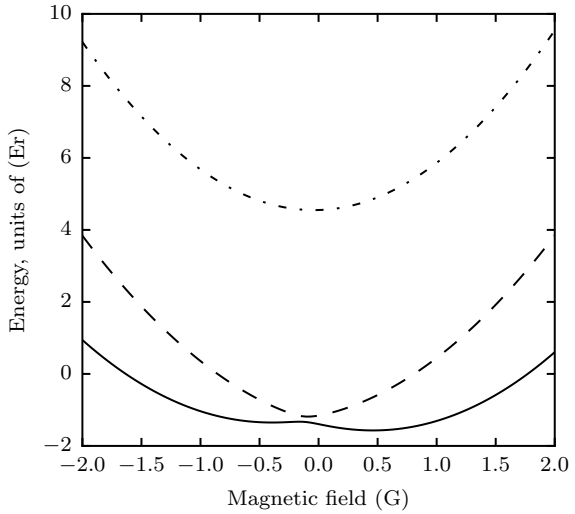

Figure 8.5: Cross-sections along q_x for Floquet bands calculated using rf basis states. $\Omega_{\rm rf} = 65E_R$, $\epsilon = -54E_R$, $\delta = 0E_R$, $\bar{\gamma} = 0$, $\Omega = 2E_R$, single-photon recoil is k_R and all Raman beams are perpendicular. These quantities are defined in the preceding sections. The least (solid) and next least (dashed) energetic states are closely spaced while the most energetic (dashed dotted) state is separated by 3Ω when $\bar{\gamma} = 0$. The Dirac point is slightly displaced from the q_x axis at these laser powers due to inter Floquet band coupling but adjusting the balance of laser intensities can return the Dirac point to the origin.

Figure (8.5) depicts a set of three dispersions that are tiled in quasienergy (not shown). The Raman laser phases $\gamma_{y,z} = \gamma_{x,z} + \gamma_{y,x}$ and the rf phase $\gamma_{\rm rf}$ cancel in the closed loop picture, but have reappeared here in the Floquet picture. There is a Dirac point where the solid and dashed dispersions meet when $\bar{\gamma} = 0$. When $\Omega^{\perp}_{j,j'}$ and $\Omega^{||}_{j,j'}$ exceed $2E_R$ the location of the Dirac point becomes mobile, indicating that band dependent coupling modifies the effective power balance. Although mobile, the Dirac point remains closed so long as the phase condition in the previous section is met.

8.5 Proposed preparation of experiment

8.5.1 Coupling with rf

We apply $B_{\rm dc}$ along $\mathbf{e}_z$ with an amplitude necessary to produce a $h \times 30$ MHz linear Zeeman splitting between the ground hyperfine states of ^{87}Rb. In the presence of this magnetic field the quadratic Zeeman shift is $\approx$ h $\times$ 250 kHz. We subsequently apply a 30 MHz rf field magnetic field polarized perpendicular to the biasing field.

The matrix elements in Eqs. (8.22, 8.24, 8.23) grow with $|\epsilon|/\Omega_{\rm rf}$. Simultaneously, the gap between $|x\rangle$ and $|y\rangle$ asymptotically approaches zero, which limits the total Raman coupling.

We compose a simple quantity that multiplies our rf eigenstate matrix elements with the ratio of the gap between the $|x\rangle$ and $|y\rangle$ and $\Omega_{\rm rf}$

$$\frac{|\Delta^{\rm rf}_{y,x}|}{\Omega_{\rm rf}} |\langle x| \hat{D}^{\perp} |z\rangle \langle z| \hat{D}^{\perp} |y\rangle \langle y| \hat{D}^{||} |x\rangle|^{1/3}/\hbar \tag{8.43}$$

where $\Delta^{\rm rf}_{y,x} = \frac{1}{2}(\epsilon + \sqrt{\epsilon^2 + 4\Omega^2_{\rm rf}})$. Maximizing this metric we find that $-0.6 < \epsilon/\Omega_{\rm rf} < -1.1$ strikes the best balance between Raman coupling and rf coupling.

A coupling dependent shift in the location of the Dirac point (see the Floquet section) occurs when the Raman coupling is not $\hbar\Omega \ll \Delta_{y,x}$ or when $2E_R \ll \Delta_{y,x}$. $2E_R$ is the typical energy spacing between the ground and first excited eigenenergies at the ground state minima.

8.5.2 Laser frequencies

We suggest a single source for the Raman light whose coherence length exceeds the path-length stretching from the laser head to the atoms. This experiment can benefit from up to $\approx$ 1 W of total laser power. It is suggested that the 'magic' frequency of $f_L = 390$ THz be used with ^{87}Rb so that the scalar light shift can be eliminated. Then, the Raman lasers do not act as a trapping potentials. In this

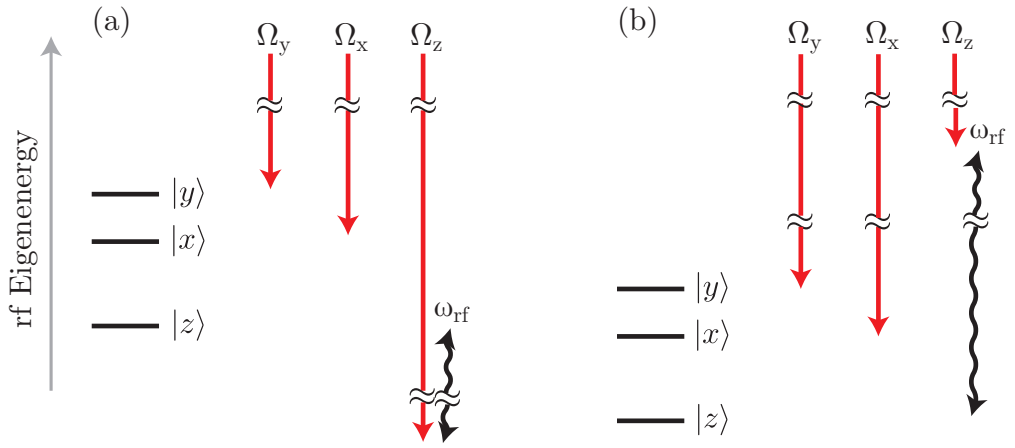

Figure 8.6: Level diagram for Raman coupling rf eigenstates. (a) Here, $|\omega_{x,z}|$, $|\omega_{y,z}| > \omega_{\mathrm{rf}}$ and hence the Raman is blue detuned relative to the rf. (b) It is possible to red detune the Raman relative to the rf and add π phase to $\bar{\gamma}$.

case, $\Omega_{j,j'}$ is always negative. Strict linear polarization for all the Raman beams eliminates single-beam vector light shifts (though large Ω_{rf} also reduces the impact of these).

We propose the use of a single 110 MHz and two 80 MHz center frequency AOMs to control the intensity and frequency of each Raman laser. The corresponding Raman frequencies are

$$\omega_j = 2\pi\left(f_L \pm 80\ \mathrm{MHz}\right) \pm \omega_{\mathrm{rf}}\delta_{j,z} \mp E_j/\hbar \tag{8.44}$$

As shown in Fig. (8.6), the upper branch of Eq. (8.44) corresponds to Raman frequency differences $\omega_{j,j'} < \omega_{\mathrm{rf}}$ for all $j, j' \in \{x, y, z\}$ while the lower branch switches the inequality, these correspond to red and blue detuning respectively. Switching from blue to red detuning engineers a π phase difference in Eq. (8.29). This is achievable by switching from using the +1 order of all the AOMs to using the -1 order. In practice, the desired Raman detuning is blue relative to ω_{rf} and red relative to the excited electronic states.

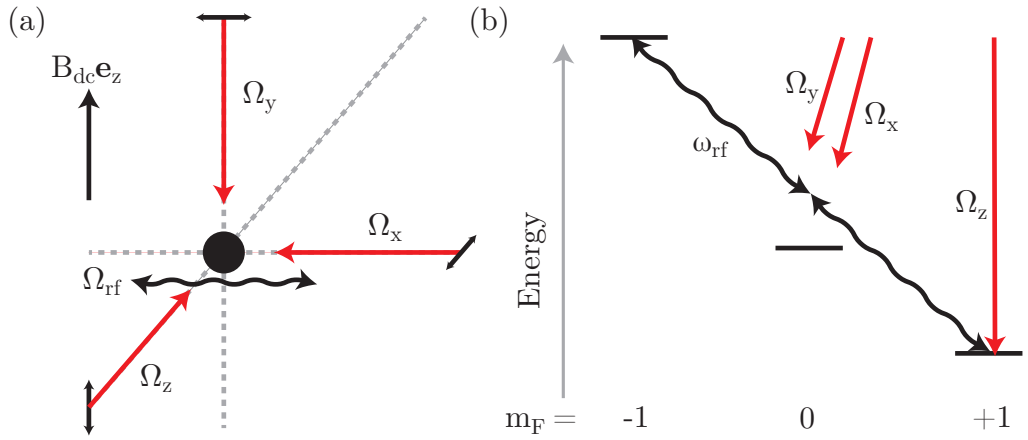

Figure 8.7: (a) All three lasers are linearly polarized. The orientation of the wavevectors for all lasers are mutually perpendicular. The polarizations for all the lasers are also mutually perpendicular. The laser labeled Ω_z couples both $|y\rangle$ and $|x\rangle$ to $|z\rangle$ and is the only laser that is π polarized. The rf coupling is a 30 MHz oscillating magnetic field applied transverse to the quantizing dc magnetic field $B\mathbf{e}_z$. (b) The frequency of Ω_z is offset by 30 MHz (nearly the rf frequency) from that of Ω_x and Ω_y.

8.5.3 Geometry

While the rf must be transverse to $B_{\rm dc}\mathbf{e}_z$ the phase and orientation of this field is physically unimportant to this laser scheme.

Three lasers produce all the Raman couplings as shown in Fig. (8.7)a. The polarization geometry is primarily limited by the requirement of Eq. (8.29). Two pairs of Raman lasers have $\mathbf{B}_{\rm eff}$ that are essentially perpendicular to $\mathbf{e}_z$, the other pair is aligned or anti-aligned with $\mathbf{e}_z$. The azimuthal projections of each Raman pair's $\mathbf{B}_{\rm eff}$ on the plane orthogonal to $\mathbf{e}_z$ should themselves be perpendicular. This is most easily accomplished by having one laser co-aligned or anti-aligned with $B_{\rm dc}\mathbf{e}_z$ and two other lasers perpendicular to both $\mathbf{e}_z$ and each other. Similarly, one of the two lasers that is perpendicular to $\mathbf{e}_z$ should be π polarized while the polarizations of the other two lasers are orthogonal to the first laser and each other. The π polarized laser couples to $|z\rangle$. It does not matter to which state each of the other two lasers couple.

8.5.4 Power balance

We may determine the ratio of additional intensity necessary to couple all of the rf eigenstates with equal coupling, $\Omega = g_F u I_0 / c\epsilon_0 \hbar g_J$. The coupling between rf eigenstates is alternatively given by $\Omega = g_F u \sqrt{I_j I_{j'}} / R_{j,j'} c\epsilon_0 \hbar g_J$ where ϵ_0 is the permittivity of free space, and c is the speed of light in vacuum. Using Eqs. (8.32, 8.31, 8.33) the ratio of additional intensity is

$$\frac{I_x}{I_0} = \frac{R_{x,y} R_{z,x}}{R_{y,z}} \tag{8.45}$$

$$\frac{I_y}{I_0} = \frac{R_{y,z} R_{x,y}}{R_{z,x}} \tag{8.46}$$

$$\frac{I_z}{I_0} = \frac{R_{z,x} R_{y,z}}{R_{x,y}} \tag{8.47}$$

For $\epsilon/\Omega_{\mathrm{rf}} = -0.8$ these ratios of additional intensity are $I_x/I_0 = 1.1$, $I_y/I_0 = 5.4$ and $I_z/I_0 = 21.5$.

8.5.5 Sources of noise

In alkali atoms, dc magnetic field fluctuations often limit the long-term stability of an experiment. Environmental noise in a lab tends to scale as 1/frequency and the energy splittings of alkali ground states depend upon the dc magnetic field present at the atoms. The rf eigenstates are largely insensitive to magnetic field fluctuations: $\Delta E_j \approx (g_F \mu_B \Delta B)^2 / 2\hbar\Omega_{\mathrm{rf}}$. With $\hbar\Omega_{\mathrm{rf}} = h \times 200$ kHz rf coupling amplitude the $h \times 1$ kHz Zeeman splitting amplitude fluctuations of a lab without active field control corresponds to $\Delta E_j \approx 5$ Hz. Hence, the rf eigenstates become engineered clock states.

The proposed experiment is linearly sensitive to changes in rf coupling amplitude Ω_{rf} and Raman coupling amplitude $\Omega_{\beta,\beta'}$. In general, laser and rf intensity may be kept stable to one part per thousand. The parameters of this experiment were deliberately chosen so that phase noise from the lasers and rf are irrelevant.

8.6 Conclusion

This proposal produces Rashba SOC with the ground atomic states of ^{87}Rb. This system is less susceptible to collisional deexcitation of many-body states and expands the lifetime of atoms in the spin-orbit coupled system from several milliseconds to hundreds of milliseconds as compared to techniques that appreciably populate the $f = 2$ manifold. Furthermore we have exchanged technical challenges and expense associated with producing phase locked lasers separated by many GHz in frequency with the challenge of producing hundreds of kHz of rf coupling with part per thousand amplitude control.

Chapter A: Vacuum management

A.1 Introduction

This appendix introduces our Bose-Einstein condensate machine. We proceed to introduce the vacuum system and name the component processes and systems necessary to produce Bose-Einstein condensation; for each of these, we describe the theory behind its function followed by its specific implementation in our experiment.

A.2 Summary of the vacuum apparatus

Figure A.1 illustrates the underlying vacuum framework of the experiment. In the text of the figure we describe the ancillary devices such as ion pumps that interface with this framework.

Our apparatus stores two different alkali metals in separate reservoirs. These reservoirs are wrapped in woven copper and fiberglass strips that heat to several hundred degrees Celsius when connected to 60 Hz AC current from the wall.

Dual species oven. 5 grams of Rubidium-87 ($Rb87$) and 2 grams of Lithium-6 (^{6}Li) are placed in separate stainless steel (SS) reservoirs. These produce a steady state atomic beam along the length of Fig. A.1.

Oven chamber. In this chamber the in-vacuum shutter prevents or allows the atomic beam to reach the glass cell (where we do our science). Uncollimated or blocked Rb vapor is also pumped.

8-way flange. This chamber is separated from the oven chamber by a narrow tube. Additional pumps are attached to this flange to ensure better vacuum than in the vacuum chamber. This chamber is separated from the rest of the experiment by a valve.

Zeeman slower. This is a magnetic coil arrangement surrounding a vacuum tube 70 cm in length which provides a position dependent shift of the magnetically sensitive internal magnetic states. This shift compensates for the evolving doppler shift of the laser light relative to the atoms as the atoms are optically slowed over the length of the slower.

Transverse cooling. Spontaneous emission events induce a random walk in momentum which accumulate over the length of the slower. The resulting transverse extent of the atomic beam appears to bloom at the end of the slower. An optical molasses at the end of the slower can be used to refocus the slowed atoms towards the center of the glass cell. We have the viewports necessary to transverse cool but we have yet not found it necessary.

Glass cell. The glass cell is outfitted with a metal bellows to reduce shear induced by clamping the apparatus on either side of the cell. In our experiment the quadrupole coils, with the option of switching to a Helmholtz configuration, are placed much closer to the atoms than would be possible in a typical chamber.

Quadrupole coils Each coil is composed of 25 turns, five layers of five turns, of square copper tubing with an inner channel for water for cooling. The top surface of each coil is approximately 0.57 in. from the center of the glass cell. These magnetically trap our atoms during one of the stages of the cooling process.

Vacuum after the glass cell. Here there are additional pumps and pressure gauges.

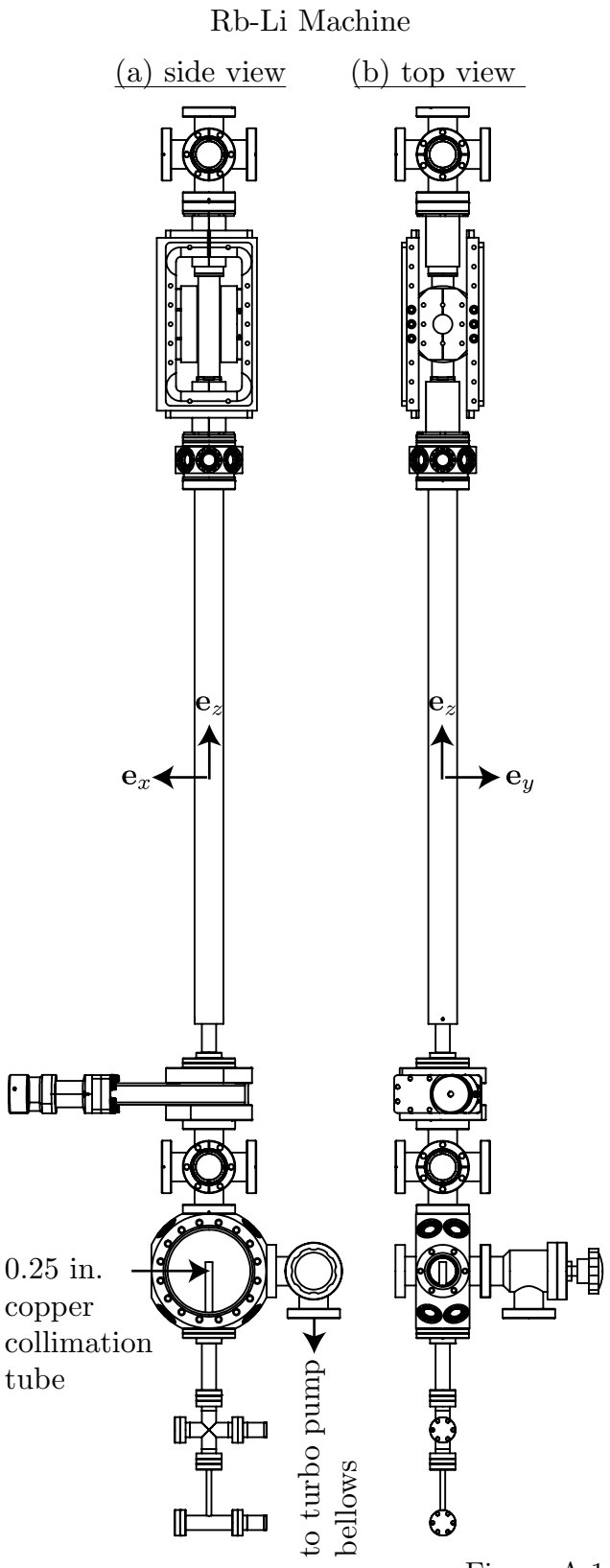

description
Ti Sub. pump ($\mathbf{e}_z$)
ion guage (-$\mathbf{e}_y$)
ion pump ($\mathbf{e}_x$)
shutter feedthrough (-$\mathbf{e}_x$)
glass cell (w bellows, $\pm\mathbf{e}_z$)
quad coils ($\pm\mathbf{e}_x$)
quad coil holders ($\pm\mathbf{e}_x$)
MOT
BEC
transverse cooling for Li
Zeeman slower for Rb
all-metal valve
ion pump ($\mathbf{e}_x$)
Ti Sub. pump (-$\mathbf{e}_x$)
0.25 in. copper feedthrough
oven shutter (in vacuum)
cold cup feedthrough ($\mathbf{e}_x$)
50 l/s ion pump (-$\mathbf{e}_y$)
mixing chamber nozzle
^{6}Li Oven
Rb nozzle
^{87}Rb Oven

Figure A.1

A.3 Production of the atomic beam and vacuum management

A.3.1 The ovens

5 grams of Rubidium-87 ($Rb87$) and 2 grams of Lithium-6 (^{6}Li) are placed in separate stainless steel (SS) reservoirs. These reservoirs are wrapped with strips of woven copper in fiberglass, commonly called heater tape, that heat to several hundred degrees Celsius when connected to the wall. The reservoirs are connected to one another as shown in Fig. A.2. We wrapped the Rb reservoir, Rb nozzle, Li reservoir and Li nozzle with electrically independent lengths of heater tape. Because SS is a poor thermal conductor we wrap this region with aluminum foil to better distribute the heat. Feedback on the temperature is accomplished using an Omega `CNi3233` temperature controller which periodically interrupts current flow to the heater tape. A variable ac transformer (variac) adjusts the voltage drop across each length of heater tape, allowing us to tune the gain of the temperature feedback.

For our reservoir temperature of 110 C the vapor pressure of ^{87}Rb is $\sim 4 \times 10^{-4}$ torr. [112]. Meanwhile, at 125 C the vapor pressure of ^{6}Li is negligible [112]; no Lithium is present in any of the experiments described in this thesis. The temperature of the Rb nozzle is maintained at 400 C to prevent the narrow tube from clogging. This nozzle is a bottleneck for mass transport of ^{87}Rb in our system. The Li nozzle is kept at a substantially lower temperature $\sim$ 140 C. This 1/4" outer diameter (OD), 0.186" inner diameter (ID) and 2" long copper collimation tube serves as the primary collimation mechanism of our atomic beam.

A.3.2 The oven chamber

The copper collimation tube intrudes into the volume enclosed by a cup-shaped copper surface maintained anywhere between -15 C and -40 C (cold cup). The cold cup is connected with an insulated copper feedthrough to a water-cooled thermo-

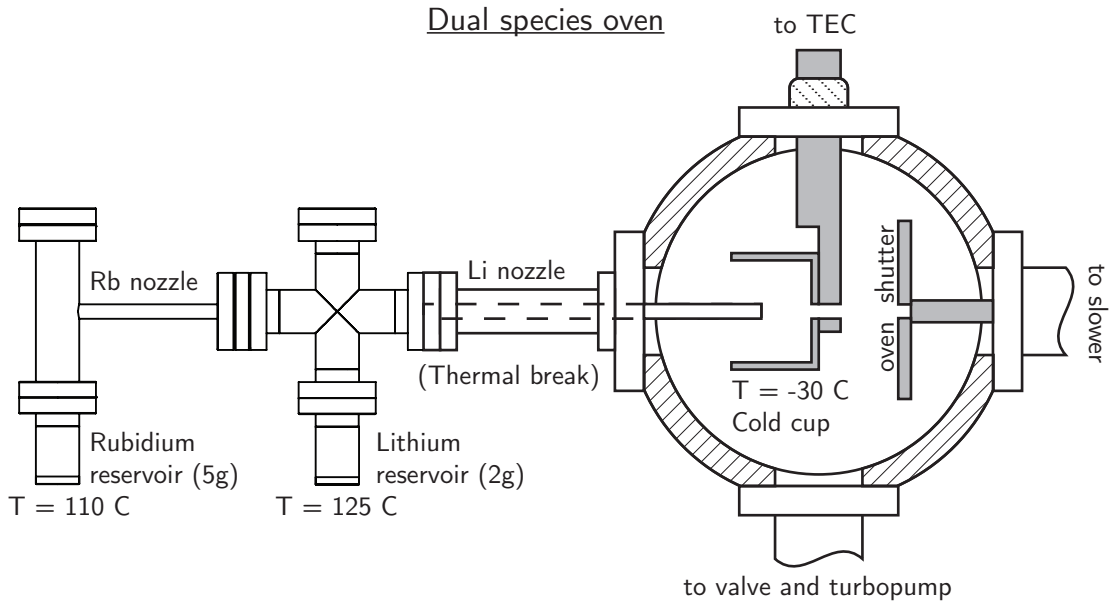

Figure A.2: This diagram shows the alkali reservoirs and the low vacuum oven chamber.

electric cooler (TEC). The hot side of the TEC is water cooled. The cold cup is an added pumping surface for our ^{87}Rb which is known to damage ion pumps. This oven configuration was the subject of Ref. [113].

A `Toshiba` hard drive shutter was repurposed to act as an in-vacuum (oven) shutter and placed at the end of a 1 in. long 3/8 in. OD copper feedthrough. `Kapton` wires soldered to an electrical feedthrough allowed actuation of the shutter from outside of vacuum. This shutter and the copper feedthrough serve as one of two breaks between the low vacuum and high vacuum portion of the experiment. The closing of the oven shutter terminates loading of the magneto-optical trap. During sub-Doppler cooling and evaporation to quantum degeneracy the presence of a thermal atomic beam causes heating. This shutter eliminates that problem.

The oven chamber also connects to an all-metal valve and an ion gauge. This valve is the only location where a roughing pump/turbopump can be attached to the apparatus.

Into the diagram in Fig. A.2 is a 50 l/s ion pump. Ion pumps effectively pump most atomic species at high vacuum. They are also low maintenance, have no moving parts and can draw as little as 1 μA at 10 kV. Out of the diagram is a

simple 6 in. diameter viewport.

A.4 Transition to high vacuum

Immediately above the oven chamber in Fig. A.1 is a custom 8-way flange (shown is a six-way cross with the same dimension along $\mathbf{e}_z$) to which we attached an ion pump in the $\mathbf{e}_x$ side of the flange and a Titanium-sublimation (Ti-sub) pump in the $-\mathbf{e}_x$ side of the flange. The Ti-sub pump coats nearby surfaces with a getter that absorbs hydrogen. Hydrogen is one of the few molecules that is poorly pumped by ion pumps.

The remaining four ports are capped with viewports and are oriented 90 degrees from one another.

In the $\mathbf{e}_z$ direction the 8-way flange is connected to a `Viton` o-ring valve. This valve allows us to break vacuum in all of the vacuum elements discussed thus far without impacting the vacuum of the rest of the apparatus.

A.5 Zeeman slower and vacuum

The 0.71 cm length of the Zeeman slower acts as an additional differential pumping tube. An additional ion pump and Ti-sub pump after the glass cell is necessary to ensure good vacuum at the glass cell.

Chapter B: Frequency control

Although it is possible to build or purchase lasers with narrow linewidths < 200 kHz in the lab environment, with day to day variation in the temperature and humidity, it is impractical to expect the center frequency of a laser to remain tuned to an atomic transition within the typical 6 MHz atomic linewidth. Our lab uses saturated absorption spectroscopy on a magnetically shielded room temperature vapor cell of ^{85}Rb to provide a signal with which we apply electrical feedback on the frequency of the laser.

With standard absorption spectroscopy of a room temperature vapor cell laser weak resonant laser light is passed through the vapor cell and captured by a photodiode (PD). As the frequency of the laser light is scanned, dips in intensity (relative to a portion of the laser light which does not pass through the PD) occur when the light is resonant with an allowed transition of some of the atoms in the atomic vapor. For ^{85}Rb at room temperature 1/e fraction of the atoms have a speed > 170 m/s. For a ^{85}Rb atom moving counter or with the propagation of the laser at $v = 200$ m/s the doppler shift $kv/2\pi \approx 200$ MHz vastly exceeds the typical ~ 6 MHz linewidth and blurs together the excited electronic ($^5P_{3/2}$) hyperfine manifolds. For this reason, simple absorption spectroscopy does not provide the necessary accuracy to lock our lasers for velocity selective optical manipulation of atoms or for imaging at low temperatures.

Instead, let us consider a "pump" laser with an intensity not too much greater than 2 mW/cm^2 where resonant illumination with at least 2 mW/cm^3 results in nearly equal populations of atoms in both their ground and excited electronic states.

In this case, the transition is considered to be "saturated" because further increases in optical intensity only modestly increase the population of atoms that are in their excited states. In a room temperature vapor cell the pump laser saturates the fraction of atoms which have a transition that is Doppler shifted into resonance with the laser. The velocities which produce the necessary Doppler shift are called a velocity class. Several atomic transitions corresponding to different excited electronic hyperfine manifolds, each with a distinct resonant velocity class, may be present simultaneously in the vapor.

Now, we add a "probe" $\ll 2$ mW/cm^2 laser that copropagates with respect to the pump laser. In a range of frequencies within the atomic natural linewidth about the pump laser's center frequency very little of the probe laser light is absorbed: the pump laser burned a hole in the atomic vapor for the probe laser. The resonance conditions for a pump and probe lasers with both frequencies ω_p and ω and wavevectors $\mathbf{k}_p$ and $\mathbf{k}$ are

$$\omega_p - \omega = (\mathbf{k}_p - \mathbf{k}) \cdot \mathbf{v} \tag{B.1}$$

$$2\omega_0 = (\omega_p + \omega) + (\mathbf{k}_p + \mathbf{k}) \cdot \mathbf{v} \tag{B.2}$$

where ω_0 is the frequency at an atomic resonance. When $\omega \neq \omega_p$, the atomic vapor absorbs the light just as it would with standard absorption spectroscopy.

When $\mathbf{k} = -\mathbf{k}_p$, the probe and pump lasers resonantly illuminate the same velocity class of atoms when $\omega_0 = (\omega_p + \omega)/2$. There are also "crossover resonances" corresponding to a velocity class where the pump resonantly couples to one excited hyperfine manifold while the probe resonantly couples to a different excited hyperfine manifold. This "V" type coherent coupling enhances the transparency of the vapor to the probe light. We label the distinct atomic transitions ω_0 and ω_0'. Likewise, a crossover resonance couples to two velocity classes which correspond to an

interchange of ω_0 and ω_0':

$$\omega_0 + \omega_0' = \omega_p + \omega \tag{B.3}$$

$$2(\omega - \omega_p) = (\mathbf{k}_p - \mathbf{k}) \cdot (\mathbf{v} + \mathbf{v}') \tag{B.4}$$

$$2(\omega_0 - \omega_0') = (\mathbf{k} - \mathbf{k}_p) \cdot (\mathbf{v} - \mathbf{v}'). \tag{B.5}$$

When the center frequency is scanned there are also "crossover" resonances corresponding to the overlap of two resonant velocity classes of the probe laser with the saturated velocity classes of the pump laser. We lock our lasers to the $\left|{}^5S_{1/2}, f = 3\right\rangle \leftrightarrow \left|{}^5P_{3/2}, f = 2\right\rangle$ to $\left|{}^5S_{1/2}, f = 3\right\rangle \leftrightarrow \left|{}^5P_{3/2}, f = 4\right\rangle$ crossover resonance of ^{85}Rb.

B.1 Doppler-free spectrum

Figure B.1 depicts the transition energies for all the ${}^5S_{1/2}$ to ${}^5P_{3/2}$ transitions in ^{87}Rb and ^{85}Rb. Four groupings of absorption features are observed corresponding to differences in isotope and the ground electronic hyperfine level. We lock to a feature in the second least energetic grouping corresponding to transitions in ^{85}Rb from the $f = 3$ ground electronic hyperfine manifold. Within this grouping the $f' = 3$ to $f' = 4$ crossover resonance is the sharpest feature: we lock to this.

B.2 The saturation absorption optical setup

A `New Focus Vortex II series laser` outputs 40 mW of light at 780.24 nm. We call this laser the "master" laser. In Fig. B.2 we show both a schematic and picture of the saturation absorption setup for locking to ^{87}Rb. Light reflected off a 4% pickoff immediately following the optical isolator becomes the probe light. About 60% of the remaining light is deflected by a polarizing beam cube (PBS) into a double passed AOM configuration; the light frequency shifted a total of 160 MHz by the AOM

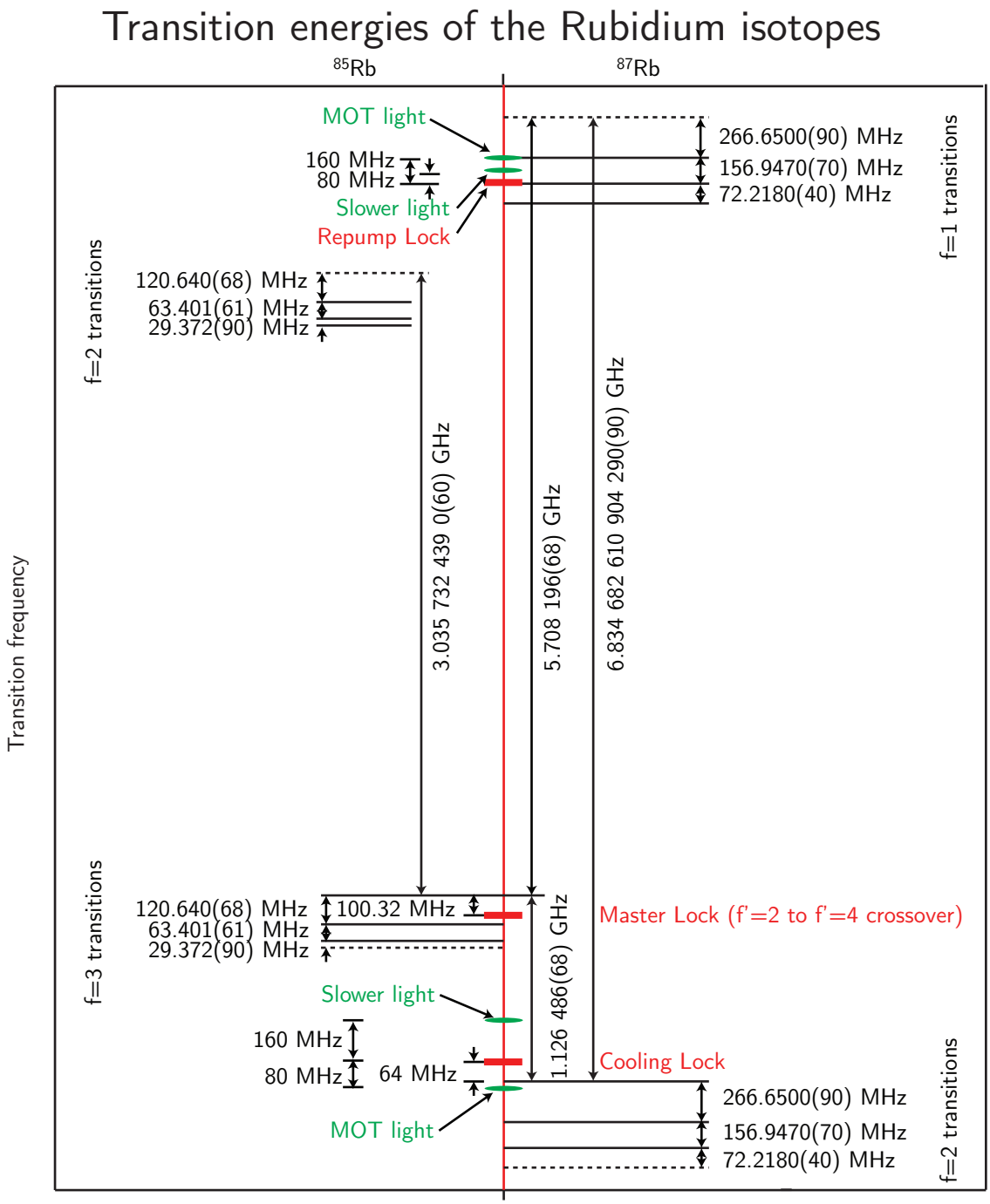

Figure B.1: Level diagram with exploded view of transition energies relative to the ground state. The ground electronic state hyperfine manifold coupled by the light is denoted (but not shown) next to each grouping of (horizontal black) transition energies. The red rectangles on the vertical centerline indicate optical frequencies input into the beatnote lock. Green ovals show the frequency after the light is double passed through an AOM.

becomes the pump light. The pump and the probe are made to counterpropagate and subsequently the probe light is measured by a PD. The light that is undeflected by the PBS continues through another optical isolator and is injected into a fiber mixer that equally redistributes the light from each of four inputs into four outputs. Using a function generator we apply a sinusoidal dither to the frequency of the rf

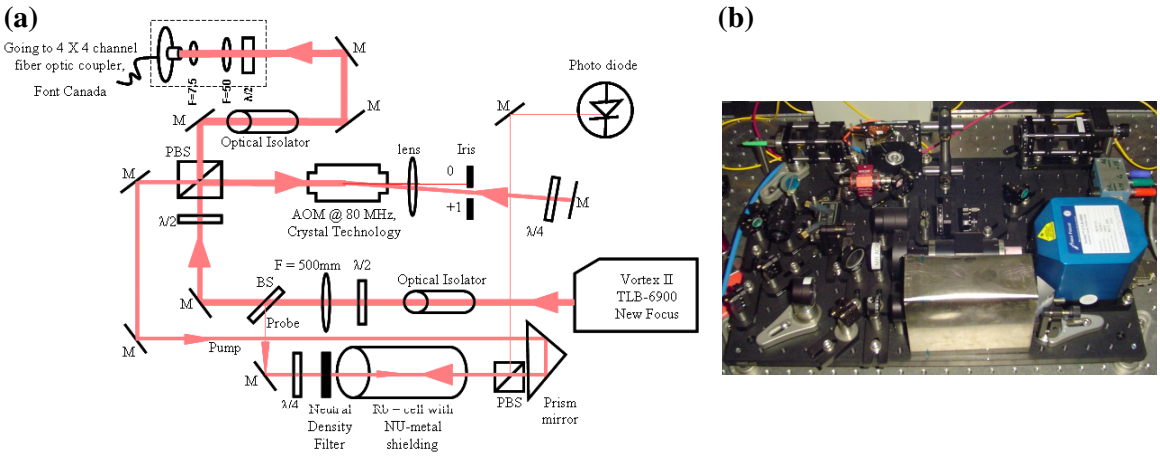

Figure B.2: a) Optical schematic of saturation absorption setup of master laser. b) Picture of saturation absorption setup. Reproduced from Rb-Li manual. Original author: Subhadeep De.

drive of the double passed AOM. The resulting frequency modulation of the probe light produces an oscillation in the probe intensity from which a lock-in amplifier can produce an error signal that is a function of the derivative of the saturation absorption spectrum. Zeros in the error signal correspond to peaks and troughs in the absorption spectrum. PID feedback on the piezo and current of the master laser may then be used to lock the center frequency of the laser to the desired trough in the saturation absorption spectrum. As shown in Fig. B.3 the dither, lock-in amplifier and PID feedback were accomplished using a home-built FPGA-based module (see the appropriate chapter of the thesis of Ryan Price).

B.3 Beatnote lock

Our cooling and trapping optical system is comprised of two lasers additional to the master laser. The "cooling" laser couples from the $f = 2$ electronic ground

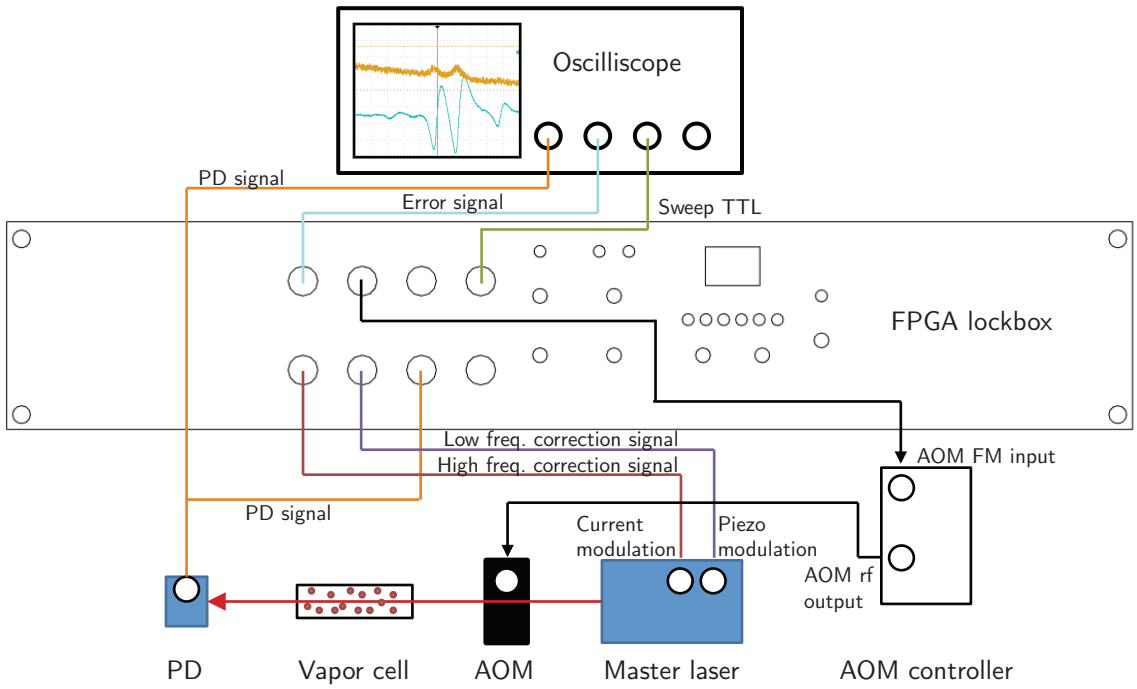

Figure B.3: Schematic of FPGA control of laser center frequency based on a PD absorption signal. Diagram adapted from the Rb-Li lab manual with permission from Ryan Price.

state of ^{87}Rb to its $^5P_{3/2}$ electronic excited states. Meanwhile, the "repump" laser couples from the $f = 1$ electronic ground state to the $^5P_{3/2}$ electronic excited states of ^{87}Rb. Using separate lasers for the 6.8 GHz separated optical frequencies is considered economical because frequency shifters (AOMs or EOMs) at microwave frequencies have low efficiencies. Some light from each of these lasers is coupled to a 4×4 fiber optic coupler: the each of the four outputs of the coupler evenly mixes all of the inputs. The light from one of these outputs is measured by a high speed PD. The PD signal is split in two: one signal passes through a series of high pass filters while the other signal passes through a series of low pass filters. An error signal is generated using a phase locked loop by comparing by comparing the beatnote frequency difference between a sinusoidal signal generated by a computer programmable `Novatech Instruments model 409B` direct digital synthesizer and the filtered signal of the PD. The error signal generated by the high pass filter is

Name	Frequency
Master frequency	384.229101 THz
Master wavelength	780.24402 nm
Master AOM	80 MHz(160 MHz)
Master-cooling Beatnote	0.9162 GHz
Cooling frequency	384.2281848 THz
Cooling wavelength	780.24588 nm
Cooling MOT AOM	−40 MHz(−80 MHz)
Cooling slower AOM	80 MHz(160 MHz)
Repump-master Beatnote	5.4130 GHz
Repump frequency	384.234514 THz
Repump wavelength	780.23303 nm
Repump MOT AOM	80 MHz(160 MHz)
Repump slower AOM	40 MHz(80 MHz)

Table B.1: Listing of beatnote frequencies and AOM rf drive frequencies (double passed frequency shift). A negative sign on the AOM frequency corresponds to a downshift in the frequency of the light. Errors on AOM frequencies are $\sim$ 10 Hz. Errors on the desired laser wavelength is approximately $\sim$ 100 kHz.

used to lock the repump laser while the error signal generated by the low pass filter is used to lock the cooling laser. Refer to Table B.1 for the beatnote frequency differences between the master and the cooling lasers and also the master and the repump lasers.

B.4 Cooling laser setup

The cooling laser is a `Toptica DL Pro` diode laser that outputs 40 mW. Approximately 10 mW of this light is reflected by a PBS for the purpose of imaging and the beatnote lock. The remaining 30 mW of light is injected into a `Toptica BoosTA` tapered amplifier system that amplifies the light to 0.7 W. We split 60 mW from the rest of the amplified light using a PBS, double pass it through the slower AOM and inject into fiber. This fiber (the 2×2 slower fiber) has two polarization maintaining (PM) input channels and two PM output channels separated by a beam cube, we treat one of these output channels as a pickoff. We expect 15 mW to emit from one output fiber as the cooling slower light at the experiment, the polarization rejected

portion of the light emits from the other output fiber. The zeroth order of the first pass through the slower AOM is deflected into another double passed AOM and fiber injection. This light is used for transverse cooling. The light that passes undeflected through the PBS is double passed through the MOT AOM and injected into a fiber. This fiber (the 2×6 MOT fiber) has two PM input channels (one of which has been discussed so far), and the light input into each of these is distributed evenly between six PM output channels. Typically we have 20 to 25 mW of MOT cooling light output from each fiber. Two pickoff channels contain approximately 1% of the MOT cooling and repump light respectively. Figure B.4 depicts the cooling laser breakout breadboard.

B.5 Repump laser setup

The repump laser is a `Toptica DL Pro` diode laser that outputs 80 mW. PBS cubes separate the light into four beams, three of which are used. Two of these beams are double passed through AOMs, the slower and repump AOMs, and subsequently injected into the other input channel of the 2×2 slower and 2×6 MOT fibers respectively. We input approximately 15 mW into the slower double passed AOM and 25 mW into the MOT double passed AOM. 1 mW is output from the slower fiber and 2 mW is output from each of the MOT output fibers. Approximately 1 mW is sent to the beatnote lock. Figure B.5 depicts the repump laser breakout breadboard.

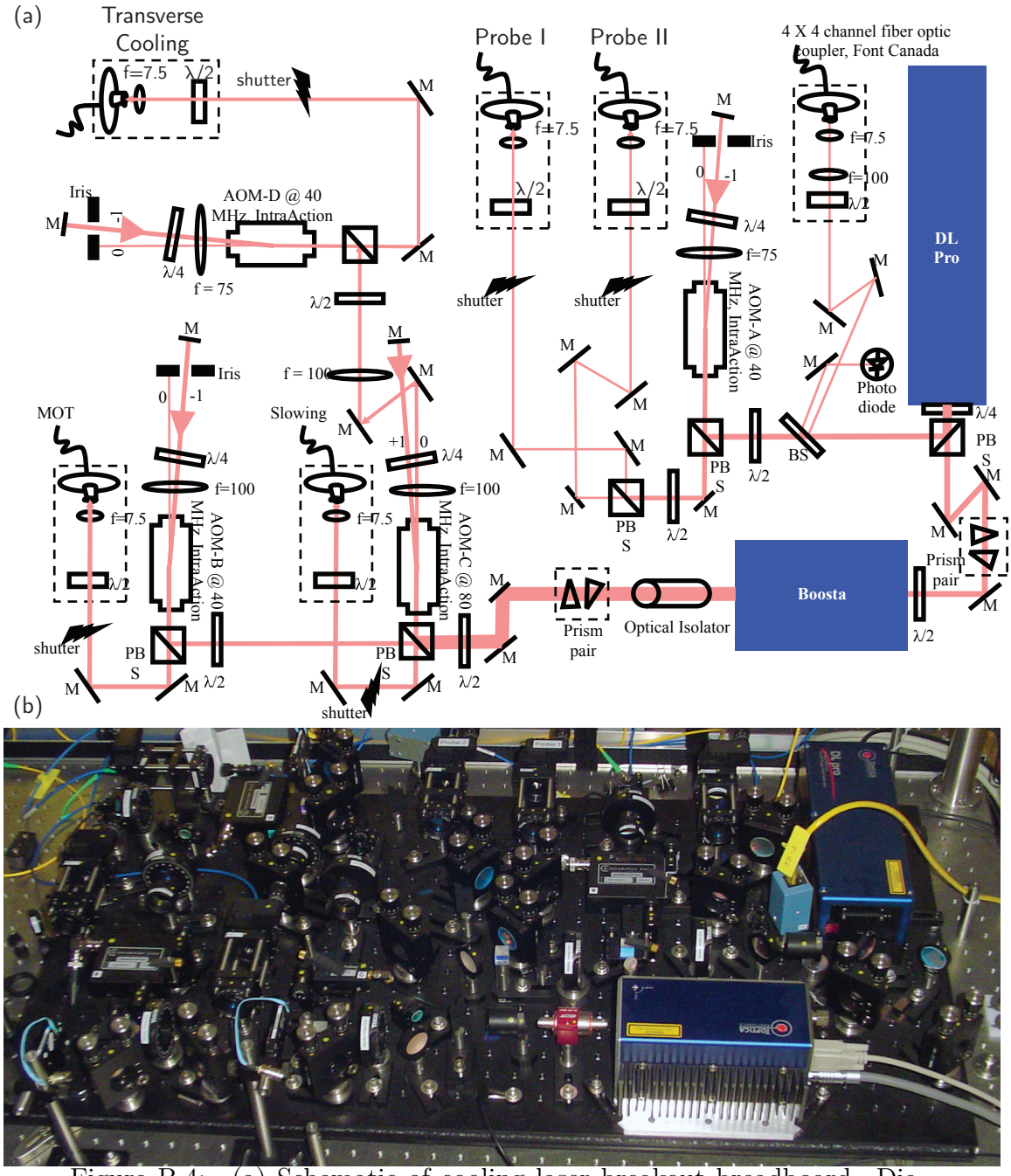

Figure B.4: (a) Schematic of cooling laser breakout breadboard. Diagram adapted from the Rb-Li lab manual. Original author: Subhadeep De. (b) Picture of the cooling breakout breadboard.

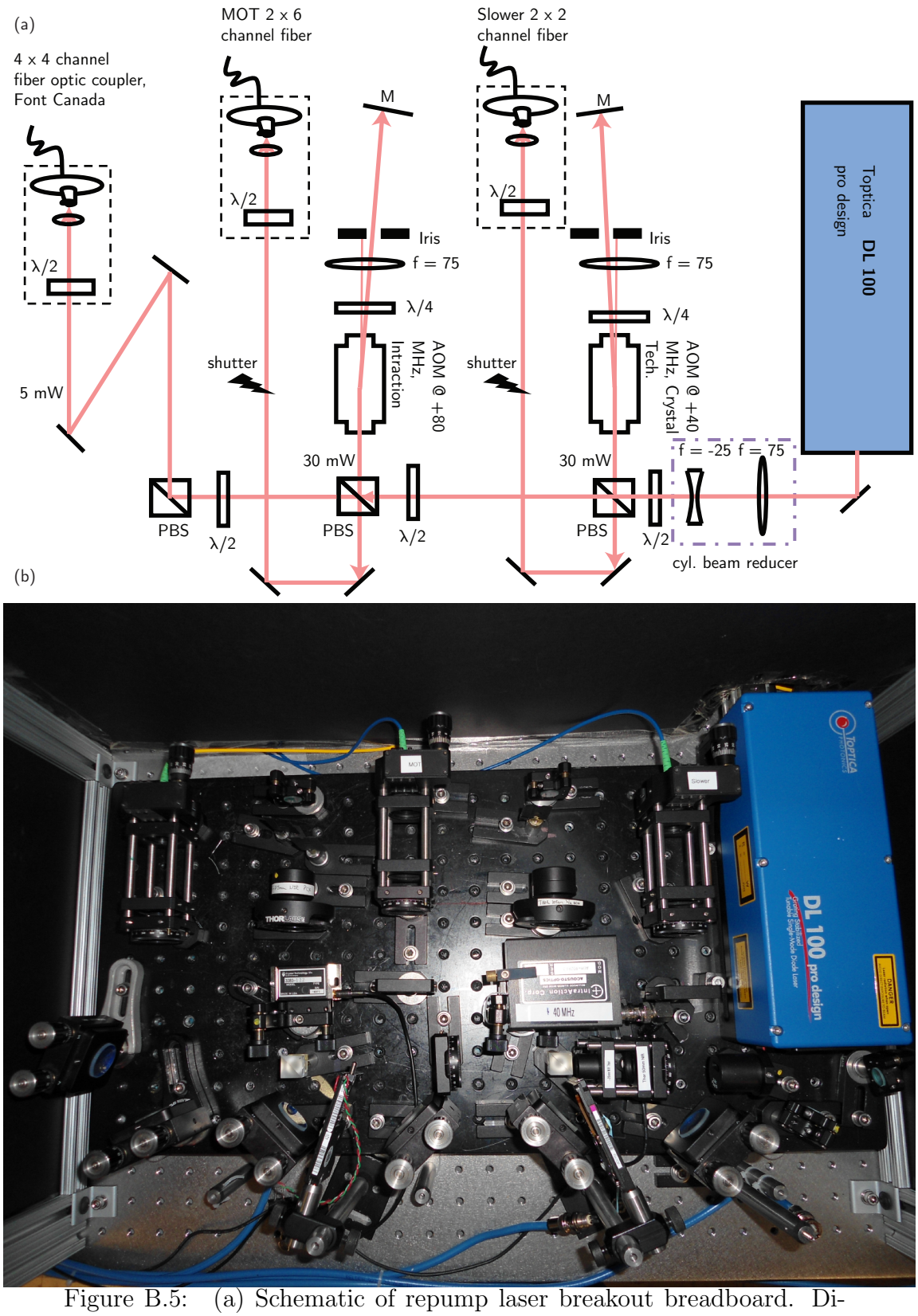

Figure B.5: (a) Schematic of repump laser breakout breadboard. Diagram adapted from the Rb-Li lab manual. (b) Picture of the repump breakout breadboard.

Chapter C: Cooling and Trapping

C.1 Introduction

The atomic electronic internal structure allows coherent as well as dissipative forces to be optically applied to ions and atoms. Crucially, optically applied forces are selective over a narrow range of atomic velocities and can be used to narrow the velocity distribution of a gas of atoms, cooling them. These cold atoms can be efficiently trapped (at very low densities) with a hybrid of optical and magnetic fields in the center of a vacuum chamber. Since these trapped gases are decoupled from the room temperature walls of the vacuum apparatus the gas may be further cooled to quantum degeneracy. These accomplishments were recognized by the 1997 Nobel Prize given to Steven Chu, Claude Cohen-Tannoudji, and William Phillips and by the 2001 Nobel Prize given to Eric Cornell, Wolfgang Ketterle and Carl Wiemann.

C.2 Cooling an atomic beam

C.2.1 The scattering force

We consider a collimated beam of atoms illuminated with a counterpropagating laser as shown in Fig. C.2a. The frequency and polarization of the incident light as well as the magnetic environment of the atom is chosen so that each atom is effectively a two-level system (we prepare the atom in a cycling transition). In the absence of spontaneous emission, a 2π pulse transfers the photon recoil mo-

mentum $\hbar k_{\mathrm{R}} = 2\pi\hbar/\lambda$ to the atom when the valence electron is excited and but it is removed when the electron returns to the ground state because the photon is coherently emitted into the modes of the laser illumination. When there is any electronic excited state population there exists a spontaneous emission process which returns some atoms to the ground state. The distribution of photons emitted during spontaneous emission is nominally isotropic. Averaged over many coherent absorption followed by spontaneous emission processes there is a net scattering force $F_{\mathrm{scatt}} = (\text{photon momentum}) \times (\text{spontaneous emission rate})$ where the spontaneous emission rate is proportional to the excited state population. In the presence of a continuous wave (CW) illumination, the population of atoms in their excited state N_{ex} averages to no more than 1/2. This may be quantified in terms of the Rabi frequency $\Omega/2\pi$, the detuning from resonance $\hbar\delta$, and the scattering rate Γ

$$N_{\mathrm{ex}} = \frac{1}{2}\frac{\Omega^2/2}{\delta^2 + \Omega^2 + \Gamma^2/4}. \tag{C.1}$$

These quantities may be connected to the laser intensity at the atoms $I/I_{\mathrm{sat}} = 2\Omega^2/\Gamma^2$ where

$$I_{\mathrm{sat}} = \frac{c\epsilon_0\Gamma^2\hbar^2}{4|\mathbf{e}_L \cdot \mathbf{d}|^2} \tag{C.2}$$

is the optical intensity necessary to "saturate" the excited state population, a somewhat arbitrarily defined intensity above which additional light asymptotically increases the excited state population [37]. We introduced the speed of light c, the permittivity of free space ϵ_0, and the unit vector of laser polarization $\mathbf{e}_L$ (this can be complex). I_{sat} and Γ depends upon exactly which spin manifolds are coupled and with what polarization. Here, we define I_{sat} and Γ with respect to the coupling between the ground electronic $|f = 2, m_F = \pm 2\rangle$ and the excited electronic $|f = 3, m_F = \pm 3\rangle$. The scattering force is simply the rate of momentum transfer

name	symbol	^{87}Rb value
Saturation intensity, $N_{\rm ex} = 1/2$	$I_{\rm sat}$	1.669(2) mW/cm^2
Decay rate	Γ	$2\pi \times 6.065(9)$ MHz
Recoil velocity	$v_r = \hbar k/M$	5.8845 mm/s
Acceleration, $N_{\rm ex} = 1/2$	$a_{\rm max} = \hbar k\Gamma/2M$	1.12×10^5 m/s
Wavevector	$k = 2\pi/\lambda$	8.055 μm^{-1}
Wavelength	λ	780 nm
Most probable velocity in beam	$v_0 = \sqrt{3k_BT/m}$	336 m/s
Minimum stopping distance	$L_0 = v_0^2/a_{\rm max}$	0.5 m
Actual stopping distance	0	0.7 m

Table C.1: List of quantities for slowing ^{87}Rb. Both Γ and $I_{\rm sat}$ are defined with respect to the ground electronic $|f = 2, m_F = \pm 2\rangle$ and the excited electronic $|f = 3, m_F = \pm 3\rangle$ states.

which is limited by the scattering rate Γ

$$F_{\rm scatt} = \hbar k \Gamma N_{\rm ex} = \hbar k \frac{\Gamma}{2} \frac{I/I_{\rm sat}}{1 + I/I_{\rm sat} + 4\delta^2/\Gamma^2} \tag{C.3}$$

where $\hbar k$ is a photon's momentum. Table C.1 lists Doppler cooling parameters typical of our experiment.

C.2.2 Atom beam velocity distribution

The intensity of an atomic beam $I_0 = \int dv I(v)$ as a function of velocity $I(v)$ when effusing from a long collimation tube is

$$I(v) = \frac{2I_0}{\alpha^4} v^3 \exp -v^2/\alpha^2 \tag{C.4}$$

as given by Ref. [114]; $\alpha = \sqrt{2k_BT/m}$ is the most probable velocity in a equilibrium thermal gas. In a collimated beam of atoms the most probable velocity becomes $v_0 = \sqrt{3/2}\alpha$.

C.2.3 Zeeman slower

Our BEC machine slows atoms with velocities ranging between $\approx$ 320 m/s and $\approx$ 40 m/s that are illuminated by a counterpropagating source of light (slower light)

as shown in Fig. C.1. Slowed atoms are distributed in a narrow range around 40 m/s at the terminus of the slower.

The slower light with wavevector $\mathbf{k}$ is Doppler shifted $\Delta f = \mathbf{k} \cdot \mathbf{v}$ with respect to the reference frame of an atom within the atomic beam moving with velocity $\mathbf{v}$. When the linewidth of the laser is much smaller than Δf the laser resonantly interacts with a narrow band of atomic velocities within the atomic beam. Atoms resonant with the light experience the scattering force detailed in Eq. C.3 and accelerate parallel to $\mathbf{k}$. As the velocity of these atoms changes the slower light is Doppler shifted to smaller frequencies and the atoms fall out of resonance with the light.

From an engineering standpoint it is desirable that the fastest slowed atoms experience constant acceleration for the entire length of the slower. This may be accomplished by chirping (changing) the frequency of the laser in time or by altering the atomic resonance spatially. Our machine implements the latter of these options.

Our scattering process can provide a nearly constant acceleration: we choose this to be around $a_{\max}/2$ which slows atoms somewhat below the peak atomic beam velocity: $0.84 v_0$. As a function of displacement the velocity of slowed atoms is

$$v(z) = 0.84 v_0 \left(1 - \frac{z}{L_0}\right)^{1/2}. \tag{C.5}$$

We compensated the position-dependent Doppler shift of the atoms $\mathbf{k} \cdot \mathbf{v}(z)$ with a state- and position-dependent detuning produced by the Zeeman effect. Following the treatment of Ref. [115] the resonance condition is a function of the slower light frequency ω, atomic velocity $\mathbf{v}$, and a position-dependent magnetic field $-B(z)\mathbf{e}_z$

$$\frac{\mu_B |\mathbf{B}|}{\hbar}(g_F^{(e)} M_e - g_F^{(g)} M_g) = \hbar\delta + \mathbf{k} \cdot \mathbf{v}(z). \tag{C.6}$$

where M_e and M_g are the magnetizations of atoms in the $f = 3$ spin manifold of the $^5P_{3/2}$ electronic excited states and the $f = 2$ spin manifold of the $^5S_{1/2}$ ground

electronic states, respectively.

We choose right circularly polarized light that couples between the ground $f = 2$ and the excited $f = 3$ manifold and align the magnetic field along the axis of laser propagation. In this case, circularly polarized light couple ground $\hat{\mathbf{F}}$ spin projections m_F to an excited $\hat{\mathbf{F}}$ projection $m_{F'} = m_F \pm 1$, where the sign choice is made by choosing right or left circular polarization for the light. Because the coherent excitation process is sensitive to the polarization of the light while spontaneous emission is not, the ensemble of atoms are "pumped" to $M_g = +2$ and $M_e = +3$ in the case of right circularly polarized light over many excitation and spontaneous emission events: see Fig. C.1. In this case the level diagram becomes effectively two level since the states in the single channel allowed for spontaneous emission $|f = 3 \to 2, m_F = 3 \to 2\rangle$ are the same states that are optically coupled: the atoms are in a cycling transition.

The cycling transition maximizes the Clebsh-Gordan coefficients and by extension the spontaneous emission rate and $\mathbf{F}_{\text{scatt}}$. Moreover, atoms in the cycling transition are unlikely to spontaneously emit into states that are weakly coupled or entirely uncoupled from the light. Impurities in the polarization and off-resonant coupling to the other hyperfine states in the $5P_{3/2}$ fine structure inevitably *do* allow atoms to decay into the $f = 1$ ground states, however. A second (repump) laser is required to return these atoms to the excited states and, eventually, the cycling transition. For an overall biasing Zeeman slower, like ours, very little repump light is needed and its polarization is unimportant.

C.2.4 Slower physiology

Our Zeeman slower consists of several layers. The innermost layer is a stainless steel (SS) tube with CF ends that has 1 in. diameter near the oven and 1.5 in. diameter near the atoms. This SS tube was wrapped in heater tape then covered with a thin SS tube with a uniform diameter. On this outer tube we wrapped

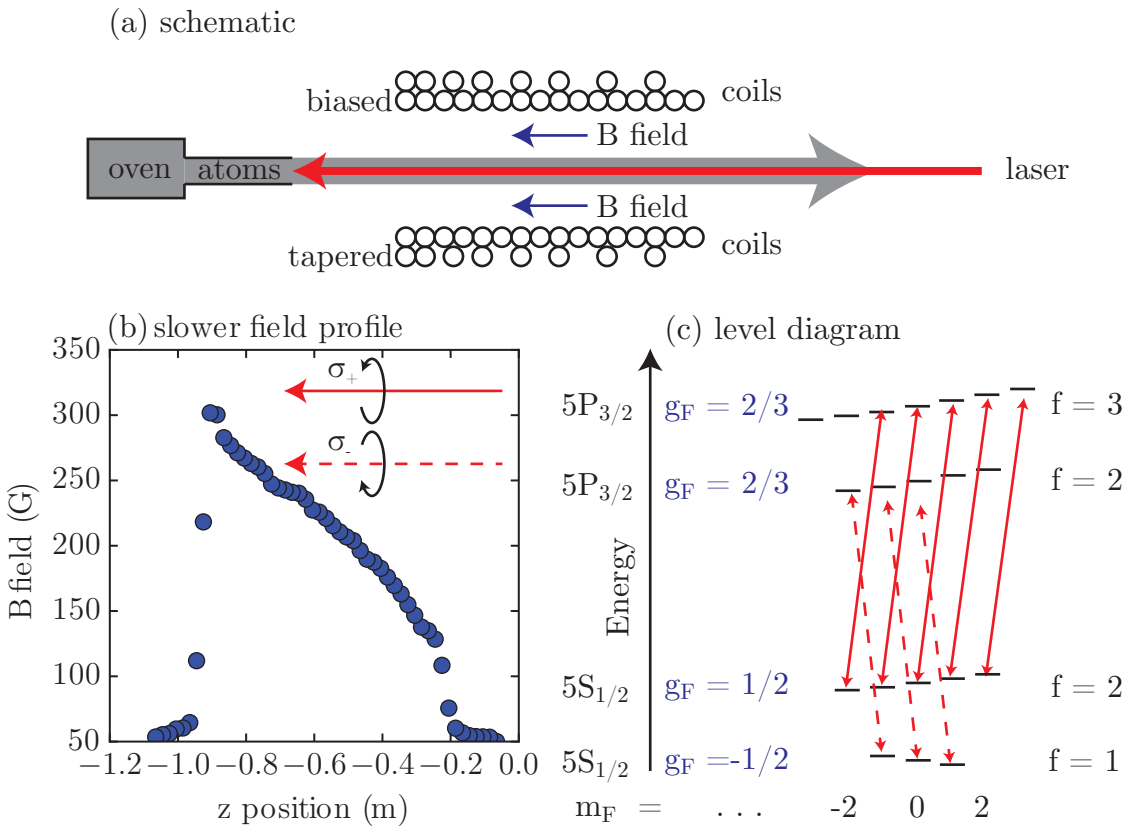

Figure C.1: (a) Slower magnetic field profile in Gauss as a function of position referenced to location of atoms. (b) We show the slower axial magnetic field profile with the propagation direction of our lasers. These lasers are right and left circularly polarized. As shown in (c) the ^{87}Rb level diagram our copropagating lasers couple different hyperfine states between the ground (S) and excited (P) electronic levels. Atoms are pumped into the states connected by the solid red line: the cycling transition. Atoms in the cycling states have selection rules that greatly reduce the probability of decay into the $f = 1$ ground electronic states, which are uncoupled by our light depicted in solid red. The light in dotted red repumps atoms that do end up in these states. The Landé g_F factors are constants of proportionality in the Zeeman term $\hat{H}_Z = g_F \mu_B \mathbf{B} \cdot \hat{\mathbf{F}}/\hbar$. Ideally, a Zeeman slower solves $kv(z) = \mu_B B(z)$ so that the magnetically induced shift between cycling states corrects for the evolving Doppler shift as atoms slow.

Slower parameters	typical values
Length	0.71 m
Biasing current	20 A
Biasing resistance	0.175 Ω
Tapered current	140 A
Tapered resistance	0.075 Ω
Biasing field	8/3 G/A
Max tapered field	9/5 G/A
Min tapered field	8/15 G/A
Cooling slower laser power	10 mW
Cooling slower laser polarization	σ_+
Repump slower laser power	2 mW
Repump slower laser polarization	σ_-

Table C.2: Typical slower parameters

1/8 in. outer diameter copper tubing with no space between the windings. The first layer of windings produces an overall biasing magnetic field. Over this layer of windings we added a second layer with windings that taper from densely spaced to sparsely spaced. The locations of these windings are precisely calculated to keep our atoms near resonant with the spacings necessary to produce uniform acceleration at $a_{\max}/2$ Fig. C.1a. To aid in heat dissipation we added a third winding of coils on top of and where possible between the tapered coils. During normal operation the temperature of the tapered coil rises to about 45 C. We summarize the typical operating conditions of the Zeeman slower in Table C.2.

C.2.5 Transverse heating

The atomic beam expands linearly from its collimation tube and also experiences a random walk due to many isotropic spontaneous emission events. The rms velocity and associated heating from the spontaneous emission increases with the square root of the number of spontaneous emission events. The maximum rate of transverse expansion of the beam occurs in the 21 cm between the end of the Zeeman slower and the atom trap. We focus our slowing light so that it is approximately the same extent as the 1 in. diameter magneto optical trap (MOT), which is centered in the glass cell, and the 1 cm diameter of the collimating tube at the aperture of the oven.

This may have the additional benefit of reducing the transverse expansion of the atomic beam to a small degree. With this configuration, the power requirements for cooling ^{87}Rb are undemanding, requiring merely 10 mW in our apparatus for cooling and less than 2 mW of repump.

C.2.6 Slower schematic

The cooling and repump light are separated by 6.8 GHz in frequency, which is most economically sourced by different lasers. The light is combined commercially using a 2×2 splitting/combining PM fiber that has an in-fiber PBS cube. We collect the light rejected by the PBS on a silicon PD. The cooling and repump light have opposite linear polarizations coming out of the fiber: a $\lambda/4$ waveplate converts the cooling light into σ_+ and the repump light into σ_- polarized light. See Fig. C.2 for a schematic representation.

C.3 Optical molasses and magneto-optical trap

The low velocity portion of the atomic beam, which is greatly enhanced by the slowing and cooling process described in the previous section, is captured directly by a MOT. A rough estimate for absolute maximum capture velocity of a MOT is given by the cooling force from the previous section $F_{\max} = \hbar k \Gamma/2$ applied over the physical extent of the optical beams 2 cm. This optimistic estimate of the MOT capture velocity $v = \sqrt{2\hbar k \Gamma d/m}$ is about 100 m/s for ^{87}Rb whereas we usually assume a capture velocity of ≤ 50 m/s.

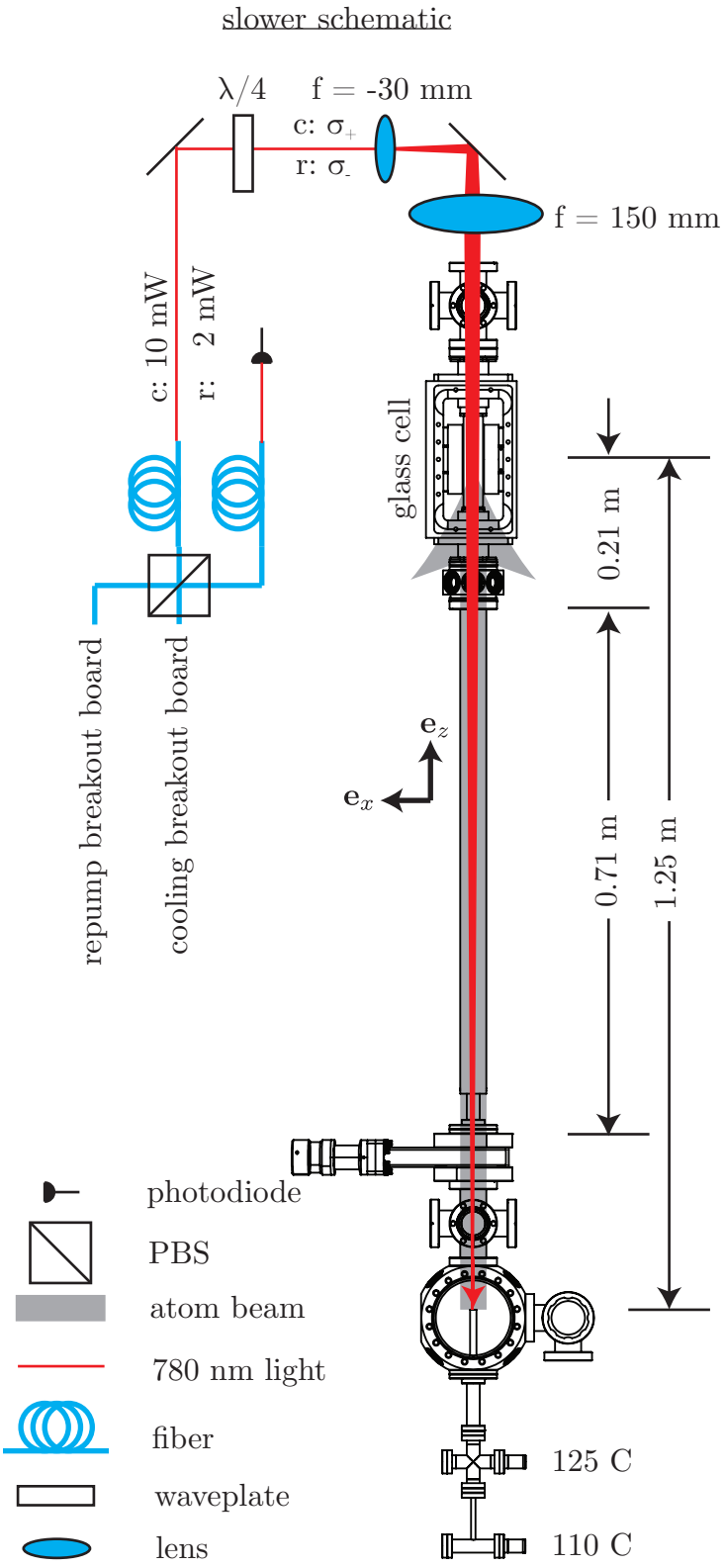

Figure C.2: Shows a schematic representation of management of repump and cooling light. The slower and repump fiber light are coupled onto the same fiber with a polarizing beam splitter (PBS).

C.3.1 Trapping forces

C.3.1.1 The optical molasses

We consider ^{87}Rb atoms illuminated by two counterpropagating laser beams along $\pm\mathbf{e}_x$. The lasers are detuned by $\delta = \omega_{\mathrm{L}} - \omega_{\mathrm{atom}}$ from the Doppler-free atomic resonance; when in motion $v\mathbf{e}_x$ the detuning of the light relative to the atomic transition becomes $\delta \pm kv$ where the sign choice corresponds to the detuning relative to the lasers propagating along $\pm\mathbf{e}_x$. When the lasers are red detuned $\delta < 0$ an atom with motion $v\mathbf{e}_x$ is closer to resonance with the laser propagating along $-\mathbf{e}_x$ and further from resonance with the laser propagating along $\mathbf{e}_x$. Hence, the atom experiences a restoring force as a function of momentum: the atom experiences viscous damping. More formally, the force on an atom is

$$\mathbf{F}_{\pm} = \pm\frac{\hbar\mathbf{k}\Gamma}{2}\frac{I/I_{\mathrm{sat}}}{1 + I/I_{\mathrm{sat}} + (2\delta/\Gamma \mp 2\mathbf{k}\cdot\mathbf{v}/\Gamma)^2} \tag{C.7}$$

$$\mathbf{F}_{\mathrm{tot.}} = \mathbf{F}_{+} + \mathbf{F}_{-}. \tag{C.8}$$

As shown in Fig. C.3a, $\mathbf{F}_{\mathrm{tot.}}$ is nearly linear for a range of velocities: we write down the force in the linear regime

$$\mathbf{F}_{\mathrm{lin}} = \hbar k\Gamma\frac{8\delta k\mathbf{v}I/I_{\mathrm{sat}}}{\Gamma(1 + I/I_{sat} + (2\delta/\Gamma)^2)^2} = -\beta\mathbf{v} \tag{C.9}$$

The velocity at maximum $\mathbf{F}_{\mathrm{tot.}}$ is $|\mathbf{v}| \approx \delta/k$ when $\delta \gg \Gamma$ and may be much greater than the power broadened linewidth $\Gamma\sqrt{1 + I/I_{\mathrm{sat}}}/k$ which roughly corresponds to the maximum velocity of the linear regime (see Fig. C.3). For a given δ we may extend the range of velocities for valid $\mathbf{F}_{\mathrm{lin}}$ and at the same time maximize β by setting the detuning equal to the power broadened linewidth $\Gamma\sqrt{1 + I/I_{\mathrm{sat}}} = \delta$. The response of β to the power broadened linewidth is very asymmetric: $\Gamma\sqrt{1 + I/I_{\mathrm{sat}}} > \delta$ reduces β very little while $\Gamma\sqrt{1 + I/I_{\mathrm{sat}}} < \delta$ can dramatically reduce both β and

the range of velocities over which viscous damping is linear.

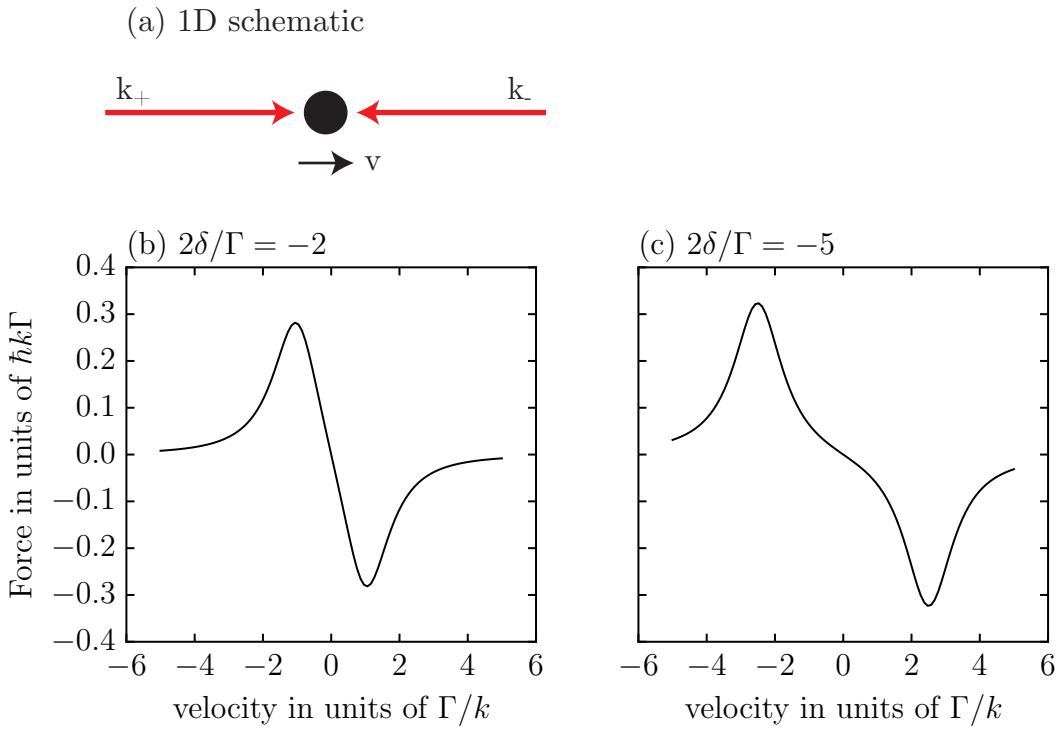

Figure C.3: (a) schematic of two counterpropagating lasers with wavevector $k_\pm$ illuminating an atom or ensemble of atoms traveling with velocity v. (b-c) The force $\mathbf{F}_+ + \mathbf{F}_-$ experienced by atoms with velocity v and $I/I_{\text{sat}} = 2$.

C.3.1.2 Optical forces with magnetic fields

In the presence of a quadrupole magnetic field, the detuning gains a state and position dependence. The quadrupole is produced by an anti-Helmholtz coil configuration with cylindrical symmetry about $\mathbf{e}_x$. The magnetic field along the x axis and within the $y-z$ plane is

$$\mathbf{B}(\rho) = \frac{\partial \mathbf{B}}{\partial \rho}\rho\mathbf{e}_\rho \tag{C.10}$$

$$\mathbf{B}(x) = \frac{\partial \mathbf{B}}{\partial x}x\mathbf{e}_x \tag{C.11}$$

$$\frac{2\partial \mathbf{B}}{\partial \rho} = -\frac{\partial \mathbf{B}}{\partial x} \tag{C.12}$$

where $\rho = y^2 + z^2$ and the gradients along $\mathbf{e}_x$ and $\mathbf{e}_\rho$ are constants near the field minimum at $x = 0$ and $\rho = 0$. At all field orientations except $\mathbf{e}_x$ and $\mathbf{e}_\rho$ the orientation of the magnetic field is not radially inward or outward with respect to the field minimum. The light propagation direction and the magnetic field orientation must be parallel or antiparallel to optically couple the cycling states, placing some restrictions on the geometry of the lasers. The cycling states are desirable because the atoms then have a well defined relationship between the atomic detuning from resonance and the magnetic field (distance from the center of the trap). We show the geometry of our lasers used to produce a magneto-optical trap (MOT) in Fig. C.4.

In ^{87}Rb the detuning from resonance varies as a function of atomic motion $\mathbf{v}$ and the magnetic field

$$\delta = \omega_L - \left(\omega_0 \pm \frac{7}{6}\mu|\mathbf{B}(x,\rho)|/\hbar + \mathbf{k}\cdot\mathbf{v}\right). \tag{C.13}$$

We engineer the system so that the magnitude of the detuning shrinks as the magnetic field increases and as the component of the velocity antiparallel to the wavevector of the optical illumination increases. Here the laser angular frequency is set below the natural frequency of the f=2 to f=3 atomic transition $\omega_L < \omega_0$ at $v = 0$ and $\mathbf{B} = 0$. The sign choice corresponds to the choice of two cycling transitions. The $|f' = 3, m'_F = -3\rangle \leftrightarrow |f = 2, m_F = -2\rangle$ cycling transition is desirable in this case (the minus sign choice) because the laser light shifts closer to resonance with the atomic transition when the atom is displaced from the center of the trap. In a quadrupole field if the magnetic field orients away from the center of the trap in the plane defined by $x = 0$ the magnetic field orients towards the center of the trap for the line defined by $\rho = 0$: this necessitates changing the laser polarization between these two cases.

For two counterpropagating beams with wavevector $\pm\mathbf{k}$ and when the majority of scattering events are in the cycling transition the total force from each beam as

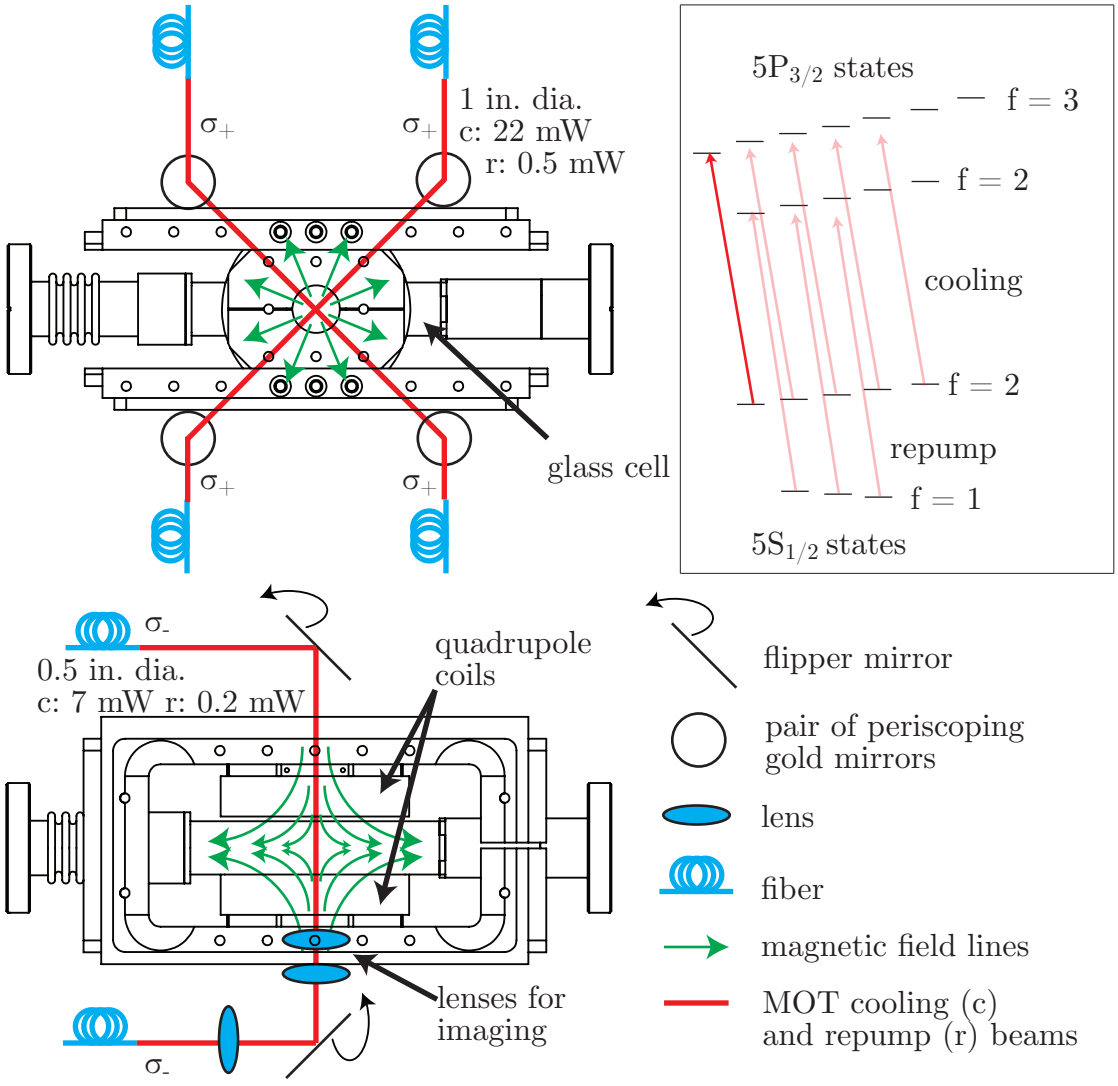

Figure C.4: Glass cell with quadrupole coils. Main portion illustrates MOT beam path and polarizations. Inset shows a level diagram with desired relationship between beam polarization and magnetization: the left-most states have negative magnetization. In the MOT the repump is particularly important because there are regions in the trap where the atomic spin cannot adiabatically follow the magnetic field, atoms leave the cycling transition and may end up in the $f = 1$ ground state.

a function of position and velocity is

$$\mathbf{F}_{\pm}(\mathbf{x},\mathbf{v}) = \pm\frac{\hbar\mathbf{k}\Gamma}{2}\frac{I/I_{\rm sat}}{1+I/I_{\rm sat}+(2\delta/\Gamma \mp 2\mathbf{k}\cdot\mathbf{v}/\Gamma \pm 2\mu B(x)/\Gamma\hbar)^2}. \tag{C.14}$$

Setting $\mathbf{v}=0$ and adding the forces from the counterpropagating beams $\mathbf{F}_{+}(\mathbf{x},\mathbf{v}=0)+\mathbf{F}_{-}(\mathbf{x},\mathbf{v}=0)$ there is a regime near $\mathbf{x}=0$ where there is a linear dependence of force on position. When $\mathbf{k}$ is parallel with $\mathbf{e}_x$

$$F(\mathbf{x}) = \frac{4k\delta\mu_B B(x) I/I_{\rm sat}}{\Gamma(1+I/I_{\rm sat}+(2\delta/\Gamma)^2)^2} \equiv -\kappa x. \tag{C.15}$$

This force is maximized at a displacement $d=\pm\hbar\delta/\mu_B\partial_x B(x)$. It is our practice to set the gradient of the magnetic field $\partial_x B(x)$ so that d is just inside the boundaries of the MOT beams, in this case a typical value for the gradient is 10 G/cm. For position in units of $\hbar\Gamma/\mu_B\partial_x B(x)$ and when $v=0$ the traces in Fig. C.3 are exactly duplicated for force vs position. As with the viscous damping force for a given δ both the range of positions over which the force is linear with position and the slope of κ are maximized when the power broadened linewidth is equal to the detuning.

We may generalize to three orthogonal pairs of counterpropagating lasers illuminating atoms situated at the zero field of a quadrupole magnetic field. The MOT equations of motion

$$\mathbf{F}_{\rm MOT} = -\beta\cdot\mathbf{v} - \kappa\cdot\mathbf{x} \tag{C.16}$$

are those of an overdamped harmonic oscillator. We list the typical parameters for our MOT in Table C.3.

C.3.2 The Doppler limit in temperature

The viscous damping which cools atoms in the MOT and the molasses is proportional to the number of photons absorption from each laser. In the absence of damping,

MOT parameters	typical values
All cooling MOT laser intensities	5.6 mW
All repump MOT laser intensities	0.56 mW
In-plane beam waist	1 in.
Axial beam waist, $\pm\mathbf{e}_x$	0.5 in.
In-plane power	23 mW
Axial power	7 mW
In-plane polarization	σ_+
Axial polarization	σ_-
Detuning δ	16 MHz
Quad gradient	13 G

Table C.3: Typical MOT parameters.

an equal number of spontaneous emission events increases the average rms velocity $\bar{v}$ as a function of time. The rms velocity produced by these processes is given by,

$$\bar{v}^2 = \frac{E_r R_{\text{scatt}}}{\beta} \tag{C.17}$$

hence the rms velocity of a gas scales with the increase of the kinetic energy during a recoil process $E_r = \hbar^2 k^2/2m$, the scattering rate Γ_{scatt}, and in inverse proportion to the slope of the viscous damping β as a function of velocity. The thermal energy at the Doppler temperature T_D is related to the rms velocity $k_B T_D/2 = m\bar{v}^2/2$; meanwhile, the Doppler temperature

$$T_D = \frac{\hbar\Gamma}{4k_B}\frac{1 + I/I_{\text{sat}} + (2\delta/\Gamma)^2}{-2\delta/\Gamma}. \tag{C.18}$$

$T_D = \hbar\Gamma\sqrt{1 + I/I_{\text{sat}}}/2k_B$ is minimized when $\delta = -\Gamma\sqrt{1 + I/I_{\text{sat}}}/2$. Figure C.5 plots the Doppler temperature as a function of the detuning and the intensity. Hence, while we may expand the capture velocity of the MOT by increasing the intensity to well above I_{sat} and correspondingly increase the detuning, the Doppler temperature also rises.

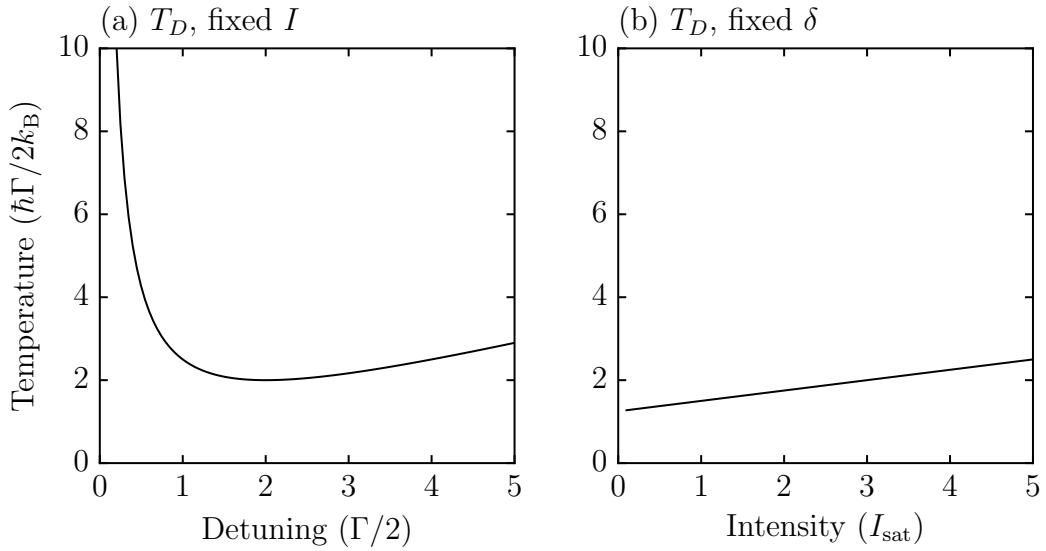

Figure C.5: Plot of Doppler temperature T_D as a function of (a) detuning at fixed $I/I_{\rm sat} = 3$ and (b) intensity at fixed $\delta = -\Gamma$ in a molasses or MOT.

C.4 Polarization gradient cooling

It is a famous result that the temperatures found in 3D optical molasses can be much lower than the Doppler temperature. This is usually attributed to Sisyphus cooling where a well detuned $|\delta| \gg \Gamma$ coupling between ground and excited states form a periodic and state-dependent potential for the atoms. As the atoms move they crest a potential in one eigenstate and radiatively decay to the lower eigenstate only to repeat. Sisyphus cooling is a property of counterpropagating beams with orthogonal linear polarizations. In our apparatus our beams are counterpropagating where each beam has the same handedness of circular polarization. For two beams this geometry produces a net linear polarization which precesses helically in space. Atoms which move in this polarization experience polarization gradient cooling. The mechanisms of sub-Doppler cooling for both these geometries are discussed in detail in Ref. [116].

cooling parameters	typical values
Beam intensity	all equal
in-plane powers	23 mW
axial powers	7 mW
in-plane polarization	σ_+
axial polarization	σ_-
initial detuning δ	-3Γ
final detuning δ	-18Γ
total time	$10 - 21$ ms

Table C.4: Typical polarization gradient cooling parameters. All the beam intensities are set as equal as possible. Since the diameter of the axial beams are half that of the in-plane beams the power of the in-plane beams is larger.

The equilibrium temperature for polarization gradient cooling is

$$k_B T \propto \frac{\hbar \Omega^2}{|\delta|}. \tag{C.19}$$

Hence, the temperature is proportional to laser intensity and inversely proportional to detuning (although there is a detuning below which there is no additional improvement). Both polarization gradient cooling and Sisyphus cooling require nearly degenerate states and nearly equal counterpropagating beam intensities. As a result, the absolute value of any magnetic fields needs to be small ≤ 10 mG; this necessitates the removal of the MOT magnetic field as well as ambient field compensation e.g. for Earth's magnetic field. We summarize the experimental conditions during our polarization gradient cooling (molasses) stage in Table C.4.

C.5 Procedure

Once we have collected and cooled $\sim 10^9$ atoms in the MOT to several times the Doppler temperature we snap off the quad and reduce our beam intensity to below I_{sat} and the detuning to 0Γ. Then, with the ambient magnetic fields cancelled, we sweep the detuning over 14 ms from -3Γ to -18Γ. The theoretical lower limit for the temperature after this stage is the recoil temperature $T_R = E_R/k_B = 180$ nK

which is substantially lower than the Doppler temperature for ^{87}Rb, $T_D = 146$ μK. In practice, the temperature of our MOT is > 100 μK and after polarization gradient cooling in a molasses our temperature falls further to around 30 μK.

Chapter D: Magnetic cooling and trapping

Magnetic traps can have trap depths of $k_B \times 100$'s mK but do not have the large capture velocities characteristic of a MOT. These have an absolute minimum in the magnetic field centered in the glass cell or vacuum chamber. In conjunction with a low-magnetic field seeking magnetic moment of the atom, these magnetic fields can trap atoms. The center of a magnetic trap may be shifted with application of dc magnetic fields. Therefore, ambient magnetic field noise is a source of heating that becomes important around 1 μK. This heating source is typically orders of magnitude smaller than heating due to spontaneous emission in near resonant MOTs. Therefore magnetic traps are usually capable of storing atoms at temperatures well below the Doppler temperature.

Unlike MOTs, magnetic traps have no intrinsic cooling mechanism. Hence, they are typically loaded after sub-Doppler cooling in an optical molasses so that atoms reach the coldest temperature possible before entering the trap. The magnetic trap has the advantage of long trap lifetimes and insensitivity to changes in optical polarization and alignment: the magnetic trap decouples the MOT stage from the later cooling stages.

The Zeeman Hamiltonian describes the potential of an atom in a magnetic field

$$\hat{H}_{\mathrm{Z}} = g_F m_F \mu_B |\mathbf{B}(x, \rho)| \tag{D.1}$$

where the Landé $g_F = -1/2$ factor is the gyromagnetic ratio for the occupied

ground hyperfine state of ^{87}Rb and $B(x, \rho)$ is the quadrupole magnetic field given in section C.3.1.2. In the $f = 1$ hyperfine manifold atoms with $m_F = -1$ gain energy as the magnetic field increases and are trapped, atoms with $m_F = 0$ are untrapped and atoms with $m_F = +1$ are anti-trapped: see Fig. D.1. When atoms pass near the center of a quadrupole field the magnetic field precesses rapidly. When this precession speed exceeds the Larmor frequency $g_F|\mathbf{B}|$ the atom can diabatically change spin projection and therefore become untrapped.

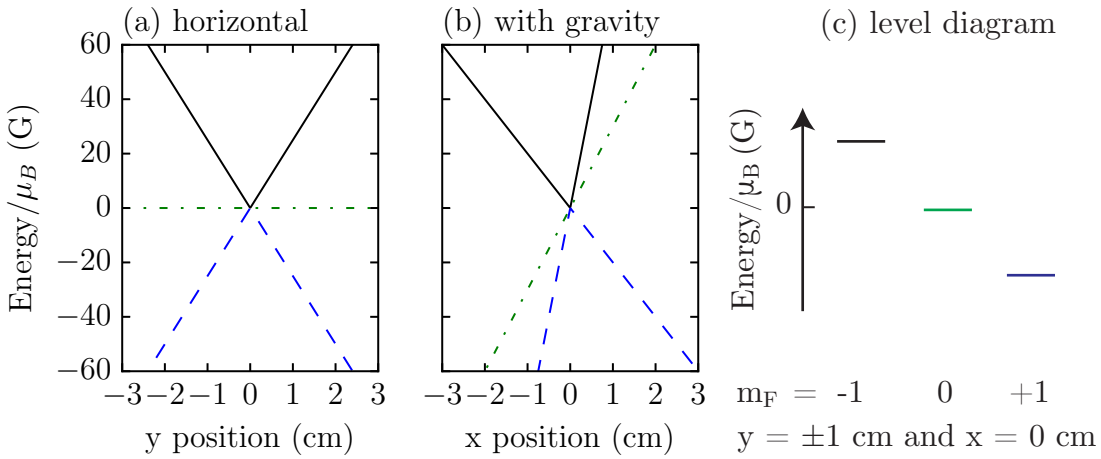

Figure D.1: Shows the quadrupole potential energy with gradient $\partial B/\partial y = 25$ G/cm and $\partial B/\partial y = 50$ G/cm as a function of position (a) orthogonal to gravity, (b) parallel to gravity and (c) with the corresponding state dependence.

D.1 Optical pumping into a dark state

Following the molasses, atoms randomly occupy spin projections in the $f = 1$ and $f = 2$ ground hyperfine states and therefore, more than half of the atoms cannot be loaded into the magnetic trap. The load into the magnetic trap can be dramatically improved by a combination of deloading and optically pumping into a state dark to the optical pumping (dark state). The deload corresponds to leaving the cooling light on very weakly with a polarization that does not load a cycling transition. Atoms then have an opportunity to occupy the $f = 1$ ground state by spontaneous emission from the excited states. As shown in Fig. D.2 we change the excited

electronic hyperfine manifolds to which the repump light couples from $f = 2$ to $f = 1$. With left circularly polarized light, the $m_F = -1$ projection of the ground hyperfine manifold does not couple to the excited hyperfine manifold. Eventually all the atoms in the optically coupled $m_F = 0, 1$ spin projections of the ground hyperfine manifold pool in the uncoupled"dark" state: this state can be trapped by the quadrupole field.

D.2 Forced evaporation

Since the magnetic trap has no intrinsic cooling mechanism we selectively remove atoms that are spatially farthest from the trap center (forced evaporation): these are the most energetic atoms. Atom-atom collisions thermalize the remaining atomic ensemble to an overall lower temperature. Selective removal may be accomplished by resonantly linking the hyperfine states with rf coupling at spatial locations in the quad where $\mu B(\mathbf{x}) = \hbar\omega_{\mathrm{rf}}$. As shown in Fig. D.3 a gap opens in the potential that connects $|m_F = -1\rangle$ to $|m_F = +1\rangle$, which is anti-trapped; some atoms have sufficient energy to enter this anti-trapped portion of the potential and are ejected from the trap. By ramping ω_{rf} to lower values the overall temperature of the atomic ensemble may be reduced. Evaporation efficiency is limited by the thermalization rate which, in turn, depends upon density; hence, evaporation may be done faster with greater trap densities. Forced evaporation becomes technically difficult at low temperatures because of gravitational sag [117] and, in a quadrupole magnetic field, atoms near the magnetic field zero can undergo a spin flip into an untrapped state [39]

D.3 Forced evaporation procedure

Immediately after the molasses we optically pump into the $|m_F = -1\rangle$ for 1 ms. Then we apply cooling light without any repump to remove any remaining atoms

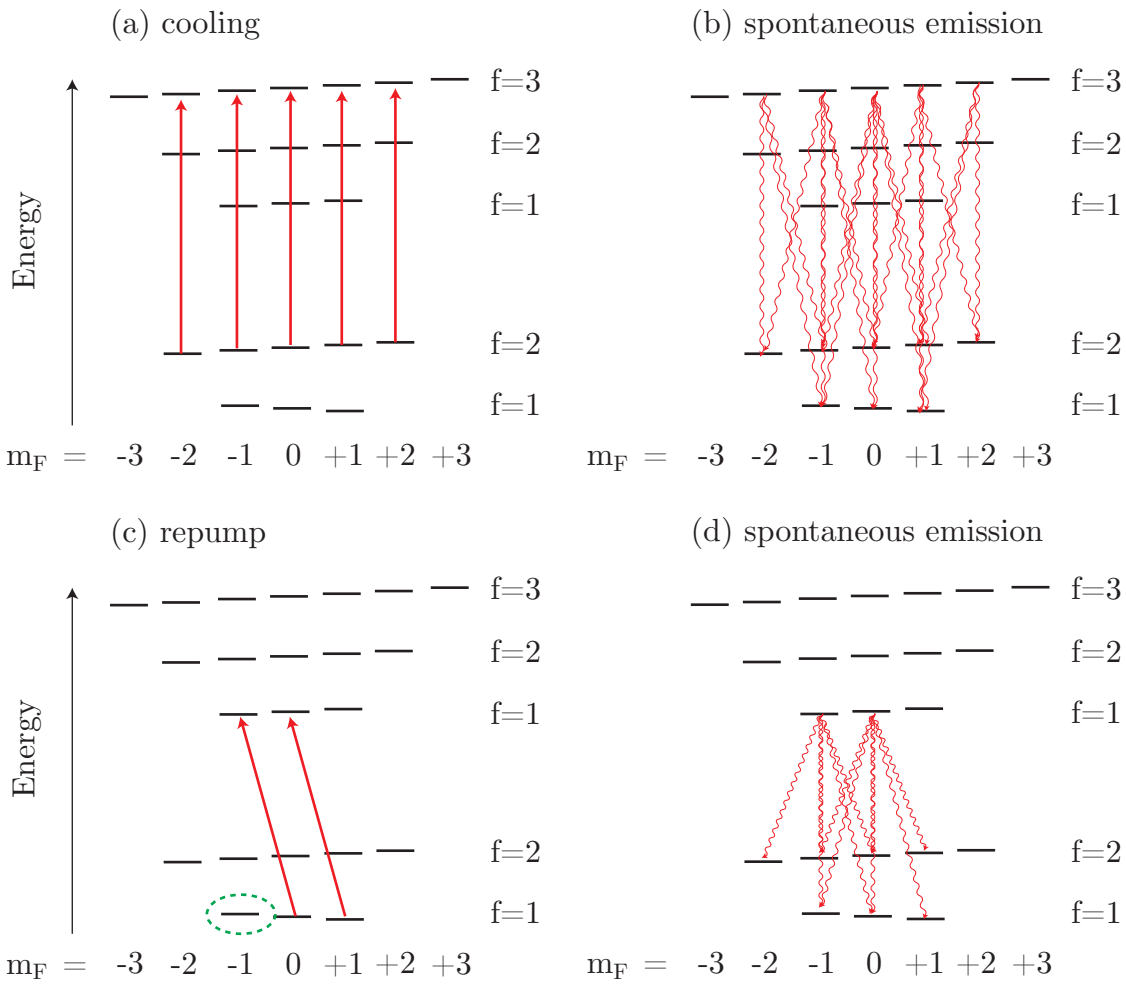

Figure D.2: Illustrates the excitation (a & c) and spontaneous emission (b & d) processes that pump atoms into the ground $|f = 1, m_F = -1\rangle$. Weak cooling light (a & b) removes atoms from the ground $f = 2$ states and redistributes them between the ground $f = 1$ and $f = 2$ states: in the absence of repump light and after many excitation and emission processes all the atoms eventually end up in the $f = 1$ states. Repump light (c & d) with left circular polarization does not excite atoms loaded in the $m_F = -1$ state (green circle). Spontaneous emission from the other states that are repumped have a chance of loading the $m_F = -1$ state. With both cooling and repump, the atoms end up "stuck" in the $m_F = -1$ state (green circle).

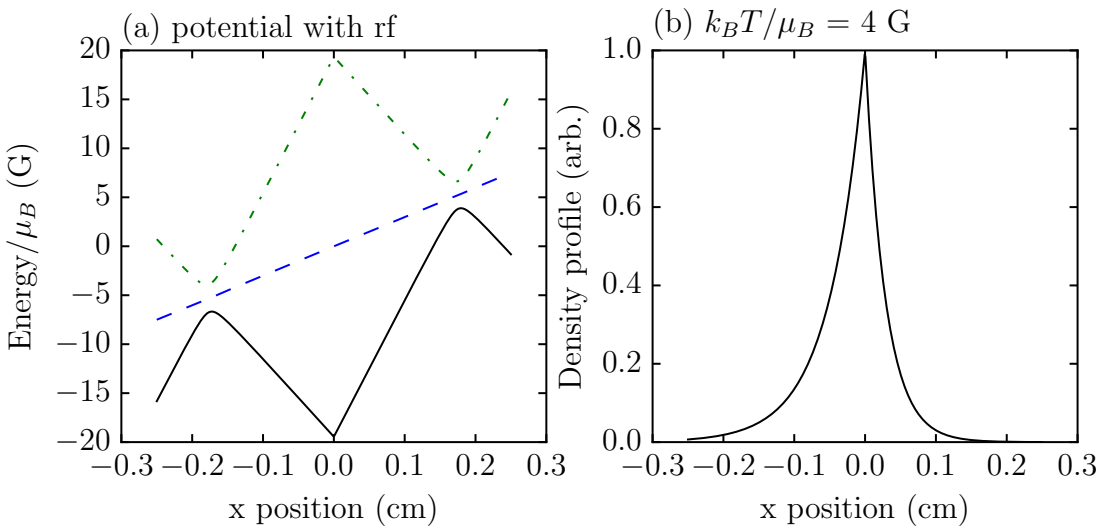

Figure D.3: (a) The magnetic quadrupole trap is dressed with 16 MHz of rf magnetic field. The trap depth $\mu_B \times 12$ G is defined by the avoided crossing. (b) Shows the density profile with cut along $y = 0$ and $z = 0$ at $T = 35$ μK without rf.

in the ground electronic $f = 2$ states. At this point we snap on a magnetic field (in 2 ms) whose potential would produce the distribution of atoms that would correspond as closely as possible to the distribution of the post molasses cloud. In our system we needed the quadrupole to have a gradient approximately 1.5 times that necessary to trap against gravity, which is a reflection of the spatial extent of our post-molasses cloud. The magnetic trap is now loaded with cold atoms.

To begin our evaporative process we start our rf at a frequency of 20 MHz and over 0.3 seconds we ramp to 13.5 MHz while adiabatically compressing the atomic ensemble by increasing the gradient of the quadrupole by a factor of three: four times the gradient necessary to trap against gravity. The compressed trap improves the effectiveness of forced evaporation because it is dense. Over 2 seconds we ramp the rf frequency to 4.5 MHz, then we turn off the rf. As the ensemble cools the density increases and evaporation may be done more quickly. Finally, we adiabatically decompress the quad over 1.5 s. Table D.1 summarizes typical magnetic trap parameters.

parameter	value
gradient equivalent to gravity	30.52 G/cm
gradient snap on	47 G/cm
compress time	0.3 seconds
compressed trap gradient	122 G/cm
initial rf frequency	16 MHz
final rf frequency	4.5 MHz
forced evaporation time	3.3 seconds

Table D.1: Typical parameters in the magnetic trap.

Chapter E: Optical dipole trap

Optical dipole traps induce a dipole moment with far off resonant light. The trap depth and spatial extent can always be increased by using more light and by detuning more from resonance. Practically speaking, the trap depth and spatial extent of these traps are limited by the budget of a lab. It is entirely possible to load an optical Dipole trap directly from an ensemble of atoms sub-Doppler cooled in a molasses. The molasses, and to a lesser extent, the MOT can fluctuate in position spatially in response to polarization and intensity variability of the lasers. The load into the optical dipole trap is very sensitive to such position fluctuations whereas the magnetic trap is much less sensitive. The location of the magnetic trap is fixed by the coil arrangement and current: the latter of which can be experimentally controlled with high precision. Therefore, the load into the optical dipole trap from the magnetic trap can be extremely consistent.

E.1 Loading the optical dipole trap

We slowly ramp our magnetic trap from 120 G/cm to 20 G/cm and at the same time lower the trap from 100 μm along $\mathbf{e}_x$ to 0: $0\mathbf{e}_x$ defines the center of the quadrupole trap center in the absence of additional uniform magnetic fields. An optical dipole beam with a waist $r_0 = 67$ μm is on during the magnetic field ramp down at 11 W of power and aligned at the quadrupole trap center. Atoms are efficiently loaded from the magnetic trap into the dipole trap when the atomic ensemble in the magnetic trap is the same spatial extent as the dipole trap. Typically, all of the atoms may be loaded into the optical dipole trap when the k_BT is 1/10 the optical trap depth $U_{\text{dipole}}(\mathbf{x} = 0) = \frac{\hbar\Gamma}{4}\frac{\Gamma\omega_0}{\omega^2-\omega_0^2}\frac{P}{\pi r_0^2 I_{\text{sat}}}$. As shown in Fig. F.1a the optical dipole trap now provides confinement transverse to its direction of propagation while the magnetic trap provides the majority of confinement parallel to the direction of propagation.

E.2 Density limitations

Narrow beam waists increase the depth of the trapping potential but tend to produce losses in interacting gases; density dependent losses are often attributed to three-body recombination. The three body recombination rate $\Gamma_{3-\text{body}}$ in ^{87}Rb is a function of the density n cubed

$$\Gamma_{3-\text{body}} = K_3 n^3 \tag{E.1}$$

where $K_3 == 2.2 \times 10^-23$ cm^6/s [118, 119]. Since these losses primarily occur where density is maximized and typically the coldest atoms in a Boltzmann distribution are at the center of the trap 3-body losses perform a sort of anti-evaporation that heats the cloud [120].

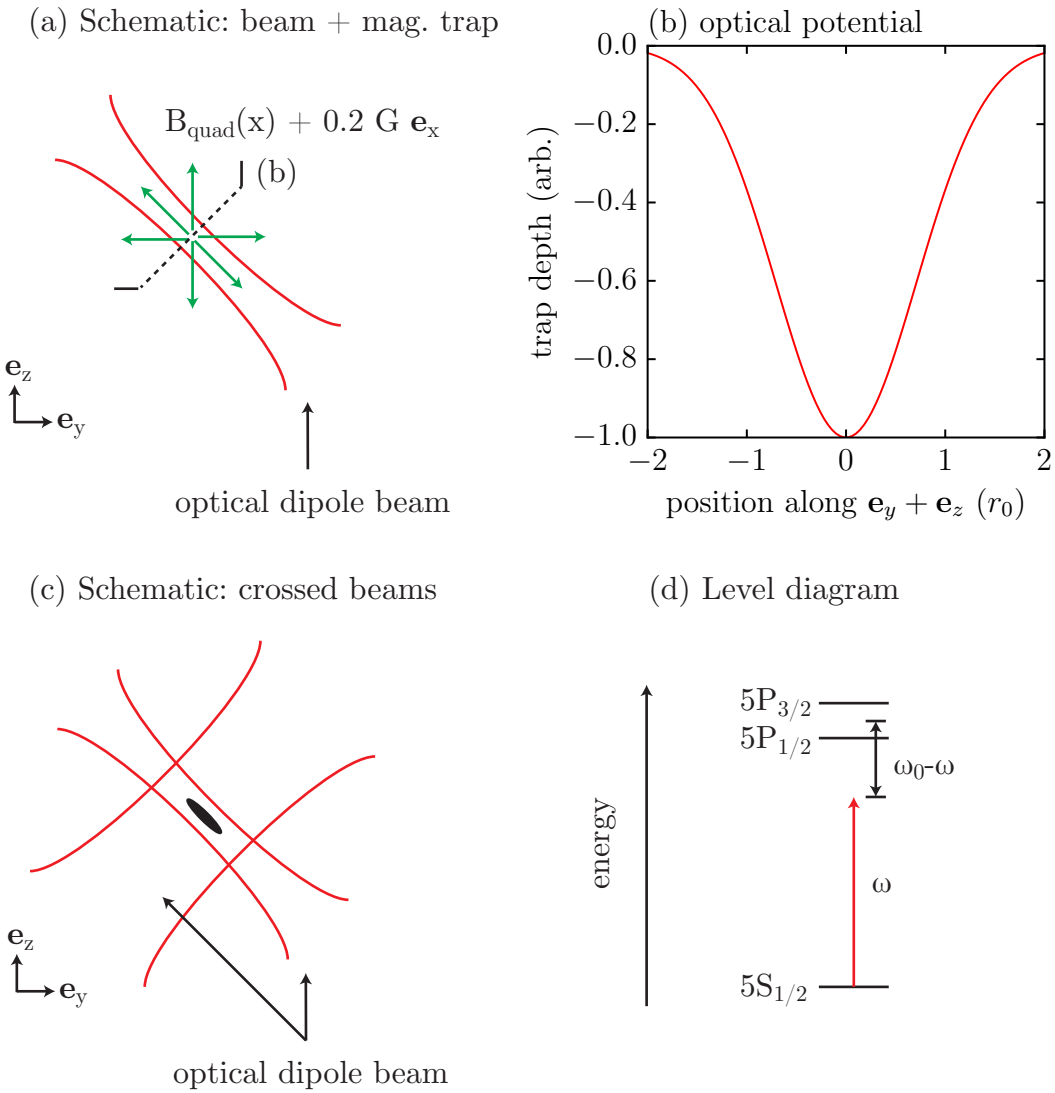

Figure E.1: (a) schematic of hybrid optical dipole trap and quadrupole magnetic trap. The optical dipole trap provides confinement in the planes transverse to the beam propagation while the magnetic trap–with gradients weak compared to those necessary to trap against gravity–provides axial confinement. (b) profile of optical dipole trap. (c) The intersection of two optical dipole beams provides full confinement of the atomic ensemble. (d) level diagram showing the coupling of ^{87}Rb with 1064 nm optical illumination.

E.3 Evaporative cooling

In optical dipole traps lowering the intensity of the beam allows the most energetic atoms to enter the continuum of untrapped states. As a rule of thumb the temperature of atoms in an optical dipole trap approximately equal 1/10th the trap depth which may be calculated using Eqs. 4.10 and 4.12: we find that the trap depth is $\propto m\omega_{\mathrm{HO}}^2$ [39]. Hence, the number of uncondensed atoms $N_{\mathrm{th}} \propto \omega_{\mathrm{HO}}^3 \propto P^{3/2}$ can always be reduced below 1.

E.4 Loading the crossed-dipole trap

Typically, we load the hybrid optical and magnetic trap at temperatures much greater than the optical trap depth. Keeping the overall optical power constant we perform evaporation over the course of 1 s by increasing the intensity in a second optical beam that intersects the first at a right angle: both are perpendicular to the axis along gravity as shown in Fig. F.1c. Over 1 s the combined optical power is lowered from 11 W to something just above the threshold for condensation; the magnetic gradient is simultaneously lowered from 20 G/cm to 10 G/cm. It is beneficial to do this evaporation quickly, especially at the beginning of the ramp, to reduce the density and the corresponding three-body recombination. We then turn off the magnetic field gradient in 1 s. Final evaporation to condensation is done by reducing the overall optical power over 1.5 s. This evaporation is typically done slowly so that we minimize the number of excitations introduced during the formation of the condensate.

E.5 Typical optical crossed-dipole setup

A `30 W IPG fiber laser` provides 11 W of 1064 nm to the experiment. There are no fibers in this setup. A 4:1 telescope reduces the initial 2 mm radial extent of the

beam to 0.5 mm. The intensity of the light is controlled by the first AOM and the remainder of the power is removed to a 30 W beam dump. We sample light from -1st order of the AOM with the uncoated glass surface of a pickoff oriented at 45 degrees and measure with an InGaAs photodiode. We found that Si photodiodes are temperature sensitive at 1064 nm. The Glan laser polarizer removed a long timescale coupling between polarization and the overall intensity that resulted from the polarization sensitivity of our pickoff. The second AOM splits the light into each of the crossed optical dipole beams. Each beam is focused with a 300 mm achromatic doublet on the quadrupole trap center. The waist of the dipole beam was adjusted between experiments using cylindrical and regular beam expanders: doubling the size of the collimated beam that precedes the final focusing lens halves the waist of the beam at the atoms. In the domain dynamics experiment a nearly cylindrically symmetric crossed dipole trap was produced with the intersection of a 67 μm beam and a 300 μm beam. We balanced the power between the beams with the second AOM to produce a 22 : 1 aspect ratio for $\mathbf{e}_z - \mathbf{e}_y$ relative to $\mathbf{e}_x$. For the spin-1 ferromagnetism experiment we investigated the three component miscibility of our system. We prepared a disc-like trap so that the spin-components could separate like pieces of a pie. In this case the collimated waist of each beam perpendicular to gravity was left around 0.5 mm but the waist of beam A in Fig. E.2 parallel to gravity was expanded by a factor of three using cylindrical optics. We summarize typical parameters of the optical dipole setup in Table E.1.

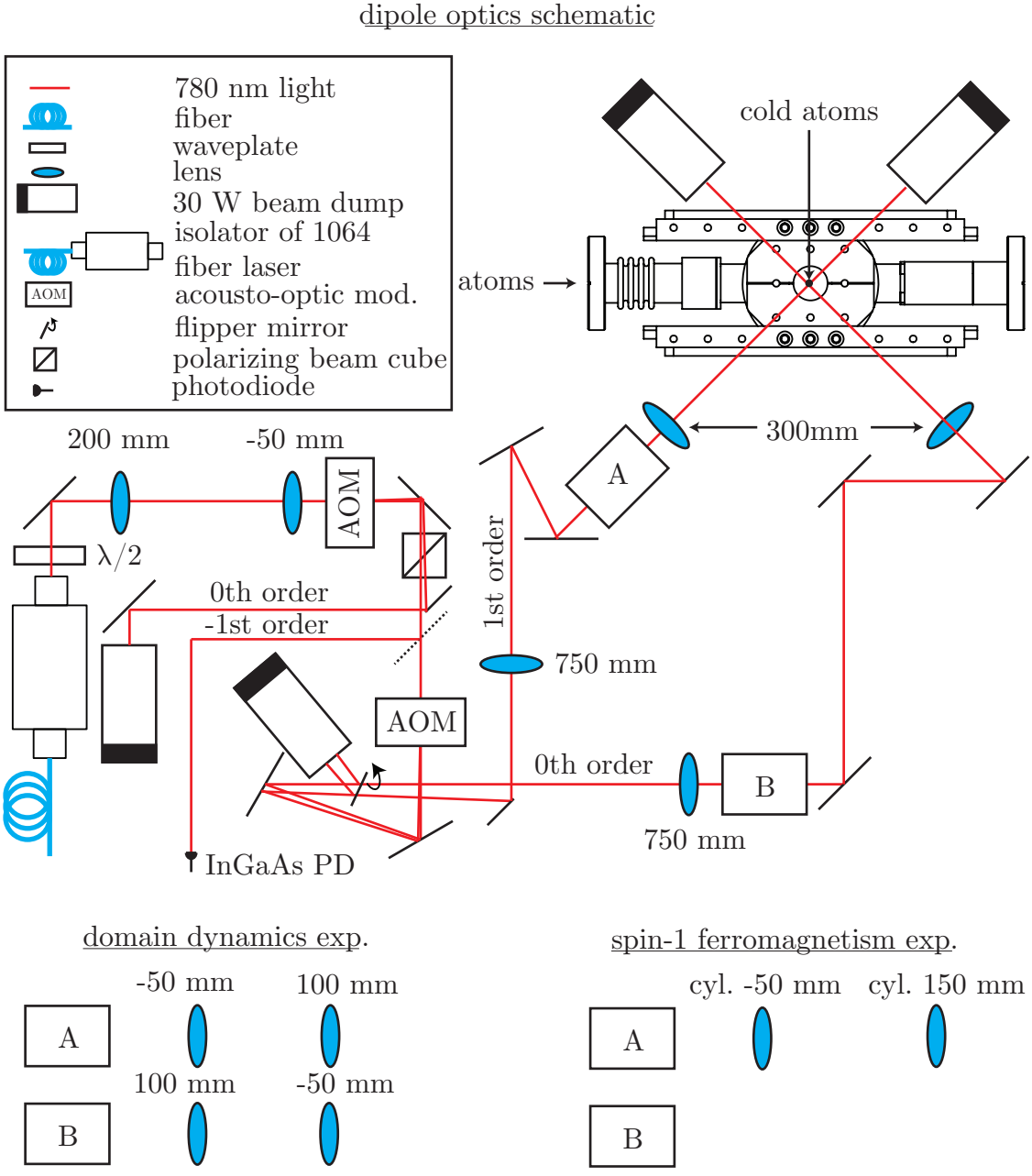

Figure E.2: Schematic of crossed optical dipole beams intersecting to produce a 3D trap for cold atoms. Our setup changes between the domain dynamics experiment and the spin-1 ferromagnetism experiment. In the first experiment beam A has a waist at the atoms that is four times smaller than that of waist B. In the spin-1 experiment the waists of beams A and B are the same in the plane of the schematic but cylindrical lenses reduce the vertical extent of beam A by a factor of 3.

parameter	value
power to trap against gravity	$3.5 \times 10^{15} r_0^3$ mW
far detuned saturation intensity	2.50 mW/cm^2
r_0 for beam A domains exp.	67 μm
r_0 for beam B domains exp.	300 μm
r_0 for beam A spin-1 exp.	$150(\mathbf{e}_z - \mathbf{e}_y)/\sqrt{2}$ μm, $55\mathbf{e}_x$ μm
r_0 for beam B spin-1 exp.	150 μm isotropic
power at fiber laser head	11 W
power in A during domain exp.	
power in B during domain exp.	
power in A during spin-1 exp.	250 mW
power in B during spin-1 exp.	250 mW

Table E.1: Typical parameters of the optical dipole setup.

Chapter F: Cooling and control sequence overview

F.0.1 From MOT to sub-Doppler cooling

Once we have collected and cooled $\sim 10^9$ atoms in the MOT to several times the Doppler temperature we snap off the quad and reduce our beam intensity to below I_{sat} and the detuning to -3Γ. Then, with the ambient magnetic fields cancelled, we sweep the detuning over 14 ms from -2Γ to -24Γ. The theoretical lower limit for the temperature after this stage is the recoil temperature $T_r = E_r/k_B = 180$ nK which is substantially lower than the Doppler temperature for ^{87}Rb, $T_D = 146$ μK. In practice, our MOT temperature ~ 100 μK and our molasses temperature ~ 30 μK. A summary of the experimental sequence that transitions from the MOT to the molasses is included in Table F.1.

Stage	Duration (ms)	MOT c. (mW)	MOT r. (mW)	MOT c. δ (Γ)
MOT load	3000-7000	22	2	-2
Equilibrate	50	22	2	-2
Decompress	50	$22 \rightarrow 15$	$2 \rightarrow 1.5$	-2
Molasses	14	1	1	$-2 \rightarrow -24$
Stage	Duration (ms)	Slower c. (mW)	Slower r. (mW)	Quad. B (G/cm^3)
MOT load	3000-7000	15	2	15
Equilibrate	50	0	0	15
Decompress	50	0	0	$15 \rightarrow 7$
Molasses	14	0	0	0
Stage	Duration (ms)	Slower B. (A)		
MOT load	3000-7000	140		
Equilibrate	50	$140 \rightarrow 0$		
Decompress	50	0		
Molasses	14	0		

Table F.1: This is the MOT to molasses sequence. There are many abbreviations in this table: cooling (c.), repump (r.), detuning (δ), magnetic field (B.) and quadrupole (quad.). The natural linewidth is 6 MHz (Γ).

F.1 Load into magnetic trap

Immediately after the molasses we optically pump into the $|m_F = -1\rangle$ for 1 ms. Then we apply cooling light without any repump to remove any remaining atoms in the ground electronic $f = 2$ states. At this point we snap on a magnetic field (in 2 ms) whose potential would produce the distribution of atoms that would correspond as closely as possible to the distribution of the post molasses cloud. In our system we needed the quadrupole to have a gradient approximately 1.5 times that necessary to trap against gravity, which is a reflection of the spatial extent of our post-molasses cloud. A summary of the experimental sequence that loads a molasses into the magnetic trap can be found in Table F.2.

F.2 Forced evaporation procedure

To begin our evaporation we start our rf at a frequency of 20 MHz and over 0.3 seconds we ramp to 13.5 MHz. We simultaneously compressing the atomic ensem-

Stage	Duration (ms)	Probe c. (mW)	MOT c. (mW)	MOT c. δ (Γ)
Optical pump	6	0	2	-4
Deload	1	0	2	-4
Blow away	1	1.6	0	-4
Load mag. trap	14	0	0	NA

Stage	Duration (ms)	Slower r. (mW)	Slower r. δ (Γ)	Quad B. (G/cm^3)
Optical pump	6	4	-26	0
Deload	1	0	0	0
Blow away	1	0	0	0
Load quad B. trap	14	0	0	48

Table F.2: This is the molasses to the magnetic trap load. There are many abbreviations in this table: cooling (c.), repump (r.), detuning (δ), magnetic field (B.), and quadrupole (quad.). The natural linewidth is 6 MHz (Γ).

Stage	Duration (ms)	Quad. B. (G/cm^3)	rf B. (G)	rf freq. (MHz)
Compress quad.	300	$48 \rightarrow 120$	0.015	$20 \rightarrow 13.5$
Forced evap.	2000	120	0.015	$13.5 \rightarrow 4.5$

Stage	Duration (ms)	Opt. dip. (W)	$\mathbf{e}_x$ B. bias (G)
Compress quad.	300	11	$0 \rightarrow 1$
Forced evap.	2000	11	1

Table F.3: The compression and forced evaporation experiment sequencing is described here. There are many abbreviations in this table: dc magnetic biasing field (B. bias), optical (opt.), dipole (dip.), evaporation (evap.), frequency (freq.), magnetic field (B.), and quadrupole (quad.).

ble adiabatically by increasing the gradient of the quadrupole magnetic trap by a factor of three: four times the gradient necessary to trap against gravity. The compressed trap improves the rate of reequilibration during forced evaporation because it increases the density of the atomic ensemble. Over 2 seconds we ramp the rf frequency to 4.5 MHz, then we turn off the rf. As the ensemble cools the density increases and evaporation may be done more quickly. Table F.3 summarizes typical magnetic trap parameters.

F.3 Loading the optical dipole trap

We slowly ramp our magnetic trap from 120 G/cm to 20 G/cm and at the same time lower the trap from 100 μm along $\mathbf{e}_x$ to 0: $0\mathbf{e}_x$ defines the center of the quadrupole trap center in the absence of additional uniform magnetic fields. An optical dipole

Stage	Duration (ms)	Quad. B. (G/cm^3)	dip. (W)	cross dip. (W)
Decomp. quad.	1500	$120 \rightarrow 30$	11	0
Load cross	1000	$30 \rightarrow 20$	$11 \rightarrow 5.5$	$0 \rightarrow 5.5$
Dip. evap.	1000	20	$5.5 \rightarrow 2$	$5.5 \rightarrow 2$
Quad. off	1000	$20 \rightarrow 0$	2	2
Stage	Duration (ms)	$\mathbf{e}_x$ B. bias (G)		
Decomp. quad.	1500	$1 \rightarrow 0.1$		
Load cross	1000	0.1		
dip. evap.	1000	0.1		
Quad. off	1000	0.1		

Table F.4: This is the experimental loading sequence from the magnetic trap to optical dipole trap. There are many abbreviations in this table: decompress (decomp.), dc magnetic biasing field (B. bias), optical dipole (dip.), evaporation (evap.), magnetic field (B.), and quadrupole (quad.).

beam with a waist $r_0 = 67$ μm is on during the magnetic field ramp down at 11 W of power and aligned at the quadrupole trap center. Atoms are efficiently loaded from the magnetic trap into the dipole trap when the atomic ensemble in the magnetic trap is the same spatial extent as the dipole trap. Typically, all of the atoms may be loaded into the optical dipole trap when the $k_B T$ is 1/10 the optical trap depth

$$U_{\text{dipole}}(\mathbf{x} = 0) = \frac{\hbar\Gamma}{4}\frac{\Gamma\omega_0}{\omega^2 - \omega_0^2}\frac{P}{\pi r_0^2 I_{\text{sat}}} \tag{F.1}$$

As shown in Fig. F.1a the optical dipole trap now provides confinement transverse to its direction of propagation while the magnetic trap provides the majority of confinement parallel to the direction of propagation.

F.3.1 Evaporation in the dipole trap

In optical dipole traps lowering the intensity of the beam allows the most energetic atoms to enter the continuum of untrapped states. As a rule of thumb the temperature of atoms in an optical dipole trap approximately equal 1/10th the trap depth which may be calculated using Eqs. 4.10 and 4.12: we find that the trap depth is $\propto m\omega_{\text{HO}}^2$ [39]. Hence, the number of uncondensed atoms $N_{\text{th}} \propto \omega_{\text{HO}}^3 \propto P^{3/2}$ can always be reduced below 1.

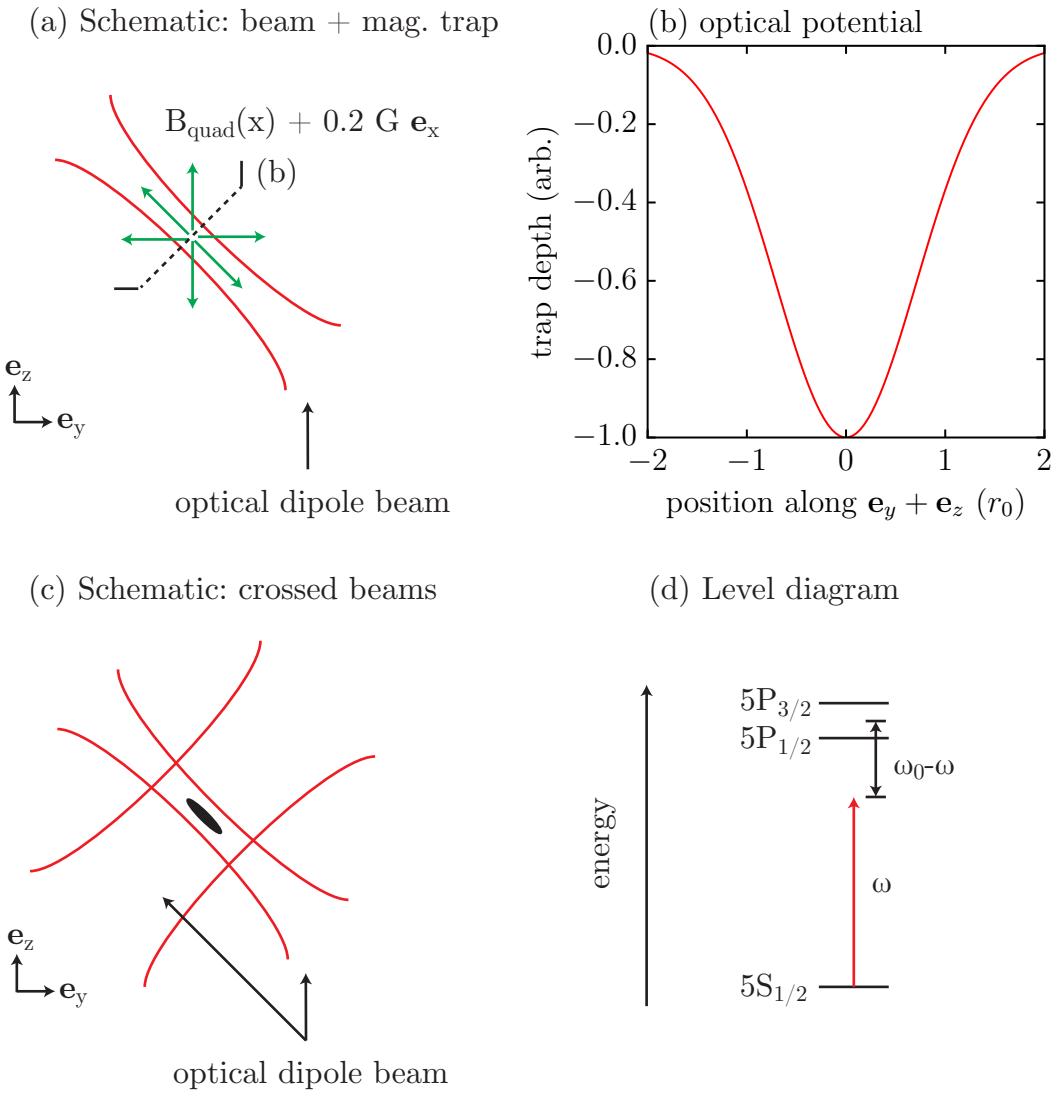

Figure F.1: (a) This is a schematic of the hybrid optical dipole trap and quadrupole magnetic trap. The optical dipole trap provides confinement in the planes transverse to the beam propagation while the magnetic trap–with gradients weak compared to those necessary to trap against gravity–provides axial confinement. (b) profile of optical dipole trap. (c) The intersection of two optical dipole beams provides full confinement of the atomic ensemble. (d) level diagram showing the coupling of ^{87}Rb with 1064 nm optical illumination.

Typically, we load the hybrid optical dipole and magnetic trap at a $k_B T$ greater than the optical dipole trap depth alone. Once atoms are partially loaded into the dimple produced by the optical dipole trap we lower the overall magnetic field to approximately 20 G/cm. Simultaneously, while keeping the overall optical power constant, we perform evaporation over the course of 1 s by shunting light into a second optical beam that intersects the first at a right angle. Both optical dipole beams are perpendicular to the axis along gravity as shown in Fig. F.1c. Over another 1 s the combined optical power is lowered from 11 W to something just above the threshold for condensation. The magnetic gradient is simultaneously lowered from 20 G/cm to 10 G/cm.

It is beneficial to do this initial evaporation quickly to reduce the density and the corresponding three-body recombination. We then turn off the magnetic field gradient in 1 s. Final evaporation to condensation is done by reducing the overall optical power over 1.5 s. This final evaporation is typically done slowly so that we minimize the number of excitations introduced during the formation of the condensate.

Bibliography

[1] M. H. Anderson, J. R. Ensher, M. R. Matthews, C. E. Wieman, and E. A. Cornell. Observation of Bose-Einstein condensation in a dilute atomic vapor. *Science*, 269, 1995.

[2] K. B. Davis, M. O. Mewes, M. R. Andrews, N. J. van Druten, D. S. Durfee, D. M. Kurn, and W. Ketterle. Bose-Einstein condensation in a gas of sodium atoms. *Phys. Rev. Lett.*, 75(22):3969–3973, Nov 1995.

[3] B. DeMarco, H. Rohner, and D. S. Jin. An enriched ^{40}K source for fermionic atom studies. *Review of Scientific Instruments*, 70(4):1967–1969, 1999.

[4] M.-S. Chang, C. D. Hamley, M. D. Barrett, J. A. Sauer, K. M. Fortier, W. Zhang, L. You, and M. S. Chapman. Observation of spinor dynamics in optically trapped ^{87}Rb Bose-Einstein condensates. *Phys. Rev. Lett.*, 92(14):140403, Apr 2004.

[5] D. Jaksch, C. Bruder, J. I. Cirac, C. W. Gardiner, and P. Zoller. Cold bosonic atoms in optical lattices. *Phys. Rev. Lett.*, 81(15):3108–3111, 1998.

[6] Markus Greiner, Cindy A Regal, and Deborah S Jin. Emergence of a molecular Bose–Einstein condensate from a Fermi gas. *Nature*, 426:537–540, 2003.

[7] Y-J. Lin, K. Jiménez-García, and I. B. Spielman. Spin-orbit-coupled Bose-Einstein condensates. *Nature*, 471(7336):83–86, 2011.

[8] P. Wang, Z.-Q. Yu, Z. Fu, J. Miao, L. Huang, S. Chai, H. Zhai, and J. Zhang. Spin-orbit coupled degenerate Fermi gases. *Phys. Rev. Lett.*, 109:095301, 2012.

[9] L. W. Cheuk, A. T. Sommer, Z. Hadzibabic, T. Yefsah, W. S. Bakr, and M. W. Zwierlein. Spin-injection spectroscopy of a spin-orbit coupled Fermi gas. *Phys. Rev. Lett.*, 109:095302, 2012.

[10] Y. K. Kato, R. C. Myers, A. C. Gossard, and D. D. Awschalom. Observation of the spin Hall effect in semiconductors. *Science*, 306(5703):1910–1913, 2004.

[11] C. L. Kane and E. J. Mele. Z_2 topological order and the quantum spin Hall effect. *Phys. Rev. Lett.*, 95:146802, 2005.

[12] M. Z. Hasan and C. L. Kane. Colloquium: Topological insulators. *Rev. Mod. Phys.*, 82:3045–3067, 2010.

[13] B. Andrei Bernevig, Taylor L. Hughes, and Shou-Cheng Zhang. Quantum spin Hall effect and topological phase transition in HgTe quantum wells. *Science*, 314(5806):1757–1761, 2006.

[14] G. Juzeliūnas, Julius Ruseckas, and Jean Dalibard. Generalized Rashba-Dresselhaus spin-orbit coupling for cold atoms. *Phys. Rev. A*, 81(5):053403, 2010.

[15] Brandon M. Anderson, Gediminas Juzeliūnas, Victor M. Galitski, and I. B. Spielman. Synthetic 3D spin-orbit coupling. *Phys. Rev. Lett.*, 108:235301, Jun 2012.

[16] D. L. Campbell, R. M. Price, A. Putra, A. Valdes-Curiel, D. Trypogeorgos, and I. B. Spielman. Itinerant magnetism in spin-orbit coupled Bose gases. *arXiv:1501.05984*, 2015.

[17] Tin-Lun Ho and Shizhong Zhang. Bose-Einstein condensates with spin-orbit interaction. *Phys. Rev. Lett.*, 107:150403, Oct 2011.

[18] T. D. Stanescu, B. Anderson, and V. Galitski. Spin-orbit coupled Bose-Einstein condensates. *Phys. Rev. A*, 78(2):023616, 2008.

[19] Tigran A. Sedrakyan, Alex Kamenev, and Leonid I. Glazman. Composite fermion state of spin-orbit-coupled bosons. *Phys. Rev. A*, 86:063639, Dec 2012.

[20] Lei Jiang, Xia-Ji Liu, Hui Hu, and Han Pu. Rashba spin-orbit-coupled atomic Fermi gases. *Phys. Rev. A*, 84:063618, Dec 2011.

[21] C. J. Pethick and H. Smith. *Bose-Einstein Condensation in Dilute Gases*. Cambridge University Press, 2nd edition, 2008.

[22] M Le Bellac, F. Mortessagne, and G. G. Batrouni. *Equilibrium and Non-Equilibrium Satistical Thermodynamics*. Cambridge University Press, 2006.

[23] H. Metcalf and P. van der Straten. *Laser Cooling and Trapping*. Springer, 1999.

[24] A. Derevianko, J. F. Babb, and A. Dalgarno. High-precision calculations of van der Waals coefficients for heteronuclear alkali-metal dimers. *Phys. Rev. A*, 63:052704, Apr 2001.

[25] ERI Abraham, WI McAlexander, JM Gerton, RG Hulet, R Côté, and A Dalgarno. Triplet s-wave resonance in ^{6}Li collisions and scattering lengths of ^{6}Li and ^{7}Li. *Physical Review-Section A-Atomic Molecular and Optical Physics*, 55(5):R3299, 1997.

[26] F. A. van Abeelen and B. J. Verhaar. Time-dependent Feshbach resonance scattering and anomalous decay of a Na Bose-Einstein condensate. *Phys. Rev. Lett.*, 83:1550–1553, Aug 1999.

[27] John L. Bohn, James P. Burke, Chris H. Greene, H. Wang, P. L. Gould, and W. C. Stwalley. Collisional properties of ultracold Potassium: Consequences for degenerate Bose and Fermi gases. *Phys. Rev. A*, 59:3660–3664, May 1999.

[28] P. S. Julienne, F. H. Mies, E. Tiesinga, and C. J. Williams. Collisional stability of double Bose condensates. *Phys. Rev. Lett.*, 78:1880–1883, Mar 1997.

[29] Paul J. Leo, Carl J. Williams, and Paul S. Julienne. Collision properties of ultracold ^{133}Cs atoms. *Phys. Rev. Lett.*, 85:2721–2724, Sep 2000.

[30] Jordan M. Gerton, Dmitry Strekalov, Ionut Prodan, and Randall G. Hulet. Direct observation of growth and collapse of a Bose-Einstein condensate with attractive interactions. *Nature*, 408(6813):692–695, 12 2000.

[31] Y. Castin and R. Dum. Bose-Einstein condensates in time dependent traps. *Phys. Rev. Lett.*, 77(27):5315–5319, Dec 1996.

[32] A. Altland and B. Simons. *Condensed matter field theory.* Cambridge University Press, second edition, 2010.

[33] Y.-J. Lin, A. R. Perry, R. L. Compton, I. B. Spielman, and J. V. Porto. Rapid production of ^{87}Rb Bose-Einstein condensates in a combined magnetic and optical potential. *Physical Review A (Atomic, Molecular, and Optical Physics)*, 79(6):063631, 2009.

[34] C. Silber, S. Günther, C. Marzok, B. Deh, Ph. W. Courteille, and C. Zimmermann. Quantum-degenerate mixture of fermionic Lithium and bosonic Rubidium gases. *Phys. Rev. Lett.*, 95(17):170408, 2005.

[35] B. Deh, C. Marzok, C. Zimmermann, and Ph. W. Courteille. Feshbach resonances in mixtures of ulatracold ^{6}Li and ^{87}Rb gases. *arxiv:0709.4554*, 2007.

[36] C. Marzok, B. Deh, C. Zimmermann, Ph. W. Courteille, E. Tiemann, Y. V. Vanne, and A. Saenz. Feshbach resonances in an ultracold ^{7}Li and ^{87}Rb mixture. *Phys. Rev. A*, 79(1):012717, Jan 2009.

[37] Daniel A. Steck. Rubidium 87 d line data. 2003.

[38] Richard C Mockler. *Atomic Beam Frequency Standards*, volume 15. National Bureau of Standards, Radio Standards Division, Boulder, Colorado, 1961.

[39] W. Ketterle, D. S. Durfee, and D. M. Stamper-Kurn. Making, probing and understanding Bose-Einstein condensates. In *La condensazione di Bose-Einstein nei gas atomici*, volume CXL of *Scuola Internazionale di Fisica*. Societa Italiana di Fisica, 1999.

[40] Jan Rubbmark, Micheal Kash, Micheal Littman, and Daniel Kleppner. Dynamical effects at avoided level crossings: a study of the Landau-Zener effect using Rydberg atoms. *Phys. Rev. A*, 23(6), June 1981.

[41] Andrew Putnis. *An Introduction to Mineral Sciences*. Cambridge University Press, October 1992.

[42] Alex Hubert and Rudolf Schäfer. *Magnetic Domains*, volume 21. Springer, 1998.

[43] T W B Kibble. Topology of cosmic domains and strings. *J. Phys. A: Math. Gen.*, 9:1387, October 1976.

[44] Chad N Weiler, Tyler W Neely, David R Scherer, Ashton S Bradley, Matthew J Davis, and Brian P Anderson. Spontaneous vortices in the formation of Bose–Einstein condensates. *Nature*, 455(7215):948–951, October 2008.

[45] D. M. Weld, P. Medley, H. Miyake, D. Hucul, D. E. Pritchard, and W. Ketterle. Spin gradient thermometry for ultracold atoms in optical lattices. *Physical Review Letters*, 103(24):245301, 2009.

[46] M Hoefer, J Chang, C Hamner, and P. Engels. Dark-dark solitons and modulational instability in miscible two-component Bose-Einstein condensates. *Phys. Rev. A*, 84(4):041605, October 2011.

[47] D. S. Hall, M. R. Matthews, J. R. Ensher, C. E. Wieman, and E. A. Cornell. Dynamics of component separation in a binary mixture of Bose-Einstein condensates. *Phys. Rev. Lett.*, 81(8):1539–1542, 1998.

[48] K M Mertes, J W Merrill, R Carretero-González, D J Frantzeskakis, P G Kevrekidis, and D. S. Hall. Nonequilibrium dynamics and superfluid ring excitations in binary Bose-Einstein condensates. *Phys. Rev. Lett.*, 99(19):190402, November 2007.

[49] J. Guzman, G.-B. Jo, A. N. Wenz, K. W. Murch, C. K. Thomas, and D. M. Stamper-Kurn. Long-time-scale dynamics of spin textures in a degenerate $f = 1$ ^{87}Rb spinor Bose gas. *Phys. Rev. A*, 84:063625, Dec 2011.

[50] J. Stenger, S. Inouye, D. M. Stamper-Kurn, H. J. Miesner, A. P. Chikkatur, and W. Ketterle. Spin domains in ground-state Bose-Einstein condensates. *Nature*, 396(6709):345–348, 11 1998.

[51] Wenxian Zhang, D. L. Zhou, M.-S. Chang, M. S. Chapman, and L. You. Dynamical instability and domain formation in a spin-1 Bose-Einstein condensate. *Phys. Rev. Lett.*, 95(18):180403, Oct 2005.

[52] L E Sadler, J M Higbie, S. R. Leslie, M. Vengalattore, and D. M. Stamper-Kurn. Spontaneous symmetry breaking in a quenched ferromagnetic spinor Bose–Einstein condensate. *Nature*, 443(7109):312–315, September 2006.

[53] M. Vengalattore, J. Guzman, S. R. Leslie, F. Serwane, and D. M. Stamper-Kurn. Periodic spin textures in a degenerate f=1 ^{87}Rb spinor Bose gas. *Phys. Rev. A*, 81(5):053612, May 2010.

[54] E Bookjans, A Vinit, and C Raman. Quantum phase transition in an antiferromagnetic spinor Bose-Einstein condensate. *Phys. Rev. Lett.*, 107(19):195306, November 2011.

[55] Dan M. Stamper-Kurn and Masahito Ueda. Spinor Bose gases: Symmetries, magnetism, and quantum dynamics. *Rev. Mod. Phys.*, 85:1191–1244, Jul 2013.

[56] A. Marte, T. Volz, J. Schuster, S. Dürr, G. Rempe, E. G. M. van Kempen, and B. J. Verhaar. Feshbach resonances in Rubidium 87: Precision measurement and analysis. *Physical Review Letters*, 89(28):283202, 2002.

[57] Tin-Lun Ho. Spinor Bose condensates in optical traps. *Phys. Rev. Lett.*, 81(4):742–745, Jul 1998.

[58] T. Ohmi and K. Machida. Bose-Einstein condensation with internal degrees of freedom in alkali atom gases. *J. Phys. Soc. Jpn.*, 67(6):1822–1825, 1998.

[59] E. G. M. van Kempen, S. J. J. M. F. Kokkelmans, D. J. Heinzen, and B. J. Verhaar. Interisotope determination of ultracold Rubidium interactions from three high-precision experiments. *Phys. Rev. Lett.*, 88:093201, 2002.

[60] Kevin E Strecker, Guthrie B Partridge, Andrew G Truscott, and Randall G Hulet. Formation and propagation of matter-wave soliton trains. *Nature*, 417(6885):150–153, May 2002.

[61] S E Pollack, D Dries, M Junker, Y P Chen, T A Corcovilos, and R G Hulet. Extreme tunability of interactions in a ^{7}Li Bose-Einstein condensate. *Phys. Rev. Lett.*, 102(9):090402, March 2009.

[62] Elizabeth A Donley, Neil R Claussen, Simon L Cornish, Jacob L Roberts, Eric A Cornell, and Carl E Wieman. Dynamics of collapsing and exploding Bose-Einstein condensates. *Nature*, 412(6844):295–299, July 2001.

[63] Z. Dutton and C. Clark. Effective one-component description of two-component Bose-Einstein condensate dynamics. *Phys. Rev. A*, 71(6):063618, 2005.

[64] Yuki Kawaguchi and Masahito Ueda. Spinor Bose–Einstein condensates. *Physics Reports*, 520(5):253 – 381, 2012. Spinor Bose–Einstein condensates.

[65] W. Gerlach and O. Stern. Der experimentelle nachweis der richtungsquantelung im magnetfeld. *Zeitschrift für Physik A*, 9(1):349–532, 1922.

[66] P. B. Blakie, A. S. Bradley, M. J. Davis, R. J. Ballagh, and C. W. Gardiner. Dynamics and statistical mechanics of ultra-cold Bose gases using c-field techniques. *Advances in Physics*, 57(5):363 – 455, 2008.

[67] Chunji Wang, Chao Gao, Chao-Ming Jian, and Hui Zhai. Spin-Orbit Coupled Spinor Bose-Einstein Condensates. *Phys. Rev. Lett.*, 105(16):160403, October 2010.

[68] Yongping Zhang, Li Mao, and Chuanwei Zhang. Mean-field dynamics of spin-orbit coupled Bose-Einstein condensates. *Phys. Rev. Lett.*, 108:035302, Jan 2012.

[69] Victor Galitski and Ian B. Spielman. Spin–orbit coupling in quantum gases. *Nature*, 494(7435):49–54, February 2013.

[70] K. Osterloh, M. Baig, L. Santos, P. Zoller, and M. Lewenstein. Cold atoms in non-abelian gauge potentials: From the Hofstadter "moth" to lattice gauge theory. *Phys. Rev. Lett.*, 95:010403, 2005.

[71] J. Ruseckas, G. Juzeliūnas, P. Öhberg, and M. Fleischhauer. Non-abelian gauge potentials for ultracold atoms with degenerate dark states. *Phys. Rev. Lett.*, 95(1):010404, 2005.

[72] Xiong-Jun Liu, Mario F. Borunda, Xin Liu, and Jairo Sinova. Effect of induced spin-orbit coupling for atoms via laser fields. *Phys. Rev. Lett.*, 102:046402, 2009.

[73] L. E. Sadler. *Dynamics of a Spin 1 Ferromagnetic Condensate*. PhD thesis, Berkeley, 2006.

[74] Stefan Natu, Xiaopeng Li, and William Cole. Striped ferronematic ground states in a spin-orbit coupled s=1 Bose gas. *arXiv*, (arXiv:1411.2990), 2014.

[75] Zhihao Lan and Patrik Öhberg. Raman-dressed spin-1 spin-orbit-coupled quantum gas. *Phys. Rev. A*, 89(2):023630, February 2014.

[76] Amikam Aharoni. *Introduction to the theory of ferromagnetism*. Oxford University Press, March 2011.

[77] Anatole Abragam. Nuclear ferromagnetism and ant ferromagnetism. *Contemporary Physics*, 33(5):305–312, September 1992.

[78] Jochen Kronjäger, Christoph Becker, Parvis Soltan-Panahi, Kai Bongs, and Klaus Sengstock. Spontaneous pattern formation in an antiferromagnetic quantum gas. *Phys. Rev. Lett.*, 105(9):090402, Aug 2010.

[79] Jonathan Simon, Waseem S. Bakr, Ruichao Ma, M Eric Tai, Philipp M Preiss, and Markus Greiner. Quantum simulation of antiferromagnetic spin chains in an optical lattice. *Nature*, 472(7343):307–312, April 2011.

[80] D Greif, T Uehlinger, G Jotzu, L Tarruell, and T. Esslinger. Short-range quantum magnetism of ultracold fermions in an optical lattice. *Science*, 240:1307–1310, June 2013.

[81] Russell A. Hart, Pedro M Duarte, Tsung-Lin Yang, Xinxing Liu, Thereza Paiva, Ehsan Khatami, R T Scalettar, Nandini Trivedi, David A Huse, and

Randall G Hulet. Observation of antiferromagnetic correlations in the Hubbard model with ultracold atoms. July 2014.

[82] E Stoner. Atomic moments in ferromagnetic alloys with non- ferromagnetic elements. *Philos. Mag.*, 15:1018–1034, August 1933.

[83] Shang-Shun Zhang, Jinwu Ye, and Wu-Ming Liu. Itinerant ferromagnetism in repulsively interacting spin-orbit coupled Fermi gas. March 2014.

[84] Juraj Radić, Stefan S Natu, and V Galitski. Stoner ferromagnetism in a thermal pseudospin-1/2 Bose gas. *Phys. Rev. Lett.*, 113(18):185302, September 2014.

[85] Ciarán Hickey and Arun Paramekanti. Thermal phase transitions of strongly correlated bosons with spin-orbit coupling. *Phys. Rev. Lett.*, 113(26):265302, September 2014.

[86] Tudor D. Stanescu and Victor Galitski. Spin relaxation in a generic two-dimensional spin-orbit coupled system. *Phys. Rev. B*, 75(12):125307, Mar 2007.

[87] J. D. Koralek, C. P. Weber, J. Orenstein, B. A. Bernevig, Shou-Cheng Zhang, S. Mack, and D. D. Awschalom. Emergence of the persistent spin helix in semiconductor quantum wells. *Nature*, 458:610–613, 2009.

[88] Ryan Barnett, Ari Turner, and Eugene Demler. Classifying novel phases of spinor atoms. *Phys. Rev. Lett.*, 97(18):180412, November 2006.

[89] Weizhu Bao, Dieter Jaksch, and Peter A. Markowich. Numerical solution of the Gross-Pitaevskii equation for Bose-Einstein condensation. *Journal of Computational Physics*, 187(1):318–342, 2003.

[90] M. V. Berry. Quantal phase factors accompanying adiabatic changes. *Proc. Roy. Soc. London A*, 392:45–57, 1984.

[91] R. Jackiw. *Comments At. Mol. Phys.*, 21:71, 1988.

[92] J. Moody, A. Shapere, and F. Wilczek. Realizations of magnetic-monopole gauge fields: Diatoms and spin precession. *Phys. Rev. Lett.*, 56(9):893, 1986.

[93] A. Bohm, B. Kendrick, M. E. Loewe, and L. J. Boya. The Berry connection and Born-Oppenheimer method. *J. Math. Phys.*, 33(3):977, 1992.

[94] A. Zee. Non-abelian gauge structure in nuclear quadrupole resonance. *Phys. Rev. A*, 38:1, 1988.

[95] Shapere. *Geometric Phases in Physics*. World Scientific, Singapore, 1989.

[96] C. Alden Mead. The geometric phase in molecular physics. *Rev. Mod. Phys.*, 64:51, 1992.

[97] A. Bohm, A. Mostafazadeh, H. Koizumi, Q. Niu, and J. Zwanziger. *Geometric Phases in Quantum Systems*. Springer, Berlin, Heidelberg, New York, 2003.

[98] D. Xiao, M.-C. Chang, and Q.Niu. Berry phase effects on electronic properties. *Rev. Mod. Phys*, 82:1959, 2010.

[99] R. Dum and M. Olshanii. Gauge structures in atom-laser interaction: Bloch oscillations in a dark lattice. *Phys. Rev. Lett.*, 76:1788–1791, 1996.

[100] P. M. Visser and G. Nienhuis. Geometric potentials for subrecoil dynamics. *Phys. Rev. A*, 57:4581–4591, Jun 1998.

[101] S. K. Dutta, B. K. Teo, and G. Raithel. Tunneling dynamics and gauge potentials in optical lattices. *Phys. Rev. Lett.*, 83:1934–1937, Sep 1999.

[102] M. P. A. Fisher, P. B. Weichman, G. Grinstein, and D. S. Fisher. Boson localization and the superfluid-insulator transition. *Physical Review B*, 40:546–570, 1989.

[103] M. Greiner, O. Mandel, T. Esslinger, T.W. Hänsch, and I. Bloch. Quantum phase transition from a superfluid to a Mott insulator in a gas of ultracold atoms. *Nature*, 415:39–44, 2002.

[104] K. Jiménez-García, R. L. Compton, Y.-J. Lin, W. D. Phillips, J. V. Porto, and I. B. Spielman. Phases of a two-dimensional Bose gas in an optical lattice. *Phys. Rev. Lett.*, 105(11):110401, Sep 2010.

[105] S. Trotzky, L. Pollet, F. Gerbier, U. Schnorrberger, I. Bloch, N. V. Prokof/'ev, B. Svistunov, and M. Troyer. Suppression of the critical temperature for superfluidity near the Mott transition. *Nat Phys*, 6(12):998–1004, 12 2010.

[106] Yu A Bychkov and E I Rashba. Oscillatory effects and the magnetic susceptibility of carriers in inversion layers. *J . Phys. C*, 17(33):6039, 1984.

[107] Shun-Qing Shen. Spin Hall effect and Berry phase in two-dimensional electron gas. *Phys. Rev. B*, 70:081311, Aug 2004.

[108] Chao-Ming Jian and Hui Zhai. Paired superfluidity and fractionalized vortices in systems of spin-orbit coupled bosons. *Phys. Rev. B*, 84:060508, Aug 2011.

[109] Jonas Larson and Erik Sjöqvist. Jahn-Teller-induced Berry phase in spin-orbit-coupled Bose-Einstein condensates. *Phys. Rev. A*, 79:043627, Apr 2009.

[110] Hui Hu, Lei Jiang, Xia-Ji Liu, and Han Pu. Probing anisotropic superfluidity in atomic Fermi gases with Rashba spin-orbit coupling. *Phys. Rev. Lett.*, 107:195304, Nov 2011.

[111] D. L. Campbell, G. Juzeliūnas, and I. B. Spielman. Realistic Rashba and Dresselhaus spin-orbit coupling for neutral atoms. *Phys. Rev. A*, 84:025602, Aug 2011.

[112] C. B. Alcock. Vapor pressure equations for the metallic elements. Technical report, 2000.

[113] S. C. Bell, M. Junker, M. Jasperse, L. D. Turner, Y.-J. Lin, I. B. Spielman, and R. E. Scholten. A slow atom source using a collimated effusive oven and a single-layer variable pitch coil Zeeman slower. *Review of Scientific Instruments*, 81(1):013105, 2010.

[114] F. B. Dunning and R. G. Hulet, editors. *Atomic, molecular, and optical physics: atoms and molecules*, volume 29B of *Experimental Methods in the physical sciences*. Academic Press, 1996.

[115] C.J. Foot. *Atomic Physics*. Oxford Master series in atomic, optical and laser physics. Oxford University Press, 2011.

[116] J. Dalibard and C. Cohen-Tannoudji. Laser cooling below the Doppler limit by polarization gradients: simple theoretical models. *J. Opt. Soc. Am. B*, 6(11):2023–2045, Nov 1989.

[117] W. Ketterle and H.-J. Miesner. Coherence properties of Bose–Einstein condensates and atom lasers. *Phys. Rev. A*, 56:3291, 1996.

[118] J Söding, D Guéry-Odelin, P Desbiolles, F Chevy, H Inamori, and J Dalibard. Three-body decay of a rubidium Bose–Einstein condensate. *Applied physics B*, 69(4):257–261, 1999.

[119] B. D. Esry, Chris H. Greene, and James P. Burke. Recombination of three atoms in the ultracold limit. *Phys. Rev. Lett.*, 83(9):1751–1754, Aug 1999.

[120] E. A. Cornell, J. R. Ensher, and C. E. Wieman. Experiments in dilute atomic Bose-Einstein condensation. In M. Inguscio, S. Stringari, and C. E. Wieman, editors, *La condensazione di Bose-Einstein nei gas atomici*, volume CXL of *Scuola Internazionale di Fisica*. Societa Italiana di Fisica, 1999.